

LITHIUM-AIR BATTERY CATHODES:
A STUDY ON THE EFFECTS OF FABRICATION METHOD
AND ACTIVE MATERIAL PROPERTIES ON BATTERY PERFORMANCE

A Dissertation

Presented to the Faculty of the Graduate School

of Cornell University

In Accordance of the Requirements of Fulfillment for

the Degree of Doctor of Philosophy

by

Christopher David Klaassen

August 2021

© 2021 Christopher David Klaassen

LITHIUM-AIR BATTERY CATHODES: A STUDY ON THE EFFECTS OF FABRICATION
METHOD AND ACTIVE MATERIAL PROPERTIES ON ELECTROCHEMICAL
DISCHARGE

Christopher David Klaassen, Ph.D.

Cornell University 2021

Abstract

Lithium Air (Li-Air) batteries have received scientific interest due to their high gravimetric energy density, which is the largest of the well known battery systems; however, the reactive chemistry of these batteries, which is the source of their high energy density, is very taxing on the battery components, creating inefficiencies that limit the progress of these batteries to becoming the replacement for the burning of fossil fuels. Although many different research groups have studied many of the different facets of these challenges, in this thesis, the effects of fabrication methods on structural properties and electrochemical performance are studied. These considerations were limited to the carbon cathode system for multiple reasons. Carbon materials, like activated carbon, graphene, reduced graphene oxide (rGO), carbon nanotubes, etc., were considered due to their relative cheapness and are already considered within the battery industry for traditional battery electrodes for other battery systems and therefore may be more easily adopted by industry for the future production of Li-Air batteries. Additionally, the focus was placed entirely on the battery cathode, as it is normally on the cathode surface where reactions, both desired and parasitic, are taking place.

Within this thesis, many different considerations and studies were performed for the Li-Air battery cathode. For experimental laboratory work, the pros and cons of dropcasting

electrospraying, and electrospinning were considered for Li-Air battery cathode fabrication. The later two methods are highlighted for their scalability for industrial production line and for the ease at which electrocatalysts can be added into the carbon matrix during the fabrication process. Many different carbon materials, such as rGO, graphene nanoribbons (GNR), and graphenes, of which the latter was made through the industrially scalable Taylor Couette Reactor (TCR) system, and electrocatalysts, such as Molybdenum Carbide (Mo_2C), were compared for their different properties as cathode active materials. These were tested both alone and in different morphological hierarchies such as stacked layers and within/on carbon fibers. Additionally, porous carbon cathodes were mathematically modeled via two different numerical model systems in an attempt to parse out the contributions and effects of the different physical and electrochemical characteristics of different Li-Air battery systems, with a level of control that would not be obtainable within traditional experimental battery methods. Altogether, this work seeks to prove the benefits of the air-controlled electrospray (ACES) technique over traditional battery fabrication methods, while still producing a wholistic understanding of both traditional and improved battery cathode systems through both physical and simulated testing of these varying carbon cathode systems.

PRE-THESIS INFORMATION SECTION

BIOGRAPHICAL SKETCH

Chris Klaassen was born pre-mature on June 13th, 1993 and grew up in Broken Arrow, Oklahoma. Taking to the liking of the sciences at an early age, especially chemistry, they went on to receive a Bachelor's Degree in Chemical Engineering from Texas Tech University. While there, they developed a fondness for polymer processing and 2D nanomaterials through their undergraduate research. Joining the PhD program of the Chemical and Biomolecular Engineering Department of Cornell University in Fall 2016, they joined the lab of Professor Yang Lak Joo due to his work on the fascinating intersection of nanomaterials for energy applications. In Professor Joo's group, he had the opportunity to dive deeply into the fabrication and characterization of cathodes for lithium air batteries and for their future use in energy storage applications.

ACKNOWLEDGMENTS

I would like to express my appreciation for my advisor, Professor Yong Lak Joo, for his guidance, encouragement, and tenacity during my varied PhD studies. Additionally, I want to thank my committee members, Professor Tobias Hanrath and Professor Jin Suntivich, for their support and the different perspectives they brought to my projects. Within the Joo Group, I'd like to thank Dr. Joe Carlin, Dr. Andrew Shah, Dr. Mounica Divvela, Dr. Somayeh Zamani, Dr. George Shebert, Dr. Mohammad AlAmer, and Mr. Yash Joshi for their guidance, research assistance, and camaraderie. I sincerely would like to thank Dr. Joe Carlin for the same, and for his friendship and support throughout the years. Lastly, I'd like to thank those whose emotional support made this degree possible, my family, my many wonderful friends here at Cornell, the continual support of my friends from Texas Tech, and Merely Technically a Group. May we all have many wonderful adventures ahead.

TABLE OF CONTENTS

PRE-THESIS INFORMATION SECTION	4
BIOGRAPHICAL SKETCH	4
ACKNOWLEDGMENTS	5
TABLE OF CONTENTS	6
LIST OF FIGURES	9
LIST OF TABLES	13
LIST OF ABBREVIATIONS	14
Chapter 1: Introduction and Background to Lithium Air Batteries	16
1.1 Role of Energy Storage	16
1.2 Lithium Air Battery Basics	17
1.3 Cell Types (coin vs. Swagelok)	20
1.4 Electrolyte Solvent Types (Aqueous vs. Organic vs. Hybrid)	23
1.5 Materials for Lithium Air Cathodes and Their Preparation	25
1.6 Electrocatalysts	28
1.7 Appendices	30
Chapter 2: Layered Cathodes	35
2.1 Introduction	35
2.1.1 Benefits of Layering/Mixing in Other Systems	35
2.1.2 Concept for Li-Air Layered Cathode	37
2.1.3 Previous Group Work in Dropcast Cathode System	39
2.2 Experimental Methods	40
2.2.1 Solution Preparation	40
2.2.2 Carbon Substrate Preparation	40
2.2.3 Layering and Loading Controls	41
2.2.4 Layered ACES Cathodes	41
2.2.5 Electrolyte and Separator	43
2.2.6 Cell Assembly	43
2.2.7 Electrochemical Characterization	44
2.2.8 Structural Characterization	45
2.3 Results and Discussion	46
2.4 Conclusion	64

2.5 Appendices.....	65
Chapter 3: Single Layer rGO Cathode Fabrication Techniques for Li-O₂ Batteries.....	68
3.1. Introduction.....	68
3.2. Experimental Section.....	74
3.2.1 Solution Preparation.....	74
3.2.2 Carbon Substrate Preparation	75
3.2.3 Dropcasting.....	75
3.2.4 Air-Controlled Electrospraying (ACES).....	76
3.2.5 Spin Coating	77
3.2.6 Slurry Coating.....	78
3.2.7 Electrolyte and Separator	79
3.2.8 Cell Assembly	79
3.2.9 Electrochemical Characterization	80
3.2.10 Structural Characterization.....	81
3.3. Results and Discussion.....	83
3.3.1 Slurry Coating and Spincoating Issues	83
3.3.2 Structure and Morphological Comparison.....	86
3.3.3 Electrochemical Comparisons	94
3.4. Conclusion	100
3.5 Future Recycling Considerations	101
3.6. Appendices.....	103
Chapter 4: Numerical Simulations of Lithium Air Batteries.....	109
4.1 Introduction.....	109
4.2 Theoretical Model – GLS Based	110
4.2.1 Electrochemical Reactions	110
4.2.2 Governing Equation and Mass Transport.....	114
4.2.3. Cell Voltages	115
4.2.4 Cell Structure and Numerical Implementation.....	116
4.2.5 Nucleation and Growth of Lithium Peroxide	119
4.3 Results and Discussion – GLS.....	122
4.4 Conclusion and Future Work – GLS	137
4.5 Theoretical Model – Lau Based	137
4.6 Results and Discussion - Lau.....	141
4.8 Appendices.....	154
Chapter 5: Continuations and Expansions: Fibrous and Catalytic Cathodes	158

5.1 Introduction.....	158
5.2 Experimental Methods	161
5.2.1. ACES Solution Preparation	161
5.2.2 GAES Solution Preparation.....	163
5.2.3. Air Controlled Electro spray (ACES) for Binderless, Substrateless, and rGO-Mo₂C Cathodes.....	163
5.2.4. PAN Fibers from GAES	164
5.2.5 General Stabilization, Carbothermal Reduction, and Activation	165
5.2.5. Compressed PAN Fibers	166
5.2.6 Carbon Substrate Preparation	166
5.2.7 Electrolyte and Separator	167
5.2.8 Cell Assembly	167
5.3 Results and Discussion.....	169
5.3.1 Binderless and Substrateless Electro spray Cathodes	169
5.3.2. Gas-Assisted Electro spinning of PAN for CNF Cathodes.....	176
5.3.3. Fused Fiber PAN Mats	180
5.3.4 Catalytic Fibers: PAN – Mo Cathodes.....	184
5.3.5 Future Catalysis Work – Taylor Couette Reactor (TCR) Graphene with Imbedded Metal Catalysts.....	194
5.4 Conclusions.....	204
5.5 Appendices.....	206

LIST OF FIGURES

Figure 1.1: Energy Density Comparison of Common Batteries to Gasoline

Figure 1.2: Image and schematic of Swagelok-type Li-O₂ battery, highlighting the electrochemical cell and the cathode's three-phase interface

Figure 1.3: Li-O₂ Battery Casings Diagram

Figure 1.4: Glass Fiber (aka. Silica Fiber) Separator Images

Figure 1.5: Carbon Paper Substrate Images

Figure 1.6: Air-Controlled Electrospraying Diagram

Figure 2.1: Design Concept of Layered Cathode Approach to Li-O₂ Cathodes

Figure 2.2: Dr. Kim's Past Dropcasting Work for Comparison

Figure 2.3: Layered Cathode Fabrication Considerations

Figure 2.4: Electron Microscopy of Carbon Powders

Figure 2.5: 1-Layer Cathodes

Figure 2.6: 1-Layer Pore Data

Figure 2.7: 1-Layer CV Data

Figure 2.8: 1-Layer EIS Data

Figure 2.9: Multilayer BET Data

Figure 2.10: Multilayer Cross-Section SEM Images

Figure 2.11: Layered Cathode EIS

Figure 2.12: Layered Cathode Battery Cycling Data

Figure 3.1: Image and schematic of Swagelok-type Li-O₂ battery, highlighting the electrochemical cell and the cathode's three-phase interface.

Figure 3.2: Schematics of 4 different fabrication processes, from top to bottom: Dropcasting, Air-Controlled Electro spray (ACES), Spincoating, and Slurry Coating

Figure 3.3: rGO Powder Information

Figure 3.4: Spin Coating Images

Figure 3.5: Slurry Coating Images

Figure 3.6: SEM Morphology Images

Figure 3.7: Thiele modulus ϕ and effective surface area explanation information

Figure 3.8: Pore Morphology Graphs

Figure 3.9: Electrochemical Characterizations

Figure 3.10: Deep Discharge Comparison

Figure 3.11: Limited Capacity Cycling Comparison

Figure 4.1: Numerical discretization of Li-O₂ battery, with inner and outer cathode areas and external O₂ diffusion

Figure 4.2: Superoxide Formation Reaction Error Consideration

Figure 4.3: Scan of microporous surface area on capacity curves, with decreasing capacity increasing in overpotential and decreasing in capacity

Figure 4.4: Concentration and Diffusion Effects

Figure 4.5: Electrodeposition and Precipitation Rate Constant Effects

Figure 4.6: Fitting Parameter Effects

Figure 4.7: Electrodeposition vs. Disproportionation

Figure 4.8: Disproportionation Current Density and O₂ Diffusivity Sweeps

Figure 4.9: Lau *et al.* Results for Comparison

Figure 4.10: Surface Area and Time Step Considerations

Figure 4.11: Coverage Control Trials

Figure 4.12: Initial Nucleate Size Graphs

Figure 4.13: Finalized Nucleate Trials

Figure 5.1: Gas-Assisted Electrospinning (GAES) Diagram

Figure 5.2: Visual Comparison of ACES Cathodes

Figure 5.3: SEM Images of Substrateless Cathode

Figure 5.4: Pore Data for Binderless rGO Cathodes

Figure 5.5: SEM Images Binderless rGO Cathodes

Figure 5.6: Cycling Curve Comparisons

Figure 5.7: Pure PAN Fiber Mats in SEM and Macroscale

Figure 5.8: Carbothermal Reduction Process

Figure 5.9: Pore Area Graphs

Figure 5.10: Example CNF Battery Curve

Figure 5.11: Compressed Fiber Support Considerations

Figure 5.12: Macroscale Images of Compressed Fiber Mats

Figure 5.13: Macroscale Images of Fiber Mats

Figure 5.14: Fibers Before and After Carbothermal Reduction in SEM

Figure 5.15: XRD Data

Figure 5.16: Activated PAN-Mo Cathodes via SEM and EDX

Figure 5.17: Viscous Film on Separator After Discharge of Activated PAN-Mo Cathode via SEM, Elemental Analysis (EDX), and Raman

Figure 5.18: Activated PAN-Mo Cycling

Figure 5.19: SEM and EDX of Mo₂C in rGO ACES and Dropcast Cathodes

Figure 5.20: rGO-Mo₂C Battery Cycling

Figure 5.21: TCR Few-Layer Graphenes TEM

Figure 5.22: TCR Few-Layer Graphene Top-View SEM

Figure 5.23: TCR Few-Layer Graphene Cross-Section SEM

Figure 5.24: ACES Graphene Porometry Compared to ACES GNR

Figure 5.25: ACES Graphene Deep Discharge Cycling Curves

LIST OF TABLES

Table 2.1: Layered Cathode Mass Loading Breakdown.

Table 2.2: 2-Point Probe 1-Layer Conductivity

Table 2.3: Bulk Density

Table 3.1: Table of Comparable Values Between Dropcasting and ACES

Table 3.2: Limited Capacity Breakdown

Table 4.1: Reaction Parameters m Reaction Index, k_m Reaction Constant, n_m Electron Number, U_{eq0} Equilibrium Voltage, K_{sp} Solubility Constant

Table 4.2: Initial Condition Parameters: $D_{0,l}$ Diffusion Coefficient, M_i Molecular Weight, ρ_i Density, c_0 Initial Concentration, $\varepsilon_{0,i}$ Initial Volume Fraction

Table 4.3: Structural and Miscellaneous Parameters

Table 4.4: Lau Parameters from Paper

Table 4.5: Estimated and Probed Parameter Ranges

Table 4.6: Initial Nucleate Radius Test Information

Table 5.1: Binderless rGO Bulk Density Comparison

Table 5.2: 1L Graphene ACES Bulk Density

LIST OF ABBREVIATIONS

(In Order of Appearance)

Li-Ion: Lithium Ion

EV: Electric Vehicle

Li-O₂ or Li-Air: Lithium Oxygen or Lithium Air (interchangeable)

O₂: Oxygen

Li₂O: Lithium Oxide

Li₂O₂: Lithium Peroxide

Li: Lithium

ORR: Oxygen Reduction Reaction

OER: Oxygen Evolution Reaction

CO₂: Carbon Dioxide

FTIR: Fourier-transform infrared spectroscopy

XRD: X-Ray Diffraction

EDS or EDX: Energy-dispersive X-ray spectroscopy (interchangeable)

LiOH: Lithium Hydroxide

Li₂CO₃: Lithium Carbonate

N₂: Nitrogen

PTFE: Polytetrafluoroethylene

ACES: Air-Controlled Electrospinning

GAES: Gas-Assisted Electrospinning

Li-S: Lithium Sulfur

2-D: Two Dimensional

1-D: One Dimensional

CNT: Carbon Nanotube

GNR: Graphene Nanoribbon

CNF: Carbon Nanofiber

rGO: Reduced Graphene Oxide

GONR: Graphene Oxide Nanoribbon

IPA: Isopropyl Alcohol or Isopropanol (interchangeable)

LiCF₃SO₃: Lithium Triflate

DME: 1,2-dimethoxyethane

Ar: Argon

EIS: Electrochemical Impedance Spectroscopy

CV: Cyclic Voltammetry

SEM: Scanning Electron Microscopy

TEM: Transmission Electron Microscopy

BET: Brunauer-Emmett-Teller pore analysis

BJH: Barrett-Joyner-Halenda pore analysis

#L: Number of Layers (# can be 1, 3, 5, 7, or 9)

LiTFSI: Bis(trifluoromethane)sulfonimide lithium salt

LiI: Lithium Iodide salt

ZnO: Zinc Oxide

PVDF: Polyvinylidene Fluoride

NMP: N-Methyl-2-pyrrolidone

DMF: Dimethylformamide

LSV: Linear Sweep Voltammetry

FDM: Finite Difference Method

BV: Butler-Volmer

LiO₂: Lithium Superoxide

PAN: Polyacrylonitrile

Au: Gold

Pt: Platinum

Pd: Palladium

Ru: Ruthenium

MnO₂: Manganese(II) Oxide

RuO₂: Ruthenium(IV) Oxide

TiC: Titanium Carbide

Mo₂C: Molybdenum Carbide

MoO₂: Molybdenum Dioxide

LiMoO₃: Lithium Molybdenyl

DMSO: Dimethyl Sulfoxide

PMMA: Polymethyl Methacrylate

PET: Polyethylene Terephthalate

PI: Polyimide

TCR: Taylor Couette Reactor

Chapter 1: Introduction and Background to Lithium Air Batteries

1.1 Role of Energy Storage

Humans have always needed energy. More importantly, humans need ways to store energy for when they need it most. Over the past few centuries, the burning of plant and animal byproducts, such as oil and coal, have become major sources of electrical energy generation because of their relatively low monetary cost and their ability to be stopped and started quickly for instantaneous power generation. One area that this is extremely noticeable is within the private and commercial vehicle sector, where consumer demand causes tons of fossil fuels to be burned each year; however, this process does come with a rapidly increasing environmental cost, with CO₂ levels rapidly increasing and causing worldwide climate change and environmental damage.^[1-4] Due to the harrows of impending climate catastrophe, electrical energy storage in the form of batteries have been widely considered for use within both the transportation market and the power grid energy generation market.^[5-8] For personal automobiles, Lithium Ion (Li-Ion) Batteries, first developed in the 1970s, have become the major focus of electric vehicle (EV) manufactures because of their general stability over a long cycle life.^[9-11] Li-Ion batteries do have one major downside, which is that their energy density is relatively limited in compared to that of fossil fuels,^[4,5,12] meaning that large battery packs of many batteries in series and in parallel must be used to generate the same amount of energy as the explosive process contained within combustion engines. Because of this, many new battery types with more reactive battery chemistries have been considered by researchers, but with these new battery chemistries, additional new hazards and challenges must be considered and overcome for a new standard of EV battery to be made.

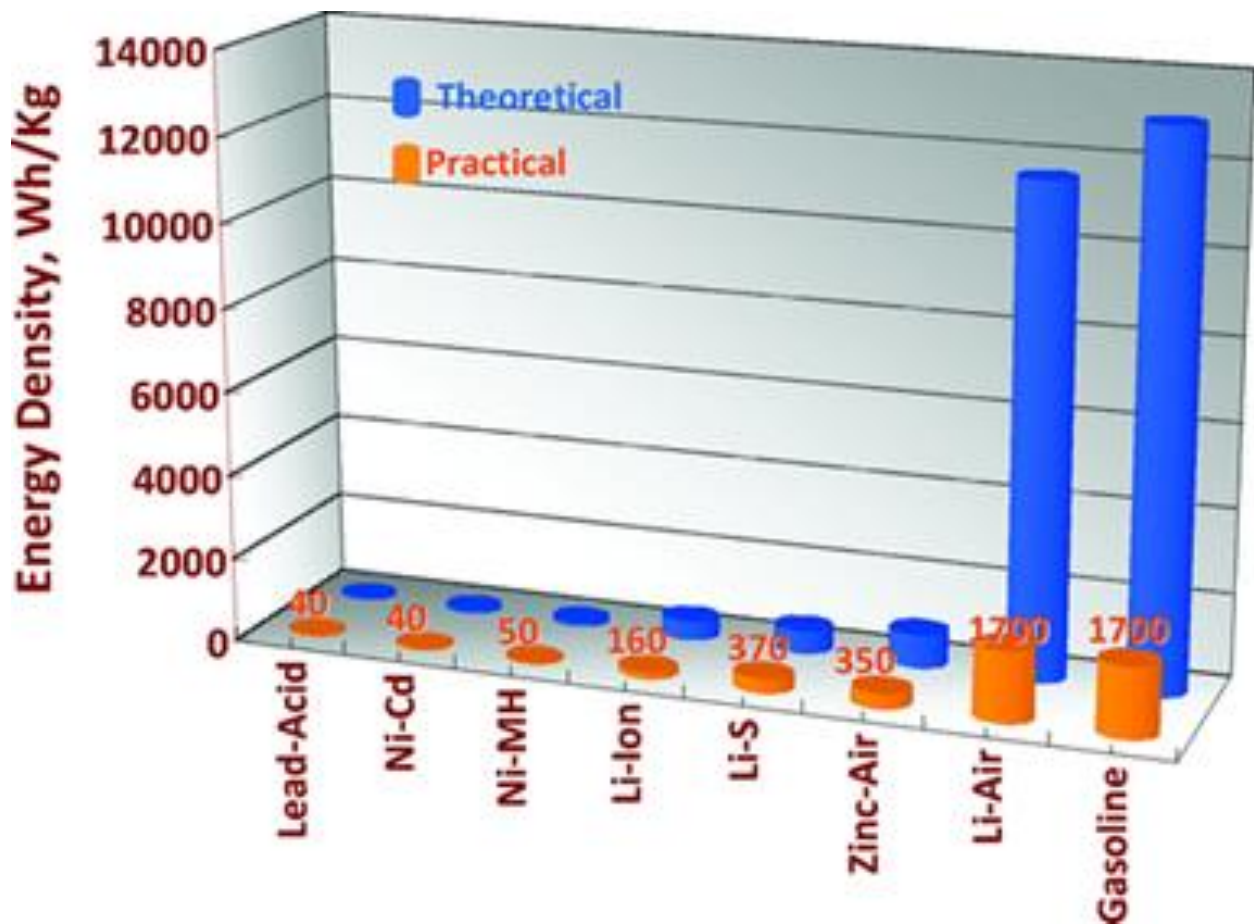


Figure 1.1: Energy Density Comparison of Common Batteries to Gasoline^[13]

1.2 Lithium Air Battery Basics

Although the Li-Ion battery has become the standard for secondary batteries, our ever-pressing need for more energy has fuel research into new battery chemistries. One such battery is the Lithium Air or Lithium Oxygen (Li-O₂) battery, which has been studied due to its high theoretical energy density of 1.17 kW*h/kg, which is near the theoretical energy density of the combustion of gasoline, at 1.3 kW*h/kg, as shown by Figure 1.1.^[4,5,12,13] With such a large theoretical energy density, and with the wheel-to-tank efficiency of gasoline combustion stalled around 15%, Li-O₂ batteries only need 18% efficiency to reach the effective energy output of gasoline combustion. Li-O₂ batteries reduce gaseous oxygen on an electrically-conductive, solid surface with lithium ions dissolved in the liquid electrolyte to form lithium oxide, Li₂O, and

lithium peroxide, Li_2O_2 [14], at the three-phase interface. [15] This proceeds by the net electrochemical reaction, $2\text{Li}^+(\text{aq}) + 2\text{e}^- + \text{O}_2(\text{g}) \leftrightarrow \text{Li}_2\text{O}_2(\text{s})$ ($E = 2.96 \text{ V}$ versus Li/Li^+) [16], where the forward reaction is the Oxygen Reduction Reaction (ORR) and the reverse reaction is the Oxygen Evolution Reaction (OER). The ORR is what gives this battery such a large energy density, but this reaction, and the components needed to create it, create many challenges that must be overcome before Li-O₂ batteries become adopted by the battery industry and consumers.

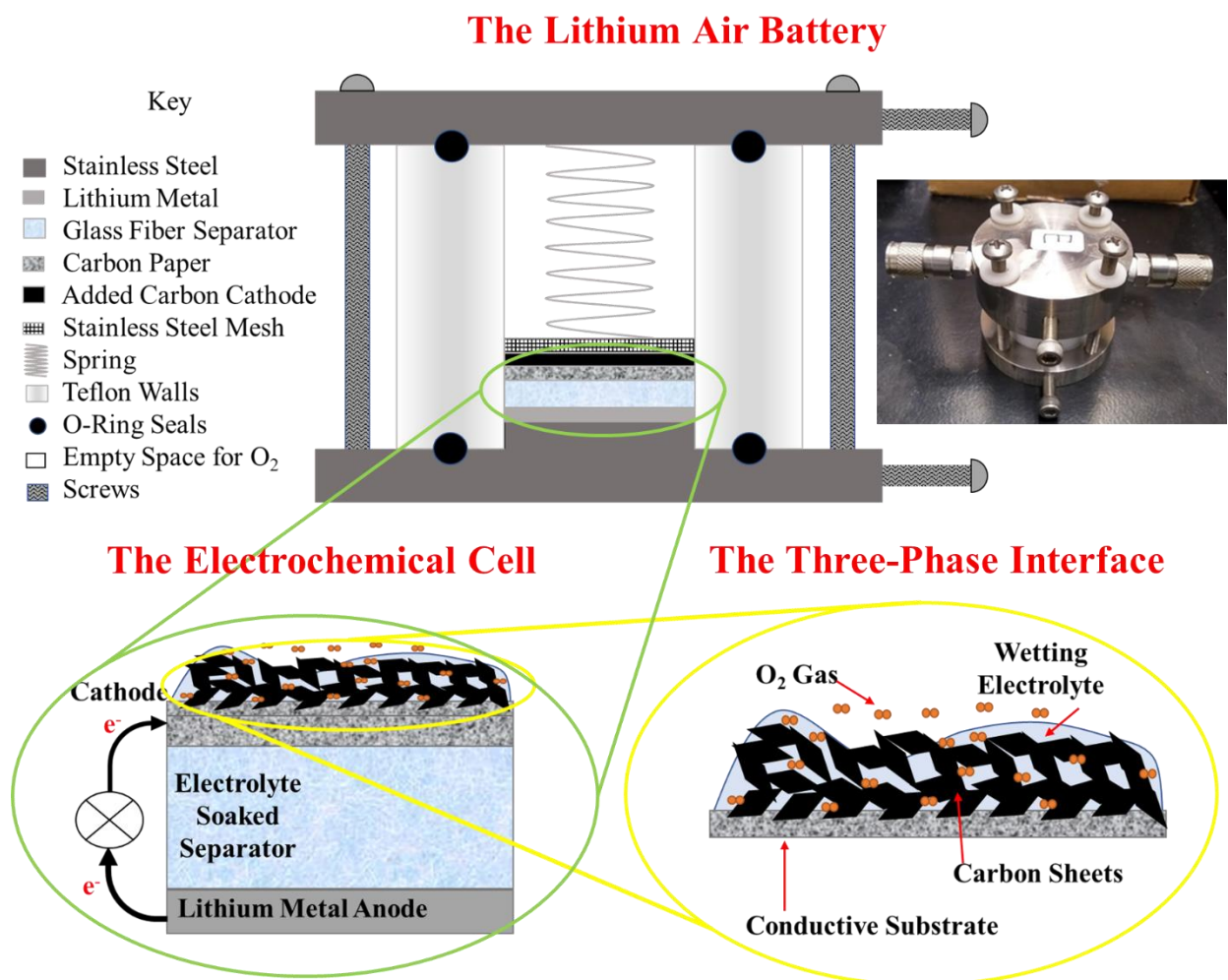


Figure 1.2: Image and schematic of Swagelok-type Li-O₂ battery, highlighting the electrochemical cell and the cathode’s three-phase interface

The basic Li-O₂ battery, as depicted in Figure 1.2, consists of a metal lithium anode, a separator, an electrolyte, and a cathode. The cathode has garnered particular attention, since it needs to be both porous, to allow for oxygen and lithium-ion diffusion, but still electrically conductive. As shown in the zoom in, one way to do this is to use a conductive substrate for structural stability and then add a material with greater surface area for the ORR/OER to proceed on. It should be noted that this is not the only way to make an Li-O₂ battery cathode, as many researchers have looked into cathodes where the conductive substrate contains reaction sites, not requiring an additional active material. A diagram of a Swagelok-type Li-O₂ battery is also displayed in Figure 1.2. This type of cell design allows for a pocket of O₂ gas to be contained within the cell, which remains in excess and pure from other contaminants that are contained in ambient air. Perforated coin-cell type cells also exist for Li-O₂ batteries, which allow for use of oxygen from ambient air, but require complex membranes to keep out unwanted contaminants, like water, CO₂, CO, and nitrogen.^[17,18] Although its production is the source of the large energy density created by these batteries, the desired Li₂O₂ product is a peroxide and therefore highly reactive. Due to this reactivity, and the high voltages needed to break down the Li₂O₂ during the charging cycle, the Li₂O₂ can react both with impurities that may be present in the system, or even with the electrolyte and/or cathode material itself. These side reactions, especially with carbon sources like CO₂ and CO, must be avoided, as many of the products are solid deposits that are electrically insulating, cover up reaction sites, and are near impossible to remove except at voltages above electrolyte decomposition thresholds. The conventional method to check for these products is to use Fourier-transform infrared (FTIR) spectroscopy, X-ray diffraction (XRD) or RAMAN spectroscopy, where residence of different bond structures works to identify the compounds that could be present within a system.^[14,17,19] Within electron microscopy, Energy-

dispersive X-ray spectroscopy (EDS or EDX) can be useful for determining the elements present on the surface of a material, but it is less useful for Li-Air batteries, as many cannot absorb energy low enough to detect lithium though they can detect oxygen, carbon, and other elements common to these byproducts.^[17]

Many of the materials within the cell design may also limit the functionality of Li-Air batteries. Pure lithium metal is usually used as the anode material, which can have violent reactions in water or acidic ionic solvents. To combat this, cells must either have protective coatings on the lithium for use in water-based system, use organic electrolytes, which have poorer Li_2O_2 solubility, or use a hybrid model with organic electrolyte near the lithium metal, a ionically conducting but solvent impervious solid separator, and aqueous electrolyte near the cathode.^[20-22] This Li_2O_2 , and Li^+ solvation, are important features for the electrolyte, as high Li_2O_2 solubility helps to remove adsorbed Li_2O_2 from the cathode surface, freeing up reaction sites for further reactions, and low Li^+ solvation leads to increased strength of Li_2O_2 deposition, which prevents further reactions from occurring at that reaction site.^[19] Like all lithium metal batteries, Li- O_2 batteries face issues with irregular Li^+ ion deposition, which causes dendrite formation during charge cycles and leads to battery life shortening or short-circuiting.^[23] Additionally, Li_2O_2 itself is electrically insulating, needing only a 7 nm film on the cathode surface to prevent further reactions.^[24] This insulating nature is one of the reasons the system has high overpotentials, requiring voltages much greater than the ideal 2.96 V to proceed, which lowers system stability and cyclability.

1.3 Cell Types (coin vs. Swagelok)

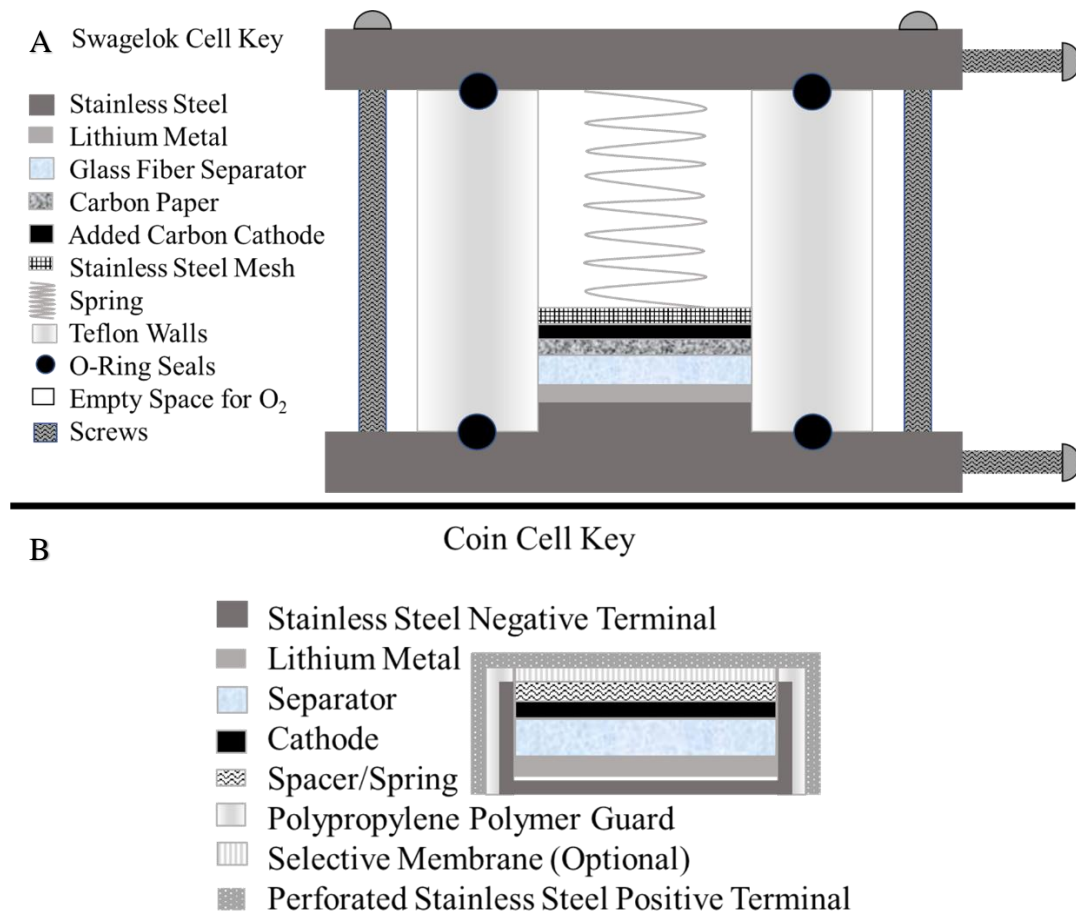


Figure 1.3: Li-O₂ Battery Casings: A: Swagelok cell. B: Perforated coin cell.

Li-Air and Li-O₂ batteries can be traditionally contained within 2 different cell types: Perforated Coin Cells and Swagelok-Type Cells, seen in Figure 1.3. The coin cell is a well-known and cheap traditional battery container, where two pieces of metal are crimped together, while being separated by a plastic ring to prevent shorting, in the shape of a small coin. These can vary in radial size, with different size standards set up all over the world, but they all will have their anode next to the negative terminal and their cathode next to the positive terminal, with some sort of thin spring/spacer to make sure that all the physical parts of the battery stay in close contact. Perforated coin cells, as their name suggests, have small holes on the cathode side

to allow oxygen from the ambient air or from an oxygen tank to diffuse to the cathode for metal-air batteries. This means that for pure O₂ testing, the coin cells must have a selective membrane, or must be cycled within an oxygen chamber to maintain O₂ purity.^[25] Swagelok-style cells have the same general internal component structure, but their outer construction is very different. Swagelok-style cell casing are much larger, with the positive and negative terminals being separated by a large, electrically non-conductive material (usually a polymer), and the spring needed to be used to connect the positive terminal to the cathode must also be much larger. Additionally, these cells are held together by screws which add pressure on O-rings to create a tight seal, and have gas inlets and outlets with Swagelok connectors to allow for easy gas supply and removal. The fundamental differences between these cell types leads to different issues that must be considered in these cells. Since perforated coin cells are very compact, they don't have any internal storage for O₂ gas, meaning that gas must diffuse in through the perforations in the cathode side. Due to the high probability for side reactions, these cells either need to be run in a pure oxygen filled outer chamber or they need to consider selective membranes to go over their perforations such that only O₂ gas may diffuse to and from the system. Swagelok cells sacrifice size and cost for additional control of the system. Due to the sealed Swagelok connectors and large size, the gas that is added to the system (either pure O₂ or dry air) is contained within the volume of the battery cell above the cathode while the entire system can remain sealed from the outside environment. It is also possible to attach openers to the Swagelok connectors to allow ambient air to be used in the system, or connections can be made to both the entrance and the exit to allow the flow of fresh gas to be used during testing instead of using the stored pocket of gas above the cathode as a reservoir. Due to these additional controls, all of the batteries that I have run for my thesis have been done within Swagelok-type cells.

1.4 Electrolyte Solvent Types (Aqueous vs. Organic vs. Hybrid)

As mentioned earlier, the choice of electrolyte solvent and salt can be very important in the Li-Air battery system. Aqueous solvents at first glance seem very appealing. Li_2O_2 has very good solubility in these solvents, leading to lower overpotential during the discharge and charge cycle, as formed Li_2O_2 dissolves into the electrolyte during discharge, leaving the reaction site open for further reactions, and soluble Li_2O_2 is easier to dissociate back into oxygen gas and lithium ions during charge.^[14,15,20] However, lithium metal violently reacts to aqueous electrolytes, meaning that the system must either greatly lower capacity by using an alternative lithium ion producer or the system must increase the cell resistance by adding a barrier to the lithium metal surface that prevents it from contacting the electrolyte directly. Additionally, with systems that contain water, it is possible that lithium hydroxide, LiOH , forms instead of Li_2O_2 , which allows for different reaction pathways to forming lithium carbonate, Li_2CO_3 , a major parasitic product that coats the cathode and cannot be dissociated during the charge cycle. Organic electrolytes fix some of these issues, but have problems of their own and have much greater variance between different solvents. Although organic electrolytes do not directly react with lithium metal, it is possible for Li_2O_2 to attack organic electrolytes to form Li_2CO_3 . Additionally, Li_2O_2 is much less soluble in organic electrolytes, meaning that it tends to stay on the cathode surface, limiting the number of available reaction sites and increasing overpotential during the charge cycle. The choice of organic solvent can make a big difference in the battery performance, as different types of organic electrolytes may be less prone to Li_2O_2 attack and have increased stability, while other types may have a higher donor number and will better solvate lithium ions and have increased Li_2O_2 stability. Hybrid electrolyte systems try to combine the best attributes of both systems.^[14,20] Using a solid, ionically conductive membrane for the separator that does not allow

for solvent molecule diffusion, these systems have an organic electrolyte near the lithium metal anode and an aqueous electrolyte near the cathode. This system does allow for the advantages of both aqueous and organic electrolyte systems to work against the disadvantages of the other, but the requirement of a solid separator that doesn't allow for solvent mixing can add resistance to the battery system and are more difficult to make than the simpler, single electrolyte systems. The system that is used within this paper is a non-aqueous electrolyte, using a glass fiber separator, seen in Figure 1.4. These separators were used due to their porous structure and use as an electrolyte storage to maintain a good three-phase interface for reactions, even as some electrolyte would evaporate into the O₂ gas chamber.

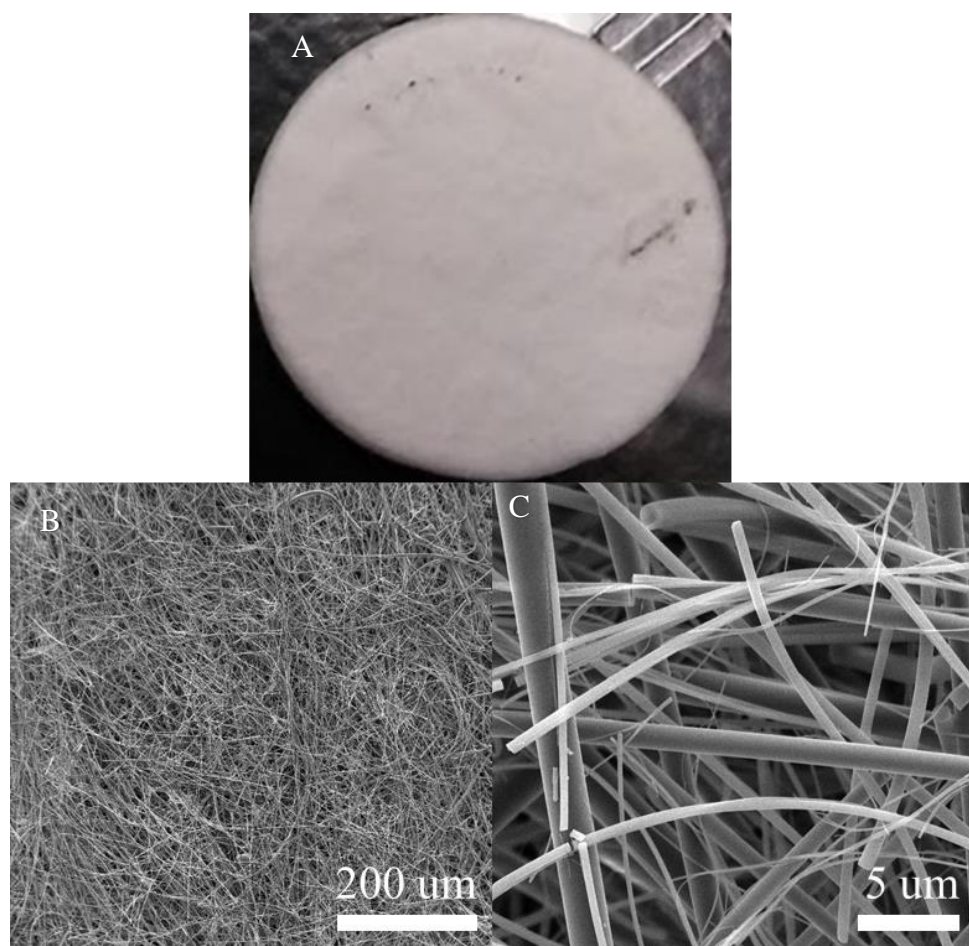


Figure 1.4: Glass Fiber (aka. Silica Fiber) Separator: A: Macroscale image. B/C: SEM of fiber mat and individual fibers

1.5 Materials for Lithium Air Cathodes and Their Preparation

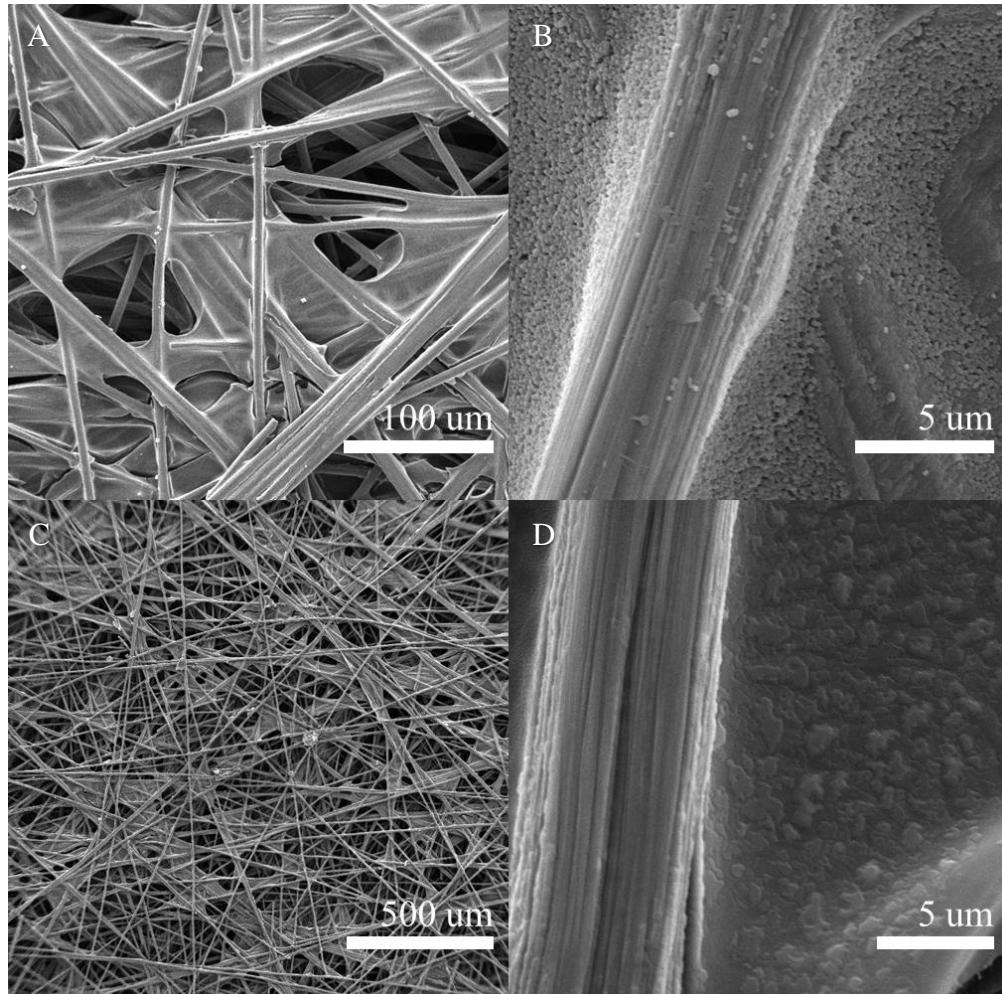


Figure 1.5: Carbon Paper Substrate: A/B: Before heat treatment. C/D: After heat treatment at 900°C for 2 hours under an N₂ atmosphere, some of the PTFE coating has been removed, and what remains is more melted together.

As Li-Air batteries mainly use pure lithium metal anodes, much research has gone into the preparation and materials of the Li-Air cathodes. Many Li-Air cathodes follow the formula of

adding an active material, a material whose surface and properties create a good reaction site, to a stable, electrically conductive, porous substrate that physically supports the active material, but a few systems use active materials that are sturdy enough to not need a secondary support. Many of these different types of fabrication methods will be discussed more in Chapter 3, but the carbon support that was used for our work can be seen in Figure 1.5. Traditional casting methods, such as dropcasting and slurry coating, add active material to a substrate by adding a solution of the active material to the top of the conductive substrate and letting it dry there using heat and/or time to produce the cathode.^[26-28] Dropcasting does this by adding the solution dropwise, building up a layer on top of the substrate. This method requires very good control of the volume of each drop and the solution concentration to reach the desired loading within allowable deviation limits. Slurry coating has slightly more control, as it is the spreading of a thick, high concentration solution of the active material over the substrate, using a Doctor Blade to achieve a desired total cathode thickness. In both cases, after the solution is added to the substrate, the cathode is dried in an oven, usually for multiple hours, to fully remove excess solvent, and it has been seen that both preparation techniques can lead to macroscopic cracking of the cathode surface during the drying step. Electro spraying is a process that creates films without the cracking issues and long drying times.^[29-33] It does this by using a potential difference and the drying of droplets of solution to form films of the active material on top of a substrate. A potential difference is created by using a voltage source to create a positive potential at the tip of a needle and adding a ground to a collector plate, which also grounds the cathode substrate. When a syringe pump is used to force a solution of the needle, a Taylor Cone forms just outside of the needle tip, and whipping instabilities causes the solution to break apart into small droplets. Due to the potential difference, these droplets head toward the collector

place, and the solution solvent dries out in the air as the droplets travel. The distance between the needle tip and collector plate can be used to control the amount of drying of the droplets, allowing for control over whether they land slightly wet or completely dry. This process can even be further improved by adding a coaxial air sheath around the charged needle by using a coaxial needle set up and a pressurized air supply, in a process called Air-Controlled Electro spraying (ACES). This process is used throughout this paper, so a diagram of it is shown in Figure 1.6. The air sheath of ACES has many advantages over regular electro spraying. The additional air flow allows for convective drying of the droplets, allowing for higher volumetric flowrate of the solution and higher process throughput, while the coaxial nature of the airflow helps to narrow the spray cone to a smaller area, allowing for a more focused loading of the active material on the cathode substrate. This method is also easily scalable, as the spray area can be increased by the use of additional needles. Lastly, Electro spinning, is a process very similar to electro spraying, but the system conditions and solution viscosity is tailored to allow the solution to not be broken apart by the whipping instabilities, creating a non-woven fiber mat. Additionally like with electro spraying, electro spinning throughput can be increased by the use of a coaxial air sheath through the process of Gas-Assisted Electro spinning (GAES), receiving many of the same benefits as ACES.^[34] The electro spinning processes are different from the other cathode preparation process, as the non-woven fiber mats act as both a support substrate and an active material, though additional active material or electrocatalysts can be added to electro spun materials, as well. One such way to create cathodes from electro spun materials is the process of Carbonization of polymer fiber mats, where heat removes impurities from the carbon surface in an inert atmosphere, creating electrically conductive fibers. These fibers can then undergo Activation via heating in a reactive atmosphere, such as in CO₂ or superheated steam, to create a

pock-marked surface upon the fibers to increase their reactive surface area. This will be discussed more in Chapter 5.

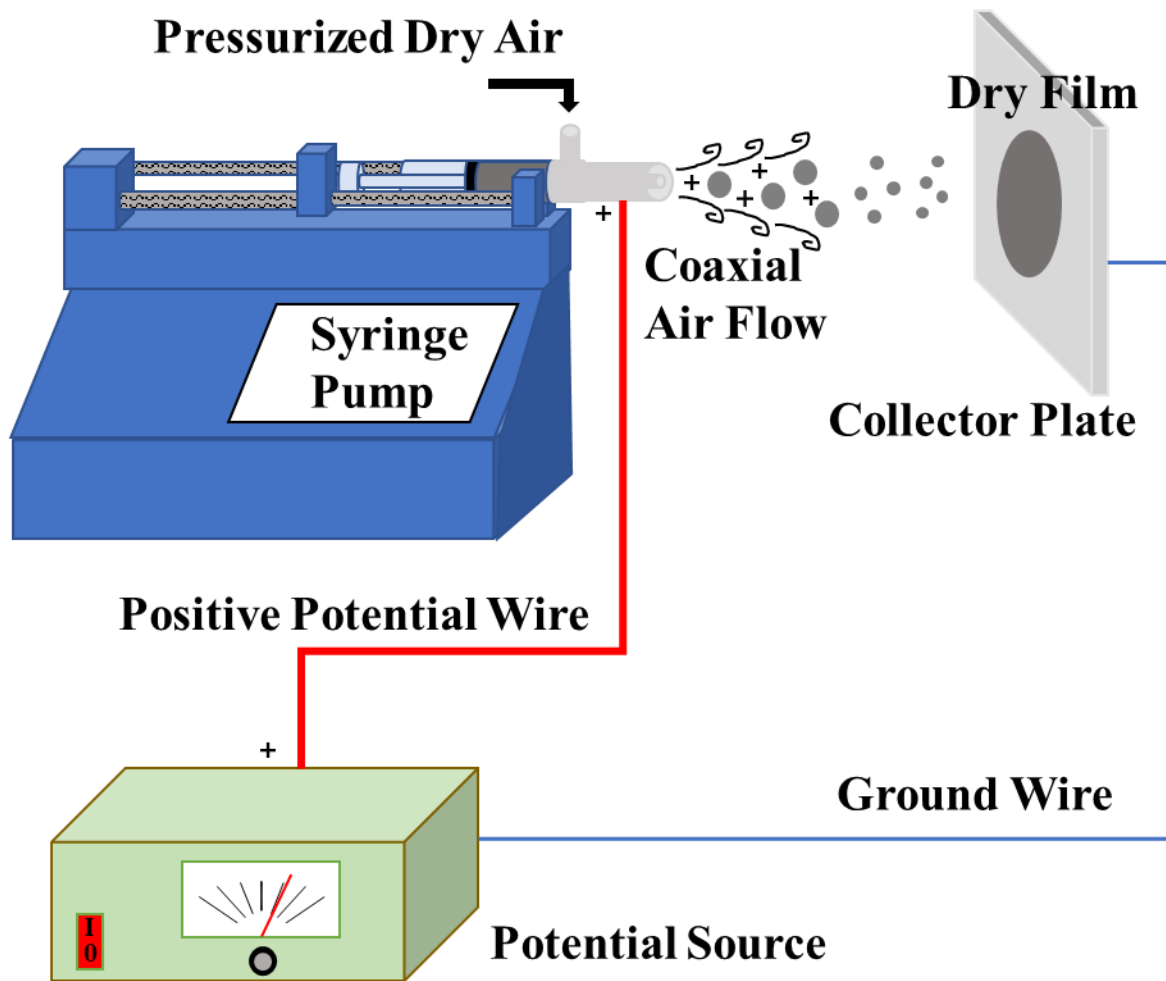


Figure 1.6: Air-Controlled Electro spraying Diagram

1.6 Electrocatalysts

Each material within a battery cathode has both a reactivity and electrical conductivity. Many active materials and support substrates have extremely high electrical conductivity, but they may lack activity for the ORR and/or the OER. This is also possible in the reverse, using highly reactive substrates/active material that are not as electrically conductive as other material

options. These second materials are called electrocatalyst, as their surfaces act as catalytic reaction sites where the ORR/OER may proceed.^[35-37] By supporting these electrocatalysts with highly electrically conductive materials, hybrid cathodes can be made with increased cyclability and efficiency, but slightly lower maximum capacity. Many such electrocatalysts have been found in different metal oxide and carbides, and have been created for both Li-Air batteries and fuel cells (which also have an OER) by many varying methods. These electrocatalysts will be discussed more in depth in Chapter 5.

1.7 Appendices

1. Barbir, F., Veziroglu, T.N., Plass Jr., H.J., “Environmental Damage Due to Fossil Fuels Use”, *Int. J. Hydrogen Energy*, **15**, 10, 739-749, (1990)
2. Lewis, N.S., Nocera, D.G., “Powering the planet: Chemical challengers in solar energy utilization”, *PNAS*, **103**, 43, 15729-15735, (2006)
3. Doney, S.C., Fabry, V.J., Feely, R.A., Kleypas, J.A., “Ocean Acidification: The Other CO₂ Problem”, *Annu. Rev. Mar. Sci.*, **1**, 169–192, (2009)
4. Tarascon, J.M., Armand, M., “Issues and Challenges Facing Rechargeable Lithium Batteries”, *Nature*, **414**, 359-367, (2001)
5. Cheng, F., Chen, J., “Metal-air batteries: from oxygen reduction electrochemistry to cathode catalysts”, *Chem. Soc. Rev.*, **41**, 2172–2192, (2012)
6. Thackeray, M.M., Wolverton, C., Isaacs, E.D., “Electrical energy storage for transportation – approaching the limits of, and going beyond, lithium-ion batteries”, *Energy Environ. Sci.*, **5**, 7854-7863, (2012)
7. Xia, Wei, Mahmood, A., Zou, R, Xu, Q., “Metal-organic frameworks and their derived nanostructures for electrochemical energy storage and conversion”, *Energy Environ. Sci.*, **8**, 1837-1866, (2015)
8. Shah, A.B., Zhou, X., Brezovec, P., Markiewics, D., Joo, Y.L., “Conductive Membrane Coatings for High-Rate Vanadium Redox Flow Batteries”, *ACS Omega*, **3**, 2, 1856–1863, (2018)
9. Etacheri, V., Marom, R., Elazari, R., Salitra, G., Aurbach, D., “Challenges in the development of advanced Li-ion batteries: a review”, *Energy Environ. Sci.*, **4**, 3243-3262, (2011)

10. Marom, R., Amalraj, S.F., Leifer, N., Jacob, D., Aurbach, D., “A review of advanced and practical lithium battery materials”, *J. Mater. Chem.*, **21**, 9938-9954, (2011)
11. Cabana, J., Monconduit, L., Larcher, D., Palacín, M.R., “Beyond Intercalation-Based Li-Ion Batteries: The State of the Art and Challenges of Electrode Materials Reacting Through Conversion Reactions”, *Adv. Mater.*, **22**, E170–E192, (2010)
12. Bruce, P.G., Freunberger, S.A., Hardwick, L.J., Tarascon, J-M., “Li-O₂ and Li-S batteries with high energy storage”, *Nature Materials*, **11**, 19-29, (2012)
13. Girishkumar, G., McCloskey, B., Luntz, A.C., Swanson, S., Wilcke, W., “Lithium-Air Battery: Promise and Challenges”, *J. Phys. Chem. Lett.*, **1**, 2193-2203, (2010)
14. Black, R., Adams, B., Nazar, L.F., “Non-Aqueous and Hybrid Li-O₂ Batteries”, *Adv. Energy Mater.*, **2**, 801-815, (2012)
15. Shao, Y., Ding, F., Xiao, J., Zhang, J., Xu, W., Park, S., Zhang, J.G., Wang, Y., Liu, J., “Making Li-Air Batteries Rechargeable: Material Challenges”, *Adv. Funct. Mater.*, **23**, 987-1004, (2013)
16. Gallagher, K.G., Goebel, S., Greszler, T., Mathias, M., Oelerich, W., Eroglu, D., Srinivasan, V., “Quantifying the Promise of Lithium-Air Batteries for Electric Vehicles”, *Energy Environ. Sci.*, **7**, 1555-1563, (2014)
17. Xie, M., Huang, Z., Lin, X., Li, Y., Huang, Z. Yuan, L., Shen, Y., “Oxygen selective membrane based on perfluoropolyether for Li-Air battery with long cycle life”, *Energy Stor. Mater.*, **20**, 307-214, (2019)
18. Zhang, J., Xu, W., Li, X., Liu, W., “Air Dehydration Membranes for Nonaqueous Lithium–Air Batteries”, *J. Electrochem. Soc.*, **157**, A940-A946, (2010)

19. Aurbach, D., McCloskey, B.D., Nazar, L.F., Bruce, P.G., “Advances in Understanding Mechanisms Underpinning Lithium-Air Batteries”, *Nat. Energy*, **1**, 1-11, (2016)
20. Manthiram, A., Li, L., “Hybrid and Aqueous Lithium-Air Batteries”, *Adv. Energy Mater.*, **5**, 1401302, (2015)
21. He, P., Wang, Y., Zhou, H., “Titanium nitride catalyst cathode in a Li-air fuel cell with an acidic aqueous solution”, *Chem. Commun.*, **47**, 10701–10703, (2011)
22. He, H., Niu, W., Asl, N.M., Salim, J., Chen, R., Kim, Y., “Effects of Aqueous Electrolytes on the Voltage Behaviors of Rechargeable Li-Air Batteries”, *Electrochim. Acta*, **67**, 87-94, (2012)
23. Goodenough, J.B., Kim, Y., “Challenges for Rechargeable Li Batteries”, *Chem. Mater.*, **22**, 587-603, (2010)
24. Viswanathan, V., Thygesen, K.S., Hummelshøj, J.S., Nørskov, J.K., Girishkumar, G., McCloskey, B.D., Luntz, A.C., “Electrical Conductivity in Li₂O₂ and Its Role in Determining Capacity Limitations in Non-Aqueous Li-O₂ Batteries”, *J. Phys. Chem.*, **135**, 214704, (2011)
25. Lau, S., Archer, L.A., “Nucleation and Growth of Lithium Peroxide in the Li-O₂ Battery”, *Nano Lett.*, **15**, 5995–6002, (2015)
26. Lv, D., Zheng, J., Li, Q., Xie, X., Ferrara, S., Nie, Z., Mehdi, L.B., Browning, N.D., Zhang, J-G., Graff, G.L., Liu, J., Xiao, J., “High Energy Density Lithium-Sulfur Batteries: Challenges of Thick Sulfur Cathodes”, *Adv. Energy Mater.*, **5**, 1402290, (2015)
27. Park, I-S., Li, W., Manthiram, A., “Fabrication of catalyst-coated membrane-electrode assemblies by doctor blade method and their performance in fuel cells”, *J. Power Sources*, **195**, 7078-7082, (2010)

28. Kim, J-K., Manuel, J., Lee, M-H., Scheers, J., Lim, D-H., Johansson, P., Ahn, J-H., Matic, A., Jacobsson, P., “Towards flexible secondary lithium batteries: polypyrrole-LiFePO₄ thin electrodes with polymer electrolytes”, *J. Mater. Chem.*, **22**, 15045, (2012)
29. Fei, L., Yoo, S. H., Villamayor, R. A. R., Williams, B. P., Gong, S. Y., Park, S., Shin, K., Joo, Y. L., “Graphene Oxide Involved Air-Controlled Electrospray for Uniform, Fast, Instantly Dry, and Binder-Free Electrode Fabrication”, *ACS Appl. Mater. Interfaces*, **9**, 9738–9746, (2017)
30. Divvela, M.J., Zhang, R., Zhmayev, Y., Pinge, S., Lee, J.H., Kim, S.W., Joo, Y.L., “Control and formation of viscoelastic droplets and distribution of nano-inclusions in functional deposition for lithium-sulfur batteries”, *Soft Matter*, **15**, 6485—6494, (2019)
31. Halim, W., Lee, J-H., Park, S-M., Zhang, R., Sarkar, S., O’Neil, T., Chaing, Y-C., Joo, Y.L., “Directly Deposited Binder-Free Sulfur Electrode Enabled by Air-Controlled Electrospray Process”, *ACS Appl. Energy Mater.*, **2**, 678–686, (2019)
32. Shah, A.B., Zhou, X., Brezovec, P., Markiewics, D., Joo, Y.L., “Conductive Membrane Coatings for High-Rate Vanadium Redox Flow Batteries”, *ACS Omega*, **3**, 2, 1856–1863, (2018)
33. Lee, J., Ko, B., Kang, J., Chung, Y., Kim, Y., Halim, W., Lee, J.H., Joo, Y.L., “Facile and Scalable Fabrication of Highly Loaded Sulfur Cathodes and Lithium-Sulfur Pouch Cells via Air-Controlled Electrospray”, *Materials Today Energy*, **6**, 255-263, (2017)
34. Williams, B.P., Joo, Y.L., “Tunable Large Mesopores in Carbon Nanofiber Interlayers for High-Rate Lithium Sulfur Batteries”, *J. Electrochem. Soc.*, **163**, 13, A2745-2756, (2016)

35. Zhang, K., Han, X., Hu, Z., Zhang, X., Tao, Z., Chen, J., “Nanostructured Mn-Based Oxides for Electrochemical Energy Storage and Conversion”, *Chem. Soc. Rev.*, **44**, 699-728, (2015)
36. Yin, J., Carlin, J.M., Kim, J., Li, Z., Park, J.H., Patel, B., Chakrapani, S., Lee, S., Joo, Y.L., “Synergy Between Metal Oxide Nanofibers and Graphene Nanoribbons for Rechargeable Lithium-Oxygen Battery Cathodes”, *Adv. Energy Mater.*, **5**, 1401412 1-8, (2015)
37. Kundu, D., Black, R., Adams, B., Harrison, K., Zavadil, K., Nazar, L.F., “Nanostructured Metal Carbides for Aprotic Li-O₂ Batteries: New Insights into Interfacial Reactions and Cathode Stability”, *J. Phys. Chem. Lett.*, **6**, 2252-2258, (2015)

Chapter 2: Layered Cathodes

2.1 Introduction

2.1.1 Benefits of Layering/Mixing in Other Systems

Most battery electrodes have to deal with many complex situations at once, and it is hard to find singular materials that meet all of those needs. Electrodes need to be electrically conductive and physically/chemically stable, but some may also need to allow for good ion transport or intercalation like in lithium ion (Li-Ion) batteries^[1-4], have high surface area and good reaction sites for reactions like in lithium sulfur (Li-S) and lithium air (Li-Air) battery cathodes^[4-9], or even allow for the expansion and contraction of battery materials during charge and discharge cycles like in silicon Li-Ion battery anodes or the encapsulation of dissolvable poly-sulfide materials in Li-S battery cathodes^[4-11]. For each battery system, it can be very difficult to find any one material that can meet all of these properties, therefore researchers have tried combining 2 or more materials together to allow each material to make up for where another material falters. Sometimes, however, care has to be taken into how these materials are mixed, with the most optimum situation allowing most of a singular material to remain together. Thus, layered cathodes have been created in many different systems, to allow the beneficial properties of different materials to exist together, while keeping each species in as great of a whole as possible.

Historically, this is most easily seen in the Li-Ion battery. Although the lithium intercalated graphite anode is a system staple, many researchers have also considered adding carbon to cathode, where an active material (usually a metal oxide, like lithium cobalt oxide, or phosphate, like lithium iron phosphate) is mixed, layered, or coated with a conductive carbon

material.^[1-3] This should not be confused with how many metal oxides, sulfide, and phosphates are themselves layered compounds, tending to align in layered structures that create space for lithium ion intercalation, but how the addition of conductive carbons can increase the electrical conductivity of systems they are present in. This layering and coating consideration becomes even more important when considering the silicon anode for Li-Ion batteries, as silicon nanoparticles can hold much more lithium ions than graphite, but will also expand and contract with the amount of stored lithium, requiring strong layered, porous, and/or expandable structures of conductive material like carbon around the silicon to prevent break-up of the anode.^[4,10,11] In the Li-S battery system, this structuring is even more important, since polysulfide shuttle leads to capacity loss, and containing the sulfur within a conductive carbon matrix helps to mitigate this effect.^[4-9]

For Li-Air batteries, many different cathode materials have been researched to optimize high reaction surface area, fast Li^+ ion conductivity, fast O_2 diffusion, high electrical conductivity, and high structural integrity, all while limiting side reactions and maintaining low overpotentials.^[4,9,12-15] Much work has considered electrocatalysts, such as metal oxides and metal carbides, both within and without a supporting conductive carbon matrix due to their lower overpotential generation and increased cycle life, but these systems tend to have lower capacity, as well.^[9,12-16] However, the carbon materials themselves, such as graphene sheets, carbon nanotubes, carbon nanofibers, graphene nanoribbons, and reduced graphene oxide, that such electrocatalysts are usually supported by boast a wide array of interesting properties to consider within the Li-Air Battery system.^[9,12] Classical carbon cathode materials are porous carbons, like Acetylene Black, Ketjen Black and Super P, which boast high surface area due to porous structures.^[12,17,18] The 2-D carbon systems, such as graphene sheets, boast high conductivity due

to their pi-electron cloud, and have increased reactivity at system edges and plane defects, and 1-D system, such as carbon nanotubes (CNT) and graphene nanoribbons (GNR), have high aspect ratios, giving even more edge reactivity for the nanoribbons and are able to create porous void spaces due to lack of alignment.^[12,16,19-23] Even larger morphologies, such as carbon nanofibers (CNF) and other 3-D macrostructures allow for mechanically sturdy cathodes, with increased quantities of mesopores and micropores for increased surface area.^[6,24] With all these different properties, it may be possible to find the correct mix of carbon compounds to create an ideal carbon cathode system, but the way that these compounds are put together may have a big effect on the capabilities of the new system.

2.1.2 Concept for Li-Air Layered Cathode

Considering these different properties, it was concluded that combining high aspect ratio 1D carbons with highly compact graphene or reduced graphene oxide (rGO) sheets would allow for an optimal design of the fully carbon Li-Air cathode. A schematic of the cathode design can be seen in Figure 2.1. Compact and thin cathodes improve battery performance and cyclability, which we will discuss at length in Chapter 3, and rGO is a very good material for creating compact cathodes, with its flat 2-D structure; however, with small pores, access to internal reaction sites is limited, as both O_2 and Li^+ ions must meet at the reaction site for Li_2O_2 to form. Due to their high aspect ratio, it is unlikely for 1-D carbons such as CNT or GNR to fully align like rGO does, which would create some void spaces within layers of these materials. This open space could allow for better O_2 and Li^+ ion diffusion within the cathode structure, allowing for further reaction on the underside of the denser rGO layers, further increasing the capacity of the battery.

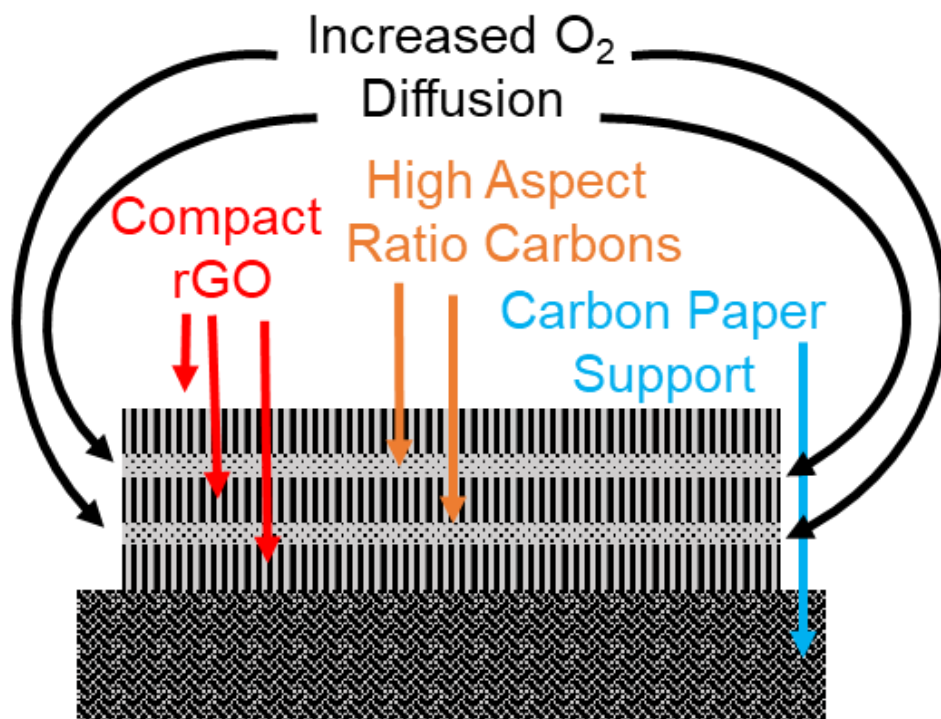


Figure 2.1: Design Concept of Layered Cathode Approach to Li-O₂ Cathodes

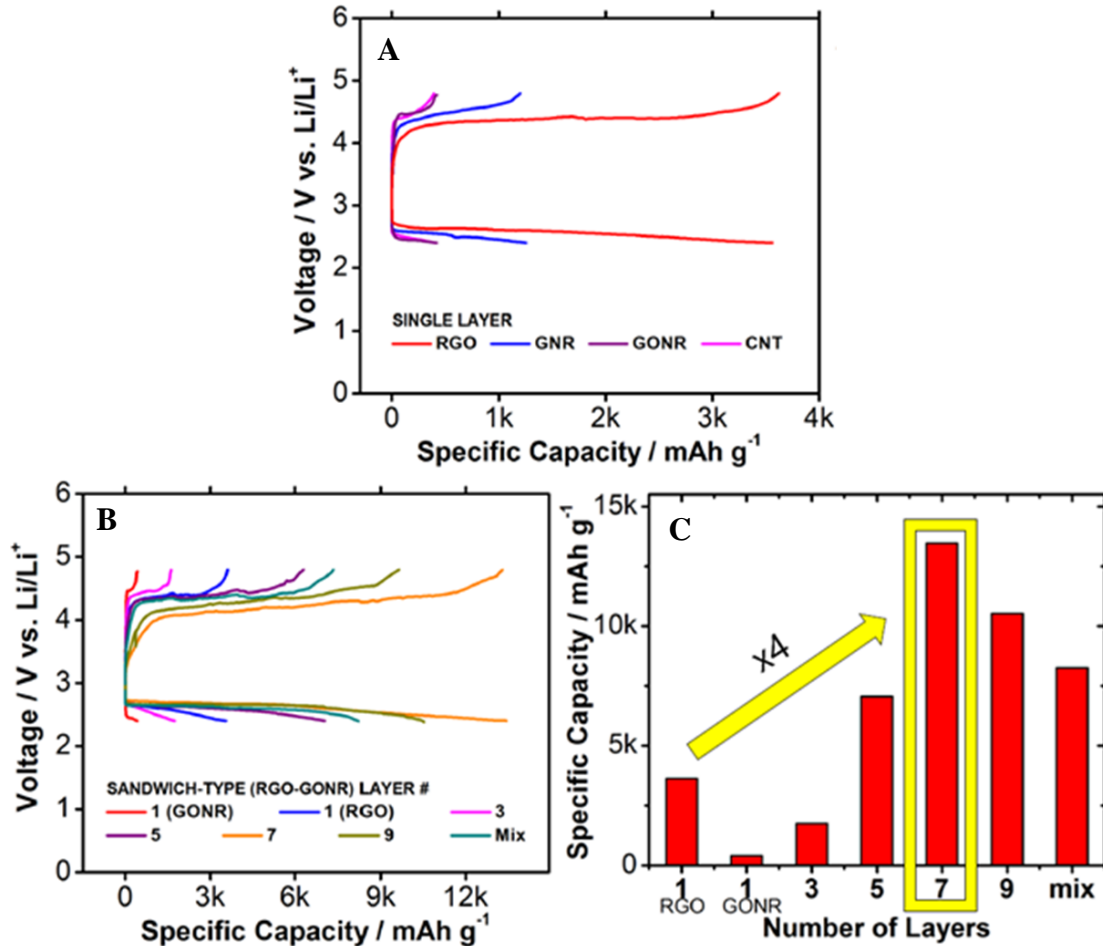


Figure 2.2: Dr. Kim's Past Dropcasting Work^[25]. A: Single layer cathode results. B: Layered rGO-GONR voltage curves. C: Layered rGO-GONR specific capacities

2.1.3 Previous Group Work in Dropcast Cathode System

This system idea of mixing and layering of carbon materials was first considered but not published for the dropcasted Li-Air cathode by Dr. Jangwoo Kim^[25], a past group member, whose results can be seen in Figure 2.2. Studying carbon cathodes, Dr. Kim saw that planar reduced graphene oxide (rGO) by far had the best individual results, while for 1-D carbons graphene nanoribbons showed best individual results while graphene oxide nanoribbons (GONR) and carbon nanotubes showed much lower performance due to high overpotential. However,

combining the 1-D carbons with the 2-D rGO lead to a great increase in capacity, especially for the rGO and GONR combination. Dr. Kim looked at both straight mixing of the two carbons and preferentially layering the carbons, with the outermost layers always being rGO. He concluded that the maximum capacity increase of the system was reached at 7 layers, where the maximum amount of increased oxygen diffusion was able to be reached.

2.2 Experimental Methods

2.2.1 Solution Preparation

Solutions for Air-Controlled Electro spraying (ACES) were prepared using reduced graphene oxide (rGO) [Dongjin Semichem], GNR [AZ Chemicals], Nafion D2020 binder [Ion Power, Inc.] and ACS Grade isopropyl alcohol (IPA) [VWR]. Solutions were constructed in a 20 mL scintillation vial with a 20:80 \pm 1 binder:carbon mass ratios in 5 mL IPA, which was maintained for all tests. The mixed rGO/GNR solution, which had 70% rGO and 30% GNR, had a binder:rGO:GNR ratio of 20:56:24 to maintain the 20:80 binder:carbon ratio. For ACES solutions, the carbon mass loading was 1%. After solutions were made, they were sonicated in an ice bath using a tip sonicator [Q500, Qsonica] for 30 minutes at 30% amplitude, using a 5 sec on/off pulse. After sonication, the solutions were stirred on a stir plate at 400 rpms overnight before use in ACES.

2.2.2 Carbon Substrate Preparation

Carbon paper [TGP-H-030, 50% Wetting, Toray], a conductive, porous carbon fiber mat was used as the conductive substrate. To remove excess Teflon coating, the carbon paper was heat treated in under an inert Argon atmosphere in a tube furnace [OTF-1200X, MTI Corp] at 900 °C for 2 hours, using a 5 °C/min temperature ramp, while being held between two alumina-

silicate ceramic plates [McMaster Carr]. After heat treatment, 15 mm diameter carbon paper substrates were punched out between two weigh paper sheets to prevent edge defects and cracking, using a hand punch [T-0.6, MTI Corp.].

2.2.3 Layering and Loading Controls

Throughout the experiments, consistent cathode loading with small tolerance was required to allow for truly comparable cathodes. For comparison to past systems, the cathodes were fabricated at a total carbon loading of 0.5 ± 0.03 mg carbon/cm² carbon paper substrate area. For the layered carbon systems to be consistent, this meant that the ratio of rGO to GNR had to stay consistent and that individual loading layers needed to remain precise. To maintain consistency to prior works, a rGO:GNR ratio of 70:30 was kept constant throughout the work, requiring total carbon loadings of 0.602 mg rGO and 0.258 mg GNR, and the outer most layers (the bottom layer touching the carbon paper and the top layer with the most direct area to the O₂ reservoir) were always rGO. As the number of layers increased, the loading of each individual layer decreased and the time required to spray each layer decreased. Table 2.1 shows a breakdown of these mass loadings.

Table 2.1: Layered Cathode Mass Loading Breakdown.

	3 Layer	5 Layer	7 Layer	9 Layer
# rGO Layers: # GNR Layers	2:1	3:2	4:3	5:4
Single rGO Layer Mass (mg)	0.301	0.201	0.151	0.120
Single GNR Layer Mass (mg)	0.258	0.129	0.086	0.065

2.2.4 Layered ACES Cathodes

As shown earlier in Figure 1.3, the ACES cathode fabrication was done using a coaxial needle (outer needle: 12 gauge; inner needle: 16 gauge) [Hamilton], where the inner needle

supplied the carbon solution and the outer needle created an air sheath using the building's process air. Using a pressure regulator, the process air was lowered to and controlled at 35 psi. For both rGO, GNR, and rGO/GNR mixed solutions, a syringe pump [Pump 11 Elite, Harvard Apparatus] was used to keep the solution flow rate steady, and an applied potential was supplied by a potential source [ES30P-5W HV Power Supply, Gamma High Voltage Research] via an alligator clip on the needle tip, and a ground from the same potential source was attached to the aluminum foil covered stainless steel collector plate. After initial ACES trials to determine the spray particle morphology and wetness, different flow rates, applied potentials, and spray distances were done with the rGO and GNR sprays. For the rGO solutions, the solution flow rate was kept at 0.09 mL/min with an applied potential of 5kV and a spray distance from the needle to the collector of 6 cm, creating an electric field of 83 kV/m between the charged tip and grounded collector and creating a flat rGO topography. This was also used for the rGO/GNR mixed solution. The GNR solutions were kept at 0.06 mL/min at an applied potential of 25 kV and a spray distance of 8 cm, creating an electric field of 312 kV/m. This lower flow rate was used to create lower loading per minute for the GNR sprays, which required very low mass loading. The carbon substrate was held in the spray area, and a mask was used so that the amount of uncoated area would always be uniform between samples. To do so, a small sheet of folded aluminum foil was hung from the top of the collector (making sure to keep the back of the folded foil in contact with the collector, and, using non-conductive paper clips, a clear polyvinylchloride sheet was used as a mask to limit the spray circle diameter to 14 mm. This 14mm hole was created using a hand punch. Additionally, before starting each spray, a cardboard barrier was used to prevent overloading from spurting sprays upon starting the syringe pump, and the removal of this barrier was the signal for starting the spray time. After every spray time

(ranging from 10 second intervals for GNR sprays for 9-layer cathodes to 1 minute or half minute intervals for 1-layer rGO cathodes), the cathode was weighed to check the current added mass and prevent overloading. For the layered spray, requiring the swapping out of carbon solutions, the same needle was used for both solutions, but was cleaned by washing with 20 mL of IPA and then blowing dry with 20 psi of compressed air. The fabricated cathodes were then moved into an ultra-high purity argon [Airgas] filled glovebox [VGB-6, MTI Corp., < 5 ppm O₂ and H₂O] for cell assembly.

2.2.5 Electrolyte and Separator

A solution of 1M Lithium Triflate (LiCF₃SO₃) [Sigma Aldrich] in ACS Grade 1,2-dimethoxyethane (DME) [VWR] was used as the electrolyte, created in a glovebox under inert Argon gas. This solution was stored within the glovebox and was kept under constant stirring to maintain solution consistency. Separators were prepared by punching 19 mm diameter disks from glass fiber filters [GF/D, Whatman], between weigh paper sheets to prevent edge defects, using a hand punch [T-0.6, MTI Corp.]. These were immediately added to the glovebox, as well, and were stored separately from each other for ease of access and to prevent damage from tweezer pressure.

2.2.6 Cell Assembly

A picture and labeled schematic of the Li-Air cells were shown in Figure 1.2. Li-Air cells were created using 316 stainless steel Swagelok style cells, made in-house, and plastic tweezers were used during cell assembly to prevent capacity loss. Cell assembly began with placing a lithium disk [16 mm dia, 0.6 mm thick, MTI] on the central stage of the negative terminal and compressing slightly with a Delrin plastic rod [McMaster Carr] for good lithium-to-stage contact. On top of that, a glass fiber separator was centered above the lithium disk and was

saturated with 310 μL of electrolyte. The separator was well saturated with electrolyte so that minor evaporation of the electrolyte into the dry oxygen would have little effect on battery results. Centered above the separator, the cathode was placed with the electrospray/dropcasted layer facing upward (away from the separator and towards the empty cell chamber) to lessen the diffusion distance of the future O_2 gas to the active material surface. An additional 50 μL of electrolyte was added to the cathode for ideal internal wetting of the rGO cathode. Then a stainless-steel mesh [316 SS, 0.032" opening, McMaster Carr,] was centered on top of the cathode to ensure good contact to the positive terminal and to balance pressure across the cathode surface. A Teflon cylinder with n-buna o-ring seals was then placed around the setup, creating the oxygen chamber. The assembly was connected to the positive terminal via a 316 stainless steel spring and was sealed using 4 screws. After cell assembly was finished, the cells were removed from the glovebox. Using Swagelok connectors, ultra-high purity O_2 gas [Airgas] was added to the cell at 16 psi. The cell was first purged of argon using the O_2 gas for 30 seconds and then immediately filled for another 30 seconds to ensure only pure O_2 was within the cell chamber. During this process, cells were checked for gas leakage and were removed from trials and re-sealed if a leak was found.

2.2.7 Electrochemical Characterization

Galvanostatic battery cycling was performed in a battery cycler [BTS8-WA (1mA), MTI Corp], using a cell potential cut off window of 2.4 V to 2.75 V versus Li/Li⁺ at constant current, both for deep discharge cases and limited capacity cycling. For all cases, constant currents of 0.05 and 0.50 mA/cm² were examined. Full discharge cases did not receive a capacity limit, while limited capacity cycling was performed to a limit of both 1 mAh and at least 20% of the deep discharge value. Electrochemical Impedance Spectroscopy (EIS) and Cyclic Voltammetry

(CV) were evaluated using an electrochemical workstation [PARSTAT 4000, Princeton Applied Research]. EIS was evaluated within a frequency range of 50,000 to 0.01 Hz, using 5 mV input potential amplitude. CV was evaluated using a 2-point probe set up, connecting the leads to the Swagelok cell positive and negative terminals. These tests were performed using a scan rate of 0.1 mV/s, between the cell potential window of 2-4.8 V. Conductivity measurements were performed using either a 2-point or 4-point probe set up [CP06, Cascade] using a Keithley 2400 Source-Meter with a tungsten carbide probe, 0.05 A source current over a 0.1 V measurement range, and run via LabView software for automatic measurements. For conductivity testing, dropcasting and electrospraying was done on non-conductive plastic sheets to prevent the conductivity of the substrate from affecting the measurements.

2.2.8 Structural Characterization

The topographical and cross-sectional morphologies of the cathodes were evaluated using scanning electron microscopy (SEM) [Mira3 FESEM, Tescan] at a beam voltage of 15 kV and beam intensity of 6, while single rGO flakes and GNR ribbons were characterized by SEM [Gemini 500, Zeiss]. Transmission Electron Microscopy (TEM) [F20 TEM STEM, FEI] on single flakes and ribbons was also performed. The mesoporous/microporous surface area was evaluated using Brunauer-Emmett-Teller (BET) and Barrett-Joyner-Halenda (BJH) pore analyses [Gemini VII, Micromeritics], using ultra high purity nitrogen. Tests were performed on 10 carbon paper disks at once to reach the desired minimum surface area threshold of 1 m² for the carbon paper alone, and was repeated for both the dropcast and electrospray cases for experimental consistency. The macroporous structure size was evaluated via porometry [CFP-1100-AEHXL, Porous Materials, Inc.], using a 6 drops of 20.1 dynes/cm oil in wet-up, dry-down method on 25 mm diameter samples.

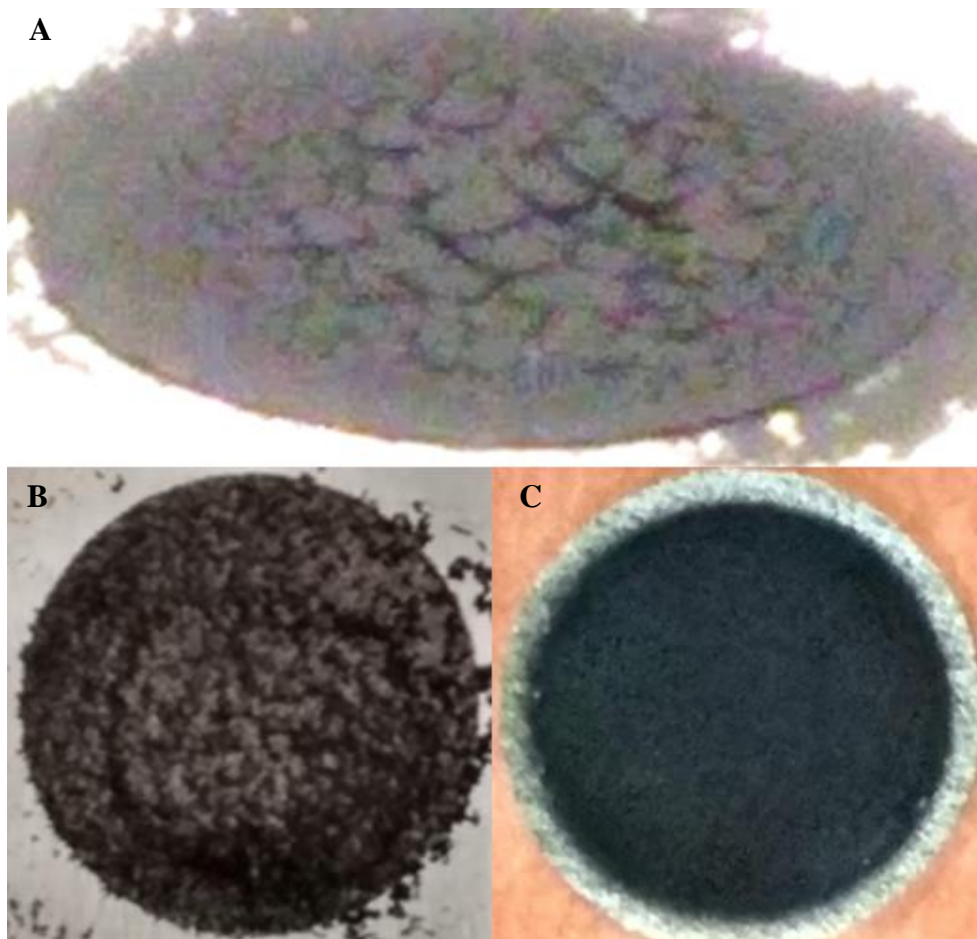


Figure 2.3: Layered Cathode Fabrication Considerations: A: Cracked 9-layer dropcasted cathode. B/C: Single rGO layer of 9-layer system via (B) Dropcasting or (C) ACES.

2.3 Results and Discussion

The initial plan for this project was to similarly compare the layering of different carbons (as done in Dr. Kim's work) and then extend beyond previous work by implementing electrospaying as an improvement to the dropcasting process. However, early work suggested that the issues within the dropcasting (and other similar traditional casting methods) would cause too much fluctuation between dropcasted cathode samples, particularly those with many layers. Dropcasting, as a whole, is not a very precise loading method, as the arrangement of the added carbon on the cathode is dependent upon the placement of the drops on the cathode surface, and

the mass loading of the carbon for each layer on the system fluctuated greatly, depending both on solution concentration and the number of drops. To attempt to control the added volume, a micropipette was first used, but the small droplet size led to intense cracking of the added carbon layers. Using a plastic pipette lessened the cracking greatly, but the concentration dependence and lack of volume control made getting the highly detailed loading, especially for the low loading GNR layers, very difficult. Figure 2.3 shows the basis of why ACES was used for the completion of this project, and identifies one reason for why Dr. Kim saw a drop off in capacity upon reaching the 9-layer cathode. Figure 2.3A is an image of a 9-layer dropcasted cathode, where increasing the number of layers (and subsequent heating steps) caused deep cracks to form in the cathode surface, which hinted at structural instability within the future battery system. Additionally, the low loading of the GNR made layer control quite difficult, as can be seen in Figure 2.3B. As the number of layers increase, the mass of each layer decreases, and in the already lower fraction of the total mass GNR layers, dropcasting becomes insufficient to create a full uniform cathode layer. The leftmost image shows how the GNR layer of dropcasted cathodes would not fully coat the cathode as a uniform layer for the nine layer dropcasted cathode, which is probably the root cause of why Dr. Kim saw a reduction in the capacity of his batteries as the number of layers increased from seven to nine. Additionally, this explains why his 9-layer battery system behaved more like the mixed battery system, because although the GONR was present as a layer on top of the rGO, they did not form a uniform layer, leading to disparate clusters of GNR which behaved half-way between a full layer of GONR and a fully mixed rGO/GNR cathode system. Due to these issues, I proceeded with using electrospraying for my layered cathode research, as Figure 2.3C shows that even at the low loading of the 9-layer system, the electrospray system creates a full uniform layer of GNR on the cathode surface. I

also proceeded with looking at the rGO and GNR cathode system, as the identical bottles of these chemicals that Dr. Kim had used were still present within the lab (the GONR had been produced in a lower quantity, due to its greater manufacturing cost, and had been used up in Dr. Kim's experiment), and the GNR itself had shown to be the greatest individual high-aspect ratio carbon that Dr. Kim had explored, when compared to the single layer capacities of both CNT and GONR.

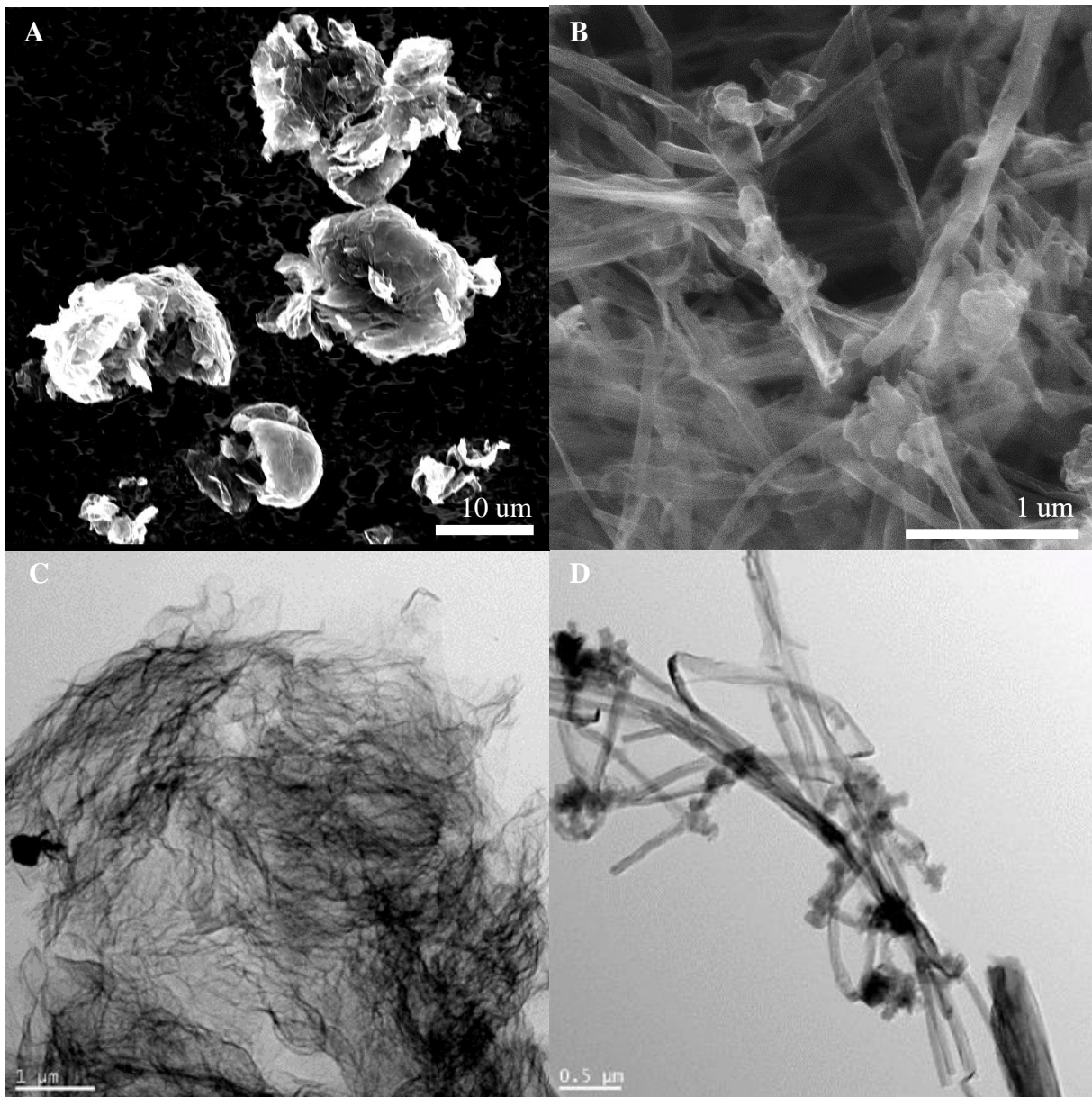


Figure 2.4: Electron Microscopy of Carbon Powders: A: SEM of rGO. B: SEM of GNR. C: TEM of rGO. D: TEM of GNR.

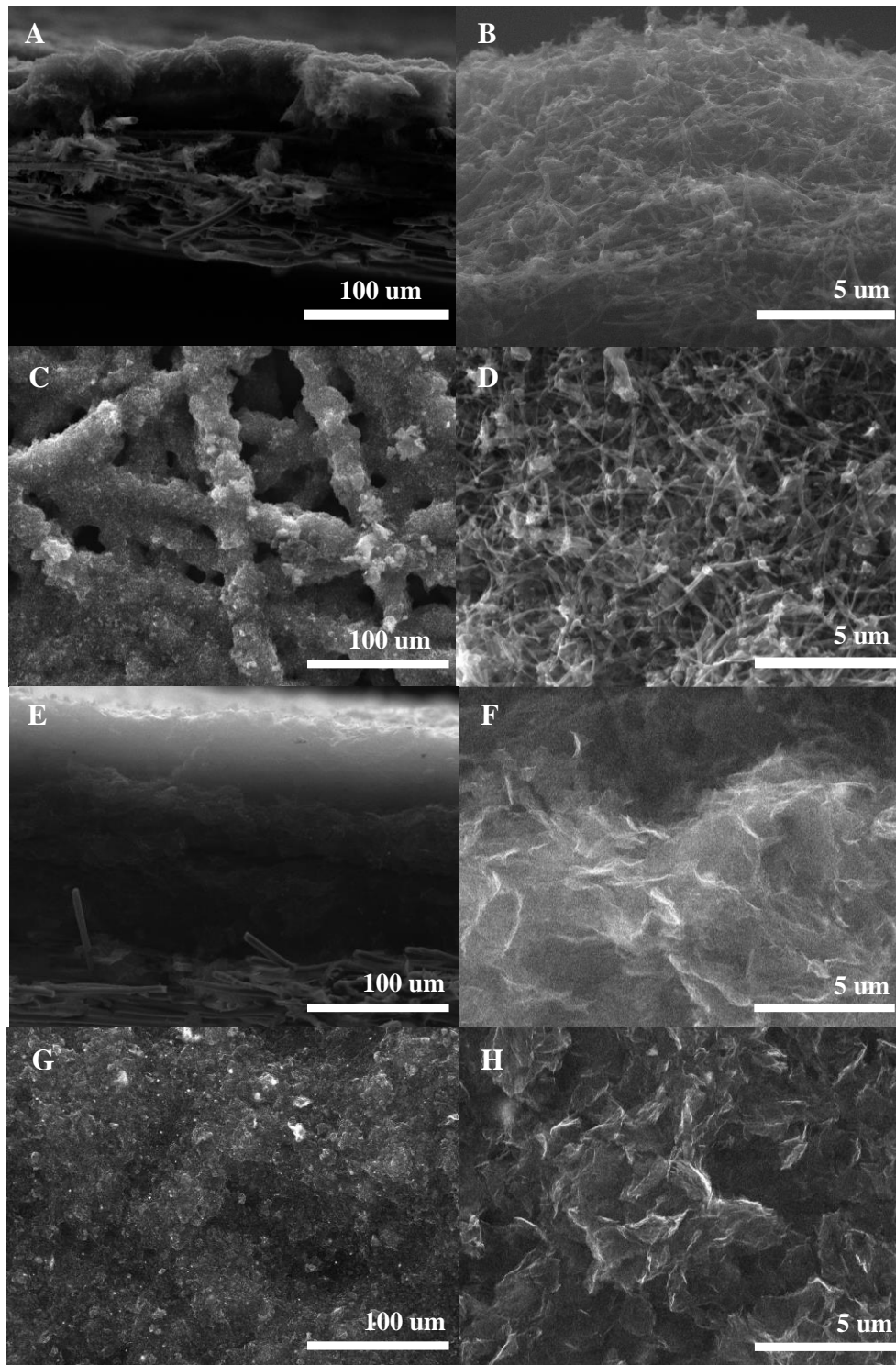


Figure 2.5: 1-Layer Cathodes: A-D: GNR 1-layer cathode (A/B) cross-sections and (C/D) top-down topography. E-H: rGO 1-layer cathode (E/F) cross-sections and (G/H) top-down topography.

First, we look at the single layer information for the electro spray rGO cathode and the electro spray GNR cathode. Figure 2.4 shows SEM and TEM images of the rGO and GNR powders. It can be seen that the two carbons are quite different from each other, with the rGO forming crumpled sheets around 1-5 μm in diameter, while the GNR powder is made of jumbled up strips that are only around 100 nm wide but can be over 2.5 μm long. Looking at the SEM images of single layer cathodes in Figure 2.5, the crumpled rGO sheets when sprayed can form a relatively uniform surface layer on top of the carbon paper, with some topography rises and falls on the surface. The cross-section image shows that the carbon layer is fairly uniform throughout the about 260 μm thickness, with no open pockets. The GNR, however, is quite different, with the top-down view showing that the GNR can both form continuous layers that bridge between carbon fibers and also wrap around the carbon fibers, leaving holes to inner sections of the carbon paper. The individual GNR ribbons can be seen to wrap around each other in a relatively random displacement, causing odd ends of ribbons to be sticking up from the surface layer. Additionally, the cross-sectional image shows that the small size of the GNRs allows them to compact together, even with their high aspect ratio and general entangling nature, creating surface layers of only 10 μm thick.

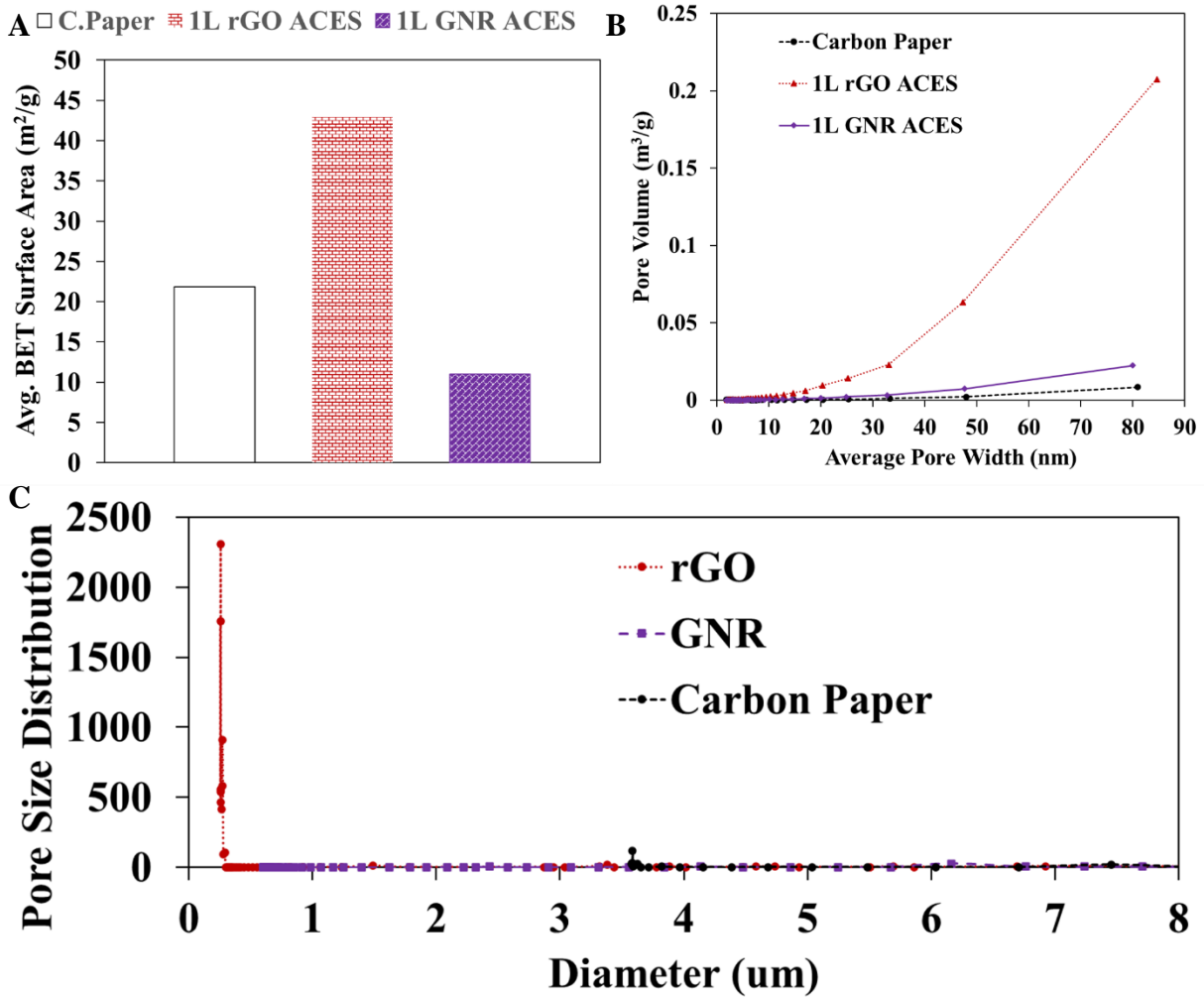


Figure 2.6: 1-Layer Pore Data: A: BET surface area from micropores. B: BJH pore volume in mesopores C: Porometry macropore size distribution

This compactness both helps and hurts the GNR cathode system. The pore data in Figure 2.6 shows the effect of this compactness on the cathode pore structure. The carbon paper support mainly forms large macropores of about 3.5 μm in diameter. While the rGO, with its mesoporous powder structure of crumpled sheets, creates a layer that increases the system surface area, as shown by the BET data, and creates porous macrostructures of around 0.3 microns, the GNR ribbons actively remove pores from the system, showing both a decrease in the microporous

surface area and an elimination of the carbon paper's macropores. However, what is lost in pore morphology is gained in conductivity. 2-point probe testing, shown in Table 2.2, shows that the GNR system is an order of magnitude more conductive than the rGO.

Table 2.2: 2-Point Probe 1-Layer Conductivity

Fabrication Method	Measurement length (mm)	Film Thickness (um)	Width (mm)	Resistance (Ω)	Conductivity (S/m)
1L rGO Electropray	5	165.6	14.8	8.355	244
1L GNR Electropray	5	10.5	14.8	10.96	2936

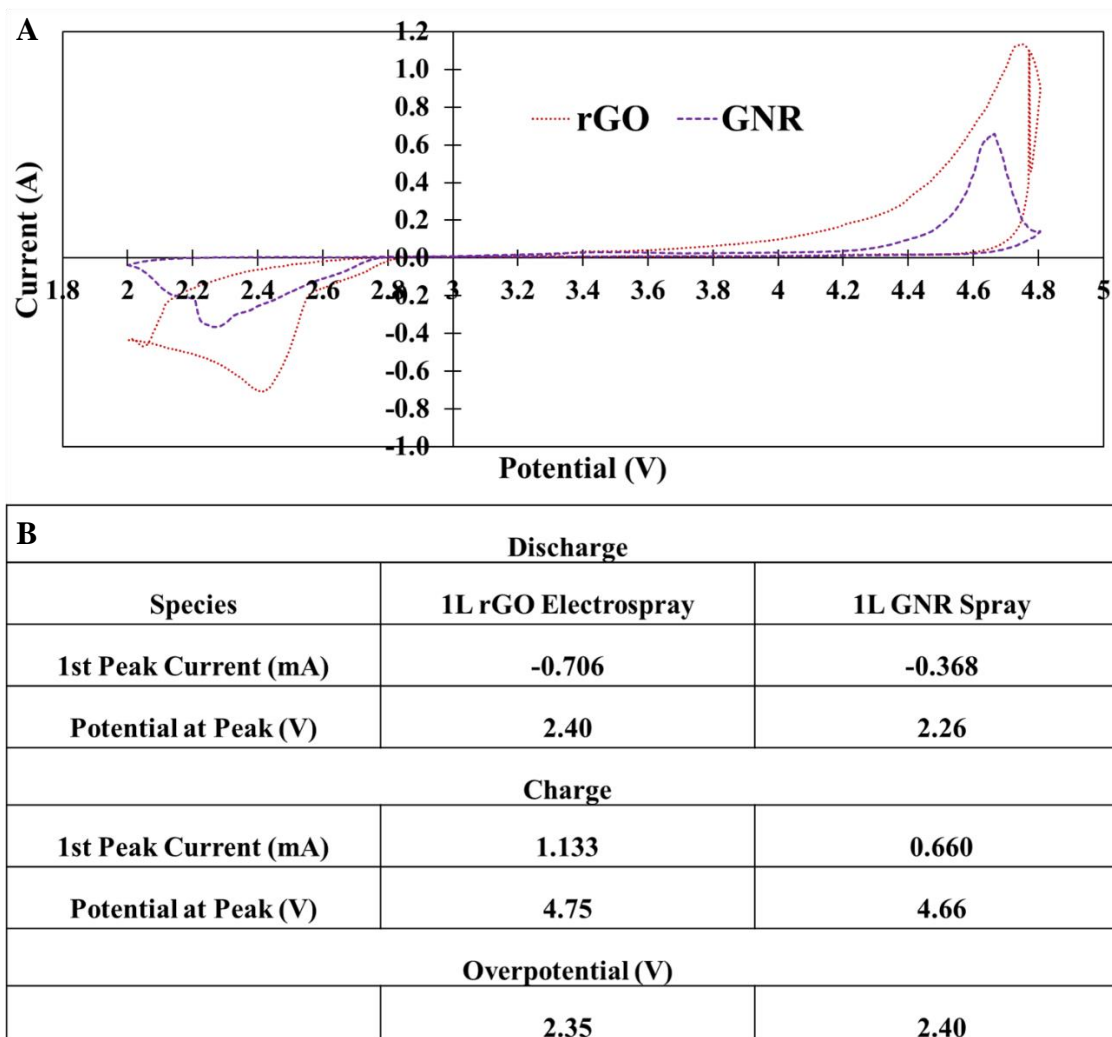


Figure 2.7: 1-Layer CV Data: A: Cyclic voltammogram. B: Peak data information

This conductivity is important to both the OER and ORR, as the removal and addition of electrons is central to this performance. This increased conductivity may hint at why the cyclic voltammetry (CV) data in Figure 2.7 shows a decrease in overpotential for the OER in comparison to the rGO, which is important because an electron is needed to break apart the Li_2O_2 and the loss of access to electrons is the usual ultimate source of battery death, since a 5-7 nm layer film of Li_2O_2 can fully insulate the cathode. However, GNR does not show as good of a reaction surface for the formation of Li_2O_2 , as the 1L GNR cathode shows an increase of

overpotential for the ORR on the left side of the graph, lowering the peak point to below 2.4 V. This is significant because below 2.4 V, it is possible to reduce the oxygen an additional time, converting the Li_2O_2 into lithium oxide (Li_2O), which is just as electrically insulating, but is not able to be removed from the system or broken up within a voltage range that does not decompose the electrolyte. Additionally, even with the increase in conductivity, the GNR cathode has a higher internal resistance to the rGO, shown by Electrochemical Impedance Spectroscopy (EIS) in Figure 2.8. The figure shows that with their similar tail angles and identical starting points, the GNR and rGO systems both have similar bulk Li^+ ion diffusion due to their similar Warburg Impedance and bulk electrolyte resistance, respectively; however, the shape and diameter of the semicircle are quite different, as the GNR shows to have increased charge transfer resistance, due to the increase in semicircle diameter, with part of that increase being due to increased Li^+ ion diffusion resistance near the GNR surface, as seen by the large magnitude of the semicircle at high frequencies (aka. Low Z_{re}).

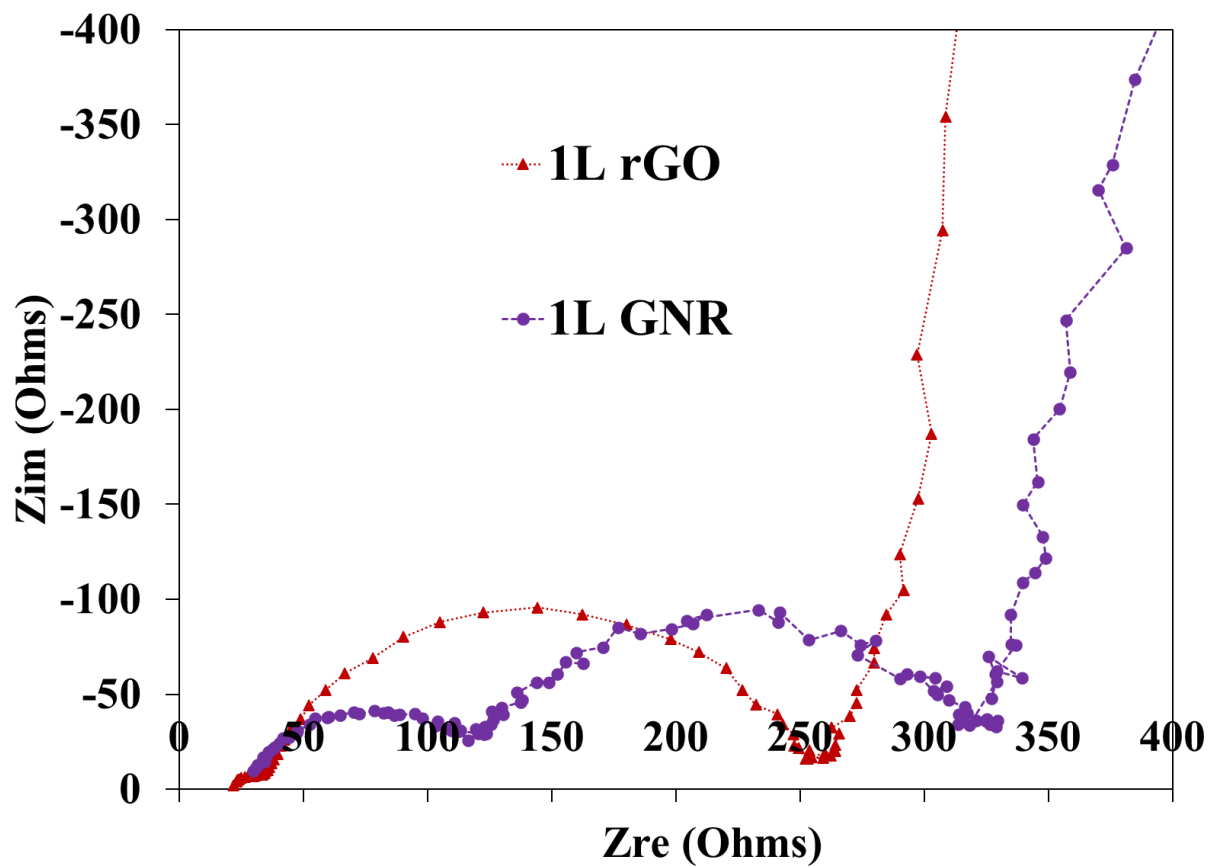


Figure 2.8: 1-Layer EIS: GNR has 2 distinct curves and increased charge transfer resistance

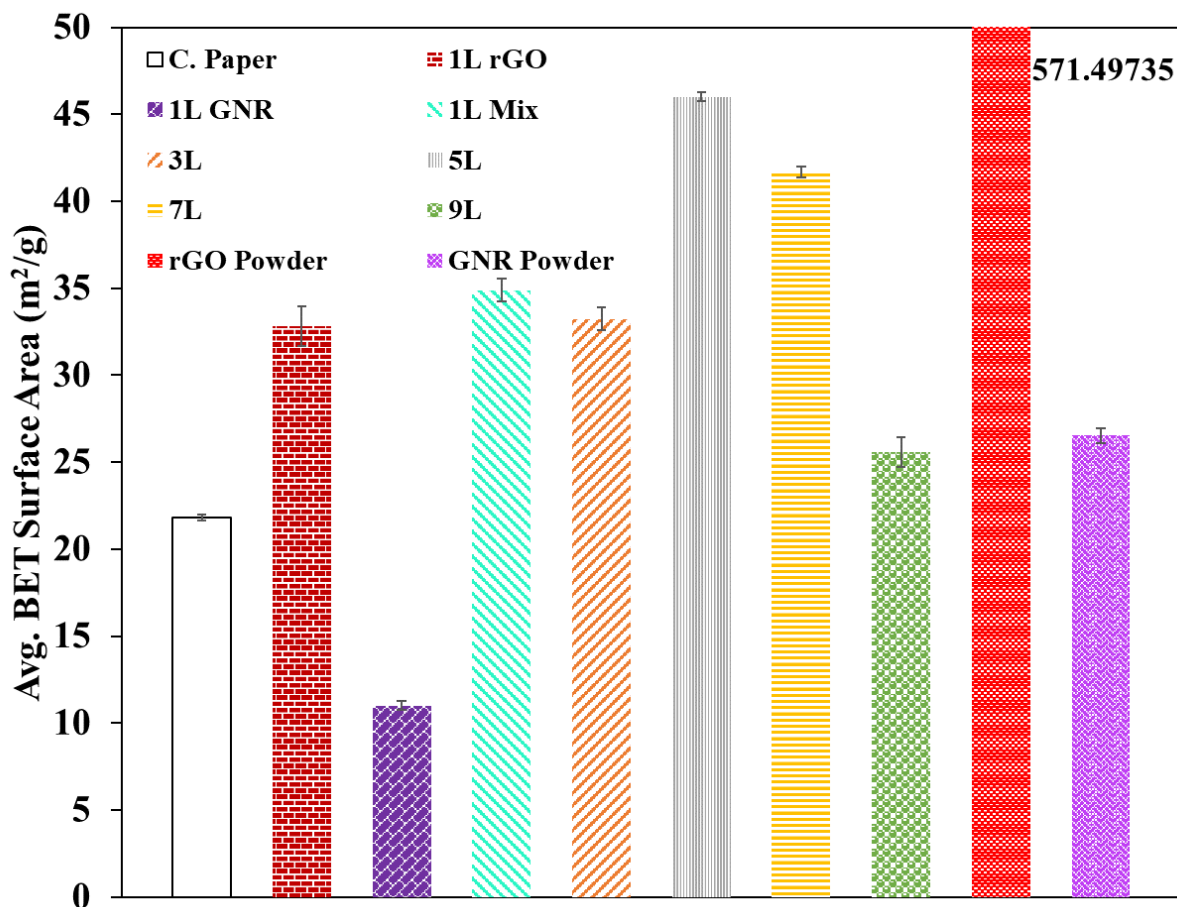


Figure 2.9: Multilayer BET Data

As the rGO and GNR are combined, we start to see some interesting effects within the cathode structure. Looking at the BET data in Figure 2.9, we see that in the three layer and the mixed system, we see a slight reduction in the available surface area, as the single layer system data suggested the GNR system has a pore-dampening quality and the three layer system has the largest connected mass of GNR layered systems and the mixed system doesn't allow the GNR to form a distinct layer; however, both the five and seven layer systems show an increase in the available surface area, meaning that it can be possible that an optimal thickness of the GNR layer is able to be created to allow for access to internal rGO pore structures. This is further corroborated by the 9-layer system, which shows a large decrease in the available pore area, as

the thin GNR layers no longer allow access to internal pores. Interestingly, the bulk density of these cathodes does not show a singular trend, though, for how the addition of the GNR changes the compactness of the cathode system.

As discussed earlier, the GNRs tend to form very small compact layers, when compared to the larger rGO sheets. Figure 2.10 shows the cross-sectional SEM images of these cathodes, while Table 2.3 shows the system bulk densities, which is how compacted the mass of these cathodes are. Although not always easy to see, the SEM images show that the layered systems do form distinct rGO and GNR layers, which are most easily seen at fracture points between GNR and rGO where the cathode did not break cleanly due to these interfacial structural differences. The bulk densities from Table 2.3, however, do not show a consistent change in cathode thickness as the layering is increased. As shown in the table for the single layer system, the density of the GNR is around fifteen times that of the rGO system, which would suggest that replacing rGO with GNR would increase the bulk density of the cathode due to the compactness of the GNR layers. Overall, this is true, as the bulk density of most of the mixed and layered systems is greater than that of the single layer rGO system, but the three-layer system is an outlier to this trend, with a slight reduction in the bulk density. It is possible that this could be due to the addition of the single GNR layer working as a single flat plane for the second rGO layer to stack upon. The first rGO layer of the three-layer system would have had to bridge between carbon fibers to form its first flat plane and could have some surface topography valleys in these areas that span over the open spaces between the carbon fibers. If the GNR layer filled in these valleys to create a new flat plane for the third rGO layer to stack upon, then this could have increased the thickness that the second rGO layer was able to achieve.

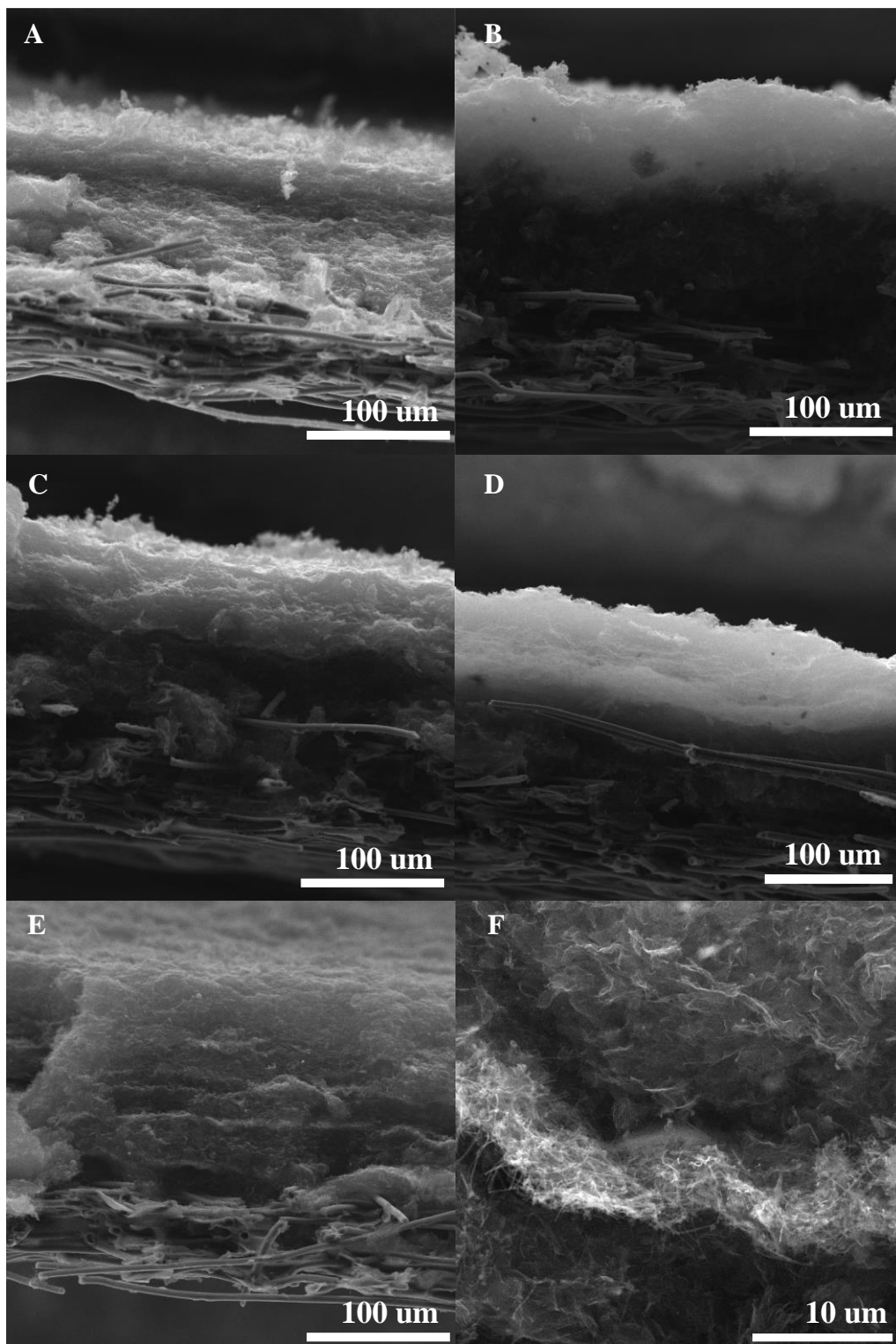


Figure 2.10: Multilayer Cross-Section SEM Images: A: 1 Layer Mix. B: 3 Layer. C: 5 Layer. D: 7 Layer. E: 9 Layer. F: Zoom in of 5 Layer GNR layer between rGO layers

Table 2.3: Bulk Density

Cathode Type	1L GNR	1L rGO	1L Mix	3L	5L	7L	9L
Bulk Density (mg/cm ³)	927.1	60.1	98.4	55.7	85.7	71.1	65.0

As seen already, the interactions between the rGO and GNR definitely have an effect on the structural behavior of the system. The layered cathode EIS data in Figure 2.11 is very interesting for the interaction that it is showing for the charge transfer resistance increase that the addition of a GNR layer provides. Overall, the data is very similar to Figure 2.8, with GNR having higher resistance and two distinct curves. However, the addition of the mixed cathode and the three-layer add quite a bit. The mixed cathode has the same low charge transfer resistance as the one-layer rGO case, hinting that the unhindered connection between rGO sheets throughout the cathode is what provides this resistance reduction; however, the mixed cathode has a definite secondary semicircle, like the 1-layer GNR case but with a smaller semicircle diameter, meaning that mixing of GNR throughout the cathode still does cause some secondary effect within the system. However, the three-layer case displays a high charge transfer resistance, like the one-layer GNR case, which makes sense since it has a full GNR layer, but the split rGO layers dampen the effect of the GNR some, as seen by the dampening of the secondary semicircle.

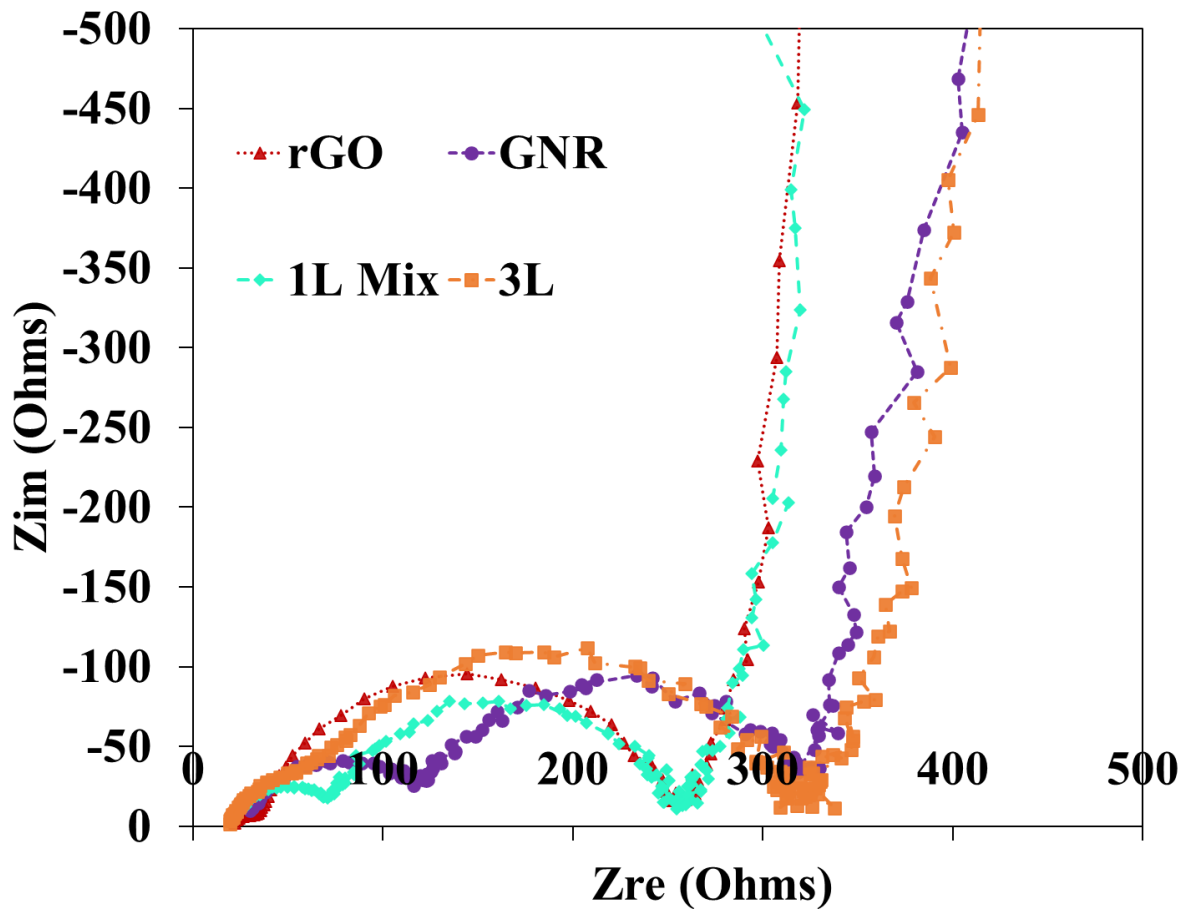


Figure 2.11: Layered Cathode EIS

After considering the structural and electrochemical properties of the cathodes, the cathodes were all ran within the Li-Air battery system. Initial single layer tests ran at 0.05 mA/cm², the current density matching the conditions of Dr. Kim's layered tests; however, the capacity results reached by our layered electrospray cathodes were significantly greater than those reached by Dr. Kim, sparking a more in-depth study on the difference between dropcasting and electro spraying (shown in a different chapter). Due to these results, the current density of the layered electrospray cathodes was increased tenfold to 0.50 mA/cm², whose cycling data and capacity curves can be seen in Figure 2.12. The deep discharge data shows that individually and combined the rGO is a better cathode material than GNR. For the single layer system, this is

readily apparent as the rGO system has almost ten times the capacity of the GNR system and the capacity curves show that the GNR system has roughly a 0.1 V increase in overpotential during discharge (the ORR) and around a 0.2 V increase in overpotential during charge (the OER). This increase in charge overpotential was not expected, since the CV data suggested that the GNR is a better surface for the OER reaction, but this could be due to the much poorer surface that the GNR is for Li_2O_2 formation (the ORR reaction) creating a more strongly deposited Li_2O_2 layer that the GNR system was not able to easily remove. The limited capacity data for the single layer systems also support the superior performance of the rGO system in comparison to the GNR system, but the effect is a lot more muted than what the deep discharge system would suggest. In the limited capacity trials, the GNR had 6 cycles at max capacity, while the rGO cathode had 11 cycles at max capacity, which is a far cry from the almost tenfold increase in capacity seen during the deep discharge trials. Considering the CV results, this could show the benefits of the GNR surface for the OER, which the CV results had said should require a lower overpotential to complete. In the deep discharge case, the cathode surface is assumed to be 100% coated with Li_2O_2 at the end of discharge, which is not the case for the limited capacity system. These results suggest that the GNR surface can better handle the removal of Li_2O_2 when the system is not completely coated, even though the possible capacity able to be maintained by the GNR system is less than that of the rGO system.

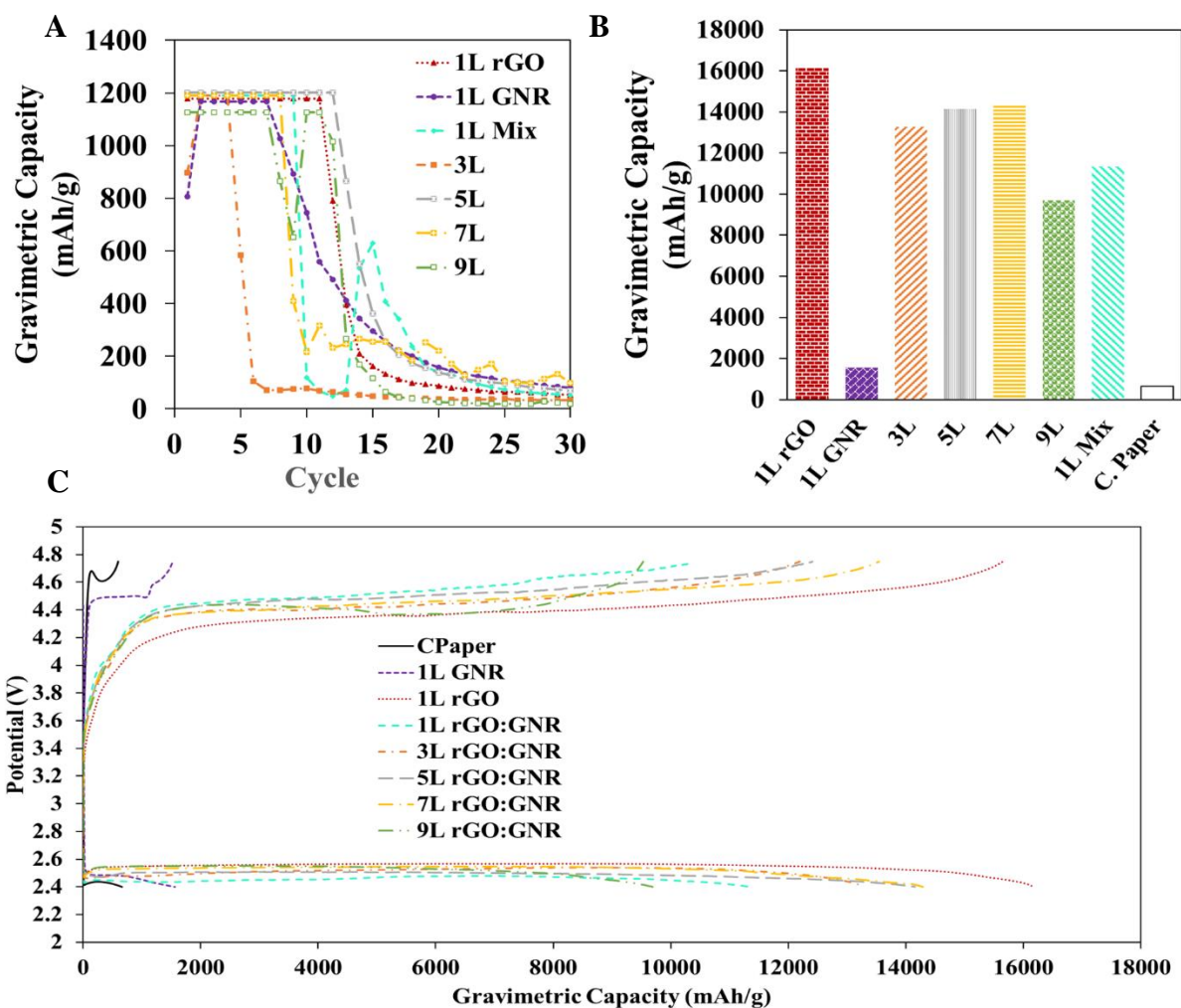


Figure 2.12: Layered Cathode Battery Cycling Data: A: 1 mAh limited capacity data. B: Gravimetric energy density comparison graph. C: Voltage-Cycling curves for overpotential comparisons

In the mixed and layered systems, the comparison of the battery data is a little more muddled. Setting aside the nine layer and mixed system, some trends within the 3, 5, and 7-layer systems can be seen. These systems show that there are some beneficial effects of layering different carbons because as the number of layers increased, the capacity increased and both the discharge and charge overpotentials decreased, though the actual difference seen is very small.

The benefits of combining different carbon structures are not seen within the mixed cathode system, which has significantly higher overpotentials and decreased capacity, meaning that layering the different carbon types specifically has a benefit within the Li-Air batteries.

However, the 9-layer system does show that these benefits are not maintained when the carbon layers start to have extremely low loading, as even though the nine-layer system retained the lower overpotentials of the other layered systems, its lower capacity shows that it was not able to handle the stress during cycling, especially during charge since the nine-layer system as a steeper curve to the terminal voltage. The downturn of the 9-layer system could be due to the large number of interfaces that are present in the 9-layer system, as each GNR layer creates 2 more rGO to GNR interfaces that electrons must pass through to reach the positive terminal. In the case of the 9-layer system, it has 8 such interfaces that the electrons of any reactions happening close to the carbon paper substrate must go through to reach the positive battery terminal. Each interface should add some resistance to the system, but the lower layered cathode systems seem to be affected by this less, possibly due to the thicker layers of the highly electrically conductive GNR and for the 5 and 7-layer systems, possibly due to the increased compactness, and therefore shorter electron pathways, of the cathode seen in the bulk density data. All of the systems containing GNR pale in comparison to the single layer rGO system for the deep discharge trials, where the single rGO layer system had lower overpotential and higher capacity. However, the limited capacity trials for the mixed system and the layered systems other than the 3-layer system reach a very similar number of cycles and total capacity to the limited capacity trial of the single layer rGO system. This again suggests that the GNR might have some beneficial properties for the OER to help improve limited capacity cycling performance when combined with the high

capacity rGO, but the 3-layer system shows that a single thicker GNR layer separating the rGO layers may not provide the same benefits.

2.4 Conclusion

Although layering carbon materials was suggested by past results to increase capacity in dropcasted cathodes, the same dramatic increase in capacity was not seen within the electro spray system. However, the lack of similar results did not result in a lack of successes, mainly due to the difference in the cathode fabrication method. In considering the layering process, it was seen that dropcasting does reach a limit on the low end of loading, where extremely low loading solutions such as those needed for a large number of layers will no longer create a uniform layer of material upon the cathode surface, and that this issue was not present within the electro spray system. Additionally, the electro spray cathodes were shown to handle much higher current densities than their dropcasted counterparts, leading to additional studies into the reasons for this incredible increase in performance. Furthermore, it was shown that some small benefits of layer do exist between rGO and GNR, as shown by the improving benefits of the 3, 5, and 7-layer systems, respectively. However, GNR may not have been the right high aspect ratio carbon to consider for this layering, as even though it had been shown in the past to have improved individual performance to other high aspect ratio carbons, its addition to the rGO electro spray system detracted from the batteries overall performance. There may be some benefit to considering other high aspect ratio carbons for future testing of the layered air-controlled electro spray system, but the major improvements of the electro spray process of cathode creation to the dropcasting process are worth pursuing, as well.

2.5 Appendices

1. Whittingham, M.S., “Lithium Batteries and Cathode Materials”, *Chem. Rev.*, **104**, 4271-4301, (2004)
2. Goodenough, J.B., Park, K-S., “The Li-Ion Rechargeable Battery: A Perspective”, *J. Am. Chem. Soc.*, **135**, 1167-1176, (2013)
3. Goodenough, J.B., Kim, Y., “Challenges for Rechargeable Li Batteries”, *Chem. Mater.*, **22**, 587-603, (2010)
4. Choi, J.W., Aurbach, D., “Promise and reality of post-lithium-ion batteries with high energy densities”, *Nat. Rev.*, **1**, 1-16, (2016)
5. Wang, H., Yang, Y., Liang, Y., Robinson, J.T., Li, Y., Jackson, A., Cui, Y., Dia, H., “Graphene-Wrapped Sulfur Particles as a Rechargeable Lithium-Sulfur Battery Cathode Material with High Capacity and Cycling Stability”, *Nano Lett.*, **11**, 2644-2647, (2011)
6. Williams, B.P., Joo, Y.L., “Tunable Large Mesopores in Carbon Nanofiber Interlayers for High-Rate Lithium Sulfur Batteries”, *J. Electrochem. Soc.*, **163**, 13, A2745-2756, (2016)
7. Zhao, M-Q., Zhang, Q., Huang, J-Q., Tian, G-L., Nie, J-Q., Peng, H-J., Wei, F., “Unstacked double-layer templated graphene for high-rate lithium-sulphur batteries”, *Natt. Comm.*, **5**, 3410, 1-5, (2013)
8. Peng H-J., Huang, J-Q., Zhao, M-Q., Zhang, Q., Cheng X-B., Liu, X-Y., Qian, W-Z., Wei, F., “Nanoarchitected Graphene/CNT@ Porous Carbon with Extraordinary Electrical Conductivity and Interconnected Micro/Mesopores for Lithium-Sulfur Batteries”, *Adv. Funct. Mater.*, **24**, 2772-2781, (2014)

9. Xu, C., Xu, B., Gu, Y., Xiong, Z., Sun, J., Zhao, X.S., “Graphene-based electrodes for electrochemical energy storage”, *Energy Environ. Sci.*, **6**, 1388-1414, (2013)
10. Shoorideh, G., Ko, B., Berry, A., Divvela, M.J., Kim, Y.S., Li, Z., Patel, B., Chakrapani, S., Joo, J.L., “Harvesting Interconductivity and Intraconductivity of Graphene Nanoribbons for a Directly Deposited, High-Rate Silicon-Based Anode for Li-Ion Batteries”, *ACS Appl. Energy Mater.*, **1**, 1106-1115, (2018)
11. Shoorideh, G., Kim, Y.S., Joo, Y.L., “Facile, Water-Based, Direct-Deposit Fabrication of Hybrid silicon Assemblies for Scalable and High-Performance Li-Ion Battery Anodes”, *Electrochim. Acta*, **222**, 946-955, (2016)
12. Li, F., Zhang, T., Zhou, H., “Challenges of non-aqueous Li-O₂ batteries: electrolytes, catalysts, and anodes”, *Energy Environ. Sci.*, **6**, 1125-1141, (2013)
13. McCloskey, B.D., Scheffler, R., Speidel, A., Bethune, D.S., Shelby, R.M., Luntz, A.C., “On the Efficacy of Electrocatalysis in Nonaqueous Li-O₂ Batteries”, *J. Am. Chem. Soc.*, **133**, 18038-18041, (2011)
14. Thotiyl, M.M.O., Freunberger, S.A., Peng, Z., Chen, Y., Liu, Z., Bruce, P.G., “A stable cathode for the aprotic Li-O₂ battery”, *Nat. Mater.*, **12**, 1050-1056, (2013)
15. Ellis, B.L., Lee, K.T., Nazar, L.F., “Positive Electrode Materials for Li-Ion and Li-Batteries”, *Chem. Mater.*, **22**, 691-714, (2010)
16. Cheng, F., Chen J., “Metal-air batteries: from oxygen reduction electrochemistry to cathode catalysts”, *Chem. Soc. Rev.*, **41**, 2172-2192, (2012)
17. Abraham, K.M., Jiang, Z., “A Polymer Electrolyte—Based Rechargeable Lithium/Oxygen Battery”, *J. Electrochem. Soc.*, **143**, 1, 1-5, (1996)

18. Beattie, S.D., “High-Capacity Lithium-Air Cathodes”, *J. Electrochem. Soc.*, **156**, 1, A44-A47, (2009)
19. Kuboki, T., Okuyama, T., Ohsaki, T., Takami, N., “Lithium-air batteries using hydrophobic room temperature ionic liquid electrolyte”, *J. Power Sources*, **146**, 766-769, (2005)
20. Mitchell, R.R., Gallant, B.M., Thompson, C.V., Shao-Horn, Y., “All-carbon-nanofiber electrodes for high-energy rechargeable Li-O₂ batteries”, *Energy Environ. Sci.*, **4**, 2952-2958, (2011)
21. Xiao, J., Mei, D., Li, X., Xu, W., Wang, D., Graff, G.L., Bennett, W.D., Nie, Z., Saraf, L.V., Aksay, I.A., Liu, J., Zhang, J-G., “Hierarchically Porous Graphene as a Lithium-Air Battery Electrode”, *Nano. Lett.*, **11**, 5071-5078, (2011)
22. Cheng, X-B., Huang, J-Q., Peng, H-J., Zhao, M-Q., Wei, F., “Aligned carbon nanotube/sulfur composite cathodes with high sulfur content for lithium-sulfur batteries”, *Nano Energy*, **4**, 65-72, (2014)
23. Bharathi, S., Nataraj, D., Mangalaraj, D., Masuda, Y., Senthil, K., Yong, K., “Highly mesoporous α -Fe₂O₃ nanostructures: preparation, characterization and improved photocatalytic performance towards Rhodamine B (RhB)”, *J. Phys. D: Appl. Phys.*, **43**, 015501, (2010)
24. Zhang, G.Q., Zheng, J.P., Liang, R., Zhang, C., Wang, B., Hendrickson, M., Plichta, E.J., “Lithium-Air Batteries Using SWNT/CNF Buckypapers as Air Electrodes”, *J. Electrochem. Soc.*, **157**, 8, A953-956, (2010)
25. Kim, J., (2017), *A Study of Engineering the Cathode Structures for Improved Performance in Lithium Batteries*, [unpublished doctoral dissertation], Cornell University

Chapter 3: Single Layer rGO Cathode Fabrication Techniques for Li-O₂ Batteries

Since their discovery in the 70s, Lithium Ion (Li-Ion) Batteries have dominated the global battery market.^[1,2] Due to their simplistic design of moving intercalated lithium ions between two relatively inert electrode substrates, they are used around the world for consistent rechargeable electrical power. However, growth in the field of Li-Ion batteries has started to slow down, nearing the theoretical capacity limit of ~600 W*h/kg due to anode and cathode material limitations.^[1,3] With ever increasing demands for higher energy density batteries than what Li-Ion batteries can supply, such as for the electric vehicle industry, newer, more reactive batteries with experimental chemistries have been considered; however, with increasing reactivity, new challenges and issues must be considered and overcome for any other battery technology to meet the needs that Li-Ion batteries may no longer handle, competing against the high 1300 W*h/kg energy density of gasoline combustion^[4]. The fabrication process of these batteries must be cheap to set up, easily usable, and scalable to be able to make abandoning the currently entrenched electrode fabrication processes worth the cost to the battery industry.

3.1. Introduction

As Chapter 2 suggested, a deeper study of the effects of the cathode fabrication method would provide enhanced knowledge of the Li-O₂ cathode system. From Chapter 1, we know that Li-O₂ batteries reduce gaseous oxygen on an electrically-conductive, solid surface with lithium ions dissolved in the liquid electrolyte to form lithium oxide, Li₂O, and lithium peroxide, Li₂O₂^[5], at the three-phase interface.^[6] This proceeds by the net electrochemical reaction, $2\text{Li}^+_{(\text{aq})} + 2\text{e}^- + \text{O}_{2(\text{g})} \leftrightarrow \text{Li}_2\text{O}_{2(\text{s})}$ ($E = 2.96 \text{ V}$ versus Li/Li⁺)^[7], where the forward reaction is the Oxygen Reduction Reaction (ORR) and the reverse reaction is the Oxygen Evolution Reaction (OER). The ORR is what gives this battery such a large energy density, but this reaction, and the

components needed to create it, create many challenges that must be overcome before Li-O₂ batteries become adopted by the battery industry and consumers. The basic Li-O₂ battery, as depicted in Figure 3.1, consists of a metal lithium anode, a separator, an electrolyte, and a cathode. The cathode has garnered particular attention, since it needs to be both porous, to allow for oxygen and lithium-ion diffusion, but still electrically conductive. As shown in the zoom in, one way to do this is to use a conductive substrate for structural stability and then add a material with greater surface area for the ORR/OER to proceed on.

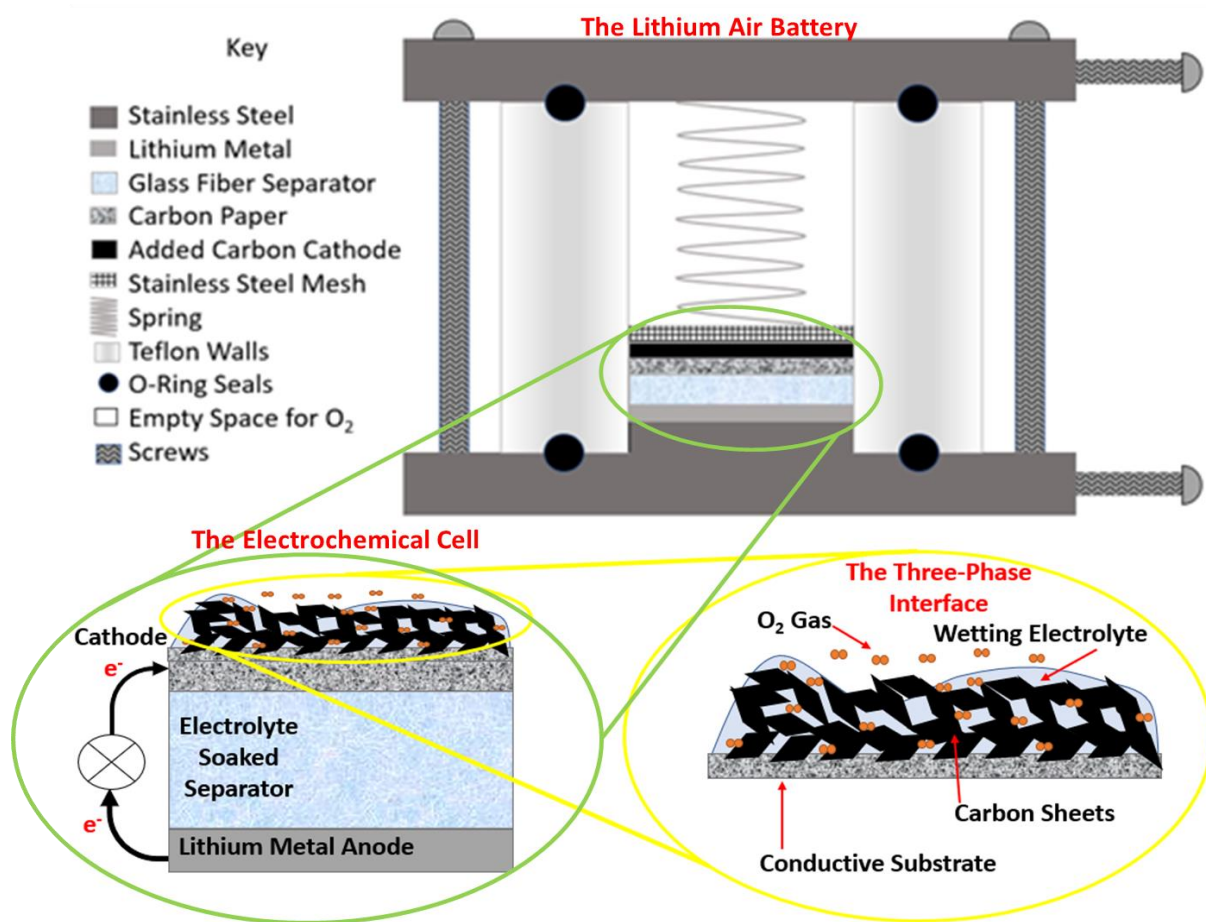


Figure 3.1: Image and schematic of Swagelok-type Li-O₂ battery, highlighting the electrochemical cell and the cathode's three-phase interface.

The Li-O₂ cathode has many properties that it must maximize all at once to allow fast reaction rates: high electrical conductivity, high reaction surface area, cathode integrity, fast

oxygen diffusion, and fast Li^+ ion conductivity. [8,9] The issue of high overpotentials can be lowered by limiting cell resistance, such as by increasing cathode electrical conductivity through cathode morphology or ordering. [10-12] Even within the carbon-based cathode system, many different cathode structures and fabrication methods have been considered over the years to accomplish this and to increase the cathode surface area. Early attempts by Kuboki, *et al.* dried 150 μm thick carbon sheets on nickel foam mesh at high temperature and time (150°C for 12 hours) to make cathodes that reached $\sim 2200 \text{ mAh} \cdot \text{g}^{-1}$ at $0.1 \text{ mA} \cdot \text{cm}^{-2}$ [13], improving upon the first non-aqueous Li-Air batteries from Abraham and Jiang that compressed a dried Chevron acetylene black carbon/polyacrylonitrile film into a porous nickel substrate for cathodes that reached $\sim 1450 \text{ mAh} \cdot \text{g}^{-1}$ at $0.1 \text{ mA} \cdot \text{cm}^{-2}$. [14] Similarly, Beattie *et al.* dip coated porous carbon Ketjen Black on a thick (1.7 mm) Nickel Foam substrate. Although requiring long drying times and high temperature, these cathodes were highly loaded (1.9 mg Ketjen Black on 7/16 in diameter substrate), creating separated clusters of Ketjen Black on the Nickel Foam matrix, and reached $5813 \text{ mAh} \cdot \text{g}^{-1}$ at $0.1 \text{ mA} \cdot \text{cm}^{-2}$. [9] Mitchell *et al.* used chemical vapor deposition to grow an 8 μm thick layer of porous carbon nanofibers on porous aluminum oxide to a loading of $0.11 \text{ mg} \cdot \text{cm}^{-2}$, reaching a capacity around $4900 \text{ mAh} \cdot \text{g}^{-1}$ at $4 \text{ uA} \cdot \text{cm}^{-2}$. [15] Zhang *et al.* created single-wall carbon nanotube via electrochemical deposition into carbon nanofibers buckypapers via filtration method to create binderless electrodes that reached $\sim 2500 \text{ mAh} \cdot \text{g}^{-1}$ at $0.1 \text{ mA} \cdot \text{cm}^{-2}$, and saw that capacity decreased as the buckypaper thickness increased. Considering beyond the carbon cathode system, many studies have looked at different cathode materials and the addition of metal oxide and metal carbide electrocatalysts to lower the overpotential of the OER and increase the reversibility of the generated Li_2O_2 . [17-21] After

optimizing the cathode structure and material, the addition of such catalysts could be key to creating stable Li-Air batteries with long cycle lifetimes.

Considering that the Li_2O_2 is formed upon the cathode surface, many researchers have looked into the Li_2O_2 formation process, showing many possible, current dependent crystal structures, but this research is restricted by the low current densities ($< 0.1 \text{ mA} \cdot \text{cm}^{-2}$) required to see these crystal morphology differences.^[22-26] Additionally, these studies show the adverse effect that increasing current density has upon discharge capacity and overpotential, causing a great decrease in capacity with a large increase in overpotential. However, many of these cathode systems require expensive carbon synthesis, such as chemical vapor deposition, or long and high temperature drying times, and very few have studied current densities beyond $0.1 \text{ mA}/\text{cm}^2$, meaning that full discharge may take days or a week to complete. Extending beyond these lower current densities is where we want to extend Li-Air battery research. In 2017, Li *et al.* reached $\sim 2100 \text{ mAh/g}$ in 0.5M DME/LiTFSI and improved to $\sim 4300 \text{ mAh/g}$ in a co-salt electrolyte of DME/LiTFSI/LiI at $0.3 \text{ mA}/\text{cm}^2$ with an activated carbon slurry-coated cathode at high carbon loading ($3.0\text{-}4.0 \text{ mg}$ on 12.7 mm diameter carbon paper disks), which would have taken between $50\text{-}67$ hours to discharge. By increasing the current density even further, the quicker the full capacity of the Li-Air battery is available to the user; however, this will in turn require a strong and dense cathode system that can withstand the forces necessary to discharge and charge at those high currents. We seek to create these durable cathodes by improving upon traditional fabrication processes, to create denser, defect free cathodes for improved battery performance, and to manufacture them with greater consistency and speed, for increased industrial relevance.

As can be seen from the literature, there are many different ways in which the active material can be added to the conductive structural support. The Air-Controlled Electrospray

(ACES) and Dropcasting were already discussed briefly in Chapter 1, but their process is shown in Figure 3.2, along with the Slurry Coating and Spin Coating processes. Since this chapter is a discussion upon these fabrication processes, we will discuss them again with a little more depth.

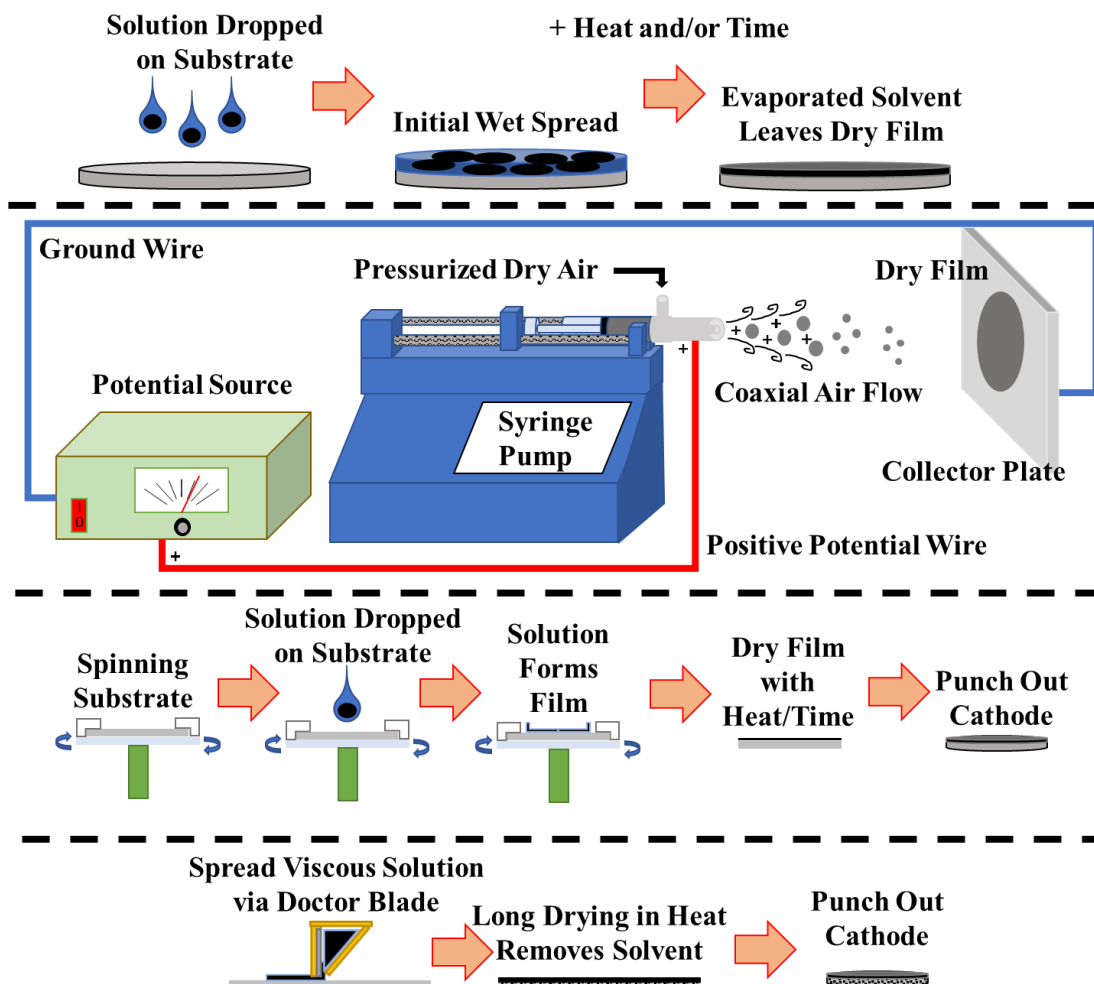


Figure 3.2: Schematics of 4 different fabrication processes, from top to bottom: Dropcasting, Air-Controlled Electro spray (ACES), Spincoating, and Slurry Coating

In this chapter, we compare the effects of these varying cathode creation processes. In this paper, we compare the Air-Controlled Electro spray (ACES) technique to the traditional electrode preparation methods of Dropcasting, Slurry Coating, and Spincoating. Due to issues with the Slurry Coating and Spincoating techniques discussed in the discussion and results section, the brunt of the comparisons made were focused on the ACES and Dropcasting systems.

A diagram of the four fabrication methods is seen in Figure 3.2. Traditional additive manufacturing processes for many different battery types, like slurry coating and dropcasting, add active material to a conductive substrate (or precursors for active material growth), where the active material dries to form the cathode.^[27,28] In the case of dropcasting, the active material is added dropwise via a solvent to the top of the porous substrate, where it is left to dry, usually sped up through the use of a furnace. This process is inherently difficult to control mass loading, leading to a poorer yield of in-spec cathodes, and the drying out of the active material is more likely to form cracks within the active material layer. Slurry coating is a traditional cathode creation process where a slurry of active material in a solvent is added to a desired substrate via a Doctor Blade, which controls the layer thickness of the slurry by removing excess slurry above a desired height.^[29-31] These substrates are then dried to remove the solvent, leaving the active material behind on the substrate, and a cathode may be punched from that material. Slurry coating has more loading control than dropcasting, due to the layer thickness control of the Doctor Blade, but the viscous slurry requires a much less volatile solvent than in dropcasting, requiring longer heating times and still retaining the cracking issues present in dropcasting. Spincoating is a film addition process that has been well developed in the polymer film industry and has been used for the addition of active material for Li-Ion battery electrodes.^[32-34] During spincoating, the substrate is rotated and the active material solution is added to its center, allowing centrifugal forces to pull the solution over the surface of the substrate to create a film on the substrate surface. These films have the benefit of being very thin, but the solution viscosity, solute volatility, and loading placement control the uniformity of the film and the centrifugal motion required by the process limits the scalability for industrial use. ACES, a process of film creation by drying solution droplets via a potential difference and convective airflow, is considered

against these more traditional processes. In ACES, a solution is forced through a small needle, and the solution gathered at the end forms a Taylor-Cone due to the potential difference between the needle and the collector. This cone then breaks apart into charged droplets, that are attracted to the grounded collector. As they travel, the solvent in the droplets dries, and the amount of drying in the air can lead to different morphologies of the particles upon landing on the collector.^[35]

Much past group research as looked at both traditional additive manufacturing process and/or in AC Electro spraying for tailoring electrodes and separators for many different battery systems.^[36-44] For Li-Air batteries, Yin *et al.* found that adding graphene nanoribbons to ZnO fibers increased cyclability, while Kim *et al.* found that void spaces within the cathode during cycling should be prevented, or removed via thermal restacking, to improve battery cycle life. Divvela *et al.* found that for the Lithium Sulfur (Li-S) battery system, AC Electro spray cathodes had many benefits over slurry coated cathodes. Due to the increased mechanical stability from the elimination of cracks present in slurry coated cathodes, ACES cathodes showed both better capacity retention, especially at high C-rates. Due to the success seen within the Li-S system, ACES should be considered within the Li-Air system, as well.

3.2. Experimental Section

3.2.1 Solution Preparation

Solutions for ACES, dropcasting, and spincoating were prepared using reduced graphene oxide (rGO) [Dongjin Semichem], Nafion D2020 binder [Ion Power, Inc.] and ACS Grade isopropyl alcohol (IPA) [VWR]. Solutions were constructed in a 20 mL scintillation vial with a 20:80 \pm 1 binder:rGO mass ratios in 5 mL IPA, which was maintained for all tests. For

electrospraying, dropcasting, and spincoating solutions, the carbon mass loading was 1%. After solutions were made, they were sonicated in an ice bath using a tip sonicator [Q500, Qsonica] for 30 minutes at 30% amplitude, using a 5 sec on/off pulse. After sonication, the solutions were stirred on a stir plate at 400 rpms overnight before use. The slurry coating solutions are made during the slurry coating process (no sonication or prep), due to their need for a “honey-like” viscosity iterative ball milling, which is discussed later in the experimental section.

3.2.2 Carbon Substrate Preparation

Carbon paper [TGP-H-030, 50% Wetting, Toray], a conductive, porous carbon fiber mat was used as the conductive substrate. To remove excess Teflon coating, the carbon paper was heat treated in under an inert Argon atmosphere in a tube furnace [OTF-1200X, MTI Corp] at 900 °C for 2 hours, using a 5 °C/min temperature ramp, while being held between two alumina-silicate ceramic plates [McMaster Carr]. After heat treatment, 15 mm diameter carbon paper substrates were punched out between two weigh paper sheets to prevent edge defects and cracking, using a hand punch [T-0.6, MTI Corp].

3.2.3 Dropcasting

The dropcasting process is shown in Figure 3.2. All dropcasting was done via plastic pipettes. Micropipettes were also considered for better volume control during loading, but these left a greater number of cracks so they were not used for testing. Initially, 2 drops of IPA were added via plastic pipette to each cathode to allow for good wetting of the carbon solution to fully cover the surface of the carbon paper substrate and lessen cracking. After 10 seconds of drying time, 7-8 drops of carbon solution were added to the center of the carbon paper substrate. After 1 minute of drying in air, the cathodes were placed in a box furnace [Vulcan3-550, Vulcan] to be dried at 50 °C for 10 hours, using a 5 °C/min ramp. After this, the cathodes were allowed to cool

to ambient temperature and placed in a glovebox [VGB-6, MTI] filled with ultra-high purity argon [Airgas].

3.2.4 Air-Controlled Electro spraying (ACES)

As shown in Figure 3.2, the Air-Controlled Electro spraying was done using a coaxial needle (outer needle: 12 gauge; inner needle: 16 gauge) [Hamilton], where the inner needle supplied the carbon solution and the outer needle created an air sheath using the building's process air. Using a pressure regulator, the process air was lowered to and controlled at 35 psi. An applied potential of 5 kV was supplied by a potential source [ES30P-5W HV Power Supply, Gamma High Voltage Research] via an alligator clip on the needle tip, and a ground from the same potential source was attached to the aluminum foil covered stainless steel collector plate. A syringe pump [Pump 11 Elite, Harvard Apparatus], was used to keep the solution flow rate at 0.09 mL/ min for 2-3 minutes, with a spray distance from the needle to the collector of 6 cm, creating an electric field of 83 kV/m between the charged tip and grounded collector. The carbon substrate was held in the spray area, and a mask was used so that the amount of uncoated area would always be uniform between samples. To do so, a small sheet of folded aluminum foil was hung from the top of the collector (making sure to keep the back of the folded foil in contact with the collector, and, using non-conductive paper clips, a clear poly vinylchloride sheet was used as a mask to limit the spray circle diameter to 14 mm. This 14mm hole was created using a hand punch. Additionally, before starting each spray, a cardboard barrier was used to prevent overloading from spurting sprays upon starting the syringe pump, and the removal of this barrier was the signal for starting the spray time. The fabricated cathodes were then moved into an ultra-high purity argon [Airgas] filled glovebox [VGB-6, MTI Corp., < 5 ppm O₂ and H₂O] for cell

assembly, and were fabricated at a carbon loading of 0.5 ± 0.03 mg rGO / cm² carbon paper substrate area.

3.2.5 Spin Coating

The spin coating samples of heat-treated carbon papers were cut into 2-inch squares that were then massed. Due to spin coating requiring suction to the central spinning shaft, the carbon paper was placed on 2-inch square glass slides, the undersides of which were marked to ensure the center of the slide was in the center of the rotating shaft. Initial attempts to affix the carbon paper used a low residue, easy-peel tape, but this caused ripping of the carbon paper upon removal from the slide. Instead, a mask of Delrin plastic was made in-house in the machine shop to hold the carbon paper in place, and it was given a sharp beveled inner edge to help guide excess solution away from the carbon paper during rotation. Once the Delrin mask was covering the carbon paper and glass, tape was used to tightly affix the plastic to the glass slide, keeping the carbon paper fixed in place during rotation. As shown in Figure 3.2, after placed on the central shaft, the apparatus was affixed by allowing the vacuum of the attached pump by a command on the spinning unit [Smart Coater 110-B with Diaphragm Vacuum Pump, Best Tools]. To prevent the acceleration during initial rotation times to be an issue, solution was added to the actively spinning samples 3 seconds into the rotation, via the sample hole at the top of the apparatus and using a micropipette for volume control. Rotation speeds between 100 and 3000 rpms were considered, and spin time for excess drying and solvent removal were considered between 10 and 30 seconds (plus the 3 second warm up time). After the spinning finished, the machine slowed down to rest on its own and the suction was automatically removed. After 1 minute of drying in air, the samples were placed in a box furnace [Vulcan3-550,

Vulcan] to be dried at 50 °C for 3 hours, using a 5 °C/min ramp, after which the samples were collected and cathodes could be punched out from the coated area.

3.2.6 Slurry Coating

Due to the need of a large mass of carbon necessary to get the high viscosity and good coverage, early slurry coating attempts used Ketchen Black, a porous carbon. Final attempts, like those discussed in this thesis, used the same rGO [Dongjin Semichem] as what was used for the other fabrication techniques, though the process can use any type of carbon material. Due to solvent/binder compatibility issues because IPA is too volatile, drying out too quickly for slurry coating, and the D2020 binder is a form of PTFE suspended in alcohol, the binder and solvent used for the slurry coating were the traditional options of choice for slurry coating, 5% polyvinylidene fluoride (PVDF) in N-Methyl-2-pyrrolidone (NMP). The binder solution was massed out to reach 5% PVDF by mass in DMF, and then mixed on a stir plate overnight to ensure good mixing. 0.3 g of rGO was added to the stainless-steel holder of a MM400 Retsch Ball Mill, along with 5 ml of binder solution and 15 3mm stainless steel balls. This initial mixture was sealed up and ball milled for 10 minutes at 20 hz. After the initial milling, 5 mL of solution was added to the sample, and the sample was ball milled for 5 minutes at 20 hz. All additional solution additions were of 1 mL of solution, with 5 minutes of ball milling at 20 hz. This process was continued until the viscosity of the solution was “honey-like”, after which the steel balls were removed and the resulting carbon slurry was collected.

Unlike the other fabrication methods, the slurry coating solution was immediately used to create cathodes to prevent the solution drying out and changing viscosity. A carbon paper sheet was affixed atop a glass slide and held in place to the slide and table via binder clips to prevent moving during the slurry coating process. As the carbon paper is around 110 um thick, a doctor

blade was set to 200 μm in attempts to achieve a 90 μm layer of carbon. As shown in Figure 3.2, the doctor blade was placed over the sample, and the slurry was placed in behind the doctor blade. Using a single steady motion, the blade was drawn over the sample and the slurry was deposited upon the carbon paper surface. The coated carbon paper was then dried in ambient air for 24 hours to evaporate all of the solvent. After 24 hours of drying in air, the samples were placed in a box furnace [Vulcan3-550, Vulcan] to be dried at 50 $^{\circ}\text{C}$ for 3 hours, using a 5 $^{\circ}\text{C}/\text{min}$ ramp, after which the samples were collected and cathodes could be punched out from the coated area. The fabricated cathodes were then moved into an ultra-high purity argon [Airgas] filled glovebox [VGB-6, MTI Corp., < 5 ppm O_2 and H_2O] for cell assembly.

3.2.7 Electrolyte and Separator

A solution of 1M Lithium Triflate (LiCF_3SO_3) [Sigma Aldrich] in ACS Grade 1,2-dimethoxyethane (DME) [VWR] was used as the electrolyte, created in a glovebox under inert Argon gas. This solution was stored within the glovebox and was kept under constant stirring to maintain solution consistency. Separators were prepared by punching 19 mm diameter disks from glass fiber filters [GF/D, Whatman], between weigh paper sheets to prevent edge defects, using a hand punch [T-0.6, MTI Corp.]. These were immediately added to the glovebox, as well, and were stored separately from each other for ease of access and to prevent damage from tweezer pressure.

3.2.8 Cell Assembly

A picture and labeled schematic of the Li-Air cells is shown in Figure 3.1. Li-Air cells were created using 316 stainless steel Swagelok style cells, made in-house, and plastic tweezers were used during cell assembly to prevent capacity loss. Cell assembly began with placing a lithium disk [16 mm dia, 0.6 mm thick, MTI] on the central stage of the negative terminal and

compressing slightly with a Delrin plastic rod [McMaster Carr] for good lithium-to-stage contact. On top of that, a glass fiber separator was centered above the lithium disk and was saturated with 310 μL of electrolyte. The separator was well saturated with electrolyte so that minor evaporation of the electrolyte into the dry oxygen would have little effect on battery results. Centered above the separator, the cathode was placed with the electrospray/dropcasted layer facing upward (away from the separator and towards the empty cell chamber) to lessen the diffusion distance of the future O_2 gas to the active material surface. An additional 50 μL of electrolyte was added to the cathode for ideal internal wetting of the rGO cathode. Then a stainless-steel mesh [316 SS, 0.032" opening, McMaster Carr,] was centered on top of the cathode to ensure good contact to the positive terminal and to balance pressure across the cathode surface. A Teflon cylinder with n-buna o-ring seals was then placed around the setup, creating the oxygen chamber. The assembly was connected to the positive terminal via a 316 stainless steel spring and was sealed using 4 screws. After cell assembly was finished, the cells were removed from the glovebox. Using Swagelok connectors, ultra-high purity O_2 gas [Airgas] was added to the cell at 16 psi. The cell was first purged of argon using the O_2 gas for 30 seconds and then immediately filled for another 30 seconds to ensure only pure O_2 was within the cell chamber. During this process, cells were checked for gas leakage and were removed from trials and re-sealed if a leak was found.

3.2.9 Electrochemical Characterization

Galvanostatic battery cycling was performed in a battery cycler [BTS8-WA (1mA), MTI Corp], using a cell potential cut off window of 2.4 V to 2.75 V versus Li/Li^+ at constant current, both for deep discharge cases and limited capacity cycling. For all cases, constant currents of 0.05 and 0.50 mA/cm^2 were examined. Full discharge cases did not receive a capacity limit,

while limited capacity cycling was performed to a limit of both 1 mAh and at least 20% of the deep discharge value. Electrochemical Impedance Spectroscopy (EIS) and Cyclic Voltammetry (CV) were evaluated using an electrochemical workstation [PARSTAT 4000, Princeton Applied Research]. EIS was evaluated within a frequency range of 50,000 to 0.01 Hz, using 5 mV input potential amplitude. CV was evaluated using a 2-point probe set up, connecting the leads to the Swagelok cell positive and negative terminals. These tests were performed using a scan rate of 0.1 mV/s, between the cell potential window of 2-4.8 V. Tafel plots were collected using Linear Sweep Voltammetry (LSV) [CHI600E Electrochemical Analyzer, CH Instruments, Inc.] at a scan rate of 0.01 V/s over a cell potential window of 2-2.96 V. Conductivity measurements were performed using a 4-point probe set up [CP06, Cascade] using a Keithley 2400 Source-Meter with a tungsten carbide probe, 0.05 A source current over a 0.1 V measurement range, and run via LabView software for automatic measurements. For conductivity testing, dropcasting and electrospaying was done on non-conductive plastic sheets to prevent the conductivity of the substrate from affecting the measurements.

3.2.10 Structural Characterization

The topographical and cross-sectional morphologies of the cathodes were evaluated using scanning electron microscopy (SEM) [Mira3 FESEM, Tescan] at a beam voltage of 15 kV and beam intensity of 6, while single rGO flakes were characterized by SEM [Gemini 500, Zeiss], shown in the Figure 3.3. TEM [F20 TEM STEM, FEI] on single flakes was also performed, shown in the Figure 3.3. The mesoporous/microporous surface area was evaluated using Brunauer-Emmett-Teller (BET) and Barrett-Joyner-Halenda (BJH) pore analyses [Gemini VII, Micromeritics], using ultra high purity nitrogen. Tests were performed on 10 carbon paper disks at once to reach the desired minimum surface area threshold of 1 m² for the carbon paper alone,

and was repeated for both the dropcast and electro spray cases for experimental consistency. The macroporous structure size was evaluated via porometry [CFP-1100-AEHXL, Porous Materials, Inc.], using a 6 drops of 20.1 dynes/cm oil in wet-up, dry-down method on 25 mm diameter samples. The rGO powder was characterized using x-ray diffraction (XRD) from a powder diffractometer [D8 Advance, Bruker] and Raman scattering [InVia Confocal Raman microscope, Renishaw], shown in the Figure 3.3.

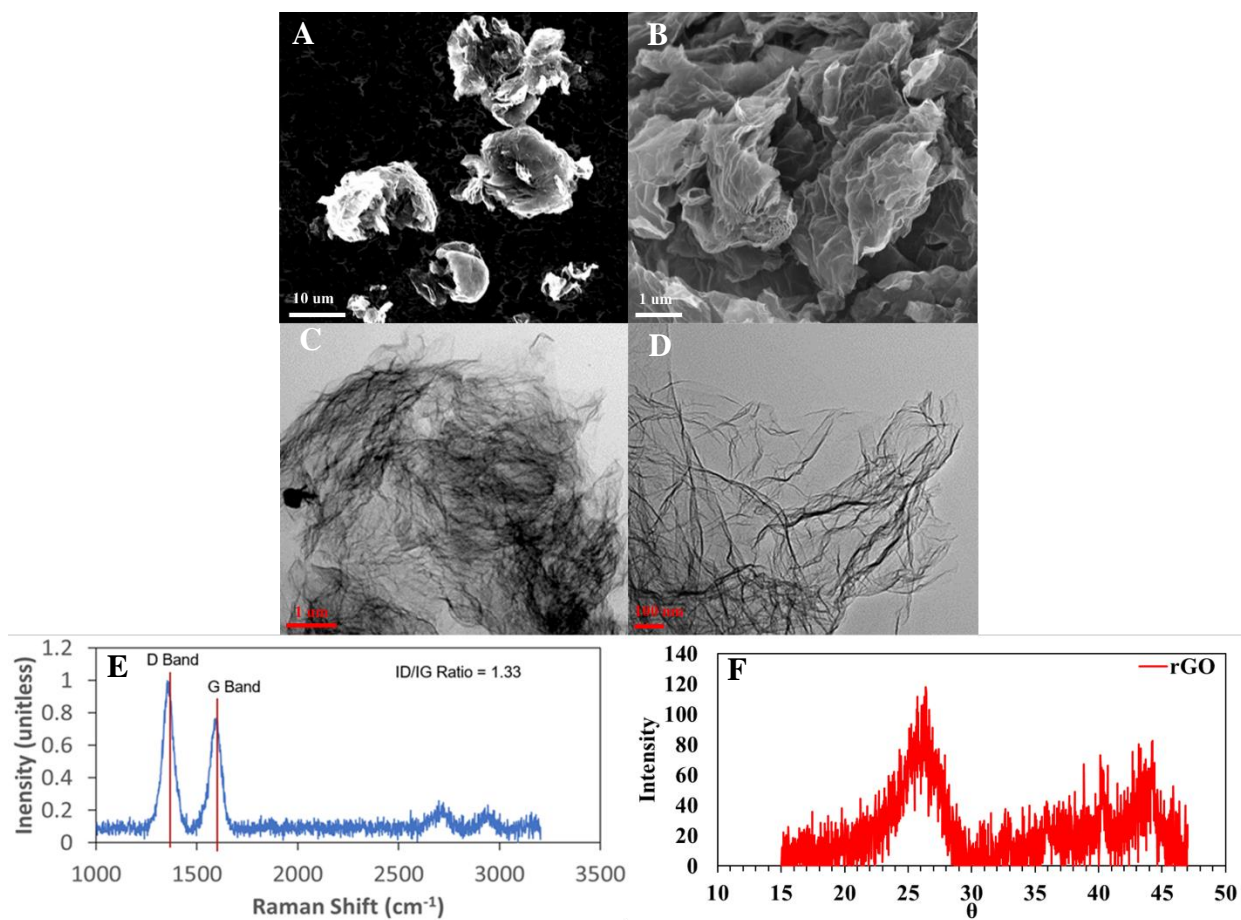


Figure 3.3: rGO Powder Information: A: Individual powder flake SEM image. B: Flake edges SEM image. C-D: TEM images of rGO powder. E: Raman spectroscopy. F: XRD peaks.

3.3. Results and Discussion

3.3.1 Slurry Coating and Spincoating Issues

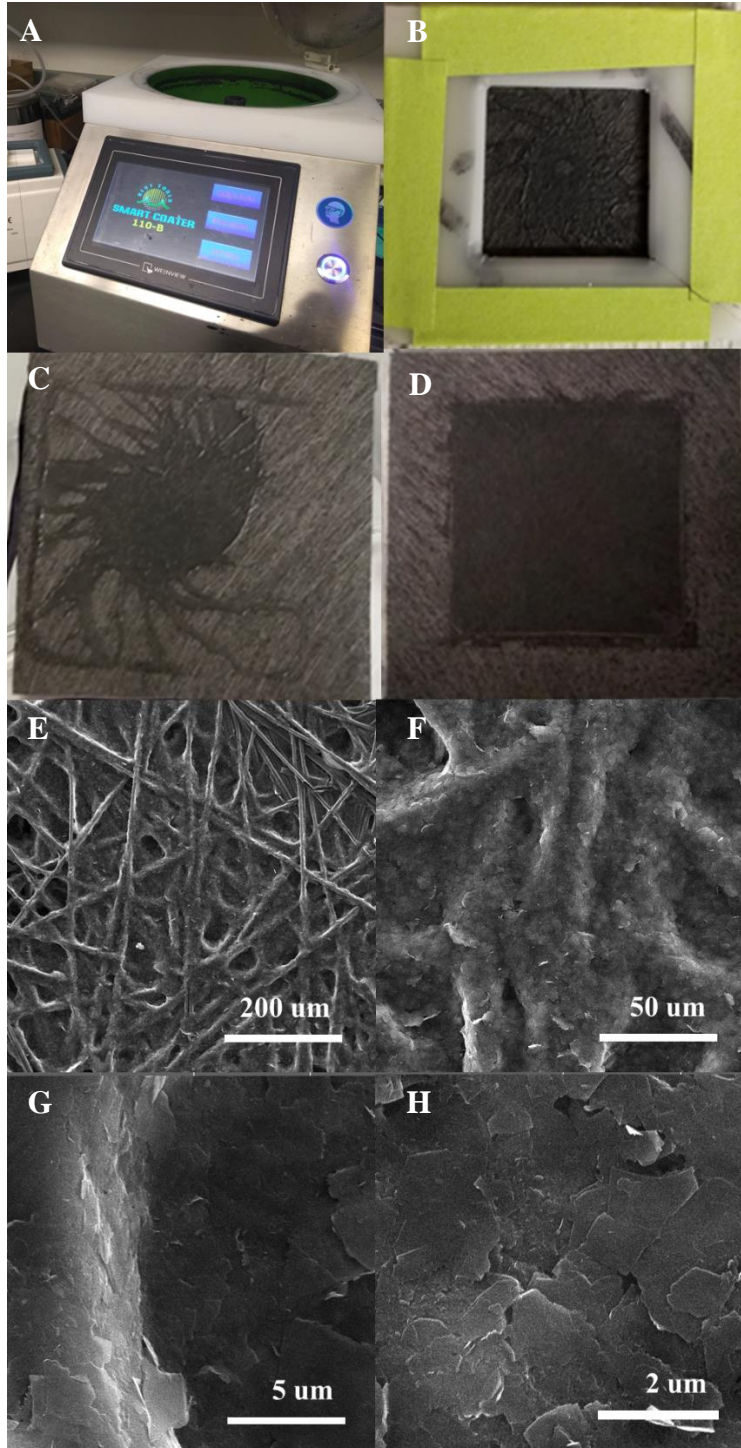


Figure 3.4: Spin Coating Images: A. Spin Coating Unit. B. Spun carbon paper with Delrin mask and tape. C. Poor coating due to high solution concentration. D. Full coating. E-H. SEM images of thin spin-coated covering on carbon paper fibers

Both the slurry coating and spincoating fabrication processes had many issues while determining their validity for Li-O₂ cathode creation. Spincoating had not before been considered for Li-O₂ cathodes and images of the spincoated carbon paper can be seen in Figure 3.4. Usually, the substrate used during spincoating would be a small thin material, such as aluminum foil, which would have a low mass and allow for good suction to the center spinning platform; however, since carbon paper is porous, it cannot be held on by suction and therefore had to be attached to a square glass slide with a plastic Delrin cover to keep the carbon paper affixed while on the rotating slide. While the solution was added to the top of the carbon paper, the placement of the solution had to be exactly in the center of the spin and the solution had to be low enough in viscosity to make sure that the solution spread equally radially. This is even more difficult for carbon paper, as it is not a complete smooth surface like metal foils are and thus the radially moving solution is also having to contend with topography changes while coating the surface. The SEM images of the coatings show that rGO film is extremely thin, showing the topography of the carbon paper underneath and sometimes even allowing the carbon paper to break through the film, but that it does not actually provide full coverage during the spin coating, leaving open spaces to deeper within the carbon paper. However, the danger to the spin coating unit was the main issue of the project, as the glass slide was large enough and heavy enough that it could obtain enough momentum while rotating to break free of the suction and slam into the wall of the spin coating unit. The potential harm to the apparatus and possible shattering of the

glass slides combined with the poor coverage hinted that this would require future consideration, but could not be continued at this time.

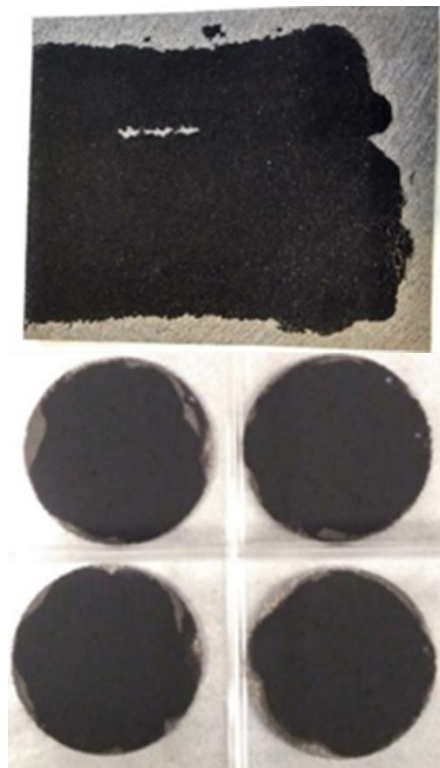


Figure 3.5: Slurry Coating Macroscale Images: Top: Slurry-Coated carbon paper. Bottom: Close-up of edge issues on punched cathodes.

The slurry coated cathodes were much more controllable in their creation, over which the rGO slurry was able to be spread over the carbon paper. However, the carbon paper would never be fully well coated, leading to very few places where a cathode with a full coating could be punched out, as can be seen in Figure 3.5. Additionally, punching out the cathode after adding the coating to the carbon paper frequently caused fracturing of the coating layer at the edges of the cathode, and would sometimes even cause more central areas of the coating to loosen and fall off later during handling. Just like with spincoating, which would also require punching out the cathode after forming the film, slurry coating would require assuming an average carbon paper

disk mass, which would also fluctuate from sample to sample, to calculate the amount of carbon loaded. These loading issues were not present within the ACES and dropcasting fabrication processes because the cathode could be pre-punched to size before adding the carbon solution to the carbon paper substrate, leading to a better understanding of the mass loading. It was considered using a masking system of punched aluminum foil to create a similar effect within the dropcasting system, which would allow for using pre-cut carbon paper and better mass loading control, but the honey-like viscosity requirement of the slurry coating would cause the carbon paper disks to move with the slurry, never fully covering their surface. With the uneven loading of the slurry upon the carbon paper and the considerable assumptions required to determine the active material loading, the slurry coated cathodes were not considered for future battery comparisons.

3.3.2 Structure and Morphological Comparison

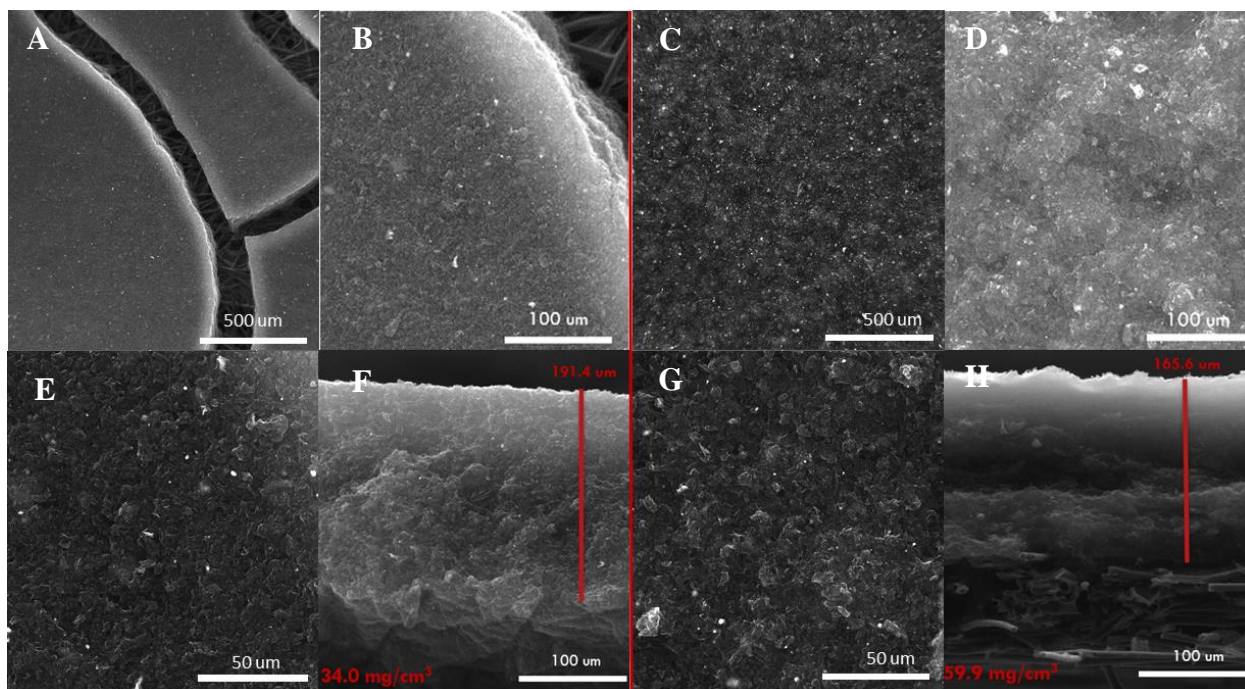


Figure 3.6: SEM Morphology Images. A -D: Dropcast top-view and cross-section. E-H: Electropray top-view and cross-section

While dropcasting has been widely used in previous works, small cracks tend to appear throughout the cathode surface during drying, shown in the Figure 3.6A. Due to the dropwise addition of the solution, boundary layers would form as individual drops on the surface dried, leading to the macrosurface cracking of the rGO layer. Although the cracks physically open up shorter O₂ diffusion pathways (i.e., diffusion through bulk electrolyte in crack area vs. diffusion through restricting pore structures) to internal reaction area, they also give weak points within the solid cathode system where future cracking could occur during the battery cycling and lower capacity by increasing resistance as the most direct electron pathways are blocked off by newly formed cracks.

Air-Controlled Electro spraying was considered due to its industry relevance of high through-put and quick drying times. Since electro spraying creates a thin film of carbon droplets, which dry mostly within the air than on the cathode surface, the cathode can be prepared without macroscopic cracking. Just with visual observation, the cathodes from both dropcasting and electro spraying, and the fabrication methods themselves, reveal many ways that electro spraying improves upon older casting methods. Since electro spraying dries mostly before reaching the collector, it does not have the cracking and loading control issues of dropcasting and can be performed at much faster rates. The microscopic topography and cross-sections of both cathode types were considered by SEM. On the macroscale, the dropcast and electro spray cathodes are quite different. Shown in Figure 3.6A, the cracks that are visible to the naked eye in the dropcast cathode are readily visible under SEM, showing islands of rGO on the carbon paper surface. In comparison, the electro spray cathode in Figure 3e shows a fairly smooth and contiguous surface.

Figure 3.6B&C and Figure 3.6F&G, for the dropcast and electrospray cathodes, respectively, all show closer view of the two cathodes surfaces. Although edge defects can be seen near the cracks of the dropcast cathode in Figure 3.6B, both cathode systems show similar surface roughness, with some topography contrasts due to the semi-spherical shape of the rGO. The cross-sectional images, Figure 3.6D and 3.6H for dropcasting and electrospraying, respectively, also show very good congruity; however, the thicknesses of the samples are drastically different, being near 190 μm thick for the dropcasted sample and 165 μm thick for the ACES sample. This 13% reduction in active area thickness almost doubled the bulk density, as shown in Table 3.1, meaning that the electrospray system has almost double the mass in the same volume space as the dropcast system. This compact structure means that less open space is available on the inside of the cathode for oxygen diffusion, but that an increase in electrical conductivity can be expected due to the lesser number of pores creating blockages for direct electron pathways within the carbon matrix.

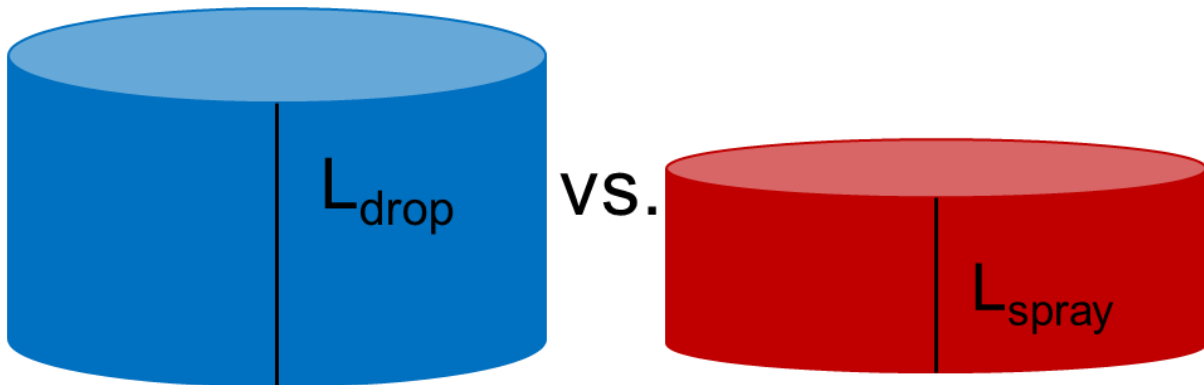
After these separated comparisons of four different cathode fabrication techniques, it is good to summarize them all together in one place. Firstly, spincoating to create thin film coatings has been well used in other film areas, but is difficult to process for Li-Air battery cathodes due to the porous nature of the carbon substrate. Due to this porous nature, direct vacuum cannot be used to attach the carbon paper for the centrifugal rotation, requiring additional apparatus to hold the carbon paper in place, which in turn increases the angular momentum during rotation. This does produce extremely thin films of rGO on the carbon paper with very little required drying time, which could be used for extremely low loading applications, but due to the added mass of the glass base and plastic mask, the entire apparatus could be dislodged due to the angular momentum, creating a glass projectile that was hazardous to both the spincoater and the

researcher. Secondly, slurry coating is a standard cathode creation method for its simplicity, requiring only heat and time to dry a “controllable thickness” carbon film; however, due to its long drying time, the film created fully permeates the porous substrate and is not just left as a controllable film of known thickness on top of the substrate. Furthermore, the drying process takes a long time in air (can be sped up by heating, but large furnaces are a major energy cost in industry), and the cathodes must be punched out to their desired size after the coating is dried, creating edge defects during the punching process and leading to variation in mass loading.

Thirdly, dropcasting is similar to slurry coating and is considered due to its simplicity. Dropcasting dries quicker than slurry coating since it can use more volatile solvents (though heating within ovens can be used to remove water), but this fast drying also allows grain boundaries to form between droplets (instead of creating a uniform coating), leading to cracking and poor connection between the active carbon layer and the carbon substrate. Additionally, since the solution is added dropwise and spread out on the surface, the total coverage area has to be approximated and the mass loading can vary greatly between samples. Lastly, ACES is quick, adaptable, and allows for much more control over mass loading and carbon film morphology. Since drying is done while the droplets are still in the air, the film is rapidly made on the substrate surface without the adsorption of water vapor into the droplets. The consistency between cathodes was much higher than in all previous cases, and the control over the spray conditions allowed for tailoring of the film morphology, which would be useful when considering ACES for other battery electrode applications.

Table 3.1: Table of Comparable Values Between Dropcasting and ACES

Fabrication Method		Dropcast	ACES
Fabrication Time (min)		600	5
Bulk Density (mg/cm ²)		34	59.9
BET Surface Area (m ² /g)		32	42
Porometry Diameter Peak (um)		0.9	0.25
Conductivity (S/m)		29.7	659
EIS Semicircle Diameter (Ω)		325	225
Exchange Current (mA/cm ²)		0.0323	0.0133
Charge Transfer Coefficient (unitless)		0.189	0.537
CV Peak Difference (V)		-	2.3
Max Discharge Capacity (mAh/g)	0.05 mA/cm ²	13731	24000
	0.50 mA/cm ²	7662	16183



$$\phi = \sqrt{t_{diff}/t_{rxn}}$$

$$\phi = \sqrt{L^2 / (t_{rxn} * D_{diff})}$$

$$t_{diff,drop} > t_{diff,Spray}$$

$$\phi_{drop} > \phi_{Spray}$$

$$A_{eff,drop} < A_{eff,Spray}$$

Figure 3.7: Thiele modulus ϕ and effective surface area explanation information

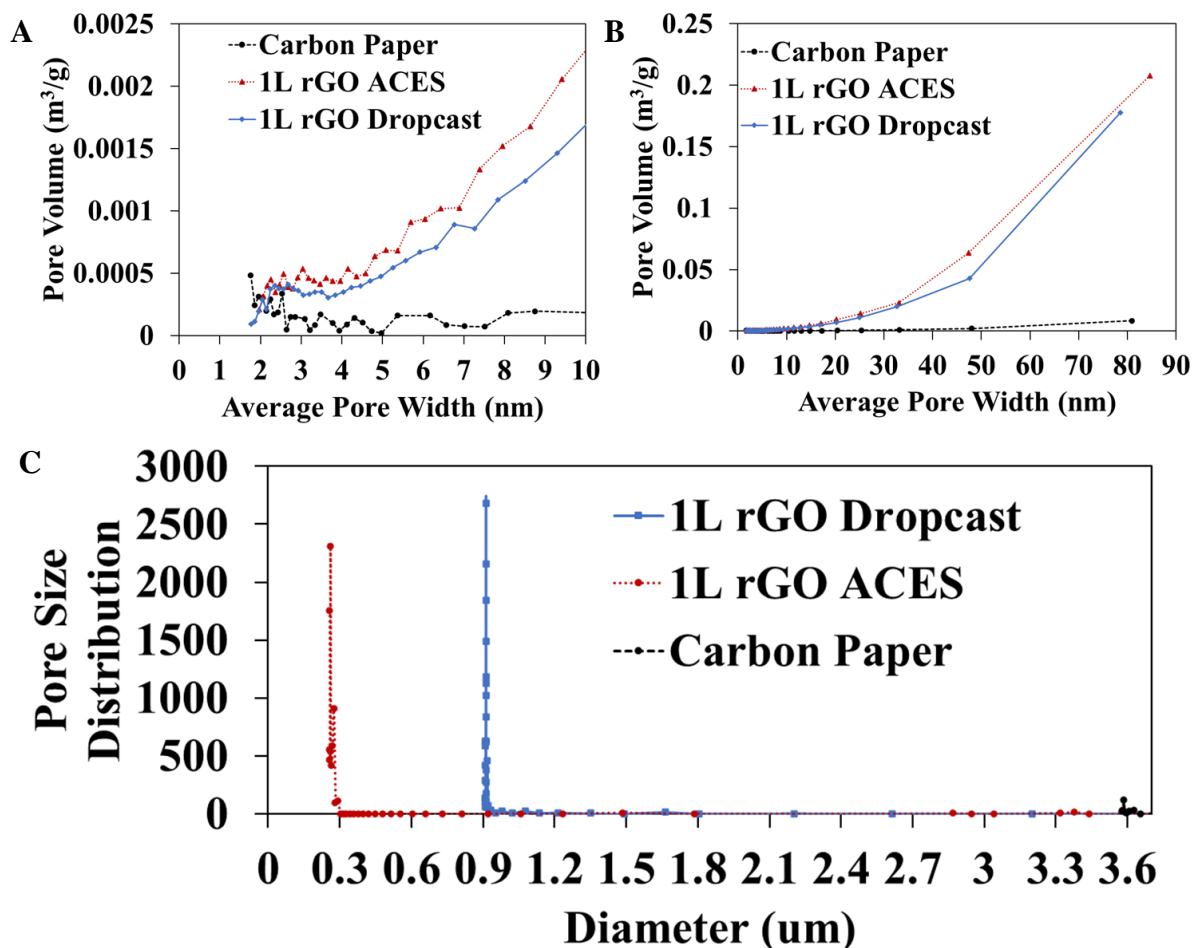


Figure 3.8: Pore Morphology Graphs. A/B: BJH pore volume; C: macropore size distribution of electro spray, dropcast, and carbon paper samples

The difference of the compactness of the samples are most relevant within the analysis of the Thiele Modulus, shown in Figure 3.7, and the pore structure, shown in Figure 3.8. The Thiele Modulus is representative of the actual accessible surface area. Considering that the Li_2O_2 formation reaction occurs on the carbon surface, and that both systems use identical electrolyte, rGO, carbon substrate, binder, and oxygen, the reaction conditions for both systems are very similar. This means that the reaction time for both systems should be near identical; however, although both systems have the same diffusion coefficient for O_2 and Li^+ , the electro spray case is

thinner, meaning that the distance that the O_2 and Li^+ ions must travel to use the full surface area is much less, lowering the diffusion time. Since the bulk density of the electro spray system is double that of the dropcast system, for cathodes of the same area and mass, this length is about half that of the dropcast cathode. By lowering the diffusion time, the Thiele Modulus of the system decreases, and the accessible surface area increases, which in turn should increase the battery capacity. However, the other half of the diffusion time is the effective diffusion, which is determined from the pore information of the two systems. Since both cathode types are made of the same rGO and carbon paper, the average BET surface area due to their micropores is very similar, as shown in Table 3.1; however, the macroporous structure in Figure 3.8 is quite different, as both systems show distinctly narrow peak macropore size distributions, and these different structure considerations will affect the effective diffusion near the cathode surface via the effective diffusion. Porometry revealed that the electro spray cathode has macropores that are one-third the size of the dropcast sample, which makes sense with the compactness of the SEM because less volume is open for microporous void space, and that neither samples have any significant number of macropores of any larger size. Due to this microporous structure, two effects must be considered. First, the smaller macropores mean for more confined space within the cathode, limiting internal diffusion. This is accounted for in the effective diffusion equation, where $D_{eff} = D_b * K_d * F_e$, where D_b is the bulk diffusion (which is equivalent in both systems), K_d is the Knudsen Component, and F_e is the Tortuosity Factor.^[45-47] The Knudsen component considers the diameter of the internal pores, while the Tortuosity Factor considers how straight those channels are. $K_d = d*u/3$, where d is the pore diameter and u is a combination of material properties like mass, all of which are the same in both systems. Looking at the BJH data in Figure 3.8A, both systems share the same mesopore distribution, meaning that the Knudsen

Component for both systems is equal, though the ACES system has greater total surface area due to its increased pore count. However, $F_e = e_t * \sigma / \tau$, where e_t is the porosity (fraction of void space) and is calculated by multiplying the macropore volume by the bulk density, σ is the constrictivity (the spread of pore sizes), and τ is the tortuosity (how crooked the average path a pore takes through the cathode is). Tortuosity is calculated from porometry, and was equal for both systems at 1.399. However, the two other variables show improvements within the spray system. The total pore volume can be found by $V_{pores, total} = \sum_{i=1}^N n_i * \frac{4}{3} \pi * \left(\frac{d_i}{2}\right)^3$, where n_i is the number of pores at diameter d_i and N is the total number of discovered pore diameters. From the Porometry data, the ratio of the ACES pore volume to dropcast pore volume was 3/10, due to the dropcast systems higher pore diameter and pore count. From the SEM images of Figure 3, we see that the bulk density of the spray system is ~2 times that of the dropcast system, meaning that the spray porosity is ~3/5 times that of the dropcast system. The constrictivity is found from Porometry data, and considers the spread between the maximum and minimum pore area and then divides by the average pore area to consider the frequency of each pore size, via the equation $\sigma = (A_{max} * A_{min}) / A_{mean}$. Due to the larger minimum pore size and average pore size, the dropcast system has a 25% smaller constrictivity than the electro spray system, or a ratio of ACES to dropcast of 5/4. This means that the Tortuosity Factor of the electro spray system is 3/4 that of the dropcast system, making the effective diffusion of the electro spray system to be 3/4 of the dropcast system. Plugging this in for the diffusion of the Thiele Modulus, and considering the effective length is about one-half and thus squared to one-fourth, and assuming identical reaction time, we find that the Thiele Modulus of the electro spray system is the square root of one-third, about 14.4% that of the dropcast system. Secondly, the lack of void space for pores should cause a large increase in conductivity, as open pore space blocks direct electron paths within the carbon

matrix. An increase in the conductivity of the carbon cathode should lower system overpotential, as less time is necessary for electrons to get to and from surface reaction sites to the positive battery terminal.

3.3.3 Electrochemical Comparisons

The structural differences of the two cathode systems relate to their electrochemical differences, as well. Shown in Table 3.1, the compact electrospray cathode is a full order magnitude more conductive than the dropcast cathode (659 vs 30 S/m, respectively). This improvement in conductivity may also explain the results of the EIS and Tafel plot data. In Figure 3.9A, the EIS data shows that both samples have similar Warburg Impedance (aka. tail angles) due to their similar lithium-ion diffusion rates in identical electrolyte; however, the diameter of the semi-circle of the electrospray case is about 70% of that for the dropcasted case, suggesting that the charge transfer resistance is much lower in the electrosprayed cathode. The Tafel plot data in Table 3.1 agrees with this assessment. Although the electrospray cathode does have a lower exchange current, the almost 3x increase in the charge transfer coefficient, α , agrees that the electrospray cathode has a lower charge transfer resistance.

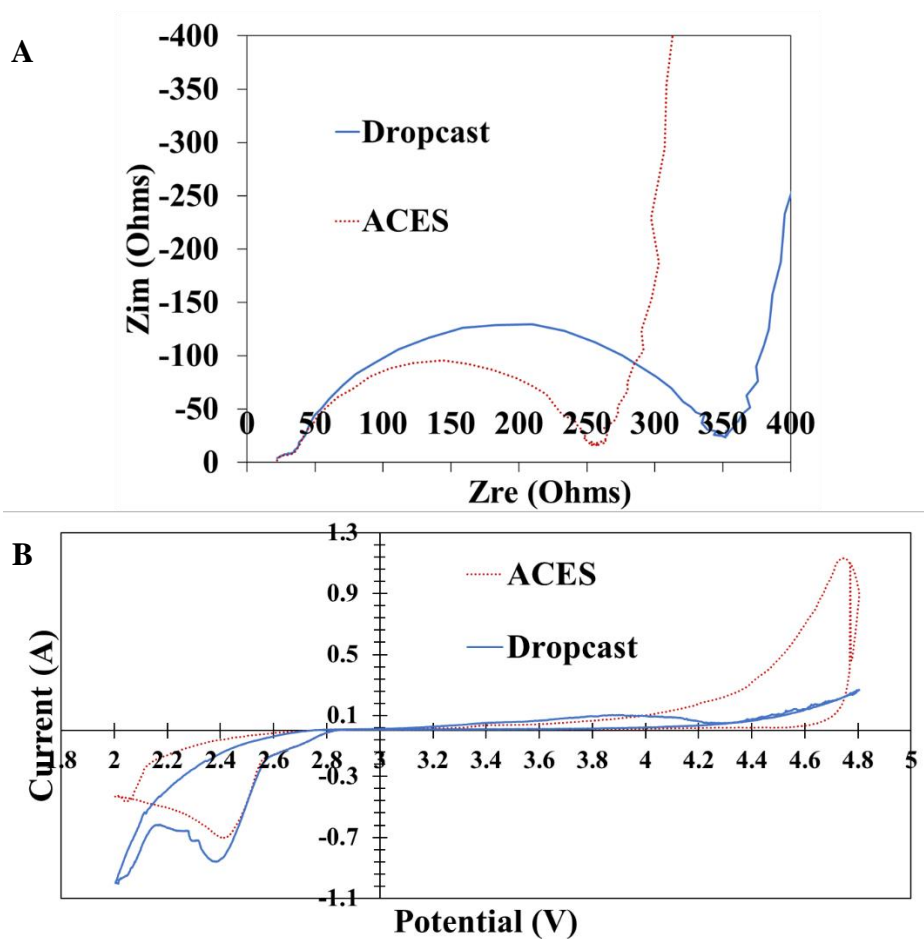


Figure 3.9: Electrochemical Characterizations. A: EIS curves show greatly reduced charge transfer resistance for ACES, while Warburg Impedance shows similar bulk Li^+ ion diffusion rates. B: CV data shows slightly lower discharge overpotential for ACES case and the charge data actually has a peak below 4.8 V.

The CV data for the two systems shows the major difficulties of the Li-Air battery and how the dropcasted cathode does not well handle these difficulties. During the discharge and the Li_2O_2 formation on the left side of Figure 3.9B, the electro spray cathode shows to have only a slight reduction of the overpotential, with a peak at ~ 2.35 V, when compared to the dropcast cathode, with a peak at ~ 2.4 V. However, the dropcast cathode begins to approach reduction of Li_2O_2 to Li_2O as it nears a second peak at the lower cell potential limit of 2.0 V. The electro spray

cathode shows to resist this further oxidation of the Li_2O_2 , which is a good sign of the cathode and Li_2O_2 stability. During the charge at high cell potential, the systems show an even starker difference. The electro spray cathode shows a peak for the breakdown of the Li_2O_2 into Li^+ and O_2 at ~ 4.7 V, while the dropcast cathode shows to be leading up to a peak by the time the terminal cell potential of 4.8 V is reached. Cell potentials above 4.8 V were not explored in this study, as the DME in the electrolyte would become unstable at higher cell potentials and would begin to break down, muddling the reaction peak profile. From the difference in peak cell potentials in the CV data, it can be seen that the electro spray system still has a high overpotential, around 2.35 V; however, the dropcast system has a much higher overpotential and less system stability, which can be seen by the state of the reaction curves near the terminal cell potential values.

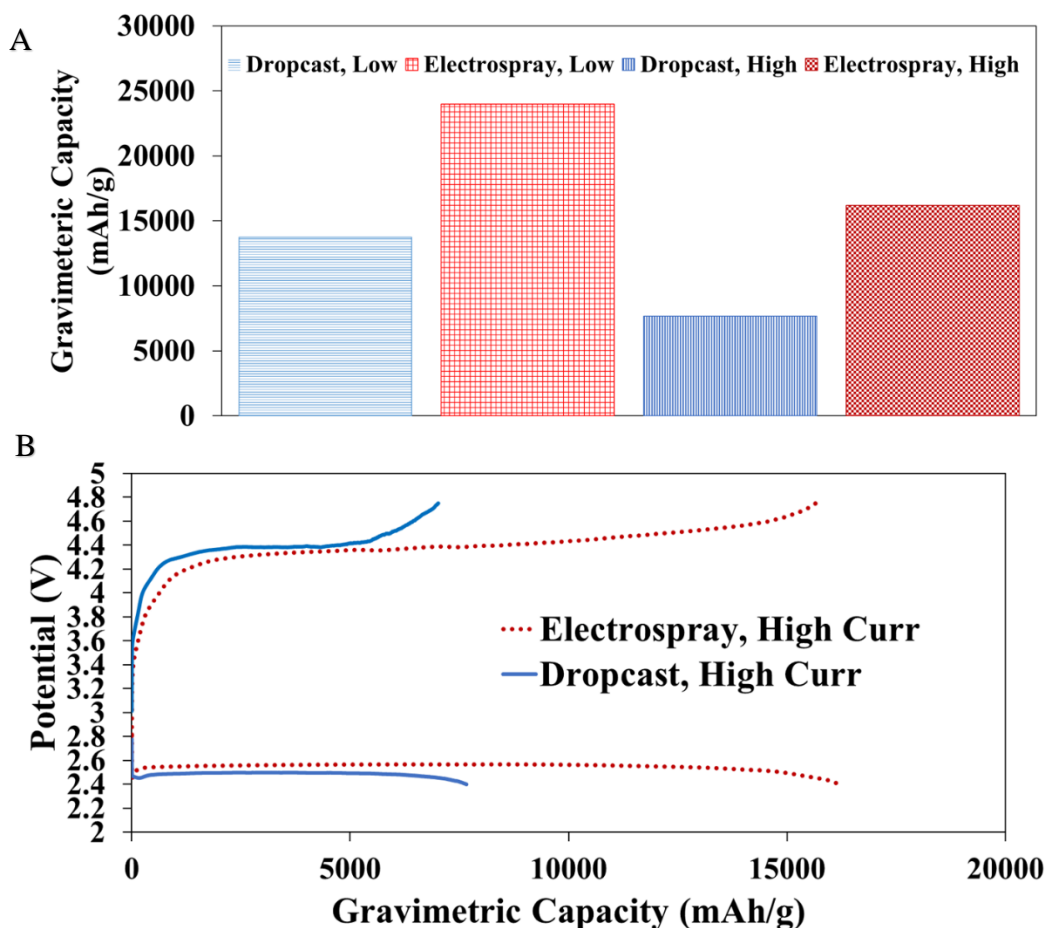


Figure 3.10: Deep Discharge Comparison. A: Gravimetric capacity results. B: Cycling curve comparison for high current tests.

The battery cycling of both systems was performed at two different current densities, 0.05 mA/cm^2 and 0.5 mA/cm^2 , to show both systems at an ideal slower current for stable reaction kinetics and a higher, more industry relevant but structurally and electrochemically taxing current. As shown in Figure 3.10A, the electro spray cathode greatly outperformed the dropcast cathode during deep discharge tests. At the slower current of 0.05 mA/cm^2 , the electro spray system reached a gravimetric capacity of about 24,000 mAh/g, while the dropcast system reached almost 14,000 mAh/g. After increasing the current by an order of magnitude, the differences between the systems become even more apparent. After this large increase in current

density, the electro spray system had 67% capacity retention, and still outperformed the low current case for the dropcast system, while the dropcast system only had 56% capacity retention. The discharge and charge curves of the high current tests, shown in Figure 3.10B, display that the electro spray system maintained a lower overpotential for both the charge and discharge curves, maintaining a lower overall overpotential of around 1.6 V compared to the 1.9 V of the dropcast system.

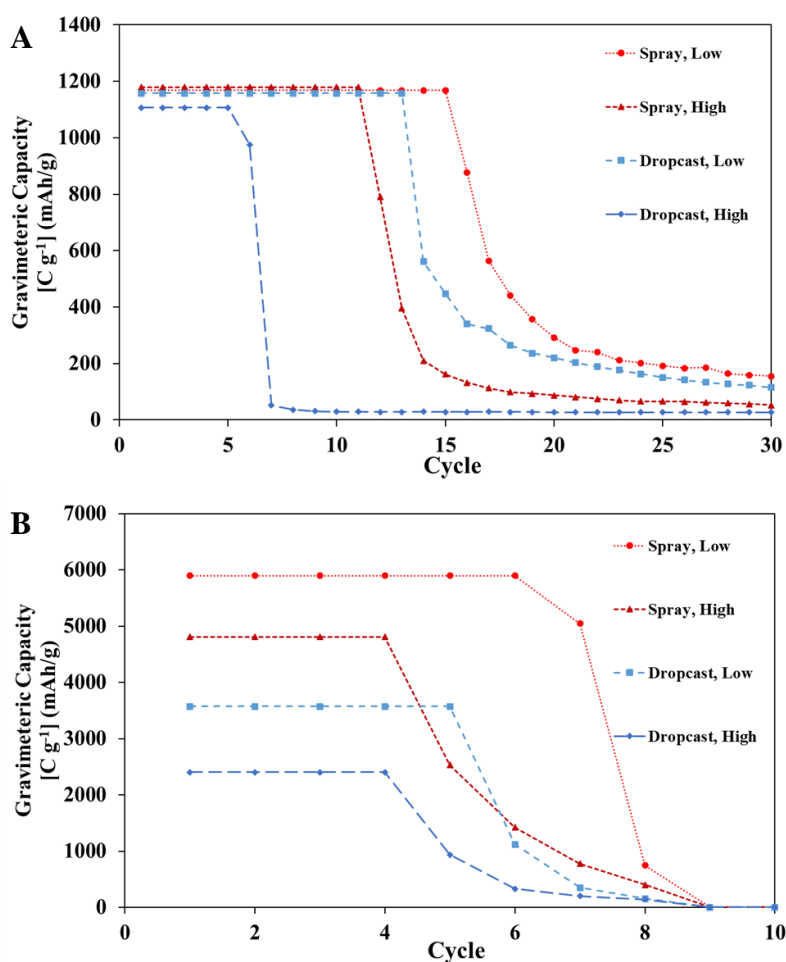


Figure 3.11: Limited Capacity Cycling Comparison. A: 1 mAh limit. B: >24% max capacity limit.

Limited capacity cycling trials were performed both at a capacity limit of 1 mAh, and at increasing capacity limits to reach a single cycle capacity greater than 20% of the deep discharge capacity. The results of these tests can be seen in Figure 3.11, and a breakdown of the comparisons are shown in Table 3.2. In the initial, lower capacity limit tests in Figure 9a, each battery trial floundered. Although the expected trends of decreasing capacity with increasing current density were plainly visible. Hypothesizing that the low-capacity limit was limiting the effectiveness of the charge cycle to remove Li_2O_2 , the capacity limit was raised and kept in proportion to the capacities reached during the single cycle deep discharging trials. Upon raising the capacity limits, all systems showed a greater total capacity reached. In the limited capacity trials, the low current electro spray case reached the highest total capacity, around 1.45x that of its deep discharge capacity, but also behaved most like a primary battery without any 2nd or 3rd discharges. Interestingly, the high current density electro spray case behaved the most like a secondary battery, retaining around 60% of its original deep discharge capacity over its 2nd and 3rd discharges. One consideration for this discrepancy is that the extremely long deep discharge of the at low current required a similarly long charge cycle, which would extend the amount of time that the system voltage was higher and possibly degrading the electrolyte, where the high current density system would be at higher voltages for much smaller amounts of time. Both of the dropcast cases showed very poor 2nd and 3rd discharge capacities, though this low total capacity reached gave them better overall capacity comparisons between their limited capacity cycling total and the deep discharging capacity. Overall, the limited capacity cycling tests showed similar, lower than expected results across all the sample cases, suggesting that the poor limited capacity cycling performance may be due to a battery component (the carbon paper, rGO,

PTFE binder, or electrolyte solvent/salt) being less than ideal for a rechargeable, secondary battery.

Table 3.2: Limited Capacity Breakdown

Cathode Type		Dropcast		AC Electropray	
Current Density (mA/cm²)		0.5	0.05	0.5	0.05
1st Deep Discharge Capacity (mAh/g)		7662	13731	16183	24000
Deep Discharge, 3 Cycle Capacity (mAh/g)		7739	16590	26148	-
1 mAh Limit	Total Limited Capacity (mAh/g)	5531	15047	12974	20834
	Single Cycle %	14	9	7	5
	Capacity Multiplier	0.71	0.91	0.50	0.87
24+% Max Capacity Limit	Capacity Limit (mAh)	2	3	4	5
	Total Limited Capacity (mAh/g)	9617	17856	19232	34724
	Single Cycle %	31	26	30	24
	Capacity Multiplier	1.24	1.08	0.74	1.45

3.4. Conclusion

In this work, the effect of the electrode fabrication process for Li-Air batteries was examined. Using rGO as the active material, electrospaying showed many improvements over traditional casting methods, both decreasing the production and drying times while maintaining greater loading control and increasing structural uniformity and density. Within Li-Air batteries, the electrospayed cathodes displayed superior performance, both increasing maximum capacity

and decreasing system overpotential. These benefits were still present even at 10x the current density, where the electrospray system had greater capacity retention than traditional casting methods.

Electrospraying shows drastic improvements over dropcasting, but this system is not without areas for improvement. This work suffers in its limited capacity cycling data, thus would be improved by the use of electrocatalysts, such as platinum or more cost-effective metal oxides or metal carbides [16-20]. As stated earlier, these catalysts lower the overpotential of the OER, limiting the cells time at high potentials and increasing battery cycle life. Our initial trials of adding Molybdenum Carbide nanoparticles to our electrospray system shows promising results, with the nanoparticle addition lowering the overpotential and discharge capacity, but increasing the cyclability. Through the use of controlled preparation techniques, the search for more promising cathode materials has a stable baseline.

3.5 Future Recycling Considerations

A consideration that is also important to consider is the end goal for Li-Air batteries, which is reliable, high energy density, secondary batteries. As it stands, the Li-Air batteries that have been discussed are mainly primary batteries, as they do not reliably maintain their capacity over multiple cycles. Although true secondary battery Li-Air batteries are still trying to be developed, Kim *et al.* suggested a different way to consider the enhancement of rechargeability for Li-Air batteries. By heating his spent cathodes while adding pressure and then adding new electrolyte, batteries that had started at over 30,000 mAh/g in the first cycle and had gone to 3800 mAh/g by the third cycle were rejuvenated to 21,000 mAh/g for the fourth cycle.^[43] This improvement was much greater than that of refreshing the electrolyte alone, and cross-sectional SEM showed that the benefits were mainly due to the thermal restacking removing void spaces

that had been created during cycling by recompacting the carbon cathode together. This may not be the complete solution for rechargeable lithium air batteries, as it would be costly to continue to take apart the batteries, dispose of the spent electrolyte, heat and compress the cathode, and then add new electrolyte, nor is it completely applicable to all battery cathodes (SEM cross-sections of the dropcast and ACES cathodes from the processes in section 3.3.2 after cycling did not show void spaces formed during cycling), but it is one of the few ways that have been seen to work on the recycling of Li-Air battery materials for future Li-Air batteries. Finding good cathodes and electrolytes for stable battery charging and discharge is very important for the Li-Air battery system to become a true secondary battery; however, being able to recycle spent materials to their original state is a good consideration that could be further explored within the literature.

3.6. Appendices

1. Whittingham, S.M., “Lithium Batteries and Cathode Materials”, *Chem. Rev.*, **104**, 4271-4301, (2004)
2. Tao, H., Feng, Z., Liu, H., Kan, X., Chen, P., “Reality and Future of Rechargeable Lithium Batteries”, *Open Mater. Sci. J.*, **5**, 204-214, (2011)
3. Etacheri, V., Marom, R., Elazari, R., Salitra, G., Aurbach, D., “Challenges in the development of advanced Li-ion batteries: a review”, *Energy Environ. Sci.*, **4**, 3243-3262, (2011)
4. Tarascon, J.M., Armand, M., “Issues and Challenges Facing Rechargeable Lithium Batteries”, *Nature*, **414**, 359-367, (2001)
5. Black, R., Adams, B., Nazar, L.F., Non-Aqueous and Hybrid Li-O₂ Batteries, *Adv. Energy Mater.*, **2**, 801-815, (2012)
6. Shao, Y., Ding, F., Xiao, J., Zhang, J., Xu, W., Park, S., Zhang, J.G., Wang, Y., Liu, J., “Making Li-Air Batteries Rechargeable: Material Challenges”, *Adv. Funct. Mater.*, **23**, 987-1004, (2013)
7. Gallagher, K.G., Goebel, S., Greszler, T., Mathias, M., Oelerich, W., Eroglu, D., Srinivasan, V., “Quantifying the Promise of Lithium-Air Batteries for Electric Vehicles”, *Energy Environ. Sci.*, **7**, 1555-1563, (2014)
8. Ellis, B.L., Lee, K.T., Nazar, L.F., “Positive Electrode Materials for Li-Ion and Li-Batteries”, *Chem. Mater.*, **22**, 691-714, (2010)
9. Beattie, S.D., Manolescu, M., Blair, S.L., “High-Capacity Lithium-Air Cathodes”, *J. Electrochem. Soc.*, **156**, 1, A44-A47, (2009)

10. Kislenco, S.A., “Effect of high donor number solvent and cathode morphology on interfacial processes in Li-air batteries”, *J. Phys.: Conf. Ser.*, **946**, 012029, (2018)
11. Li, Y., Huang, Y., Zhang, Z., Duan, D., Hau, X., Liu, S., “Preparation and structural evolution of well aligned-carbon nanotube arrays onto conductive carbon-black layer/carbon paper substrate with enhanced discharge capacity for Li–air batteries”, *Chem. Eng. J.*, **283**, 911–921, (2016)
12. Kim, H., Lim, H.D., Kim, J., Kang, K., “Graphene for advanced Li/S and Li/air batteries”, *J. Mater., Chem. A*, **2**, 33, (2014)
13. Kuboki, T., Okuyama, T., Ohsaki, T., Takami, N., “Lithium-air batteries using hydrophobic room temperature ionic liquid electrolyte”, *J. Power Sources*, **146**, 766-769, (2005)
14. Abraham, K.M., Jiang, Z., “A Polymer Electrolyte—Based Rechargeable Lithium/Oxygen Battery”, *J. Electrochem. Soc.*, **143**, 1, 1-5, (1996)
15. Mitchell, R.R., Gallant, B.M., Thompson, C.V., Shao-Horn, Y., “All-carbon-nanofiber electrodes for high-energy rechargeable Li-O₂ batteries”, *Energy Environ. Sci.*, **4**, 2952-2958, (2011)
16. Zhang, G.Q., Zheng, J.P., Liang, R., Zhang, C., Wang, B., Hendrickson, M., Plichta, E.J., “Lithium-Air Batteries Using SWNT/CNF Buckypapers as Air Electrodes”, *J. Electrochem. Soc.*, **157**, 8, A953-956, (2010)
17. Harding, J.R., Lu, Y.C., Tsukada, Y., Shao-Horn, Y., “Evidence of Catalyzed Oxidation of Li₂O₂ for Rechargeable Li-Air Battery Applications”, *Phys. Chem. Chem. Phys.*, **14**, 10540-10546, (2012)
18. Zhang, K., Han, X., Hu, Z., Zhang, X., Tao, Z., Chen, J., “Nanostructured Mn-Based Oxides for Electrochemical Energy Storage and Conversion”, *Chem. Soc. Rev.*, **44**, 699-728, (2015)

19. Cho, D., Park, J.H., Jeong, Y., Joo, Y.L., “Synthesis of Titanium Carbide-Carbon Nanofibers via Carbothermal Reduction of Titania with Carbon”, *Ceram. Int.*, **41**, 10974-10979, (2015)
20. Kwak, W.J., Lau, K.C., Shin, C.D., Amine, K., Curtiss, L.A., Sun, Y.K., “A Mo₂C/Carbon Nanotube Composite Cathode for Lithium-Oxygen Batteries with High Energy Efficiency and Long Cycle Life”, *ACS Nano*, **9**, 4, 4129-4137, (2015)
21. Kundu, D., Black, R., Adams, B., Harrison, K., Zavadil, K., Nazar, L.F., “Nanostructured Metal Carbides for Aprotic Li-O₂ Batteries: New Insights into Interfacial Reactions and Cathode Stability”, *J. Phys. Chem. Lett.*, **6**, 2252-2258, (2015)
22. Horstmann, B., Gallant, B., Mitchell, R., Bessler, W.G., Shao-Horn, Y., Bazant, M.Z., “Rate Dependent Morphology of Li₂O₂ Growth in Li-O₂ Batteries”, *J. Phys. Chem. Lett.*, **4**, 4217-4222, (2013)
23. Xia, C., Waletzko, M., Chen, L., Pepler, K., Klar, P., Janek, J., “Evolution of Li₂O₂ Growth and Its Effect on Kinetics of Li-O₂ Batteries”, *ACS Appl. Mater. Interfaces*, **6**, 12083-12092, (2014)
24. Zakharchenko, T.K., Sergeev, A.V., Bashkurov, A.D., Neklyudova, P., Cervellino, A., Itkis, D.M., Yashina, L.V., “Homogeneous nucleation of Li₂O₂ under Li-O₂ battery discharge”, *Nanoscale*, **12**, 4591-4601, (2020)
25. Li, Z., Ganapathy, S., Xu, Y., Heringa, J.R., Zhu, Q., Chen, W., Wagemaker, M., “Understanding the Electrochemical Formation and Decomposition of Li₂O₂ and LiOH with Operando X-ray Diffraction”, *Chem. Mater.*, **29**, 1577-1586, (2017)
26. Adams, B.D., Radtke, C., Black, R., Trudeau, M.L., Zaghbi, K., Nazar, L.F., “Current density dependence of peroxide formation in the Li-O₂ battery and its effect on charge”, *Energy Environ. Sci.*, **6**, 1772-1778, (2013)

27. Ahmad, S., Copic, D., George, C., De Volder, M., “Hierarchical Assemblies of Carbon Nanotubes for Ultra flexible Li-Ion Batteries”, *Adv. Mater.*, **28**, 6705–6710, (2016)
28. Gerber, L. C. H., Frischmann, P. D., Fan, F. Y., Doris, S. E., Qu, X., Scheuermann, A. M., Persson, K., Chiang, Y.M., Helms, B. A., “Three-Dimensional Growth of Li₂S in Lithium–Sulfur Batteries Promoted by a Redox Mediator”, *Nano Lett.*, **16**, 549–554, (2016)
29. Lv, D., Zheng, J., Li, Q., Xie, X., Ferrara, S., Nie, Z., Mehdi, L.B., Browning, N.D., Zhang, J-G., Graff, G.L., Liu, J., Xiao, J., “High Energy Density Lithium-Sulfur Batteries: Challenges of Thick Sulfur Cathodes”, *Adv. Energy Mater.*, **5**, 1402290, (2015)
30. Park, I-S., Li, W., Manthiram, A., “Fabrication of catalyst-coated membrane-electrode assemblies by doctor blade method and their performance in fuel cells”, *J. Power Sources*, **195**, 7078-7082, (2010)
31. Kim, J-K., Manuel, J., Lee, M-H., Scheers, J., Lim, D-H., Johansson, P., Ahn, J-H., Matic, A., Jacobsson, P., “Towards flexible secondary lithium batteries: polypyrrole-LiFePO₄ thin electrodes with polymer electrolytes”, *J. Mater. Chem.*, **22**, 15045, (2012)
32. Becerril, H.A., Mao, J., Liu, Z., Stoltenberg, R.M., Bao, Z., Chen, Y., “Reevaluation of Solution-Processed Reduced Graphene Oxide Films as Transparent Conductors”, *ACS Nano*, **2**, 3, 463-470, (2008)
33. Yan, H., Chen, Z., Zheng, Y., Newman, C., Quinn, J.R., Dötz, F., Kastler, M., Facchetti, A., “A high-mobility electron-transporting polymer for printed transistors”, *Nature*, **457**, 679-686, (2009)
34. Im, J-H., Lee, C-R., Lee, J-W., Park, S-W., Park, N-G., “6.5% efficient perovskite quantum-dot-sensitized solar cell”, *Nanoscale*, **3**, 4088-4093, (2011)

35. Fei, L., Yoo, S. H., Villamayor, R. A. R., Williams, B. P., Gong, S. Y., Park, S., Shin, K., Joo, Y. L., “Graphene Oxide Involved Air-Controlled Electrospray for Uniform, Fast, Instantly Dry, and Binder-Free Electrode Fabrication”, *ACS Appl. Mater. Interfaces*, **9**, 9738–9746, (2017)
36. Divvela, M.J., Zhang, R., Zhmayev, Y., Pinge, S., Lee, J.H., Kim, S.W., Joo, Y.L., “Control and formation of viscoelastic droplets and distribution of nano-inclusions in functional deposition for lithium-sulfur batteries”, *Soft Matter*, **15**, 6485—6494, (2019)
37. Halim, W., Lee, J-H., Park, S-M., Zhang, R., Sarkar, S., O’Neil, T., Chaing, Y-C., Joo, Y.L., “Directly Deposited Binder-Free Sulfur Electrode Enabled by Air-Controlled Electrospray Process”, *ACS Appl. Energy Mater.*, **2**, 678–686, (2019)
38. Lee, J.H., Kang, J., Kim, S-W., Halim, W., Frey, M.W., Joo, Y.L., “Effective Suppression of the Polysulfide Shuttle Effect in Lithium–Sulfur Batteries by Implementing rGO-PEDOT:PSS Coated Separators via Air-Controlled Electrospray”, *ACS Omega*, **3**, 16465–16471, (2018)
39. Shoorideh, G., Ko, B., Berry, A., Divvela, M.J., Kim, Y.S., Li, Z., Patel, B., Chakrapani, S., Joo, Y.L., “Harvesting Interconductivity and Intraconductivity of Graphene Nanoribbons for a Directly Deposited, High-Rate Silicon-Based Anode for Li-Ion Batteries”, *ACS Appl. Energy Mater.*, **1**, 31106–1115, (2018)
40. Shah, A.B., Zhou, X., Brezovec, P., Markiewics, D., Joo, Y.L., “Conductive Membrane Coatings for High-Rate Vanadium Redox Flow Batteries”, *ACS Omega*, **3**, 2, 1856–1863, (2018)

41. Lee, J., Ko, B., Kang, J., Chung, Y., Kim, Y., Halim, W., Lee, J.H., Joo, Y.L., “Facile and Scalable Fabrication of Highly Loaded Sulfur Cathodes and Lithium-Sulfur Pouch Cells via Air-Controlled Electrospray”, *Materials Today Energy*, **6**, 255-263, (2017)
42. Zhang, Y-C., You, Y., Xin, S., Yin, Y-X., Zhang, J., Wang, P., Zheng, Z-S., Cao, F-F., Guo, Y-G., “Rice husk-derived hierarchical silicon/nitrogen-doped carbon/carbon nanotube spheres as low-cost and high-capacity anodes for lithium-ion batteries”, *Nano Energy*, **25**, 120-127, (2016)
43. Kim, J., Carlin, J.M., Smith, S.A., Yin, J., Joo, Y.L., “Thermal Restacking of Graphene Structure to Improve Lithium-air Battery Cyclability”, *Electrochemistry Communications*, **70**, 43–46, (2016)
44. Yin, J., Carlin, J.M., Kim, J., Li, Z., Park, J.H., Patel, B., Chakrapani, S., Lee, S., Joo, Y.L., “Synergy between Metal Oxide Nanofibers and Graphene Nanoribbons for Rechargeable Lithium-Oxygen Battery Cathodes”, *Adv. Energy Mater.*, **5**, 1401412, (2015)
45. Bini, F., Pica, A., Marinozzi, A., Marinozzi, F., “A 3D Model of the Effect of Torouosity and Constrictivity on Diffusion in Mineralized Collagen Fibril”, *Scientific Reports*, **9**, 2658, (2019)
46. Mu, D., Liu, Z-S., Huang, C., Djilali, N., “Determination of the effective diffusion coefficient in porous media including Knudsen effects”, *Microfluid Nanofluid*, **4**, 257-260, (2007)
47. Malek, K., Coppens, M-O., “Knudsen self- and Fickian diffusion in rough nanoporous media”, *J. Chem. Phys.*, **119**, 5, 2801-2811, (2003)

Chapter 4: Numerical Simulations of Lithium Air Batteries

Lithium Air (Li-Air) batteries have received a lot of attention, due to their high gravimetric energy density, near that of the combustion of gasoline, as a possible alternative to the Lithium Ion (Li-Ion) battery for electric vehicles. Although Li-Air batteries have this great advantage over Li-Ion batteries, passivation of reaction sites and lithium peroxide (Li_2O_2) solubility and reactivity limit system capacity, capacity retention, and electrolyte/cathode stability. To aid in the design of future batteries, two different numerical models were considered to understand transport inside the battery and the passivation of the cathode during discharge. The first was a more complex, continuum-level numerical simulation, considering the passivation effects of the nucleation and growth of the insulating Li_2O_2 precipitate on a two-region representation of a carbon cathode. The model was adapted from the work of Dr. George Shebert on Lithium Sulfur (Li-S) batteries. The second was a simplified model of a completely planar cathode, based on the work of Lau *et al.*, where complete coverage of the cathode resulted in cell death. In both simulations, various battery parameters were probed to determine their affect upon battery discharge curves.

4.1 Introduction

Simulations of battery systems are extremely useful for determining productive future avenues to consider for physical batteries. Such simulations are useful because of their comparatively shorter completion times to physical experiments, thus making them essential for preventing research down unproductive avenues. Furthermore, such simulations allow for singular control of battery parameters that are impossible to implement within a physical cell, allowing for deep considerations over all the possible parameter changes that go with swapping out a single battery component. There are many different ways that one can go about devising a

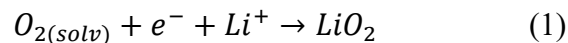
battery model, with many models being based upon models that other groups and individuals have made. Additionally, there are many different areas within the Li-Air system that models in the past have focused on, such as dendrite growth at the anode^[1] or passivation at the cathode.^[1-3]

4.2 Theoretical Model – GLS Based

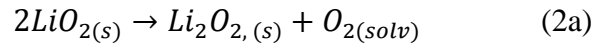
4.2.1 Electrochemical Reactions

The first considered model is adapted from the work of Dr. George Shebert on Li-S batteries.^[4,5] Lithium Air battery models can be very interesting to consider, as multiple reaction pathways exist during battery discharge, depending mainly on the current density, and seen experimentally by Li_2O_2 morphology differences.^[6,7] The oxygen reduction reaction (ORR), displayed in the first chapter of this thesis, can be split up into multiple sub reactions, and it has been shown that only a subset of these is necessary for achieving characteristic discharge behavior.^[8] For this model, we considered a 3 reaction system, with a toggle option for the $\text{Li}_2\text{O}_{2,(aq)}$ formation step to consider the two different reaction pathways:

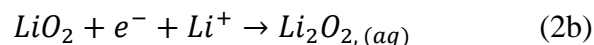
Superoxide Formation



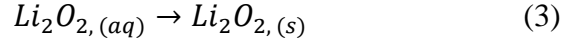
Disproportionation (low current)



Electrodeposition (high current)



Li_2O_2 Precipitation



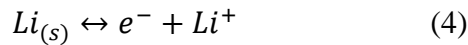
The first and last reactions steps, the superoxide formation step and Li₂O₂ precipitation step respectively, occur regardless of the current density. The second reaction step(s), disproportionation or electrodeposition, are debated by the Li-Air community^[8,9], but the electrodeposition reaction dominates heavily at high current densities. To consider these two reaction pathways, the model was created to be able to swap reactions sets between trials, allowing for data to be taken considering conditions when either pathway is dominate. Due to higher current densities prevailing in my experimental system, the electrodeposition system is considered most often, with some test detailing differences between the two reaction pathways.

Table 4.1: Reaction Parameters m Reaction Index, k_m Reaction Constant, n_m Electron Number, U_{eq0} Equilibrium Voltage, K_{sp} Solubility Constant ^aAssumed Parameters

Reaction	Index m	k_m (mol/(m ² *s))	n_m	$U_{eq0,m}$ (V)	$K_{sp,m}$ (mol/L)
LiO ₂	1	$4*10^{-15}$ [10],a	1	3.0 ^[11]	-
Disproportionation	2a	$5*10^{-17}$ [10],a	0	-	-
Electrodeposition	2b	$8*10^{-17}$ [10],a	1	3.1 ^[11]	-
Precipitation	3	$8*10^{-10}$ [10],a	0	-	$4.2*20^{-20}$ [12]

For this model, the anode system is considered in much simpler terms. At the anode, the production of lithium ions is determined by the applied current I , via the following reaction:

Lithium-Ion Formation



The electrolyte salt is also considered fairly simply, with the negative anion, trifloromethanesulfonate, denoted as A^- , with the charge being balanced by positive lithium ions. As the solid lithium peroxide precipitates into a solid form, its volume fraction, ε_i , will change with time, t , and this change is considered by Equation 1:

Volume Fraction Change

$$\frac{\partial \varepsilon_i}{\partial t} = \frac{M_i}{\rho_i} * \sum_m a_s * v_{i,m} * r_m \quad (1)$$

For all equations, subscript i represents species and m represent reactions. For Equation 1, i refers to $\text{Li}_2\text{O}_{2(s)}$, m refers only to reaction 3, and M_i is the molecular weight of $\text{Li}_2\text{O}_{2(s)}$, ρ_i is the density of $\text{Li}_2\text{O}_{2(s)}$, a_s is the specific surface area, $v_{i,m}$ is the stoichiometric coefficient of $\text{Li}_2\text{O}_{2(s)}$ in reaction 3, and r_m is the reaction rate of reaction 3. For reference, all of the reaction parameter information is available in Table 4.1, while the structural parameters, such as surface area and diffusion coefficients, are provided in Table 4.2. The volume fraction of the electrolyte, ε , is calculated directly from the volume fraction of the carbon, ε_C , and volume fraction of the solid Li_2O_2 precipitate, $\varepsilon_{\text{Li}_2\text{O}_2}$, via Equation 2:

$$\varepsilon = 1 - \varepsilon_C - \varepsilon_{\text{Li}_2\text{O}_2} \quad (2)$$

The reaction rates for reaction 1 and 2b (the electrochemical reactions) are defined by the modified passivation limited Butler-Volmer (BV) equation in Equation 3, as used by Dr. George Shebert^[1], where the equation uses the form modified by Bazant *et al*^[13] with:

Passivation Limited Butler-Volmer

$$r_m = k_m * (a_{re} * a_{prod})^{0.5} * (1 - \theta) * \left(e^{\frac{-1 * \Delta \mu_m}{2 * R * T}} - e^{\frac{\Delta \mu_m}{2 * R * T}} \right) \quad (3)$$

where r_m is the surface area scaled reaction rate, k_m is the reaction constant, a_{re} and a_{prod} are the activities of the reactants and products, respectively, the symmetry coefficient is assumed to be 0.5 and the activity coefficients are assumed to be 1, θ is the surface coverage fraction of $\text{Li}_2\text{O}_{2(s)}$, R is the universal gas constant, T is the temperature, and $\Delta\mu_m$ is the change in chemical potential for reaction m . Reaction 2a (the disproportionation reaction), as it is diffusion limited and not electrochemical in nature, was approximated by a 2nd order rate equation in Equation 4, using a subset of the same variables as Equation 3:

Disproportionation Reaction Rate

$$r_m = k_m * a_{re} \quad (4)$$

The electrochemical reactions used equation 5 and 6 to calculate their chemical potential and equilibrium voltages, while Reaction 3 is the precipitation reaction for Li_2O_2 , which instead considers the solubility of Li_2O_2 for its chemical potential, as seen in equation 7.

Chemical Potential – Electrochemical Reactions

$$\Delta\mu_m = n_m * F * (\varphi_{Cath} - U_{eq,m}) \quad (5)$$

Equilibrium Voltage

$$U_{eq,m} = U_{eq0,m} + R * T * \ln\left(\frac{a_{prod}}{a_{re}}\right) \quad (6)$$

Chemical Potential – Precipitation Reaction

$$\Delta\mu_m = R * T * \ln\left(K_{sp,m} * \frac{a_{prod}}{a_{re}}\right) \quad (7)$$

where n_m is the number of electrons per reaction m , F is the Faraday constant, φ_{Cath} is the voltage of the carbon cathode, $U_{eq,m}$ is the open circuit potential for reaction m , $U_{eq0,m}$ is the open circuit potential at reference conditions, and $K_{sp,m}$ is the solubility product of Li_2O_2 . The parameters used in these reactions are listed in Table 4.1.

Table 4.2: Initial Condition Parameters: $D_{0,I}$ Diffusion Coefficient, M_i Molecular Weight, ρ_i Density, c_0 Initial Concentration, $\varepsilon_{0,i}$ Initial Volume Fraction ^aAssumed Parameters ^bLit. Value ^cExperimental Value

Species i	$D_{0,I}$ (m ² /s)	M_i (kg/mol)	ρ_i (kg/m ³)	$c_{0,I}$ (mol/m ³)	$\varepsilon_{0,i}$ (unitless)
Li ⁺	$7.2 \cdot 10^{-10}$ [14],a	-	-	1000 ^c	0
O _{2(solv)}	$6.9 \cdot 10^{-9}$ [15]	-	-	8.8 ^[1,16]	0.2 ^a
LiO ₂	$9 \cdot 10^{-10}$ [10],a	-	-	$1 \cdot 10^{-5,a}$	0
Li ₂ O _{2(aq)}	$5 \cdot 10^{-12}$, a	-	-	$1 \cdot 10^{-5,a}$	0
Li ₂ O _{2(s)}	-	0.0459 ^b	2310 ^b	$1 \cdot 10^{-5,a}$	$1 \cdot 10^{-5,a}$
A ⁻	$9 \cdot 10^{-10}$ [3,17],a	-	-	1000 ^c	0

4.2.2 Governing Equation and Mass Transport

The change in concentration of each species is both reaction and mass transport dependent, considering the mass flux of each species i over the distance dimension z as $\frac{\partial N_i}{\partial z}$ in Equation 8:

Change in Concentration Equation

$$\frac{\partial}{\partial x}(\varepsilon c_i) = -1 * \frac{\partial N_i}{\partial z} + \sum_m a_s * v_{i,m} * r_m \quad (8)$$

This transport is considered purely diffusive for ease of computation in a discretized model. Due to this assumption, the flux is given as Fick's Law in Equation 8, where $D_{eff,i}$ is the effective diffusion coefficient, and is then adjusted based on porosity by the Bruggeman correlation in Equation 10 for porous cathode media, using the bulk diffusion coefficient, $D_{0,i}$, and the Bruggeman coefficient, β ^[18]:

Fick's Law

$$N_i = -1 * D_{eff,i} * \frac{\partial c_i}{\partial z} \quad (9)$$

Bruggeman Correlation

$$D_{eff,i} = D_{0,i} * \varepsilon^\beta \quad (10)$$

4.2.3. Cell Voltages

Determined externally by the discharge rate, the total current, I , can be found by integrating over the total cell length, l_c , in Equation 11, and can then be used with the concentration of species to find the cathode voltage:

Current Integration

$$I = \int_0^{l_c} (\sum_m -n_m * F * a_s * v_{i,m} * r_m) dz \quad (11)$$

Additionally, the total cell voltage, V_{cell} , can be found using the Equation 12, the difference between the cathode and anode voltages, where the anode voltage, φ_{Anode} , is estimated using Nernst's equation for lithium metal oxidation in Equation 13, and a reference lithium concentration, $c_{Li+,ref}$ ^[19]:

Total Voltage

$$V_{Cell} = \varphi_{Cath} - \varphi_{Anode} \quad (12)$$

Anode Voltage from Nernst's Equation

$$\varphi_{Anode} = \frac{R \cdot T}{F} * \ln \left(\frac{c_{Li^+,anode}}{c_{Li^+,ref}} \right) \quad (13)$$

4.2.4 Cell Structure and Numerical Implementation

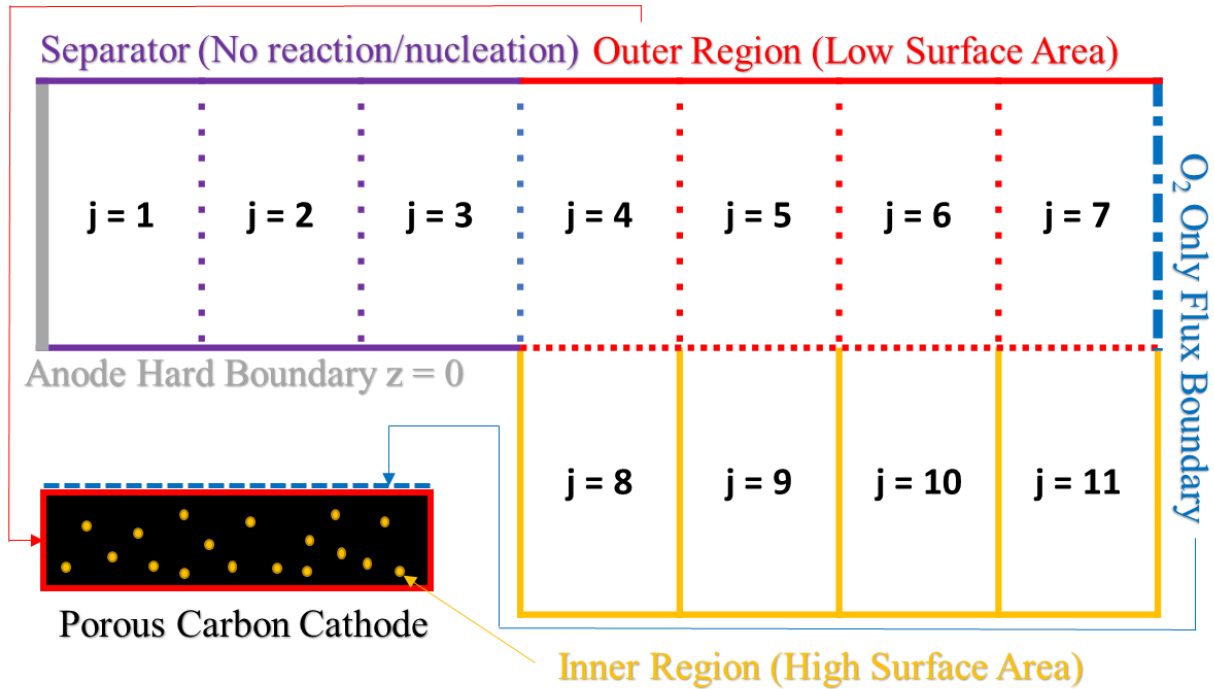


Figure 4.1: Numerical discretization of Li-O₂ battery, with inner and outer cathode areas and external O₂ diffusion

The concept idea behind the cell structure for the model can be seen in Figure 4.1. This model is a one dimensional in time numerical approach, considering only the dimension separating the anode and cathode, since it is between this space that all reactions occur and the system is relatively symmetric in all other directions. The governing equations are discretized using the Finite Difference Method (FDM) into 11 segments, following equation 14:

Finite Difference Method

$$\frac{d^2}{dz^2}(C_i) = c_{i,j} * \frac{c_{i,j+1} - 2*c_{i,j} + c_{i,j-1}}{dz*dz} \quad (14)$$

where j is the discretized box index and dz is the distance between boxes. However, there are exceptions to this where no-flux boundaries exist, such as the anode boundary in box $j=1$, the O_2 permeation boundary in box $j=7$, and the inner cathode pore region in boxes $j=8-11$. For box $j=1$, the no-flux boundary condition applies in the negative z direction, using the FDM variant, Equation 15. A variant of this exists for the inner cathode region, where diffusion can only occur between box $j > 7$ and $j-4$, shown in Equation 16. Equation 17 shows the variant for box $j=7$, where all species, except for O_2 are not able to pass the O_2 flux boundary, where O_2 is able to flow into the system from the bulk outside source, as shown in Equation 18:

No Flux Anode Boundary Finite Difference Method

$$\frac{d^2}{dz^2}(C_i) = c_{i,j} * \frac{c_{i,j+1} - c_{i,j}}{dz*dz} \quad (15)$$

No Flux Inner Cathode Boundary Finite Difference Method

$$\frac{d^2}{dz^2}(C_i) = c_{i,j} * \frac{c_{i,j-4} - c_{i,j}}{dz*dz} \quad (16)$$

No Flux O_2 Boundary Finite Difference Method

$$\frac{d^2}{dz^2}(C_i) = c_{i,j} * \frac{c_{i,j-1} - c_{i,j}}{dz*dz} \quad (17)$$

Flux O_2 Boundary Finite Difference Method

$$\frac{d^2}{dz^2}(C_{O_2}) = c_{O_2,7} * \frac{c_{O_2,Bulk} - c_{O_2,7}}{dz*dz} \quad (18)$$

where $c_{O_2,Bulk}$ is the concentration of O_2 outside the cathode. In most cases, this concentration is treated as the saturation concentration of O_2 within the electrolyte solvent, but also can be adjusted to test the effect of increased oxygen diffusion into the Li-Air battery system.

Mentioned briefly above, this model separates the cathode region into two distinct sections, the outer and inner cathode regions, to represent the porous nature of the carbon cathode system. The exterior system represents the exterior flat plane of the carbon particles, surrounded by the electrolyte, where the interior system represents the nano/mesoporous, tortuous nature of the carbon particles, which have a much higher surface area. For a species to travel to the inner boxes, it must travel from the corresponding outer box (j-4) over a distance l_{i0} . This discretization method is similar to that of Dr. George Shebert^[1,19], modified to include the oxygen diffusion boundary. The system of equations for concentration, porosity, nuclei growth rate, and nucleation rate was solved in MATLAB using the ode15s stiff solver, due to the varying reactions and diffusion timescales. The initial conditions are listed in [Table 4.2](#), while the cell structure parameters are listed in [Table 4.3](#).

Table 4.3: Structural and Miscellaneous Parameters: ^aAssumed Parameters ^bLit. Value
^cExperimental Value

Symbol	Description	Value	Units
N	Number of Boxes	11	-
N _o	Number of Outer Cathode Boxes	4	-
N _i	Number of Inner Cathode Boxes	4	-
l _c	Cell Length	9.1*10 ^{-4,c}	m
l _{io}	Distance Between Inner and Outer Region	1*10 ^{-6,a}	m
ε _c	Carbon Volume Fraction	0.28 ^a	-
a _{s0,meso}	Mesoporous Area (Outer Cathode)	4*10 ^{5,a}	m ² /m ³
a _{s0,micro}	Microporous Area (Inner Cathode)	1.19*10 ^{7,c}	m ² /m ³
R	Gas Constant	8.314 ^b	J/(mol*K)
T	Temperature	298.15 ^b	K
F	Faraday Constant	96485	s*A/mol
β _o	Bruggeman Outer Coefficient	1.5 ^a	-
β _i	Bruggeman Inner Coefficient	5.0 ^{[20],a}	-

4.2.5 Nucleation and Growth of Lithium Peroxide

Many model passivation limited models have existed for battery systems with electrically insulating products^[1-3], with this particular model expanding upon two meant for the Li-S battery system by Andrei *et al.* and Ren *et al.*^[21,22] Although originally meant for Li-S batteries, this model was readily adapted to the Li-Air system due to the many similarities between Li₂O₂ and

lithium sulfide. Li_2O_2 is produced during the discharge step only on the carbon surface and then deposits there due to its low solubility in organic electrolytes. Although it is possible for Li-Air batteries to further reduce Li_2O_2 to lithium oxide (Li_2O), we do not consider that reduction within this model, as the ideal voltage for this reduction, 2.2 V, is below the cut-off voltage of our battery system and its production would be minute. Additionally, Li_2O_2 has extremely low conductivity, and although this thickness can vary based on the crystal structure, the film of Li_2O_2 created at high current densities only needs to be 7 nm thick to be fully insulating to electrons.^[23] Due to this, the electrochemical reactions necessary for Li_2O_2 production may only take place on open reaction sites on the cathode surface until no such place exists upon the cathode, creating total passivation. As this condition near, the system begins to struggle to maintain the potential necessary for the reaction, causing an increase in overpotential and dropping the potential into the cut-off value. Due to this passivation, where the nucleation and growth of each Li_2O_2 particle happens matters because complete passivation of the outer cathode region will lock off access to the inner cathode region. This can fully prevent further reaction within the higher surface area inner region, and modeling this behavior is one of the ways this model takes a more realistic approach to the interaction between nucleation and growth behavior and cathode structure.

The nucleation/growth of the Li_2O_2 nuclei during discharge is considered from a modified version of the oversaturation model by Andrei *et al.*^[21]:

Oversaturation Nucleation Model

$$P = a_s * V * P_0 * \left([C_{\text{Li}^+}^2 * (C_{\text{LiO}_2} - \lambda * R_{\text{LiO}_2 \text{ Prod}}) * K_{sp}]^{N_0} - 1 \right) * \frac{1}{1-\theta} \quad (19)$$

where P is the nucleation rate in nuclei per second, a_s is the specific surface area, V is the volume of the discretized box, P_0 is the initial nucleation rate, λ is a boundary layer parameter, $R_{LiO_2 Prod}$ is the LiO_2 reaction rate, K_{sp} is the solubility product, N_0 is a fitting parameter, and θ is the Li_2O_2 surface coverage. The values of these parameters are listed in Table 4.3. This model has the nucleation rate governed by the oversaturation of the LiO_2 ions near the cathode surface, as these ions will either diffuse back into the bulk, nucleate new Li_2O_2 , or grow an existing Li_2O_2 nuclei. All LiO_2 is produced at the carbon surface, and the oversaturation is dependent upon the difference between the bulk concentration of LiO_2 and the rate at which the LiO_2 is being produced from the available Li^+ and O_2 . This dependency on open reaction sites on the carbon surface is reflected by the $\frac{1}{1-\theta}$ factor, causing the nucleation rate to increase as the system increases in coverage. If LiO_2 is produced slowly due to mass transport outweighing the reaction rate, then the LiO_2 will have time to diffuse onto an existing nucleus, but if LiO_2 is produced quickly, a new nuclei is deposited. As discussed for the Li-Air system, this growth is mainly dependent upon the discharge current density, where high current densities for thin films via electrodeposition, while low current densities produce growing crystalline nuclei via disproportionation.

To limit system complexity, the created nuclei are assumed to be hemispherical. Although Li_2O_2 has been known to form disks, toroids, and films at different current densities^[6,7,9,20,24], an assumption of even radial growth rate allows for good tracking of each nuclei's radius r , which changes via Equation 20, allowing the total surface coverage to be determined by Equation 21, following Kolmogorov's two-dimensional phase transformation to account for hemispherical overlap at the nuclei grow in size:

Radial Growth Rate

$$\frac{dr}{dt} = \frac{V}{2*(1-\theta)*\pi*\sum_{All\ Nuclei} r^2} \quad (20)$$

Surface Coverage Calculation

$$\theta = 1 - e^{-1*\frac{\pi}{a_s}*\sum_{All\ Nuclei} r^2} \quad (21)$$

Each box calculates its own surface coverage separately, and the cell will approach a passivation failure as the surface coverage of any box nears 1. To model the discussed inaccessibility of the inner region reaction sites as the outer region reaction sites increase in coverage, the available inner surface area, $a_{s,in}$, is adjusted from the initial available surface area, $a_{s0,in}$, by both the inner coverage, θ_{in} , and outer coverage, θ_{out} , in Equation 22, meaning that the entire inner particle region will become inactive due to inaccessibility from the outer surface coverage:

Available Inner Surface Area Equation

$$a_{s,in} = a_{s0,in} * (1 - \theta_{in}) * (1 - \theta_{out}) \quad (22)$$

4.3 Results and Discussion – GLS

With its many possible reactions and side reactions, the Li-O₂ battery system has been very difficult to create a complete model for, meaning that each model that is created must have some simplifications and assumptions that are considered during its construction and testing. Additionally, the many different parameters that make up any model are changed and adjusted over time, as optimized systems are discovered and used as baselines. Within the graphs displayed in this results section, a comparison of numerical capacities reached should not be made between different graphs, as small changes in the considered reaction volume of the simulation will affect the final capacity output, which would be fixed once the system is set and defined for comparison to a physical experimental system. Additionally, as with many models,

my simplifications require ignoring side reactions and to use a simplified number of equations; however, the simplification of reaction equations required deeper considerations than just what equations to consider together and apart, which led to an early and persistent error within the model that should be understood at the beginning of this work.

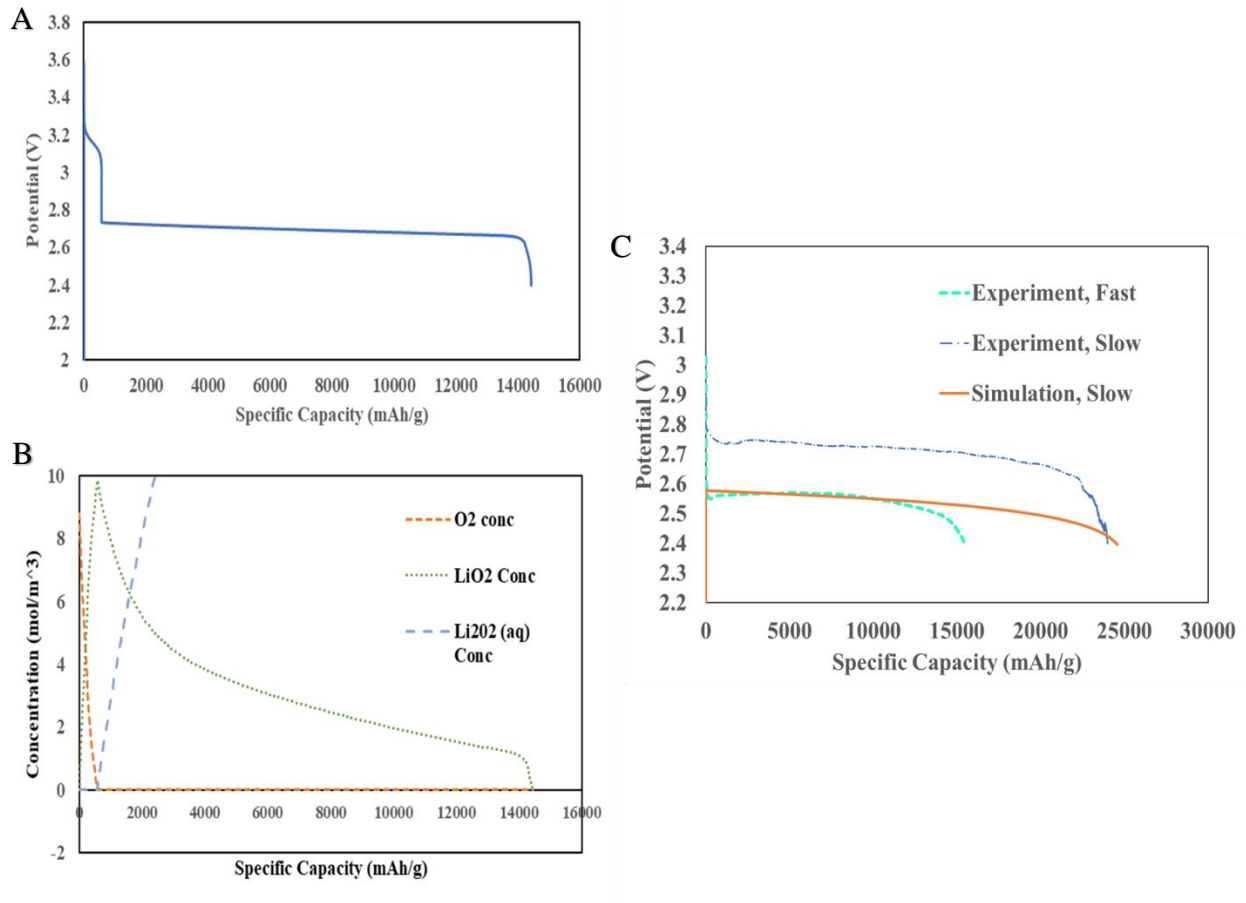


Figure 4.2: Superoxide Formation Reaction Error Consideration: A: Initial test with increased $kf_0(1)$. B: Concentration profile of graph A. C: Comparison graph of discharge curve with lowered $kf_0(1)$

In considering the reaction 1, the superoxide formation reaction, we simplified the model by considering the direct reduction to the superoxide within a single step; however, this can be modeled as two separate steps, the reduction of the solvated oxygen ($O_{2(soln)} + e^- \rightarrow O_{2(soln)}^-$)

and the combination of oxygen and lithium to form lithium superoxide ($O_{2(solv)}^- + Li^+ \rightarrow LiO_2$), where the latter has a reaction rate that is eight orders of magnitude faster than the other. This discrepancy in reaction rate is very large, leading to an interesting phenomenon in the early run times of the battery system, which can be seen the capacity curves in Figure 4.2 for some of the first models of this system and are explained in the concentration profiles during the cycle. The capacity curve shows generally the correct shape for Li-O₂ battery discharge, a slowly sloping plateau of battery capacity followed by a terminal death curve due to a lack of reactants; however, a secondary high plateau of very lower overpotential is seen in this graph, which is caused by the domination of the overly-fast superoxide formation reaction while an excess of the oxygen reactant is present within the system. Once the oxygen reaches a steady state, as the only oxygen available is that which diffuses into the reaction box, the simulation behaves as expected, showing the curvature and battery features that the experimental systems exhibit. For comparison purposes, the final result of how the capacity curves are affected by this first reaction rate is also displayed in this figure, showing that the reduction of the first reaction rate to the order of magnitude of the oxygen reduction step, the exact value of which is listed in Table 4.1, removes this initial plateau, showing that the simulation system can behave similarly to experimental battery system. The removal of this plateau changes where the steady state concentration of oxygen is at, meaning that the system is not limited to the oxygen concentration at the end of each time step being zero, but that the steady state reached by the reaction rate causes the amount of oxygen being consumed by the peroxide formation reaction to equal the same amount of oxygen diffusing into the system.

Due to the error of the first reaction rate, much of the work within this system was done to determine the effects and validity various battery parameters, mainly for the reduction of the

erroneous initial plateau; however, as the simulation proceeds normally after reaching the steady state due to oxygen diffusion, the probing of the parameters still shows good agreement to how the increase or reduction of these parameters should affect the experimental system. The first of these parameters was the surface area of the cathode, which was split into both mesoporous/macroporous surface area, contributed by the macrostructure of the cathode and the large microporous surface area contributed by surface area locked within the pores of the cathode material. As conventional wisdom and Figure 4.3 shows, an increase in the microporous surface area causes an increase in capacity and a decrease of the overall overpotential, with extremely low surface areas leading to a lack of a terminal curve structure. With all of the considerations being equal, this means that increasing the available surface area, through material choices, and/or effective surface area, through structural and fabrication method choices, of the cathode system is one good way for increasing the performance of the Li-O₂ battery system.

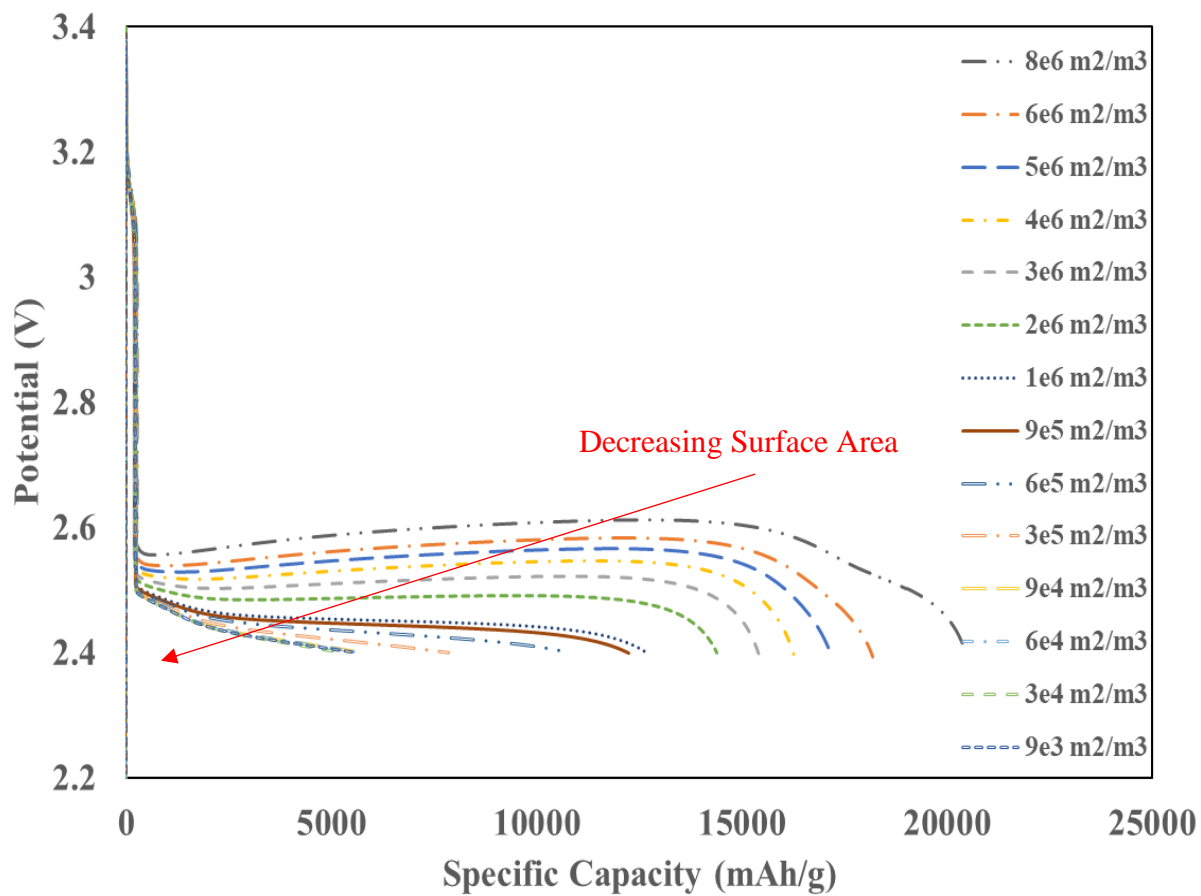


Figure 4.3: Scan of microporous surface area on capacity curves, with decreasing capacity increasing in overpotential and decreasing in capacity

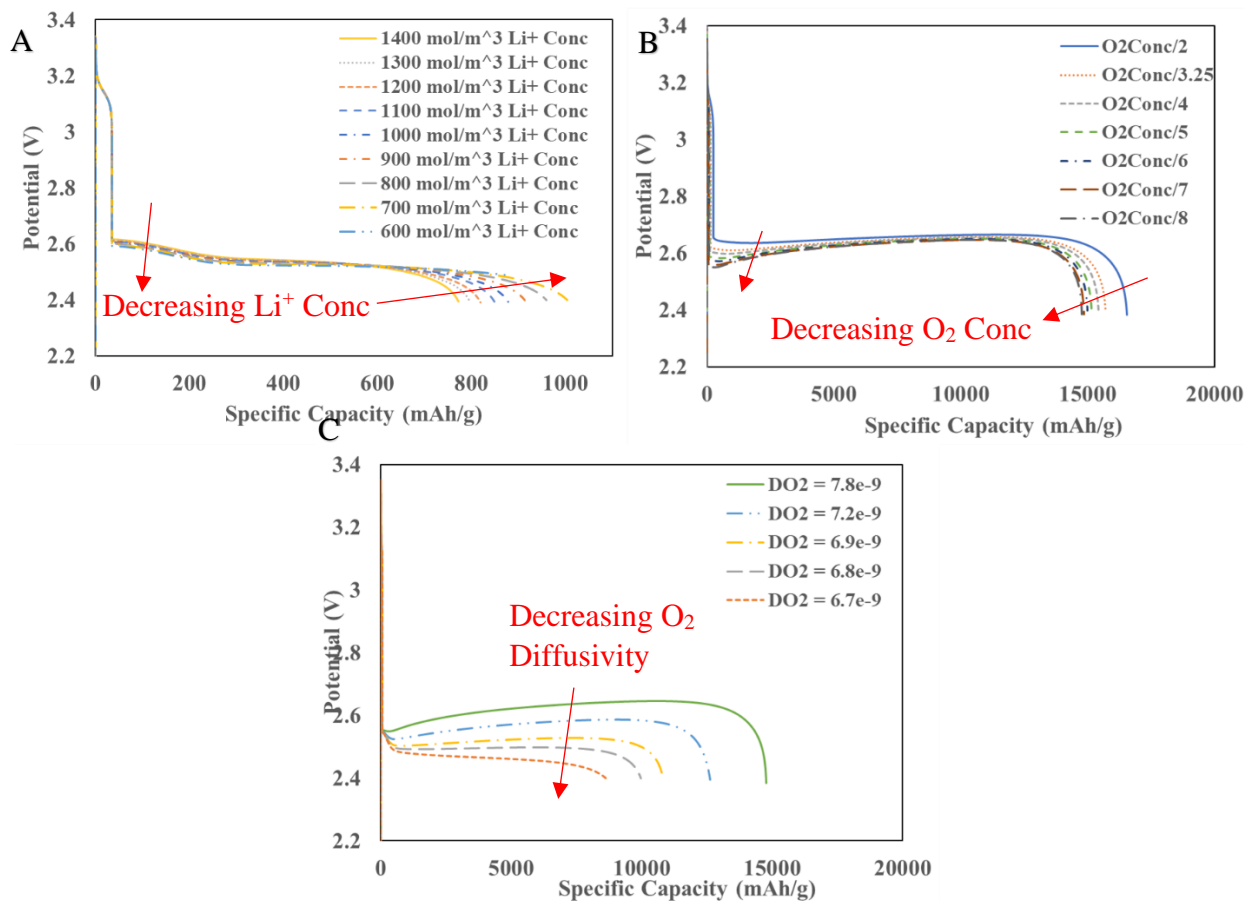


Figure 4.4: Concentration and Diffusion Effects: A: Initial Li^+ concentration sweep B: Initial O_2 concentration sweep C: O_2 diffusivity sweep in mol/s

As oxygen and lithium are the reactants of the first reaction, their diffusion and concentrations are key for controlling the capacity and overpotential of the Li- O_2 system. As the lithium ions are in excess, the ability of oxygen is a must for continued battery function, as it is a reactant of the first reaction and without the superoxide product, no further reactions can take place; however, if that excess is removed causing a lithium ion deficiency by lowering the initial lithium ion concentration within the system, we see in Figure 4.4 a reduction in the capacity and an increase in the overpotential, and the inverse is true for an increase in the initial concentration. In the electrodeposition case, this makes considerable sense, since lithium ions are required in

both the superoxide and peroxide formation steps. However, these effects are fairly minor overall, as more lithium is produced at the anode throughout the test to balance out the initial differences between the systems and maintain a steady concentration of lithium ions. The initial concentration of O_2 and its diffusivity have a much greater effect on the system. All electrolyte solvents have a natural saturation limit of oxygen, with the considered DME system being at 8.79 mol/m^3 . These saturation limits and diffusivities being electrolyte dependent can show how the electrolyte solvent can affect the capacity curves (assuming no parasitic side reaction from electrolyte decomposition are occurring). This initial saturation amount does have a small effect on the capacity and a minor effect on the overall overpotential, but it has a very major effect on the initial overpotential of the flat plateau of the capacity curve. As expected, with the incorrectly high rate of the disproportionation reaction, the lowering of the initial oxygen concentration lowers the width of the false initial plateau, leading to lower LiO_2 production before the O_2 concentration has reached steady state; however, once the oxygen runs out and the electrodeposition and precipitation reactions are allowed to occur, the lowering of the available LiO_2 causes a large initial spike in the overpotential because of the lack of initial $Li_2O_{2(aq)}$ in the system to behave as a limiter of the electrodeposition reactions activity. As the $Li_2O_{2(aq)}$ is produced, the reaction rate lowers, leading to a more stable overpotential and a flatter capacity curve. The changes in this curvature are even more apparent as the O_2 diffusivity, as this is what allows fresh O_2 from outside the battery system to be able to more quickly diffuse into deeper section of the cathode. When the diffusivity is increased in excess, there is bulging of the capacity curve, as the steady state of the system overpotential is lowered and the battery is able to reach much greater capacities and requiring sharper termination curves. As the O_2 diffusivity is lowered, the discharge curve creates a flatter charge profile as the steady state overpotential

also maintains a much higher value due to the lowered O₂ availability. Some experimental battery curves can have this initial curvature issue, where the initial overpotential is quite high, but the cell can still recover and run to a good capacity with a reasonable overpotential, suggesting that some initial oxygen concentration deficiency could have been a factor in the battery.

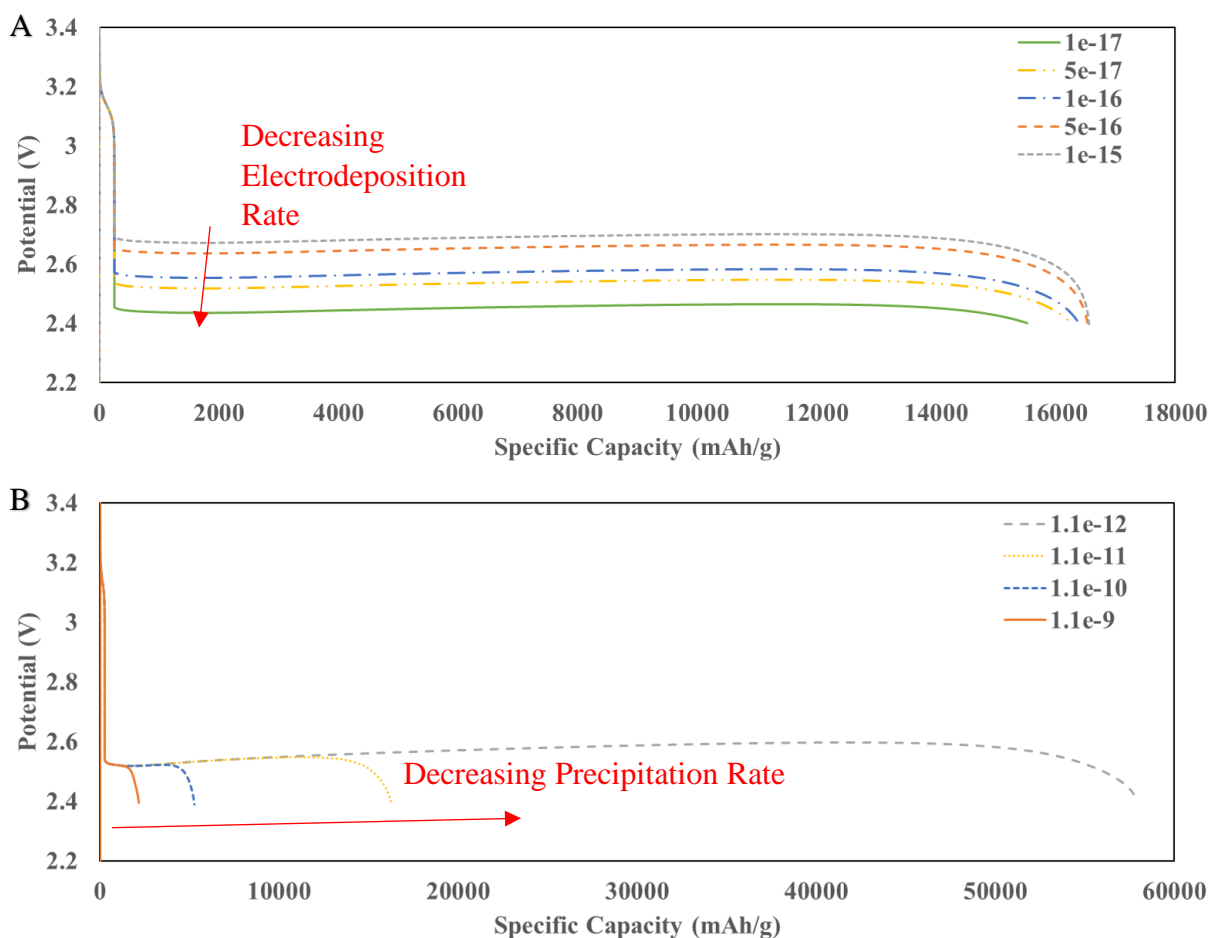


Figure 4.5: Electrodeposition and Precipitation Rate Constant Effects: A. Electrodeposition rate constant sweep. B. Precipitation rate constant sweep

Reaction rates the reaction rates of the model system can be affected directly via their activity, which is dependent upon the available concentrations of the reactants and products, and

the reaction constant, which is both dependent upon the type of reaction occurring and a material property of the available reaction surface. Directly changing the reaction rate constant is similar to changing how well or poorly the cathode surface or present electrocatalysts affect a single reaction step of this multi-reaction system. Not all surfaces are good catalysts for all reactions, so the directly studying the effect of these reaction constants can be good for approximating small differences that are present in similar surface structures and materials. Some consideration for these reaction rates has already been discussed by the error present in the first reaction rate, while electrodeposition and precipitation are studied in Figure 4.5. The rate of the electrodeposition has a pretty strong correlation to the plateau overpotential, with an order of magnitude increase in the reaction rate giving a steady ~ 0.7 V increase in overpotential. The effect on the overall capacity though is quite limited, with increasing reaction rate causing increased steepness of the termination curve. This could be due to the reaction limiting effect of the activity coefficients, because as the reaction coefficient increases, the initial generation of the $\text{Li}_2\text{O}_{2(\text{aq})}$ product increases, which will in turn limit the subsequent time step's reaction rate. This self-limiting behavior would lower the overpotential, as less product concentration is needed for subsequent reactions even though the rate of reaction is higher, but as these products run out, the increased reaction rate breaks through the steady state conditions more quickly, creating a steeper termination curve. With the precipitation reaction, which is already fairly slow, decreasing the reaction constant greatly increases the battery capacity and decreases the overpotential, due to the lower amounts of $\text{Li}_2\text{O}_{2(\text{s})}$ clogging up reaction sites. This nature of the precipitation reaction is dependent both upon the electrolyte solubility of Li_2O_2 and is similar to considerations of disproportionation. As the name "electrodeposition" suggests, Li_2O_2 going through the electrodeposition pathway usually is tightly adsorbed to the cathode surface, being

deposited there by the reaction. However, with good Li^+ solvation, it is possible to high donor number solvents to prevent this immediate deposition, which is further enhanced by good Li_2O_2 solubility, which many organic electrolytes do not have and is why hybrid electrolyte systems, where the electrodeposition reaction occurs within an aqueous electrolyte, have been considered. The results here show that these systems that would hamper the precipitation of the Li_2O_2 as a solid on the cathode surface cause a major decrease in system overpotential and increase in capacity; however, as these systems have other means that may increase resistance in the battery system (such as solid separators, which decrease Li^+ ion diffusion), more complex models would be needed to wholly consider what is probably not considered by this simpler model.

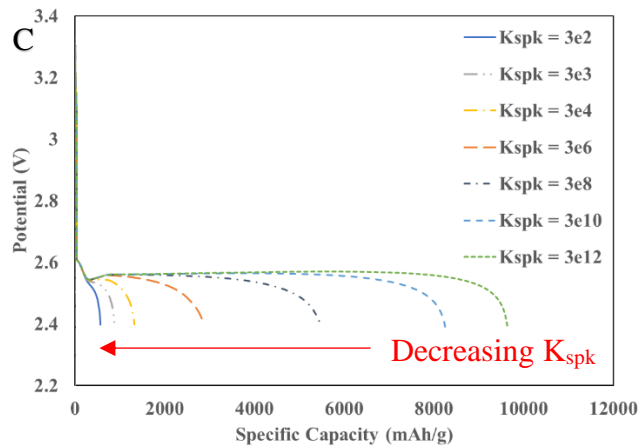
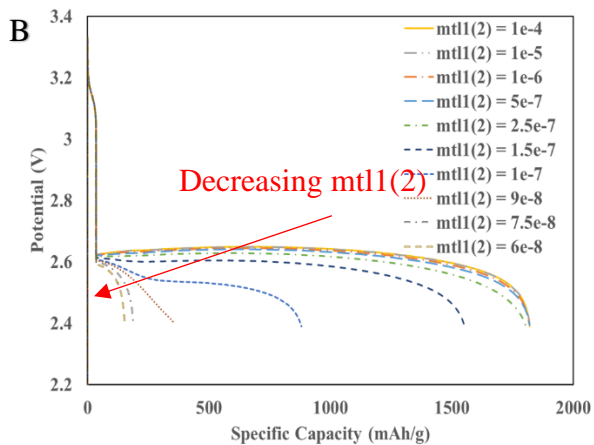
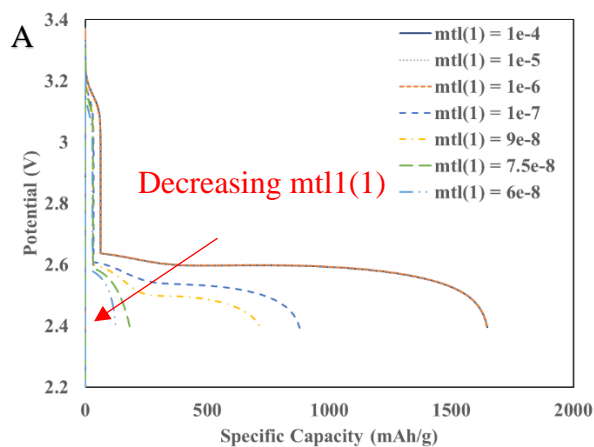


Figure 4.6: Fitting Parameter Effects. A: BV parameter 1 sweep. B: BV parameter 2 sweep. C: Particle growth rate parameter sweep

Although we did not apply this model to other experimental battery systems, it is prudent to discuss the capabilities of the model to do so. The adjustment of this model to other systems can be seen within the fitting parameters, $mtl(1)$ and $mtl(2)$ within the Butler-Volmer anodic and cathodic currents, and the particle growth rate parameter K_{spk} , which are shown in Figure 4.6. K_{spk} is one of the adjustable parameters within the nucleation and growth equations, and works as a good case model for how those parameters can be used to tailor the discharge curve. K_{spk} is the parameter for controlling the areal growth of the particle already present within the system, which can change depending upon the how well Li_2O_2 is able to grow from existing particles or how likely it is for new particles to grow instead of growing existing particles, and is an unknown quantity depending upon the electrolyte solvent's Li_2O_2 solubility (related to the energy barrier of the Li_2O_2 to be able to leave the surface after reacting) and the cathode material. As this parameter acts as a retardant to particle growth, increasing K_{spk} slows the growth of existing particles and slows the rate at which the available reaction sites are being covered up by Li_2O_2 , increasing the capacity able to be reached by the simulation while not affecting the minimum overpotential of the plateau. The first BV parameter, $mtl(1)$ affects the magnitude of the of the anodic and cathodic limiting currents, while the second parameter, $mtl(2)$, determines the magnitude the current reduction effect of deposited Li_2O_2 on the cathode surface, and could be a potential source of future improvement where changes could be made to increase this reduction affect where Li_2O_2 deposits near the terminal thickness of 7 nm. These parameters require more nuance in their control, as they effect all electrochemical reactions, and will have different separate values for different reactions. An example of these is shown for the

superoxide formation reaction. Again, both parameters affect the curvature of the cycling curve due to changes in overpotential, which in turn affects the maximum capacity achieved. As the first parameter affects the magnitude of the limiting current, as it becomes smaller and smaller, there comes to be a point when the amount of reduction is negligible and the system maintains a singular, fairly flat plateau region with a set maximum capacity. However, as the parameter increases, the limiting current starts to greatly increase the overpotential within the Butler-Volmer equation, causing a like-wise reduction in capacity and forming distinct regions where different electrochemical reactions have more dominance, even to the point where the overpotential increases enough to cause early battery termination. The second parameter can be used in an opposite manor, where increasing it flattens out possible regime curves within the cycle curve and increasing the capacity. Through the adjustment of these three parameters, the model is meant to be flexible and could be applied to other battery systems, with differing electrodes and electrolytes.

Lastly, this model was meant to consider multiple reaction pathways, as electrodeposition should be dominant at higher current densities and disproportionation should be dominant at lower current densities. With the electrodeposition pathway, both the first and second reaction rates are dependent upon the current density, meaning that changes in current density cause large increases in reaction rates and overpotentials, so much so that I could not increase the current density to the highest current density that ran in my lab experiments, 0.5 mA/cm^2 at 0.86 mA . Trying to increase the current density above the low current density of 0.05 mA/cm^2 at 0.086 mA caused very large increases in overpotential, showing a major flaw within the model because the electrodeposition model is currently overly dependent on the current density. This over-dependence could be modified by considering the BV fitting parameters, or by considering a

different limiting parameter upon the electrochemical reactions. However, it can also be considered that some reactions will occur via the disproportionation reaction, which removes the dependence of electrons (and therefore the current density) from Li_2O_2 formation, which is what causes eventual cell death as Li_2O_2 deposits on the cathode surface. This in turn also means that less electrons are being created by the system, as now there is only one reaction producing them. Figure 4.7 shows the difference between the electrodeposition and disproportionation pathway at the same current density. As the disproportionation system has less dependence upon the current, we see both an increase in capacity, and very interesting increase in overpotential, as well. This lowered overpotential is explained by the lowered steady state oxygen concentration seen for the disproportionation reaction, which no longer has a second electrochemical reaction and therefore is able to react and form $\text{Li}_2\text{O}_{2(\text{aq})}$ “quicker” than in the electrodeposition case. This is even more apparent because disproportionation also creates O_2 as a reaction product, increasing the amount of O_2 present directly after the reaction step, but possibly lowering the diffusion rate into the system due to the oxygen generation. Using the term “quicker” is a bit of a misnomer, as the disproportionation reaction also produces less electrons, requiring more reactions of the superoxide formation step to generate the same current as the electrodeposition system.

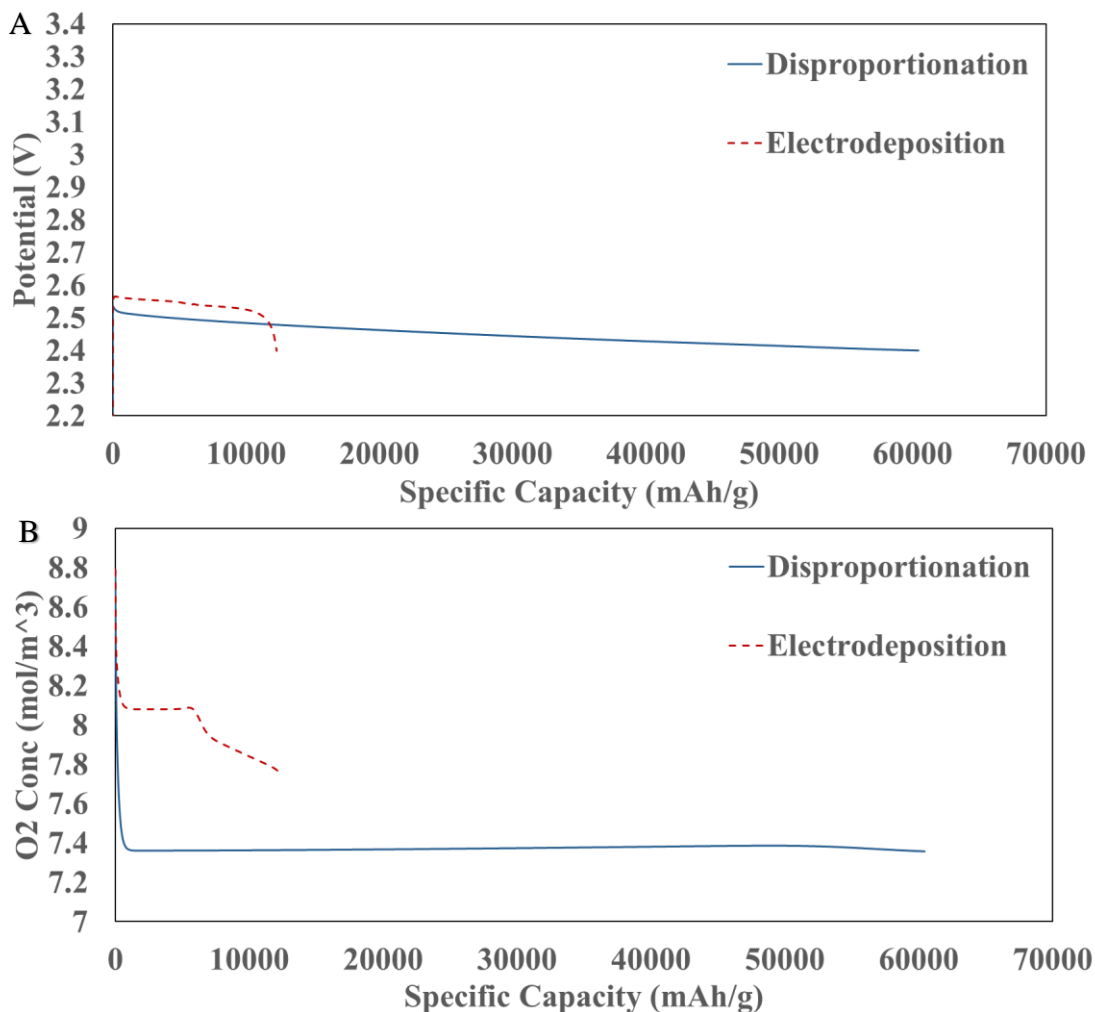


Figure 4.7: Electrodeposition vs. Disproportionation. A: Discharge capacity curves. B: O₂ concentration profile

This becomes even more apparent as we studied the effects of current change on the disproportionation system, which is able to handle more current change due to its lowered dependence on electrons. In Figure 4.8, we see the effects of lowering the current density at 3 different oxygen diffusion rates. In all three systems, lowering the current density lowered the initial overpotential, which would be expected, but the capacity also lowered as current density lowered, with some of the systems even failing quickly after onset, or showing secondary, jumping plateaus. This seems very out of place until the Li₂O_{2(s)} graphs are considered, showing

how $\text{Li}_2\text{O}_{2(s)}$ production is much greater at lower capacities for lower current densities. Since only the first reaction is dependent upon the current density, lowering the current density lowers the production rate of LiO_2 , giving the disproportionation and precipitation reactions plenty of time to react at each recorded step of capacity. Even though the concentrations of reactants are lowered by the lowered reaction rate of the superoxide formation step, the remaining reactions are independent of the current and are not slowed, causing what looks like quicker generation of the final, cathode coating $\text{Li}_2\text{O}_{2(s)}$ species.

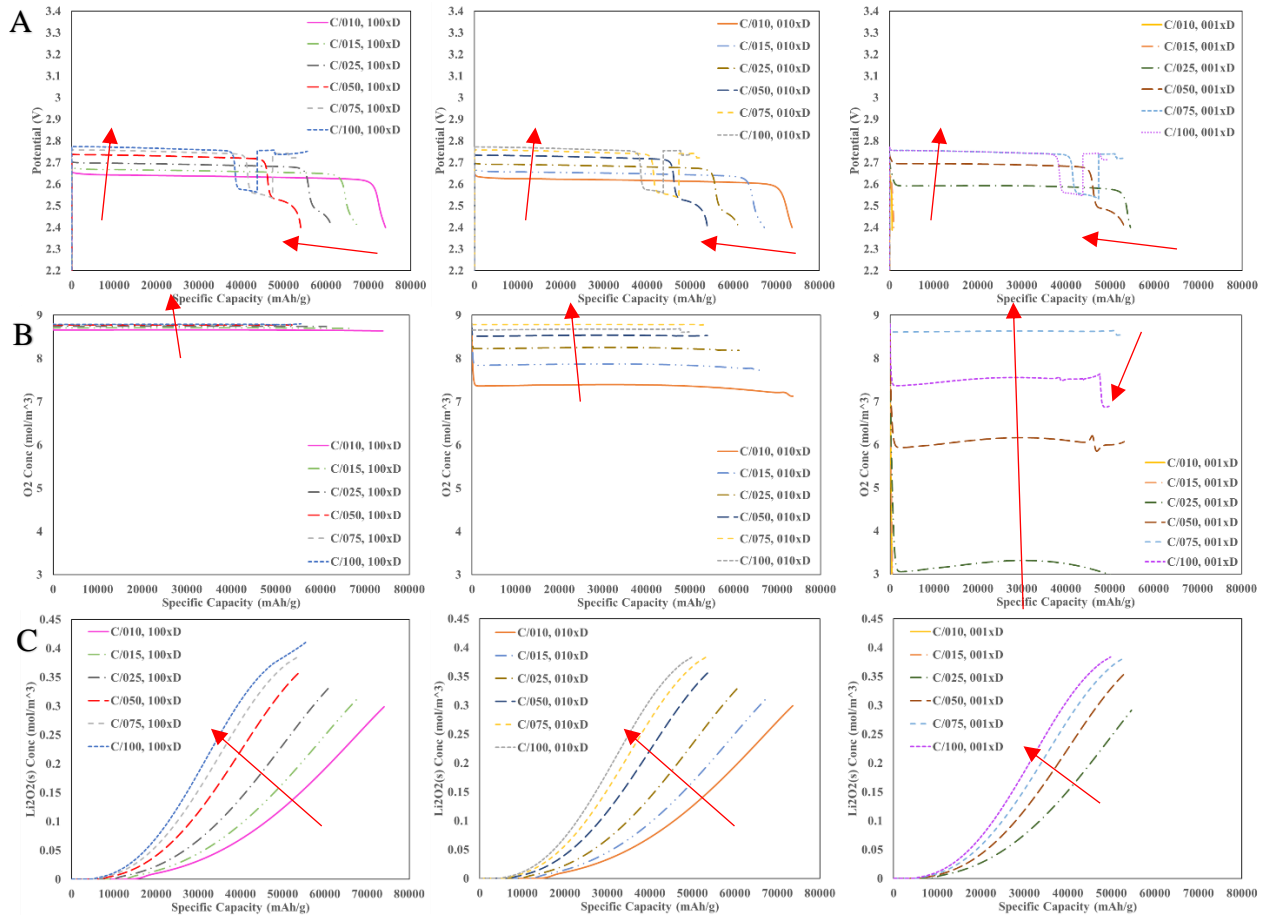


Figure 4.8: Disproportionation Current Density and O_2 Diffusivity Sweeps: Row A: Capacity curves. Row B: O_2 concentration profile. Row C: $\text{Li}_2\text{O}_{2(s)}$ concentration. Columns left to right: High to low O_2 diffusivity. Red arrows show decreasing current density.

4.4 Conclusion and Future Work – GLS

Looking at both the electrodeposition and disproportionation systems, it is understandable how researchers studying the current density effects on Li_2O_2 production in Li-O₂ batteries have suggested different reaction pathways. As the model I created shows, the electrodeposition case is a film forming, highly current density dependent reaction set, as would be expected of a system with many electrochemical reactions, and that the availability of reactants (or the lack thereof) is the main contributor of the discharge capacity and the curvature of the capacity data. However, the current model is too tightly controlled by the current density, as small increases in current cause the model to break down. The disproportionation reaction, which is believed to be the reaction set for low current densities where crystalline toroids and disks are formed, shows an inverse relationship of current density and capacity, actually lowering in capacity as the current density increases. It too is very concentration dependent for its failure, but it is more dependent upon the concentration of the end products and the coating of the cathode surface for its failure mechanism than the on the concentration of reactants and the overpotentials created from their lack. The last hurdle for this model system would be to lessen the strictness of the electrodeposition system on the current density, and to combine the two reaction pathways in parallel, allowing for both the reactant and current dependence of the electrodeposition reaction and the current independent Li_2O_2 generation of the disproportionation reaction to work in tandem to create a more robust model of the Li-O₂ battery system.

4.5 Theoretical Model – Lau Based

Additionally, some consideration was given to a more simplistic model, created by Lau *et al.*^[2] Whereas the Shebert model^[4] attempted to bring many different aspects of the Li-S battery system together into a single model, Lau's model considers the Li-Air cathode area as a single

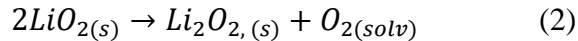
plane, focusing on the effects of current density on the nucleation and growth of Li_2O_2 during discharge. Lau created this model to answer why he saw that increasing the current density do multiple things: lower the discharge capacity, lower the Li_2O_2 particle diameter, and increase the number of Li_2O_2 particles. As expected, as these particles grew, eventually coating the cathode in a non-uniform layer, the system would increase in overpotential and reach a cut-off voltage. For his experimental system, Lau considered a slurry coated carbon cathode of Super P, a porous carbon, and used these as the comparison point for his modeling work.

The reaction system that Lau considered was adapted from a theory from Milchev *et al.*,^[25] considering a two-step formation of Li_2O_2 via the lithium superoxide, LiO_2 , intermediate and disproportionation:

Superoxide Formation



Disproportionation



With these two chemical equations to consider, the model iteratively focuses on 4 main equations, each calculated in turn to create the life cycle of the Li-Air discharge curve. Firstly, the current overpotential of the system is calculated via Equation 1, using a modified Tafel equation:

Modified Tafel Equation

$$\eta = \frac{k*T}{e_0*\alpha} * \ln\left(\frac{i}{i_0} * \frac{1}{1-\theta}\right) \quad (1)$$

where k is Boltzmann's constant, T is the temperature, e_0 is the electron charge, α is the overall charge transfer coefficient on Super P, i is the system current, i_0 is the Tafel Plot reference current, and θ is the surface coverage. As a passivation model, this means that as θ increases, the overpotential will increase, decreasing the batteries potential towards its cut-off value and failure when θ approaches 1.

This overpotential is then considered within the nucleation rate equation in Equation 2:

Nucleation Rate Equation

$$J = J_0 * e^{\left(\frac{2*\alpha'*e_0*\eta_0}{k*T}\right)} * e^{\left(\frac{\alpha*e_0*\eta}{k*T}\right)} * (1 - \theta) \quad (2)$$

where J_0 is the preexponential constant, the background rate of attachment and detachment (an analog of the exchange current density of the Tafel equation), α' is the charge transfer coefficient of the superoxide formation step, and η_0 is the onset overpotential. The first exponential represents the effect of overpotential on the LiO_2 formation step, while the second exponential represents the overpotentials effect on the adsorption rate, where both are scaled by the coverage since the number of available reaction sites decreases as the coverage increases.

The radial growth rate is determined in Equation 3, where F is Faraday's Constant, M is the molecular weight of Li_2O_2 , ρ is the density of Li_2O_2 , and the summation represents the total covered area where r_j is a particular particle radius and n_j is the number of particles with that particular radius:

Radial Growth Equation

$$\frac{dr}{dt} = \frac{1}{1-\theta} * \frac{i}{2*F} * \left(\frac{M}{\rho}\right)_{\text{Li}_2\text{O}_2} * \frac{1}{2*\pi*\sum_j n_j*r_j^2} \quad (3)$$

which just like in Shebert's model, this growth model uses Kolmogorov's phase transformation to consider particles as half-spheres with an extended volume such that the particles cannot overlap. The coverage equation is similarly related, considering Kolmogorov's 2D phase transformation theory, relating the expanded coverage to the total surface area in Equation 4:

Coverage Equation

$$\theta = 1 - e^{-\theta_{ex}} = 1 - e^{\left(\frac{-1*\pi}{A}*\sum_j n_j*r_j^2\right)} \quad (4)$$

where θ_{ex} is the extended coverage and A is the cathode surface area. As the new surface coverage is determined, the overpotential can be redetermined via equation 1 and the cycle begins anew. For consideration, the parameters consider by Lau *et al.* are listed in Table 4.4.

Table 4.4: Lau Parameters from Paper

Parameter	Symbol	Value	Units
Overall Charge Transfer Coefficient	α	0.656	dimensionless
Tafel Plot Current	i_0	$3.7*10^{-3}$	A/m ²
Preexponential Constant	J_0	$2.8*10^7$	nuclei / (m ² *s)
Superoxide Formation Charge Transfer Coefficient	α'	0.549	dimensionless
Initial Nuclei per Area	n_0	2.9	nuclei / μm^2
Current Density	i	10, 20, 40, 50, or 100	$\mu\text{A}/\text{cm}^2$

4.6 Results and Discussion - Lau

Although this system has less complexity than the previous system, it brought up a whole new set of challenges when trying to recreate Lau's results, which the main graphical results are shown in Figure 4.9. Lau's model showed good alignment with his experimental Super P batteries, showing the expected decrease in capacity and increase in overpotential as the current density increased, and showing that the coverage gradually increases, causing battery termination when the cathode was fully covered. The model itself seemed straight-forward, but attempting to recreate Lau's results proved rather difficult, mainly due to information that wasn't present or explicitly stated within Lau's paper or supplementary. However, these areas where information was lacking proved to show insight into the model's use and limitations.

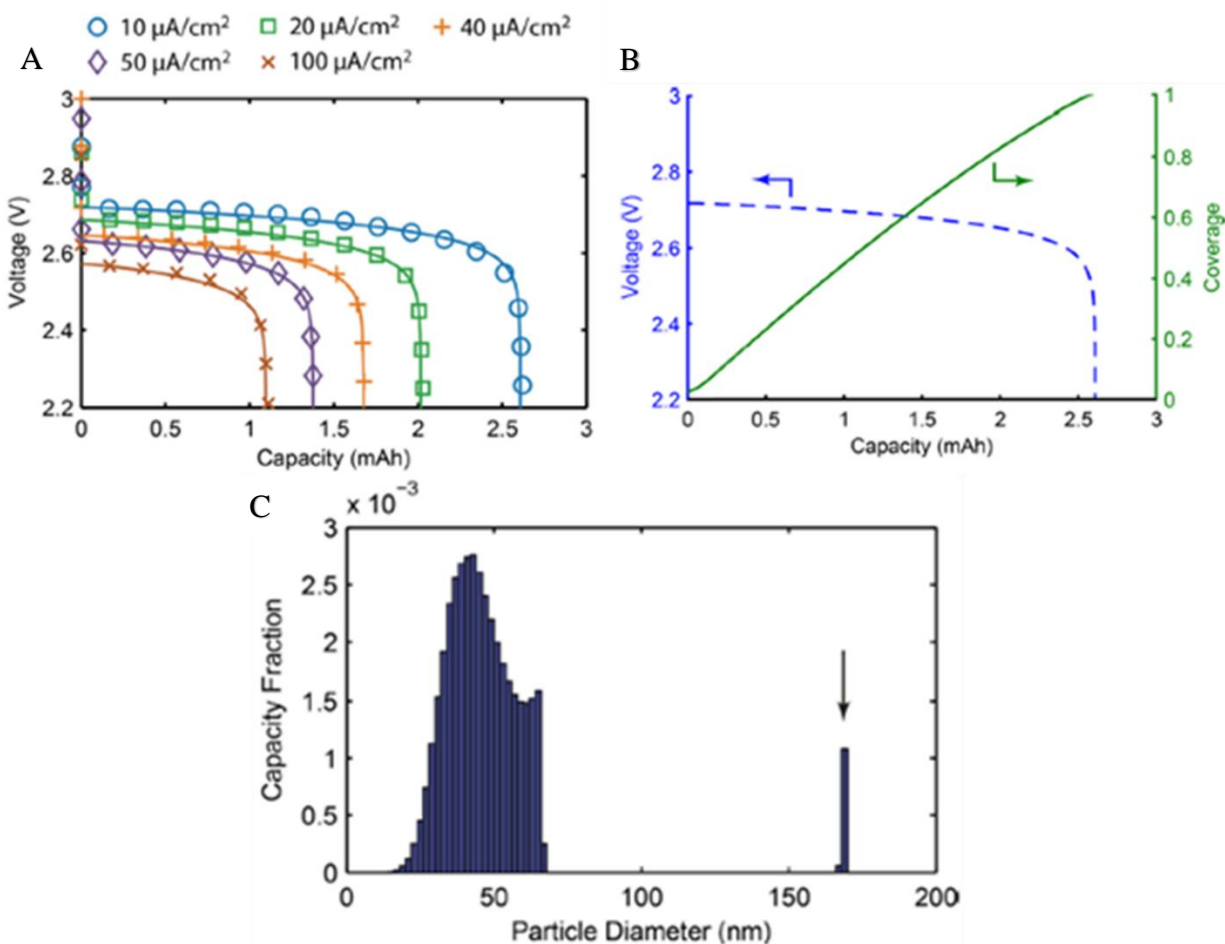


Figure 4.9: Lau *et al.* Results for Comparison. A: Capacity curves. B: Coverage curve. C: Li₂O₂ particle size distribution

While setting up the system, it was clear that some information for the system was not present within the source paper, meaning that exactly replicating the system for verification purposes would be difficult; however, this also meant that these variables would need to be probed within the system or approximated by other sources, with these ranges shown within Table 4.5. One such variable is the surface area, most notably considered in Equation 4 for the coverage. For a best approximation, the surface area of Super P was obtained from a supplier and found to be 62 m²/g (aka. 0.062 m² for Lau's experimental cathodes). This would probably be an overestimate, but without Brunauer–Emmett–Teller (BET) analysis, there is no way to exactly confirm how much surface area has been lost with the addition of the polyvinylidene fluoride (PVDF) binder. Considerations for this surface area were originally looked at in Figure 4.10. Initial testing at 10 uA/cm² showed that the system only reached a meager capacity at this surface area, about 0.2 mAh, and the coverage was significantly higher than what was seen in Lau's tests. Carbon materials exist with much higher surface areas than this, so the surface area was considered at multiple increasing values, and Figure 4.10 shows these results. As expected, with increasing surface area, the initial coverage decreased, which also lowered the initial overpotential (seen by the intersection point of each trial with the y-axis) and increased the system capacity. Due to surface area being a useful tool for allowing comparisons between trial runs, this value could be adjusted to allow for better comparison capabilities within single experimental runs with multiple trials, but also that directly comparing between different test runs, such as comparing the capacity reached during the Surface Area trials and the Timestep trials in Figure 4.10 is not an accurate comparison to make.

Table 4.5: Estimated and Probed Parameter Ranges

Parameter	Symbol	Parameter Value	Tested Range	Units
Surface Area	SA	-	22.32-100.44	m ²
Cathode Area	A	1.98*10 ⁻⁴	-	m ²
Initial Nucleate Radius	r ₀	-	1.28-2521.6	nm
Reaction Time Step	t	-	0.3-1	s
Equilibrium Voltage	V	2.96	2.8-2.96	V

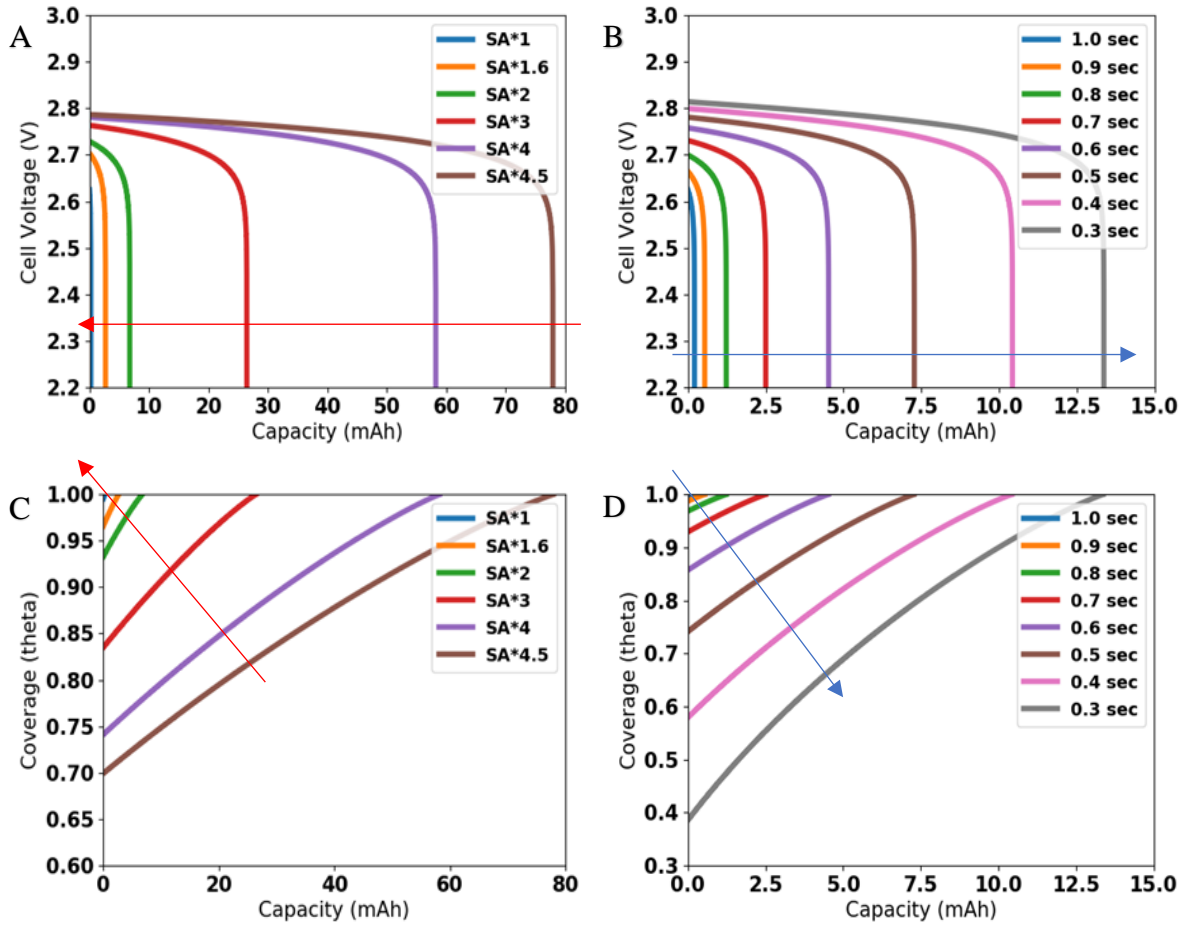


Figure 4.10: Surface Area and Time Step Considerations. A/C: Surface area capacity curves and coverage curves. B/D: Timestep capacity curves and coverage curves. Red arrows show decreasing surface area, while blue arrows show decreasing time step size.

As previously mention, the timestep of the reaction system was also considered in Figure 4.10. As they system was run directly in an iterative process, MATLAB assumes a time step of 1 second natural, even though many reactions are considerably faster than 1 second.

Understandably, the lowering of the time step was very important for increasing system accuracy, as large steps caused the high-rate reaction processes to overestimate their formation and growth rates for a large time step. Since the coverage acts as a limit to both the nucleation and growth rate, these overestimations cause the system to fail prematurely, especially for the case of nucleation, because each nuclei formed is never removed and therefore must grow with each new growth rate, even if later nucleation rates are very low due to the increased coverage. This is readily seen in Figure 4.10, as the initial over potential and coverage decreased dramatically as the time step was decreased; however, decreasing the timestep also increases the trial run time significantly, causing trials that would run for a few seconds to take twelve to eighteen hours to complete. Due to this fact, the time step for all future tests was lowered as much as possible while still allowing tests to be run within a single day to the value of 0.3 seconds. With additional computational resources, this timestep may have been able to be lowered to increase the system accuracy, but this was not available at this time.

As the initial coverage graphs all showed, the initial coverage is an important part of this theoretical model, as systems that create a large initial coverage, either due to very high nucleation and/or growth rates, reach their end curves due to full coverage much quicker than those with low initial coverage values. In Lau's results in Figure 4.9, it can be seen for the 10

$\mu\text{A}/\text{cm}^2$ trial that the coverage starts very low and increases almost linearly to 1, where the battery curves off to the cutoff value. It is not explicitly stated whether the higher current density trials also showed this effect, but two lines of logic can be followed. The first is observationally, as it makes sense that the coverage should start off pretty small, as the opposite would mean that simultaneously across the entire cathode that a large part of the cathode is immediately covered by deposited products (depending on the original surface area size, as was discussed earlier). Conversely, after plugging equation 1 into equation 2, and directly looking at equation 3, the nucleation rate and the growth rate are both directly proportional to the current density, meaning that higher current densities should create larger coverages sooner.

To consider this, I looked at a few different ways that the initial coverage is controlled. Firstly, I looked at increasing the system current density without any adjustments to the initial coverage value, shown in Figure 4.11. In graph A, the initial overpotential response with increasing current density seems proportional to that of Lau's results in Figure 4.9A, except for the outlier of the $100 \mu\text{A}/\text{cm}^2$ test; however, the discharge curve endpoints do not follow a similar trend as Lau's. Where Lau's tests showed almost linear capacity loss with the non-linear increase in current, with the gap between 10 and $20 \mu\text{A}/\text{cm}^2$ being slightly larger than the rest, the current simulation system showed much smaller decreases in capacity from closer current densities (such as 10 and 20 or 40 and $50 \mu\text{A}/\text{cm}^2$), with much larger capacity loss between large jumps in current density (such as between 20 and 40 or 50 and $100 \mu\text{A}/\text{cm}^2$). Additionally, the coverage data in Figure 4.11B shows a pretty large increase in initial overpotential with increasing current density. Although an increase in initial coverage does make sense, due to the increase in the nucleation and growth rates with increasing current density, the actual effect of this data seemed

much too large, as reaching initial coverage values of above 50% seemed unlikely to happen in a physical battery system.

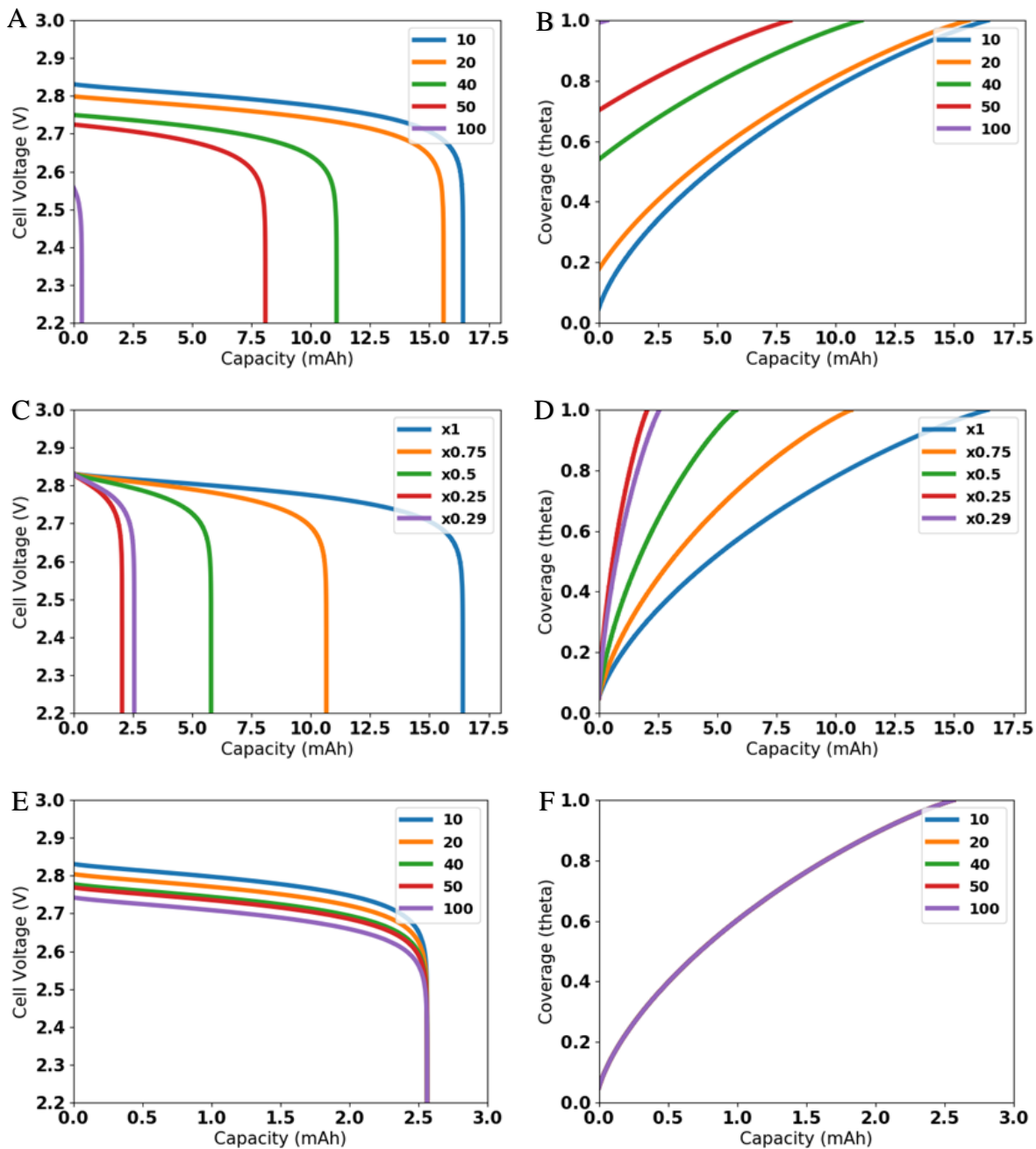


Figure 4.11: Coverage Control Trials: A/B: Current density sweep, showing capacity and coverage curves without any control measures. C/D: Capacity and coverage curves forced at 5%

initial coverage. Lowering surface area to reach ideal 10 uA/cm^2 capacity. E/F: Current density sweep at forced 5% initial coverage and lowered surface area.

Secondly, I looked at what setting the initial coverage to 5% would mean for the battery system. Since the initial coverage for the higher current densities was not shown in any of Lau's results, this runs on the assumption that coverage must always start low and gradually increase to the final value of 1. Figures Figure 4.11C and D show the potential curves and coverage curves, respectively, when the initial coverage is set to 5%, the surface area is lowered to determine when the correct capacity is reached for the 10 uA/cm^2 system. As expected from earlier results, lowering the surface area lowered the capacity, and this lowered capacity was reached because system was more quickly able to cover the smaller surface area. However, when the increase in current density was tried in this fixed initial coverage system, as shown in Figure 4.11E and F, the system unexpectedly showed no decrease in capacity or increase in the coverage rate as the current density was increased. Of the two graphs, only the potential curve graph showed any distinction to the increasing current density, which was to increase the system overpotential proportional to the way that Lau's system increased in overpotential in Figure 4.9, but not to the same magnitude as Lau's system.

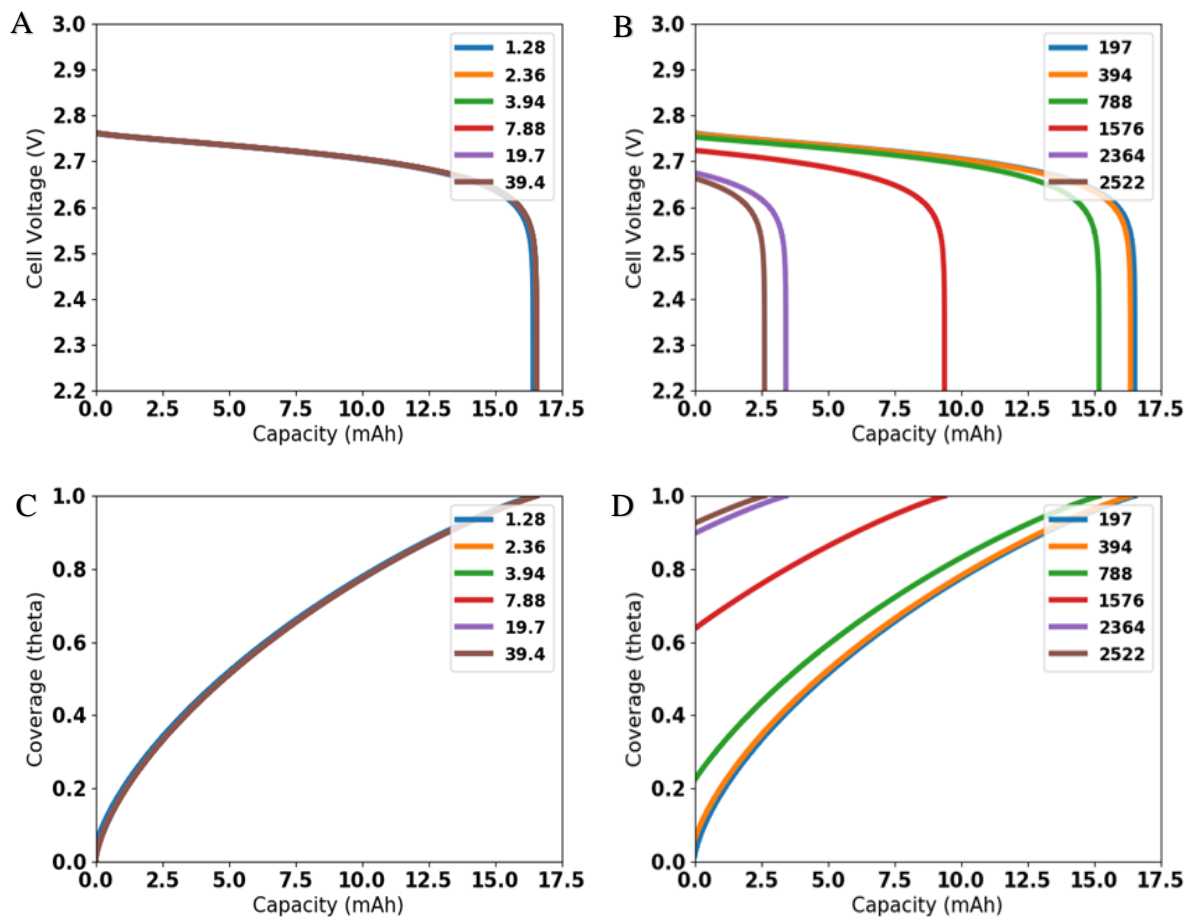


Figure 4.12: Initial Nucleate Size Graphs. A/C: Voltage and coverage curves for 1.28-39.4 nm nucleates (the realistic and close to realistic range). B/D: Voltage and coverage curves for 197-2522 nm nucleates (an unrealistic range, but actually shows initial coverage differences)

These results begged to look at just what was happening in the early time steps of the system, focusing on the nucleation and growth of the Li_2O_2 nuclei. Although Lau had reported the number of initial nucleates that were counted from SEM images, the size of these nucleates was not provided. I assumed that for a single Li_2O_2 particle that the largest possible nucleate size would be the sum of the atomic radii at around 1.28 nm. As this was an assumption, I looked at the effect of increasing the radii of these initial nucleates, and the results of this can be seen in Table 4.6 and Figure 4.12. The table shows that the actual initial coverage is much smaller than

what is easily viewable on the previous coverage vs. capacity graphs, as for low particle sizes, the initial coverage is actually near 0; however, a very small initial coverage causes a massively large initial growth rate, meaning that the 2nd time step had a disproportionately large coverage value due to the millions of initial nuclei present within the system. This explained the earlier results of how increasing current density seemed to cause massive increases in what was thought to be the initial coverage. As the initial nuclei radius is increased, the large difference between the early time steps for coverage became more stable, as the increase in the true initial coverage acted as a retardant upon the growth rate, causing it to stabilize; however, to reach an actually fully stable growth rate, the initial nucleate size had to be increased to values much larger than the termination thickness of the Li₂O₂ film, which is around 7nm. Additionally, the potential and coverage curves show that the actual end capacity of the system really isn't affected by this initial value all that much, until it again is similarly outside of the realm of physical sense. The nucleation rate was independent of this coverage, as plugging Equation 1 into Equation 2 removes coverage from Equation 2. Considering the effects that the high growth rate would have as the current density increased, it was decided that the initial radii value would be maintained at 7.88 nm, near the terminal layer thickness, to maximize growth rate stability while retaining some physical relevance. This value was chosen because the simplicity of this model suggests that the nuclei grow radially outward to cover up the available surface area. Since the already covered area is not available for future reactions, a starting thickness at the terminal layer thickness is an applicable representation of the initially unavailable area, with all further decreases in surface coverage being due to the outward radial growth of these or new particles.

Table 4.6: Initial Nucleate Radius Test Information

Initial Radius (nm)	Coverage (unitless)			Nucleation (nuc/t)		Growth (nm/t)	
	1st Step	2nd Step	3rd Step	1st Step	2nd Step	1st Step	2nd Step
1.28	0	0.04763	0.04763	0.822	0.746	344.503	1.281
2.36	0	0.00436	0.00436	0.822	0.815	101.078	2.364
3.94	0.00001	0.00066	0.00068	0.822	0.821	36.388	3.940
7.88	0.00003	0.00012	0.00015	0.822	0.822	9.097	7.880
19.70	0.00016	0.00018	0.00021	0.822	0.822	1.456	1.262
39.40	0.00063	0.00065	0.00066	0.821	0.821	0.364	0.357
197.00	0.0157	0.0157	0.0157	0.797	0.797	0.01479	0.01479
394.00	0.0614	0.0614	0.0614	0.725	0.725	0.00388	0.00388
788.00	0.22	0.22	0.22	0.495	0.495	0.00117	0.00117
1576.00	0.64	0.64	0.64	0.108	0.108	0.00063	0.00063
2364.00	0.90	0.90	0.90	0.009	0.009	0.00099	0.00099
2521.60	0.93	0.93	0.93	0.005	0.005	0.00119	0.00119

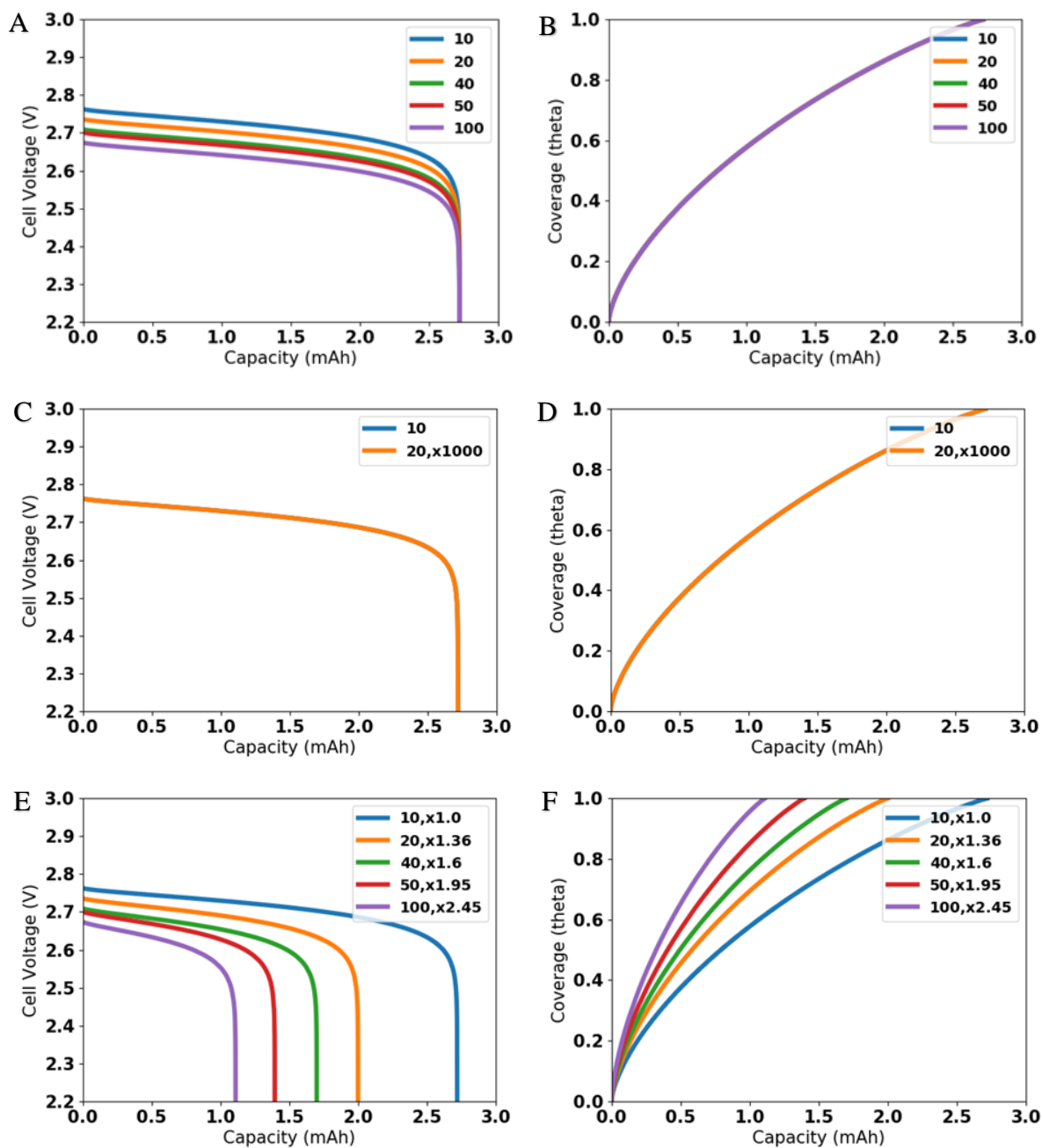


Figure 4.13: Finalized Nucleate Trials. A/B: 7.88 nm nucleate baseline voltage and coverage curves. C/D: Voltage and coverage curves for increased nucleation rate. E/F: Voltage and coverage curves for increased growth rate to match Lau's original graphs

Although this thought process seemed well aligned, the actual increased current density test results at 7.88 nm initial nuclei size were lack luster. Seen in Figure 4.13, the potential and coverage curves show results very similar to those of Figure 4.11, with the system being largely independent of current density. Looking into the nucleation rate again, the system continued to show an indifference to the nucleation rate value, as Figure 4.13 shows that even at a flat 1000x increase, the system remains independent of the nucleation rate. This does make sense, considering Lau's data, who found that a large fraction his capacity comes from the initial nuclei present that grew to a very large size, with only very small particles making up the rest of the capacity and which nucleated and grew only near the end of the simulation, as seen in Figure 4.9C. Attenuation of the growth rate, however, showed to have much more delicate control upon the system than the nucleation rate. Using very small flat increases in growth rate (1.36x to 2.45x), Figure 4.13 shows that an almost identical match to the potential curves seen by Lau's system can be created. The coverage curves for this system show less agreement to Lau's model in Figure 4.9, as they do not have the more linear increase that his data showed. This shows that even in this simpler system, more unknown considerations need to be applied to the model to exactly match the results that Lau achieved.

4.7 Lau Conclusions

Although this project was not finished and expanded to consider the 1L rGO cathode, many results and conclusions can be made about the model and about the considerations that go into making such a model. Early testing results showed that the most precise simulation data requires a continuum modeling approach, where extremely small time steps give the most accurate data; however, lowering the separation of time between data points comes with experimental cost, as stronger computational equipment is required to quickly process the large

number of data points. For this model specifically, the surface area, current density, and growth rate all play a major controlling part. The surface area's effect on the system is easy to conceptually understand and model, as increasing the surface area gives a larger area that needs to be covered and a larger capacity is able to be reached before full coverage is achieved. The effects of the current density and growth rate are much more nuanced. As the equations entail, the direct increase of the current density causes a proportional increase of the nucleation and growth rates, with this increased growth rate effect being most prevalent at early time steps where the system is more readily destabilized as it attempts to reach a stable growth rate. Since the nucleation rate stays fairly low, the growth rate really is the main driving force behind this simulation system, causing the slow steady increase in the coverage as the initial nucleates in the system grow to cover the cathode entirely. Although this project was not fully completed, it was instructive in teaching a focus on small details over small scales for simulation work. Although sweeping changes in results may be seen with small changes in singular variables, the entire system is all interconnected and values and considerations that may have been assumed to have been accurate from previous lines of thought may not be so concrete and are worth exploring.

4.8 Appendices

1. Li, X., Huang, J., Faghri, A., “A critical review of macroscopic modeling studies on Li O₂ and Li-air batteries using organic electrolyte: Challenges and opportunities”, *Journal of Power Sources*, **332** 420-446, (2016)
2. Lau, S., Archer, L.A., “Nucleation and Growth of Lithium Peroxide in the Li-O₂ Battery”, *Nano Lett.*, **15**, 5995–6002, (2015)
3. Sergeev, A.V., Chertovich, A.V., Itkis, D.M., Goodilin, E.A., Khokhlov, A.R., “Effects of cathode and electrolyte properties on lithium-air battery performance: Computational Study”, *Journal of Power Sources*, **279**, 707-712, (2015)
4. Shebert, G., “Modeling the Dynamics of Materials Processing and Electrochemical Systems for Energy Storage and Applications”, Diss. Cornell University, 1-191, 2019.
5. Kumaresan K., Mikhaylik, Y., White, R.E., “A Mathematical Model for a Lithium-Sulfur Cell”, *J. Electrochem. Soc.*, **155**, 8, A576-A582, (2008)
6. Horstmann, B., Gallant, B., Mitchell, R. Bessler, W.G., Shao-Horn, Y., Bazant, M.Z., “Rate-Dependent Morphology of Li₂O₂ Growth in Li-O₂ Batteries”, *J. Phys. Chem. Lett.*, **4**, 4217–4222, (2013)
7. Xia, C., Waletzko, M., Chen, L., Peppler, K., Klar, P.J., Janek, J., “Evolution of Li₂O₂ Growth and Its Effect on Kinetics of Li-O₂ Batteries”, *ACS Appl. Mater. Interfaces*, **6**, 12083–12092, (2014)
8. Peng, Z., Freunberger, S.A., Hardwick, L.J., Chen, Y., Giordani, V., Bardé, F., Novák, P., Graham, D., Tarascon, J-M., Bruce, P.G., “Oxygen Reactions in a Non-Aqueous Li⁺ Electrolyte”, *Angew. Chem. Int. Ed.*, **50**, 6351 –6355, (2011)

9. Adams, B.D., Radtke, C., Black, R., Trudeau, M.L., Zaghbi, K., Nazar, L.F., “Current density dependence of peroxide formation in the Li-O₂ battery and its effect on charge”, *Energy Environ. Sci.*, **6**, 1772–1778, (2013)
10. Grübl, D., Bergner, B., Schröder, D., Janek, J., Bessler, W.G., “Multistep Reaction Mechanism in Nonaqueous Lithium-Oxygen Batteries with Redox Mediator: A Model-Based Study”, *J. Phys. Chem. C*, **120**, 24623-24636, (2016)
11. Laoire, C.O., Mukerjee, S., Abraham, K.M., Plichta, E.J., Hendrickson, M.A., “Elucidating the Mechanism of Oxygen Reduction for Lithium-Air Battery Applications”, *J. Phys. Chem. C*, **113**, 20127-20134, (2009)
12. Cheng, L., Redfern, P., Lau, K.C., Assary, R.S., Narayanan, B., Curtiss, L.A., “Computational Studies of Solubilities of LiO₂ and Li₂O₂ in Aprotic Solvents”, *J. Electrochem. Soc.*, **164**, 11, E3696-E3701, (2017)
13. Bazant, M. Z. “Theory of chemical kinetics and charge transfer based on nonequilibrium thermodynamics”, *Acc. Chem. Res.* **46**, 1144–1160 (2013).
14. Park, C., Kanduč, M., Chudoba, R., Ronneburg, A., Risse, S., Ballauff, M., Dzubiella, J., “Molecular simulations of electrolyte structure and dynamics in lithium-sulfur battery solvents”, *Journal of Power Sources*, **373**, 70-78, (2018)
15. Hartmann, P., Grübl, D., Sommer, H., Janek, J., Bessler, W.G., Adelhelm, P., “Pressure Dynamics in Metal-Oxygen (Metal-Air) Batteries: A Case Study on Sodium Superoxide Cells”, *J. Phys. Chem. C*, **118**, 1461-1471, (2014)
16. Kwabi, D.G., Bryantsev, V.S., Batcho, T.P., Itkis, D.M., Thompson, C.V., Shao-Horn, Y., “Experimental and Computational Analysis of the Solvent-Dependent O₂/Li⁺-O₂⁻

- Redox Couple: Standard Potentials, Coupling Strength, and Implications for Lithium–Oxygen Batteries”, *Angew. Chem. Int. Ed.*, **55**, 3129–3134, (2016)
17. Han, K.S., Chen, J., Cao, R., Rajput, N.N., Murugesan, V., Shi, L., Pan, H., Zhang, J-G., Liu, J., Persson, K.A., Mueller, K.T., “Effects of Anion Mobility on Electrochemical Behaviors of Lithium-Sulfur Batteries”, *Chem. Mater.*, **29**, 9023–9029, (2017)
18. Tjaden, B., Cooper, S. J., Brett, D. J., Kramer, D. & Shearing, P. R. “On the origin and application of the Bruggeman correlation for analysing transport phenomena in electrochemical systems”, *Current Opinion in Chemical Engineering*, **12**, 44–51 (2016).
19. Thangavel, V., Xue, K-H., Mammeri, Y., Quiroga, M., Mastouri, A., Guery, C., Johansson, P., Morcrette, M., Franco, A.A., “A Microstructurally Resolved Model for Li-S Batteries Assessing the Impact of the Cathode Design on the Discharge Performance” *J. Electrochem. Soc.*, **163**, A2817–A2829 (2016).
20. Zakharchenko, T.K., Sergeev, A.V., Bashkirov, A.D., Neklyudova, P., Cervellino, A., Itkis, D.M., Yashina, L.V., “Homogeneous nucleation of Li₂O₂ under Li–O₂ battery discharge”, *Nanoscale*, **12**, 4591–4601, (2020).
21. Andrei, P., Shen, C. & Zheng, J. P., “Theoretical and experimental analysis of precipitation and solubility effects in lithium-sulfur batteries”, *Electrochim. Acta*, **284**, 469–484, (2018).
22. Ren, Y. X., Zhao, T. S., Liu, M., Tan, P. & Zeng, Y. K., “Modeling of lithium-sulfur batteries incorporating the effect of Li₂S precipitation”, *J. Power Sources*, **336**, 115–125 (2016).
23. Viswanathan, V., Thygesen, K.S., Hummelshøj, J.S., Nørskov, J.K., Girishkumar, G., McCloskey, B.D., Luntz, A.C., “Electrical Conductivity in Li₂O₂ and Its Role in

Determining Capacity Limitations in Non-Aqueous Li-O₂ Batteries”, *J. Phys. Chem.*, **135**, 214704, (2011)

24. Li, Z., Ganapathy, S., Xu, Y., Heringa, J.R., Zhu, Q., Chen, W., Wagemaker, M.,
“Understanding the Electrochemical Formation and Decomposition of Li₂O₂ and LiOH
with Operando X-ray Diffraction”, *Chem. Mater.*, **29**, 1577–1586, (2017)
25. Milchev, A.; Stoyanov, S.; Kaishev, R., “Atomistic Theory of Electrolic Nucleation: I”
Thin Solid Films, **22**, 255–265, (1974)

Chapter 5: Continuations and Expansions: Fibrous and Catalytic Cathodes

5.1 Introduction

All of my previously work has focused on results around the electrospray cathode system; however, there are still issues that can be addressed that other cathode systems might be able to solve. Three such issues are the high overpotential of Li-Air batteries, the carbon paper cathode support, and the use of polymer binders within the battery cathode. Binders, usually polymers, in traditional electrodes are used within lithium ion (Li-Ion), lithium sulfur (Li-S), and lithium air (Li-Air) batteries to hold together the battery active material and conductive material, but are not reaction sites themselves and therefore don't contribute to battery capacity.^[1-4] Binders are useful in traditional electrodes for holding together various electrode materials together, but they do have the downside of adding to the battery volume while not actively contribute to capacity, and the film-like nature of these polymers can also coat active material, leading to the loss of pore area. This added volume and loss of surface area has led to many studies on binderless electrode battery systems, many of which use different support materials than traditional methods.^[2,3,5] These support materials are important to the electrode system, as they create structural rigidity in the battery system, but are usually supposed to be fairly inert, such as with porous nickel foam or stainless steel meshes, or create significantly less reactivity than the active material, such as with carbon paper, where the examples included here were for Li-Air batteries.

Many different ways of creating binderless support materials exist, such as buckypapers of carbon nanofibers via filtration method^[6], electrospinning and carbonizing polymer fiber mats^[7,8] or electrospinning of metal, metal oxide, or silica fibers^[9-11], or carbonizing block-copolymers for structural mesoporous carbons^[12]. Similar to Electrospaying mentioned in

earlier chapters, Electrospinning uses a potential difference to draw a solution from a charged needle tip to a grounded collector; however, in Electrospinning, the solution withstands the whipping instabilities that would usually break the solution into droplets during Electro spraying, forming strands of the solute that whip around randomly as the solvent dries from their surface before landing on the grounded collector^[8,10,13-18]. Again, just like with Air-Controlled Electro spraying (ACES), an additional air sheath can be added to the system to allow for increased throughput of the electrospun fiber, making the process Gas-Assisted Electro spinning (GAES). A frequently used method of making carbon cathodes is through the electrospinning of polyacrylonitrile (PAN) fibers, which can be stabilized at low temperature and carbonized at high temperature to create carbon fibers^[8,13,15-19], as seen in Figure 5.1. These fibers are very modifiable, as sacrificial polymers can be added to burn away during later heating for increasing porous structure for surface area^[8,13], reactive atmospheres can be used during heating to pit the fiber surface for similar improvements, coaxial needles can be used to create fibers with specific core-shell morphologies^[16,19] or use outer air sheaths to increase throughput (called Gas-Assisted Electro spinning, or GAES), or carbon or metal additives can be included in the spinning solution for addition of these elements to the fiber surface or the fibers can be soaked in a solution to add such materials only to the fiber surface^[7,13,15-19]. This customizability of electrospun PAN for battery electrodes makes it an ideal candidate for combating some of the many issues within the Li-Air battery system.

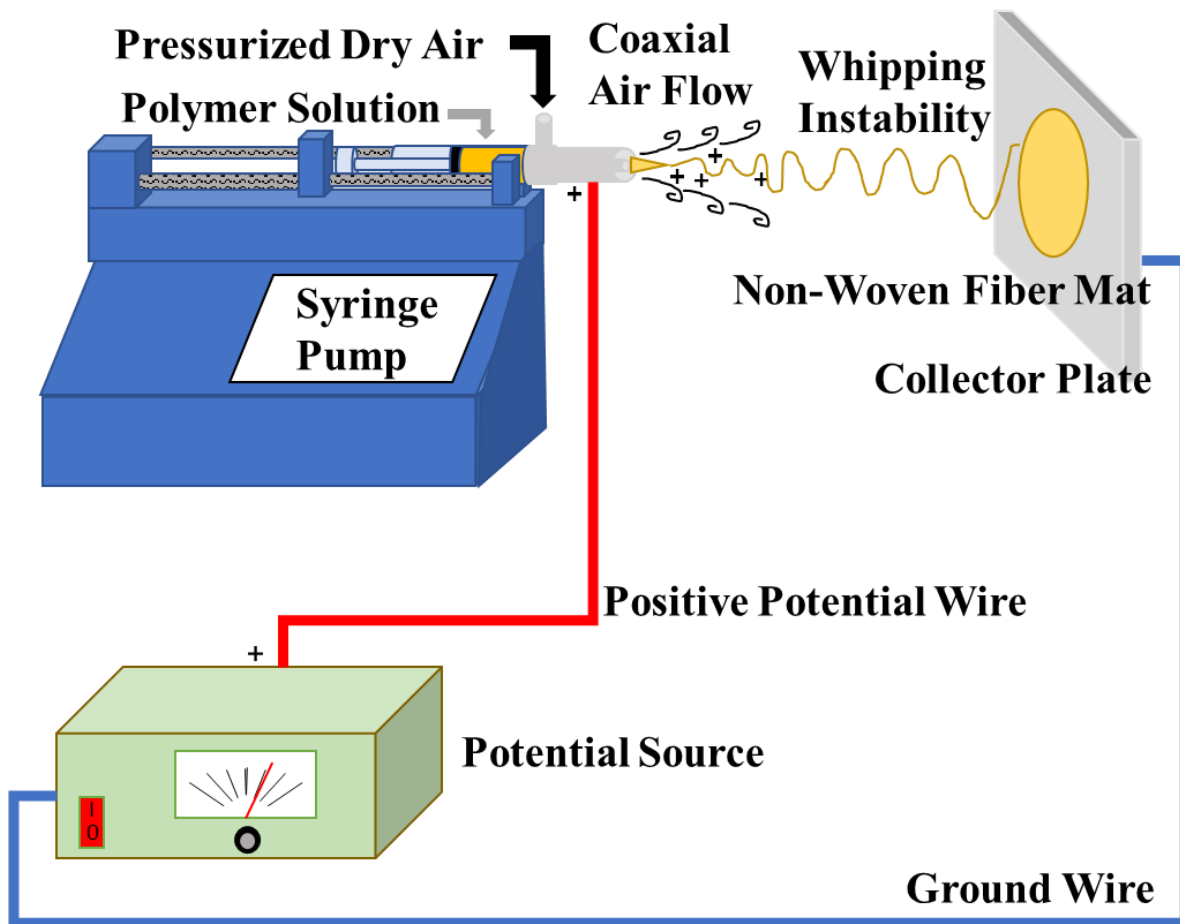


Figure 5.1: Gas-Assisted Electrospinning (GAES) Diagram

Binderless support materials are useful to the Li-Air system, but alone they don't solve the high overpotential issues. One such area that does, however, are electrocatalysts. Just like catalysts in chemical reactions, electrocatalysts are chemicals that speed up (or lower the barriers of) electrochemical reactions. Many different forms of these electrocatalysts exist, both freestanding and supported within a different active material, such as traditional pure metal catalysts like Au, Pd, Pt, and Ru^[20-23], metal oxides like MnO₂, ZnO, and RnO₂^[2,20,21,24-30], metal carbides like TiC and Mo₂C^[31-34], and even bifunctional perovskite catalysts^[35,36], with much of the catalytic activity of these catalysts being considered for both metal-air batteries and fuel cells, both of which have a form of the Oxygen Evolution Reaction (OER). While these

electrocatalysts lower the energy barrier for the OER and Oxygen Reduction Reaction (ORR), many challenges exist for these catalysts, as it has also been seen that some can reduce the energy barrier of parasitic side reactions, degrade themselves over time and cause issues in later cycles, and their inclusion must have a limited detraction from the electrical conductivity or oxygen and Li^+ ion diffusion within the porous cathode.^[33,34,37,38]

One such interesting electrocatalyst to consider is Molybdenum Carbide, Mo_2C , which is shown to have a high ORR activity in the DMSO electrolyte $\text{Li}-\text{O}_2$ system and has a “self-cleaning” behavior.^[33,34] When in the presence of O_2 , the surface of the Mo_2C forms a small layer of Molybdenum Oxide, MoO_2 , which reacts with the insoluble Li_2O_2 to form soluble LiMoO_3 . This reaction is interesting because it provides a separate reaction pathway for Li_2O_2 removal, one of the main issues of the Li -Air battery, then just the usual oxygen reduction reaction, which normally requires a high overpotential. However, the MoO_3^- ions will build up overtime, forming a viscous colloidal dispersion within the separator, which will decrease diffusion within the separator and increase the resistance within the battery system. This self-cleaning, self-limiting reaction pathway makes the $\text{Mo}_2\text{C}/\text{MoO}_2$ electrocatalyst a very unique system to study for the Li -Air system, and using carbothermal reduction of electrospun PAN with a metal acetate, it should be possible to add the Mo_2C to an electrospun carbon nanofiber cathode.^[7,14,32]

5.2 Experimental Methods

5.2.1. ACES Solution Preparation

Solutions for ACES for substrateless cathodes were prepared using reduced graphene oxide (rGO) [Dongjin Semichem], Nafion D2020 binder [Ion Power, Inc.] and ACS Grade

isopropyl alcohol (IPA) [VWR], while the binderless cathodes were prepared without the binder. Solutions were constructed in a 20 mL scintillation vial with a 20:80 \pm 1 binder:rGO mass ratios in 5 mL IPA, which was maintained for all tests at a carbon mass loading was 1%. The rGO-Mo₂C solutions also included Mo₂C nanoparticles [Aldrich, ~325 mesh and 99.5%], which were added in a 1:4 mass ratio with the rGO, being one fifth of the total active material. These solutions were constructed in a 20 mL scintillation vial with a 20:80:20 \pm 1 binder:rGO:Mo₂C mass ratios in 5 mL IPA, which was maintained for all tests at an active material mass loading was slightly greater than 1%. After all solutions were made, they were sonicated in an ice bath using a tip sonicator [Q500, Qsonica] for 30 minutes at 30% amplitude, using a 5 sec on/off pulse. After sonication, the solutions were stirred on a stir plate at 400 rpms overnight before use.

ACES solutions for the graphene project were created by my collaborator, Naman Gupta (Joo Group, MS) using the Taylor Couette reactor (TCR), using exfoliation of graphite, surfactants, and stabilizers in water to form graphene. The amount of carbon to “binder” (actually surfactants plus stabilizers) for these cathodes was approximated by the original ratio of polymer to carbon before entering the Taylor Couette reactor. Early systems had polymer:carbon ratios of 20:80, while later systems, which are the ones shown in this thesis, had been lowered to 2:98. This ratio is an approximate, as it was not possible to determine the percentage of the binder or carbon that would be in the graphene in the supernatant solution or in the crashed out, excess graphite after centrifugation. The supernatant graphene and polymer solutions in water were what was sprayed for this thesis, using the same spraying and mass loading considerations as past experiments, but considering a polymer to carbon ratio that was much lower (2:98 vs older 20:80) and therefore meaning less total loading on the carbon substrate, as the areal loading

remained the same because the amount of carbon being added was much greater due to the smaller amount of binder in the spray solution. This however is considering only the ideal situation of the polymer:carbon ratio being maintained through the TCR process. It could easily be possible that either more polymer or more binder crashed out during centrifugation, leading to a possible range of carbon loading.

5.2.2 GAES Solution Preparation

Pure PAN fiber solutions were prepared by dissolving 1 g of PAN [Sigma-Aldrich, 150,000 g/mol] in 9 g of Dimethylformamide (DMF) [BDH Chemicals, ACS Grade] on a heated stir plate at 65°C and 400 rpm for 12 hours. Mesoporous PAN/PMMA fiber solutions were prepared by dissolving 0.5 g of PAN and 0.5 g of polymethyl methacrylate (PMMA) [Sigma-Aldrich, 15,000 g/mol] in 9 g of DMF on a heated stir plate at 65°C and 400 rpm for 12 hours. To get Molybdenum Dioxide (MoO_2) / Molybdenum Carbide (Mo_2C) loadings similar to literature^[39], PAN-Mo fiber solutions were prepared by dissolving 0.5 g of PAN and 2.3 g of Bis(acetylacetonato)dioxomolybdenum(IV) [Sigma] in 6.75 g DMF on a heated stir plate at 65°C and 400 rpm for 12 hours, and PAN/PMMA-Mo fiber solutions were by dissolving 0.5 g of PAN, 0.5 g PMMA and 2.3 g of Bis(acetylacetonato)dioxomolybdenum(IV) in 6.75 g DMF on a heated stir plate at 65°C and 400 rpm for 12 hours.

5.2.3. Air Controlled Electro spray (ACES) for Binderless, Substrateless, and rGO-Mo₂C Cathodes

As shown in Figure 3.2, the ACES was done using a coaxial needle (outer needle: 12 gauge; inner needle: 16 gauge) [Hamilton], where the inner needle supplied the carbon solution and the outer needle created an air sheath using the building's process air. Using a pressure regulator, the process air was lowered to and controlled at 35 psi. An applied potential

of 5 kV was supplied by a potential source [ES30P-5W HV Power Supply, Gamma High Voltage Research] via an alligator clip on the needle tip, and a ground from the same potential source was attached to the aluminum foil covered stainless steel collector plate. A syringe pump [Pump 11 Elite, Harvard Apparatus], was used to keep the solution flow rate at 0.09 mL/ min for 2-3 minutes, with a spray distance from the needle to the collector of 6 cm, creating an electric field of 83 kV/m between the charged tip and grounded collector. The carbon substrate was held in the spray area, and a mask was used so that the amount of uncoated area would always be uniform between samples. To do so, a small sheet of folded aluminum foil was hung from the top of the collector (making sure to keep the back of the folded foil in contact with the collector, and, using non-conductive paper clips, a clear poly vinylchloride sheet was used as a mask to limit the spray circle diameter to 14 mm. This 14mm hole was created using a hand punch. Additionally, before starting each spray, a cardboard barrier was used to prevent overloading from spurting sprays upon starting the syringe pump, and the removal of this barrier was the signal for starting the spray time. The fabricated cathodes were then moved into an ultra-high purity argon [Airgas] filled glovebox [VGB-6, MTI Corp., < 5 ppm O₂ and H₂O] for cell assembly, and were fabricated at an active material loading of 0.5±0.03 mg active material / cm² carbon paper substrate area.

5.2.4. PAN Fibers from GAES

The PAN GAES was performed similarly to the ACES, using the same equipment, but with polymer solutions and different equipment conditions. As shown in Figure 5.1, the GAES was done using a coaxial needle (outer needle: 12 gauge; inner needle: 16 gauge) [Hamilton], where the inner needle supplied the carbon solution and the outer needle created an air sheath using the building's process air. Using a pressure regulator, the process air was

lowered to and controlled at 10 psi. An applied potential of 20 kV was supplied by a potential source [ES30P-5W HV Power Supply, Gamma High Voltage Research] via an alligator clip on the needle tip, and a ground from the same potential source was attached to the aluminum foil covered stainless steel collector plate. A syringe pump [Pump 11 Elite, Harvard Apparatus], was used to keep the solution flow rate at 0.08 mL/ min until 3.2 mL of solution was spun, with a spray distance from the needle to the collector of 25 cm, creating an electric field of 100 kV/m between the charged tip and grounded collector. Before starting each spin, a cardboard barrier was used to prevent dissolving of the fiber mat from spurting solution upon starting the syringe pump, and the removal of this barrier was the signal for starting the spray time. These conditions would create a visible Taylor Cone at the end of the syringe tip, creating a whipping fiber that could be collected on the collector plate. Once the syringe was empty, the fiber mats were collected by gently peeling the fibers mats by gently pushing beneath the mat with gloved fingers. These mats were then folded and stored in petri dishes until heat treatment could be done to form the carbon fiber cathode.

5.2.5 General Stabilization, Carbothermal Reduction, and Activation

This section will discuss the heat treatment of the non-compressed fiber mats. The fibers mats were placed between two ceramic plates to prevent curling during heat treatment. The stabilization process was performed within a box furnace [KSL-1500X-S, MTI Corp.], where the fibers were heated at 250 °C for 2 hours, with a 5 °C/min temperature ramp. After stabilization, the fiber mats were placed in a tube furnace [OTF-1200X, MTI Corp.] for all further heat treatment. Carbothermal reduction was performed under a flow of high purity nitrogen gas [Airgas] at 900 °C for 2 hours with a 5 °C/min temperature ramp to create carbon fiber mats. Mats undergoing activation were then heat treated under a high purity carbon dioxide [Airgas]

flow within the same furnace, at a temperature of 900 °C and a 5 °C/min temperature ramp. The activation time was varied for different trials, ranging between 30 min and 2 hours. The heat-treated carbon fiber mats had 15 mm diameter cathodes punched out of them via a hand punch [T-0.6, MTI Corp.]. The fabricated cathodes were then moved into an ultra-high purity argon [Airgas] filled glovebox [VGB-6, MTI Corp., < 5 ppm O₂ and H₂O] for cell assembly

5.2.5. Compressed PAN Fibers

PAN fibers undergoing compression testing had a different stabilization process. Using two stainless steel plates instead of ceramic plates, the fiber mats were placed on a hot press [CRC, 200°C and 1600 lbf limits] for compressed stabilization. The press platens were lowered to onto the stainless-steel plates, quickly compressed, with a held pressure between 150 and 650 lbf for varying tests and then heated to 200°C for 2 hours, at a ramp rate of 5 °C/min. The lower temperature for stabilization was used here due to equipment limits. After stabilization, the mats were cooled and retrieved from the press.

5.2.6 Carbon Substrate Preparation

Carbon paper [TGP-H-030, 50% Wetting, Toray], a conductive, porous carbon fiber mat was used as the conductive substrate. To remove excess Teflon coating, the carbon paper was heat treated in under an inert Argon atmosphere in a tube furnace [OTF-1200X, MTI Corp] at 900 °C for 2 hours, using a 5 °C/min temperature ramp, while being held between two alumina-silicate ceramic plates [McMaster Carr]. After heat treatment, 15 mm diameter carbon paper substrates were punched out between two weigh paper sheets to prevent edge defects and cracking, using a hand punch [T-0.6, MTI Corp.].

5.2.7 Electrolyte and Separator

A solution of 1M Lithium Triflate (LiCF_3SO_3) [Sigma Aldrich] in ACS Grade 1,2-dimethoxyethane (DME) [VWR] was used as the electrolyte, created in a glovebox under inert Argon gas. This solution was stored within the glovebox and was kept under constant stirring to maintain solution consistency. Separators were prepared by punching 19 mm diameter disks from glass fiber filters [GF/D, Whatman], between weigh paper sheets to prevent edge defects, using a hand punch [T-0.6, MTI Corp.]. These were immediately added to the glovebox, as well, and were stored separately from each other for ease of access and to prevent damage from tweezer pressure.

5.2.8 Cell Assembly

A picture and labeled schematic of the Li-Air cells is shown in Figure 3.1. Li-Air cells were created using 316 stainless steel Swagelok style cells, made in-house, and plastic tweezers were used during cell assembly to prevent capacity loss. Cell assembly began with placing a lithium disk [16 mm dia, 0.6 mm thick, MTI] on the central stage of the negative terminal and compressing slightly with a Delrin plastic rod [McMaster Carr] for good lithium-to-stage contact. On top of that, a glass fiber separator was centered above the lithium disk and was saturated with 310 μL of electrolyte. The separator was well saturated with electrolyte so that minor evaporation of the electrolyte into the dry oxygen would have little effect on battery results. For the substrateless cathodes, which contain rGO directly on the separator, the carbon coating was placed upward, facing the positive terminal and an additional 50 μL of electrolyte was added to this system. No additional cathodes were added to these batteries. For all other batteries, centered above the separator, the cathode was placed and an additional 50 μL of electrolyte was added to the cathode for ideal internal wetting of the cathode. For the binderless

cathodes and sprayed rGO-Mo₂C cathodes, the spray layer was placed facing upwards, towards the positive terminal to less O₂ diffusion. The fiber cathodes are identical on both sides, so the orientation was not an issue. Then for every battery system, a stainless-steel mesh [316 SS, 0.032" opening, McMaster Carr,] was centered on top of the cathode to ensure good contact to the positive terminal and to balance pressure across the cathode surface. A Teflon cylinder with n-buna o-ring seals was then placed around the setup, creating the oxygen chamber. The assembly was connected to the positive terminal via a 316 stainless steel spring and was sealed using 4 screws. After cell assembly was finished, the cells were removed from the glovebox. Using Swagelok connectors, ultra-high purity O₂ gas [Airgas] was added to the cell at 16 psi. The cell was first purged of argon using the O₂ gas for 30 seconds and then immediately filled for another 30 seconds to ensure only pure O₂ was within the cell chamber. During this process, cells were checked for gas leakage and were removed from trials and re-sealed if a leak was found.

5.3 Results and Discussion

5.3.1 Binderless and Substrateless Electro Spray Cathodes

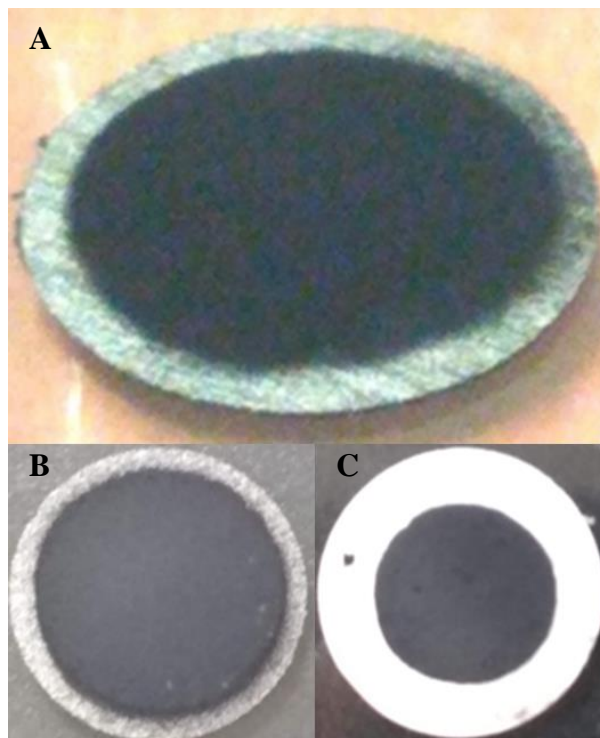


Figure 5.2: Visual Comparison of ACES Cathodes: A: Regular 1L rGO cathode. B. Binderless rGO cathode. C: Substrateless rGO cathode on silica fiber separator. The silica fiber separator has a larger diameter than the carbon paper substrates, which makes its central spray area seem smaller in the image.

Before considering the electrospun CNF cathode system, a short study was performed in the 1-layer electro spray system to determine the necessity of the binder and the carbon paper support within the electro spray cathode system, and these are shown in Figure 5.2. Binderless cathodes were created by electro spraying the usual rGO solution without any Nafion D2020 binder onto carbon paper cathodes, while substrateless cathodes were made by electro spraying the usual rGO solution with the binder directly on the glass fiber separator, with a visual result of

both of these sprays shown in Figure 5.2 to have similar visual macroscale topography to that of the usual 1L rGO spray. However, subtle differences are definitely present within these new systems. The idea to spray directly on the separator for the substrateless system came from considering carbon interlayers in lithium sulfur batteries that did just that for trapping in polysulfides. However, the differences between Li-Air and Li-S battery separators caused issues within its implementation in the Li-Air system. In most coin cell systems like Li-S and Li-Ion, Celgard polypropylene separators are the standard separator, as they are very thin, but still porous to allow ion diffusion. In Li-Air batteries, the separator also contains the electrolyte for the system, as some will evaporate into the oxygen or open atmosphere that the cell is contained in, thus requiring thicker separators, like glass fiber separators, to be able to hold excess electrolyte and prevent the drying out of the three-phase interface within the cathode. As the SEM images of Figure 5.3 show, the glass fiber separator is actually quite open, with a lot of vacant space between the non-uniform fibers, making it a poor surface to electrocoat onto. Additionally, the substrateless cathodes, being on the less rigid silica fiber separator, were very difficult to break apart cleanly for cross-sectional imaging, leading to some pinching of the glass fiber substrate and uneven breaking of the rGO layer. Although the imaging of the substrateless cathode suggested that the rGO created a good surface layer, battery cycling was not possible in this system, as the deep channels of the separator allowed rGO to penetrate into the separator, leading to short circuiting of the battery system. This could be rectified by including a thin Celgard separator with the glass fiber separator, which can be directly sprayed upon without leading to short circuiting, but would require excess electrolyte to fill the Celgard separator pores and to overcome the poor wicking of the Celgard with organic electrolytes, while increasing the

diffusion resistance within the system by adding additional separator thickness and smaller separator pores.

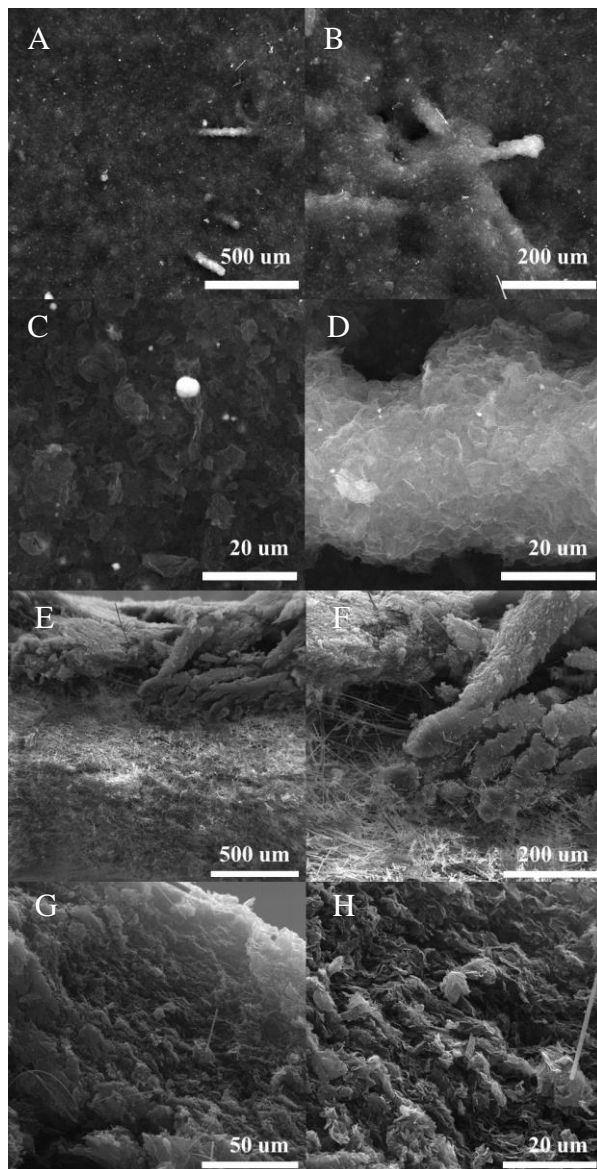


Figure 5.3: SEM Images of Substrateless Cathode: A-D: Top-view. A: Bulk spray topography. B: Separator fiber poking through spray layer. C: rGO morphology away from fiber. D: rGO morphology on extended fiber. E-H: Cross-section view. E: Full carbon layer and silica fiber support. F: Morphology loss due to blade. G: Morphology/layer thickness at clean break. H: Morphology of rGO cross-section.

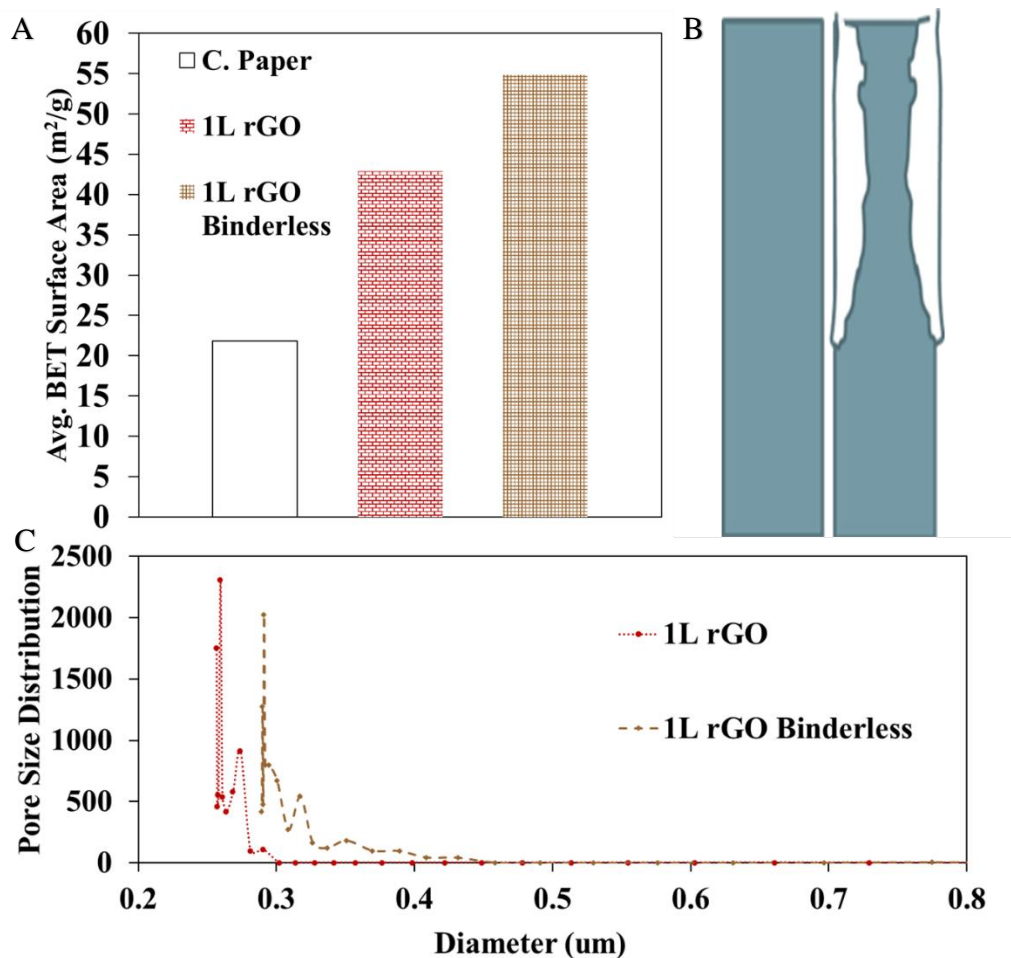


Figure 5.4: Pore Data for Binderless rGO Cathodes: A: BET microporous surface area. B: Pore diameter decrease from binder on the pore walls. C. Porometry macropore diameters.

As the binderless spray does not have the polymer binder that can cover up pores, the BET data in Figure 5.4 show the increase in micropores and macropores due to the lack of the binder does increase the cathode surface area, giving more reaction sites, but the Porometry data shows that the lack of the binder increased the macropore size. This decrease in macropore size makes sense for the addition of the binder, as the polymer binder acts as a sticky film to connect the particles that make up the cathode. For smaller pores, like mesopores, this film might cover

the pore completely, removing access to the internal pore structure, while with larger pores, the film will start to flow down the pore sides, both decreasing the diameter of the pore and increasing the topography of the pore wall. Additionally, the top view and cross-sectional SEM images of the binderless system show a system fairly similar to the binder system, with a flat surface morphology and uniform cross-section, but without the binder, the rGO is able to pack significantly closer, causing a decrease in the layer thickness and an increase in the bulk density, as shown in Figure 5.5 and Table 5.1. Early data would suggest that this decrease in cathode thickness and increase in surface area would cause an increase in battery capacity; however, the deep discharge data in Figure 5.6 suggests that the binder plays a more important role in the electro spray cathode system. Comparing the binderless spray case to the electro spray with binder and the dropcast with binder, we see an interesting comparison within the cycling curves at a current density of $0.5\text{mA}/\text{cm}^2$. During discharge and charge, the binderless electro spray case retains the reduction of the overpotential that is seen within the case with binder; however, the discharge curve of the binderless system has a much steeper slant, only slightly outperforming the dropcasting case, reaching around $\sim 8100\text{mAh}/\text{g}$, about half that of the electro spray case with binder. However, on the charge cycle, the binderless spray case retained many of its beneficial properties, showing a lowered overpotential compared to the dropcasting case and having good coulombic efficiency. This could mean that without the binder, the electro spray cathode system is not able to withstand the electrodeposition of the Li_2O_2 , and although it does not have the initial macroscale cracks of the dropcasting case, it may still have some structural instability without the binder being present to hold the cathode together. This was most apparent when looking at SEM images of the spent cathodes for the binderless system, which can be seen in Figure 5.5. Although the cross-sectional images of the binderless spray system are comparable to

those of the regular electro spray system, the binderless system had a tendency to break apart and peel off of the carbon paper substrate after cycling, just like the dropcasting case would do, implying that the structural enhancements of electro spraying do require some amount of binder to maintain good attachment of the rGO layer to the carbon paper substrate.

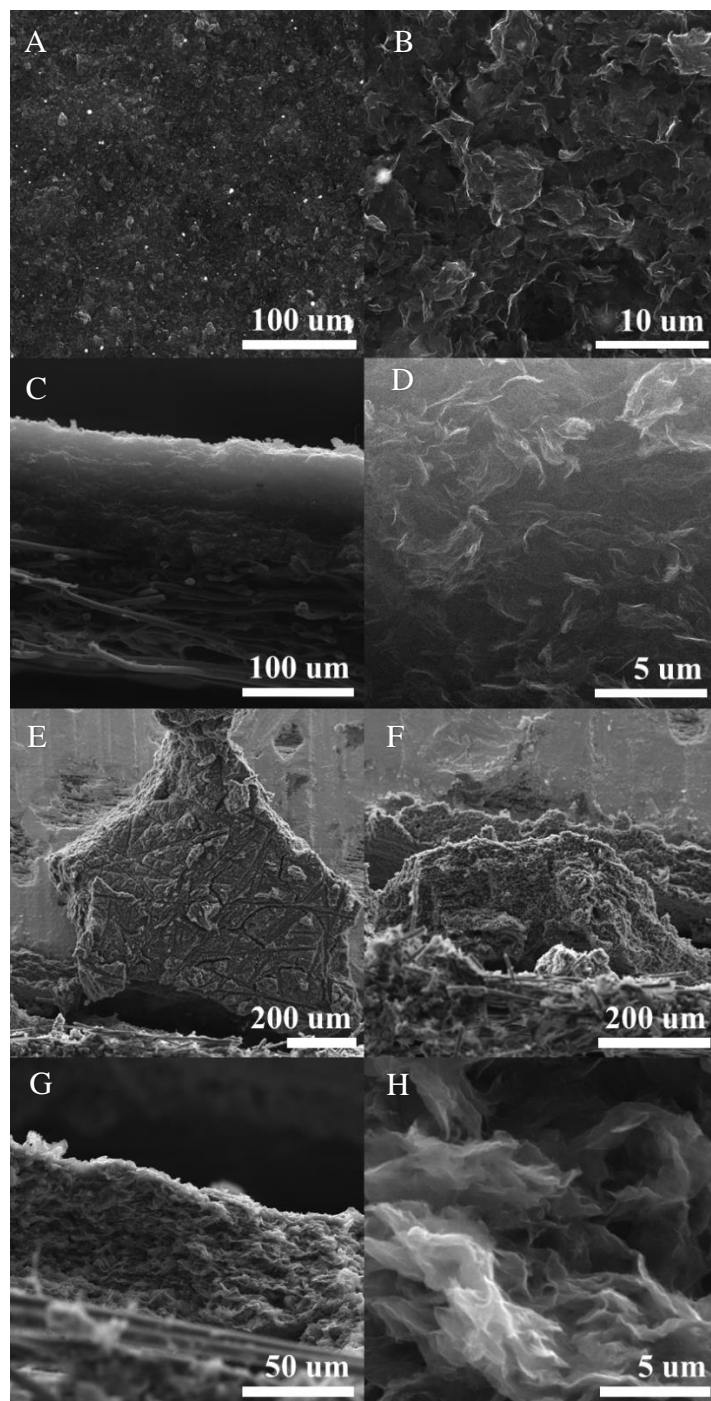


Figure 5.5: SEM Images Binderless rGO Cathodes: A-D: As fabricated cathode. A/B: Top-view morphology. C/D: Cross-sectional image and morphology. E-H: Spent cathode. E/F: Fragility of spent cathode connection to carbon paper. E shows the underside of a piece that fell from the carbon paper. F/G: Cross-sectional image and morphology.

Table 5.1: Binderless rGO Bulk Density Comparison

Cathode Type	Total Bulk Density (mg/cm ³)
1L rGO	60.1
1L rGO Binderless	68.7

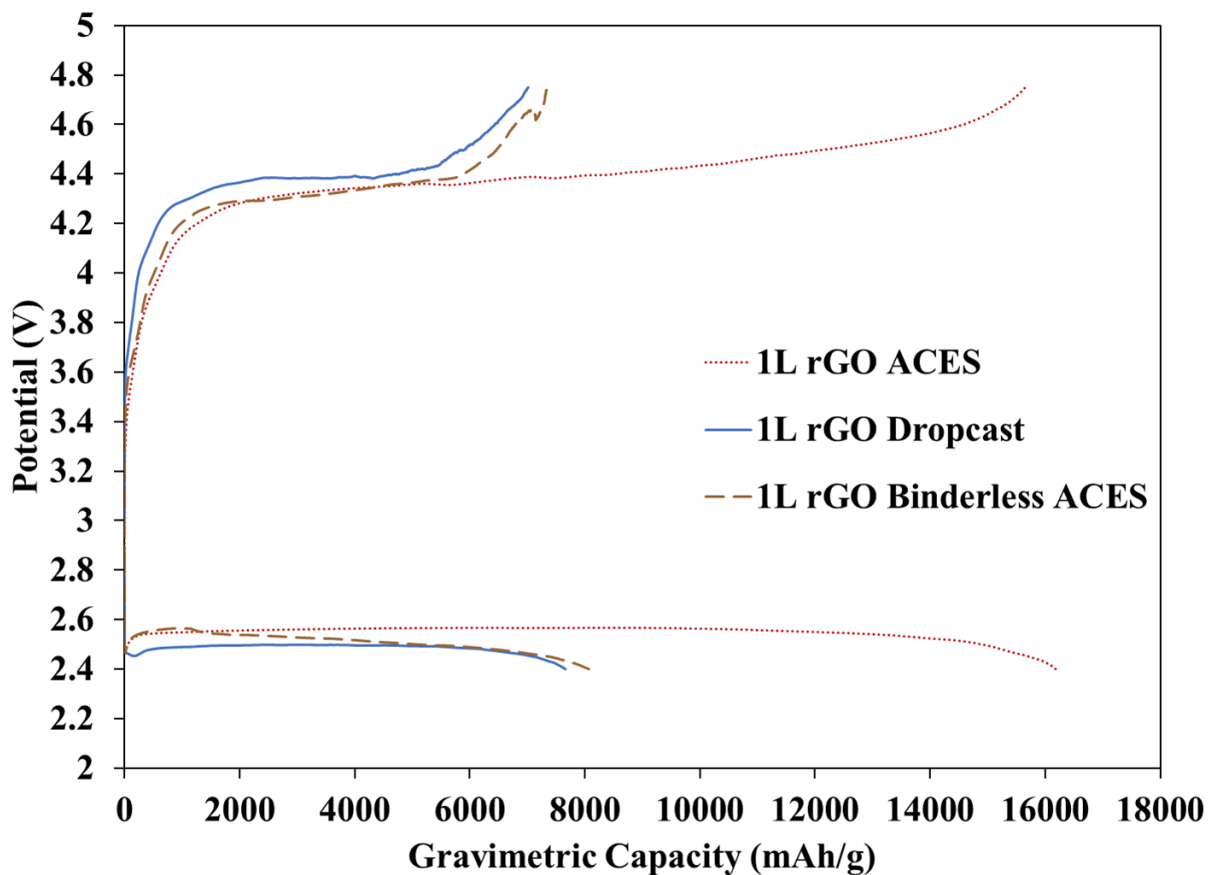


Figure 5.6: Cycling Curve Comparisons

5.3.2. Gas-Assisted Electrospinning of PAN for CNF Cathodes

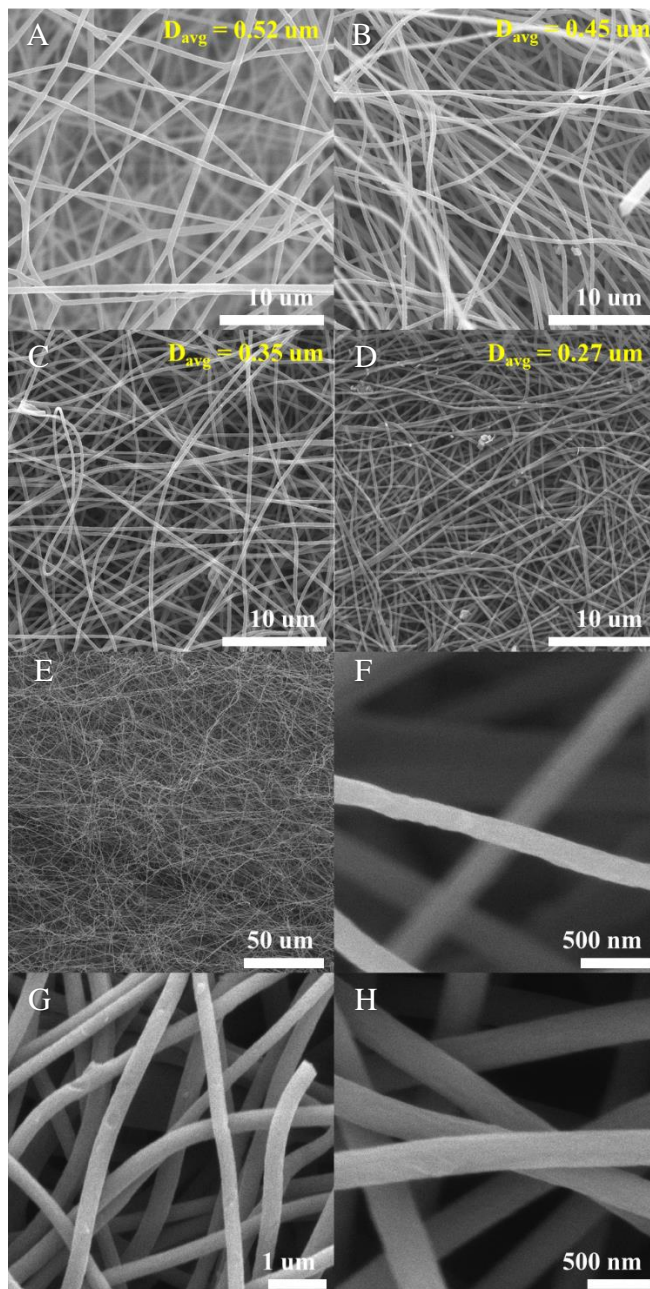


Figure 5.7: Pure PAN Fiber Mats in SEM and Macroscale: A-B: Single mat as-spun (A), stabilized (B), carbonized (C), and activated (D) with fiber diameters. E: Macroscale image of fiber mat. F: As spun fiber surface. G/H: carbonized fibers with pitting.

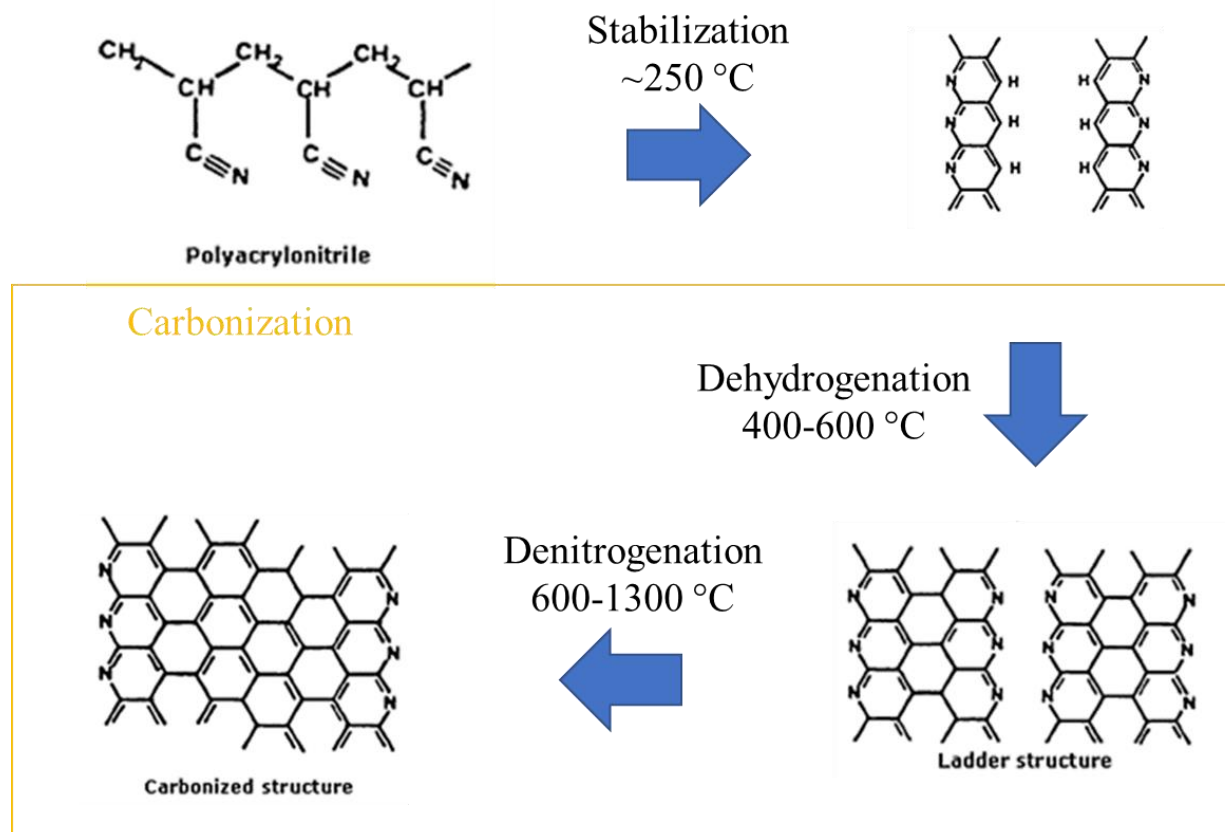


Figure 5.8: Carbothermal Reduction Process: area in orange box shows the carbothermal reduction steps.^[19]

When first considering electrospun cathodes, I first considered the fiber mats that make up the cathode. The Gas-Assisted Electrospinning (GAES) process creates a non-woven fiber mat, with the fibers arranging themselves randomly over each other, and with their fiber diameters dependent upon the spinning conditions, which have been well documented by others in the past. However, the process of carbonization, that is making the non-conductive polymer fibers into conductive carbon fibers changes the surface structure of the fibers, and this topography/morphology change can be seen in Figure 5.7, while the heat-treatment process structural effects on the polymer is shown in Figure 5.8. The stabilization process at low heat helps to fuse the fibers together under mild compression, increasing the contact points between

the fibers while adding few oxygen structures to the fibers. Carbothermal Reduction (aka. Carbonization), under high temperature and an inert atmosphere, removes the oxygen defects and side chains within the PAN matrix, leaving just the carbon backbone, shrinking and slightly wrinkling the fiber surfaces, with some fibers splitting in the process. At this point, the fiber mats are conductive enough to be used for cathodes, but Activation, under a reactive atmosphere at high temperature, continues to shrink the carbon fibers and add pitting to the carbon surface, further increasing the surface area through the creation of additional mesopores and micropores. This is most readily seen in Figure 5.9, where the BJH pore area shows additional activation doubles the number of micropores and greatly increases the number of low diameter mesopores and the BET data shows a 10% increase in the surface area (from 464 to 500 m²/g).

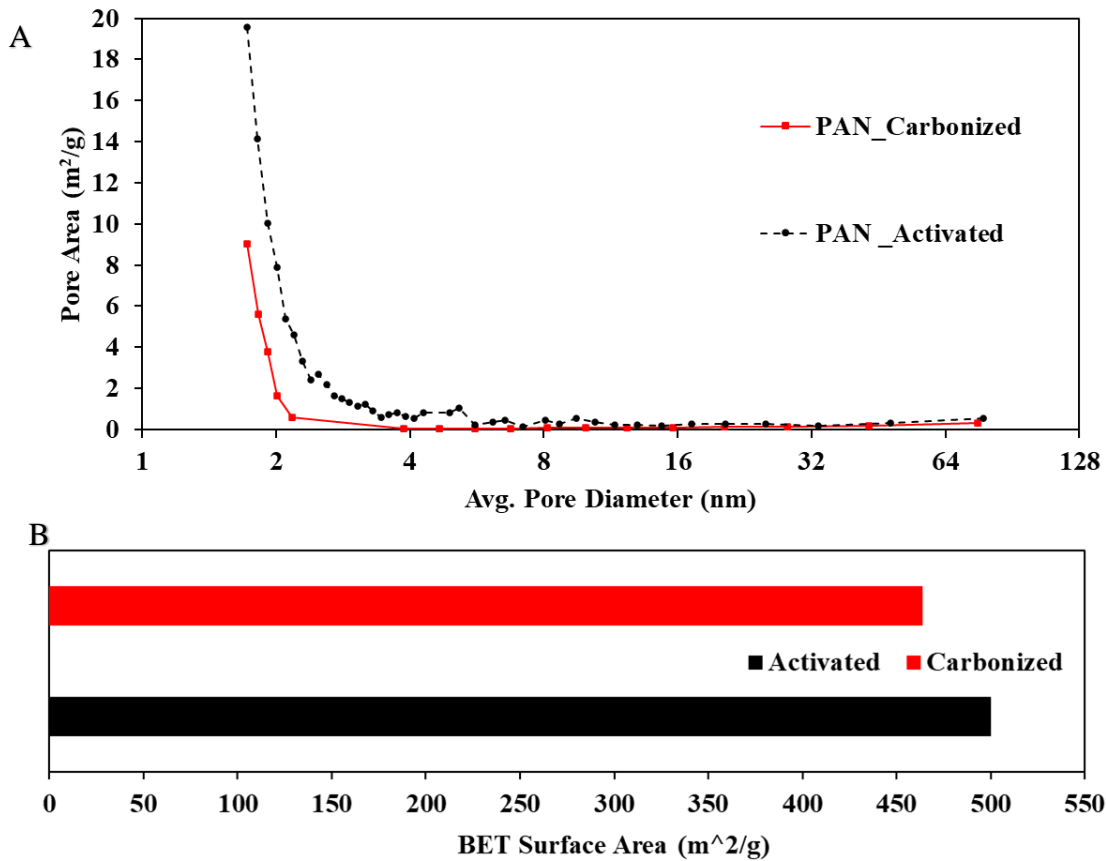


Figure 5.9: Pore Area: A: BJH pore area. B: Total BET Surface Area

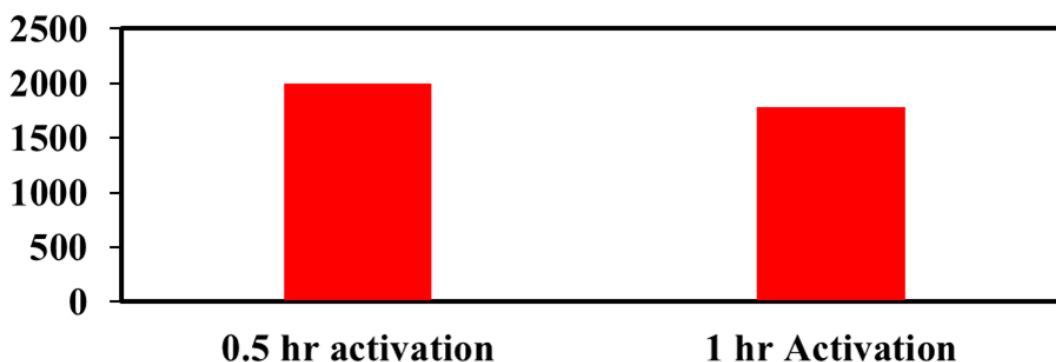
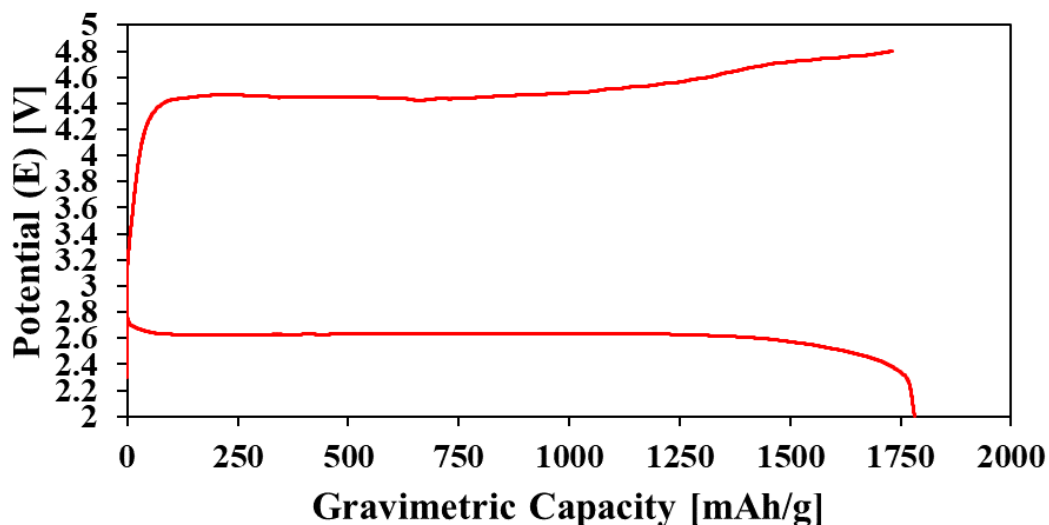


Figure 5.10: CNF Capacity: Top: Example CNF battery curve: 1.0-hour CO₂ activation. Bottom: Minor capacity increase with lessened activation time.

As battery cathodes, the PAN fibers had intermediate success. The PAN fiber cathodes had more carbon active material than previous electro spray cathodes, and were run at a gravimetric current density of 60 mA/g. However, these cathodes showed much more instability than the carbon paper and spray system during the charging cycle. The activated carbon fibers would regularly reach around 1750 mAh/g, as can be seen in Figure 5.10, but the CNF cathode charge curve tended to reach a high overpotential early on in the cycle, leading the curve to

slowly approach the terminal voltage while at high overpotential. As the electrolyte solvent, DME, is prone to decomposition at high overpotential, this could cause two different extended charging issues. The first caused the coulombic efficiency to go over 100%, as the charge curve would extend farther than the discharge curve as the electrolyte was being decomposed within the battery system. The second was an infinite fluctuation of the voltage profile due to short circuiting, most likely from dendrite growth at the high voltage.

5.3.3. Fused Fiber PAN Mats

One thing considered during PAN fiber creation was how well the fiber mats were mechanically fused together. As their structure is non-woven, the electron pathways within the fibers can only run along the fiber axis, or can jump between connecting fibers. It has been shown by past group members that adding pressure during the stabilization step will help to fuse the PAN fibers together, though a deep study upon this phenomenon has not been performed in the literature. For increased pressure control, and to be able to look at high pressure ranges, a hot press was used for the fiber stabilization step, to still allow for a furnace-like control of the temperature, while still allowing for detailed control of the pressure.

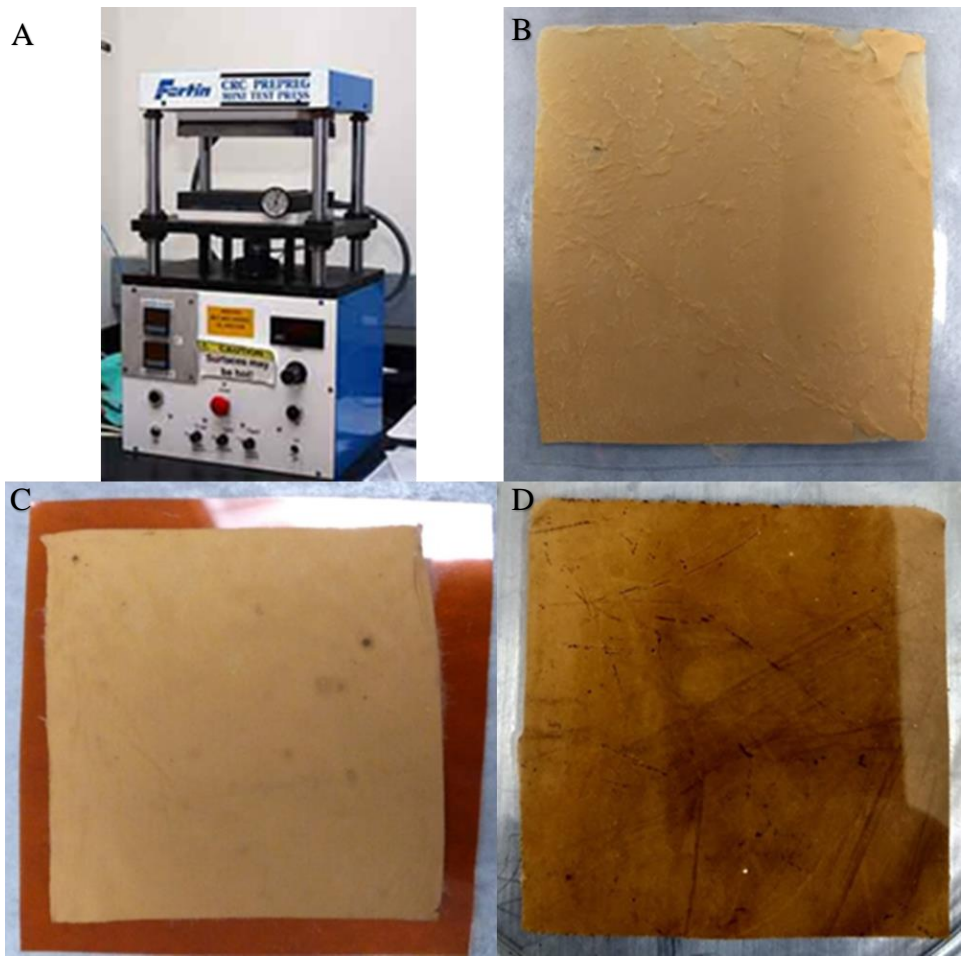


Figure 5.11: Compressed Fiber Support Considerations: A: Hot Press. B: PET backed fiber mat. C: PI backed fiber mat. D: Stainless Steel backed fiber mat.

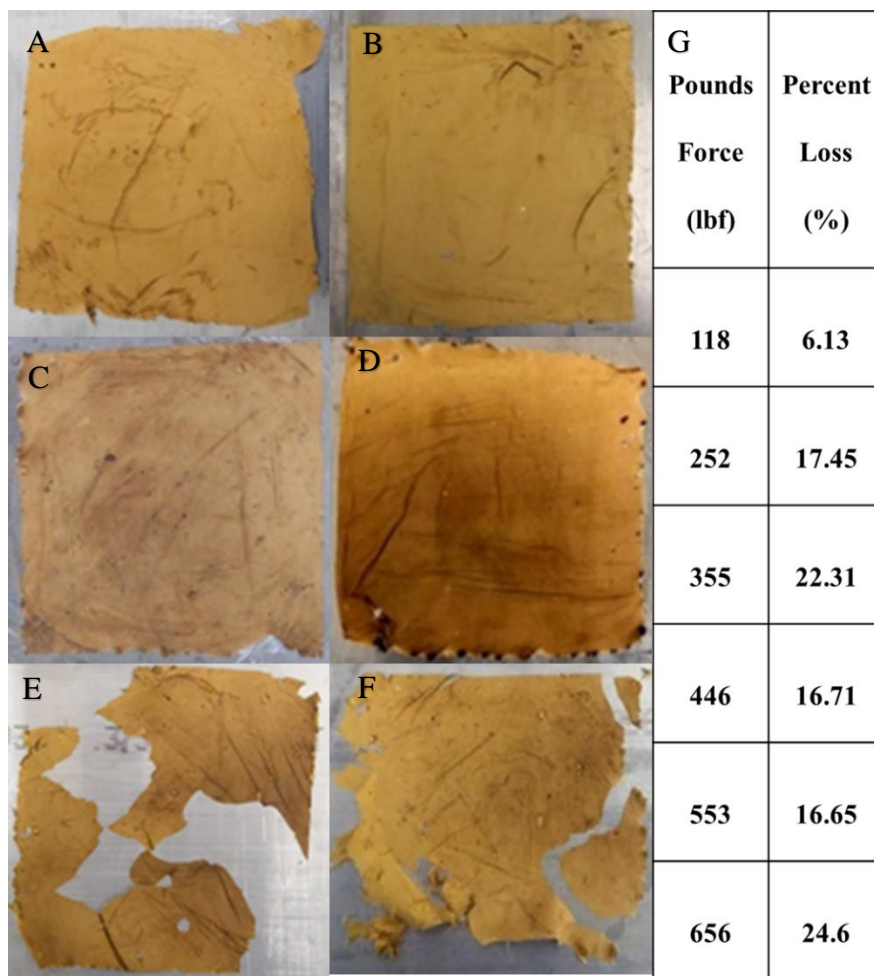


Figure 5.12: Macroscale Images of Compressed Fiber Mats: A-F: Fiber mats after stabilization at 200°C for 2 hours at increasing lb_f , respectively, 118, 252, 355, 446, 553, 656. G: Mass loss after stabilization.

Although the hot press system was similar to the furnace system, the high pressures involved would no longer allow the use of ceramic plates to keep the fiber mat flat. The hot press plates themselves had to be kept clear of debris, so we tried three different interlayer options, two heat resistant polymer films, Polyethylene terephthalate (PET) and Polyimide (PI), and 316 stainless steel sheets (316SS), as can be seen in Figure 5.11. All 3 systems had some sticking issues, however, though it was much worse with the polymers. The PET film fully attached to

the PAN mat, splitting the mat in half upon collection, while the PI film proved to be robust, with one film coming off completely clean, but the bottom film that everything was pressed in to stuck firmly to the PAN mat. The stainless steel produced darker PAN films after pressurized stabilization, and only really had sticking issues when at significantly high pressures. Looking at a pressure range of 110-650 lb_f, the compressed fiber mats showed a general trend of increasing mass loss with increasing force, but higher forces also created much more brittle fiber mats that were prone to cracking and sticking to the stainless-steel sheets, as can be seen in Figure 5.12. The validity of these mats as cathodes, however, was unable to be determined. Upon the necessary activation step in a CO₂ atmosphere, the thin mats were burned off in the more reactive atmosphere, not leaving enough usable cathode for battery testing. The use of thicker initial PAN mats was explored, but these showed to have higher mass loss and retained the brittle nature of the earlier compressed mats and the project was abandoned.

5.3.4 Catalytic Fibers: PAN – Mo Cathodes

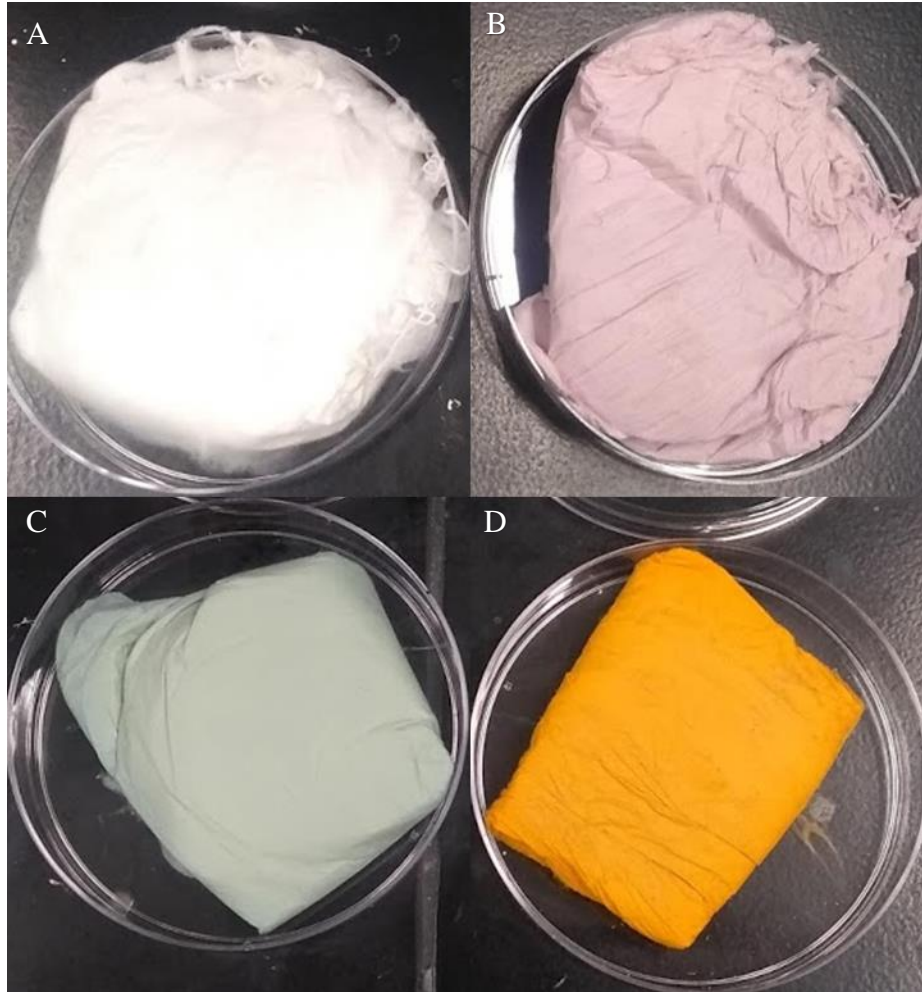


Figure 5.13: Macroscale Images of Fiber Mats: A: Pure PAN fibers. B: PAN-Co fibers. C: PAN-Mo fibers D: PAN-Fe fibers.

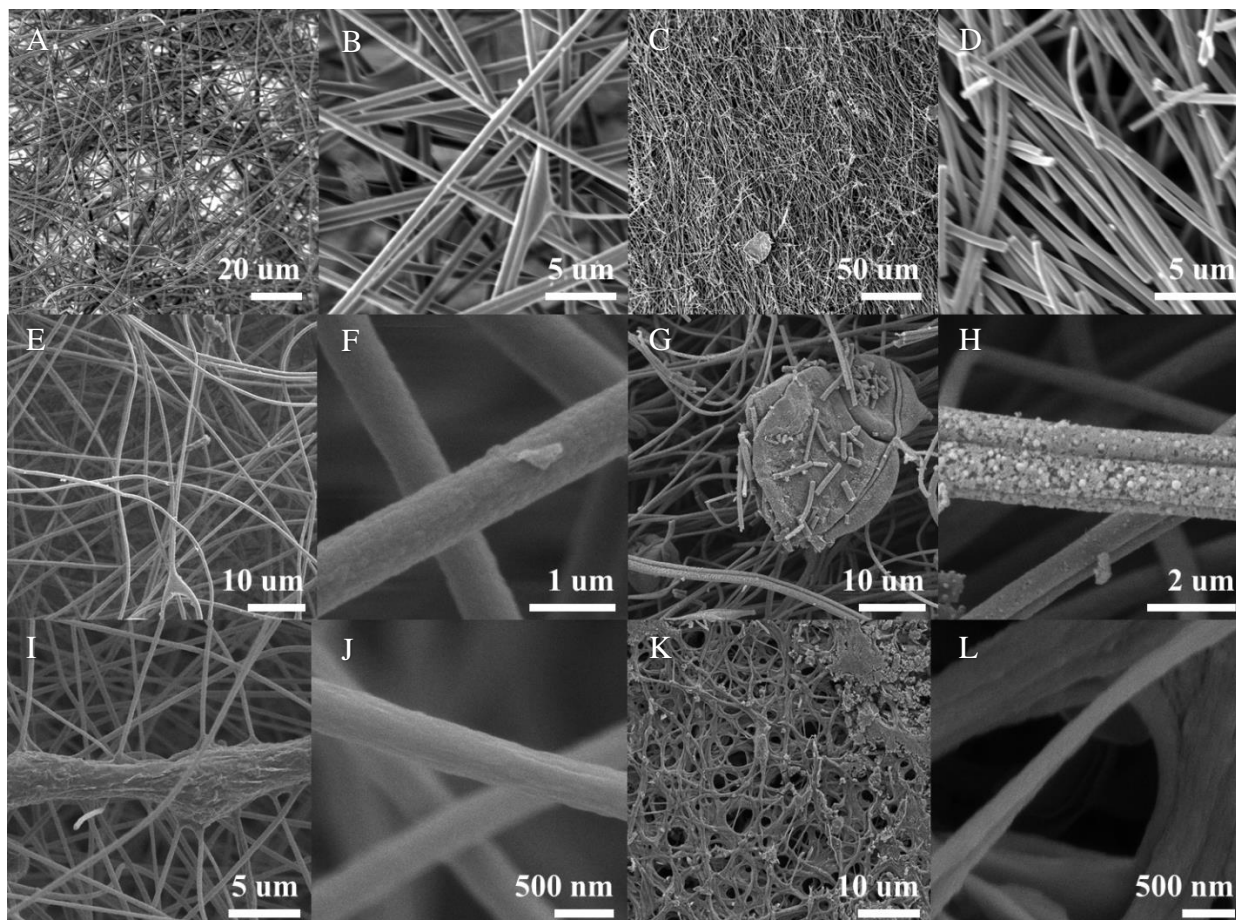


Figure 5.14: Fibers Before and After Carbothermal Reduction in SEM: A-D: PAN Fibers A/B: Before. C/D: After. E-H: PAN-Fe Fibers. E/F: Before. G/H: After. I-L: PAN-Mo Fibers. I/J: Before. K/L: After.

Although the PAN fiber mats had issues during the charging cycle, the effects of electrocatalysts made *in situ* during the fiber formation process were considered. Through the process of including metal acetate in the standard GAES process, it was possible to incorporate many different metals into the usually white PAN fiber system, as can be seen in Figure 5.13 for Cobalt, Iron, and Molybdenum impregnated fibers. To increase the mesoporous content of the fibers, the fibers were spun with PMMA, as sacrificial polymer, which would be removed by the carbonization step. The PAN/PMMA, PAN-Fe, and PAN-Mo as-spun fiber mats can be seen up

close in the SEM images in Figure 5.14, showing that both have rougher surfaces than PAN GAES fibers, probably due to both the sacrificial PMMA and the metal acetates, of which there are some surface particles of. After the carbothermal reduction step, it can be seen for all the fibers that the fiber surfaces take on a rougher appearance, and have some fiber breakages; however, the PAN-metal fibers show two significant differences, forming crystalline structures on the outside of the fibers and forming large aggregates within the fiber mat system. XRD analysis of the PAN-Metal fibers in Figure 5.15 show that before the carbothermal reduction in inert N₂ gas, the PAN-Fe system is difficult to pin down, showing peaks for mainly Fe₃C, while the PAN-Mo fibers relates best to Mo₆C₄. After carbothermal reduction, the PAN-Mo system shows pretty clear conversion to Molybdenum Carbide, Mo₂C, with a wider initial peak showing some Molybdenum Oxide, MoO₂, is present, as well.

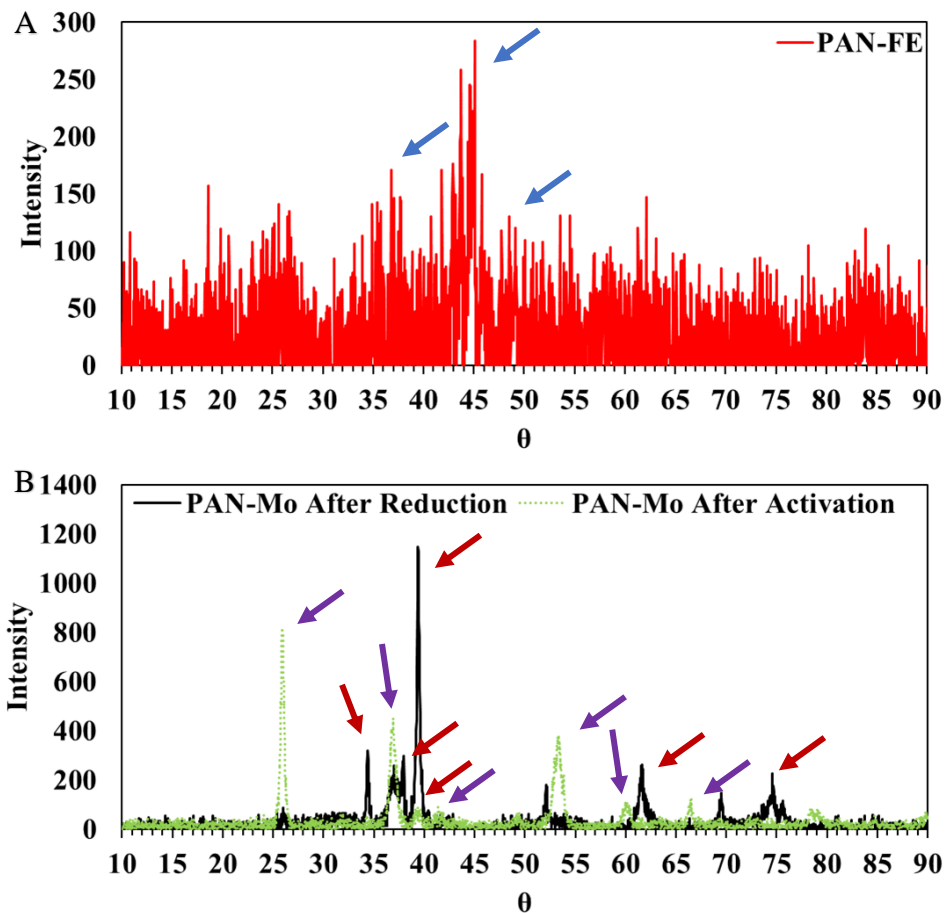


Figure 5.15: Fiber XRD Data: A: PAN-Fe after CTR. Blue arrow shows Fe_2C Peak B: PAN-Mo both after CTR and after Activation. Red arrows show Mo_2C peaks, while purple arrows show MoO_2 peaks.

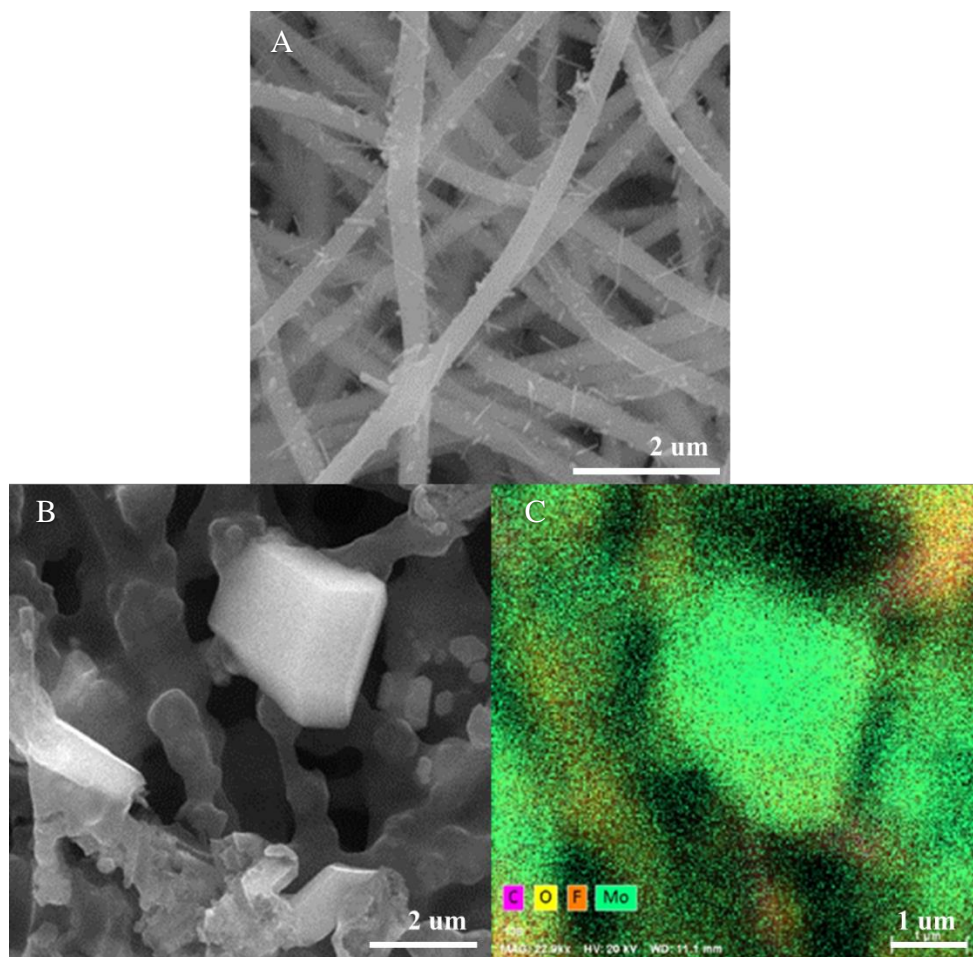


Figure 5.16: Activated PAN-Mo Cathodes via SEM and EDX: A: Before cycling SEM. B: After cycling SEM. C: After cycling, Energy Dispersive X-Ray Analysis (EDX) confirms large Mo deposits

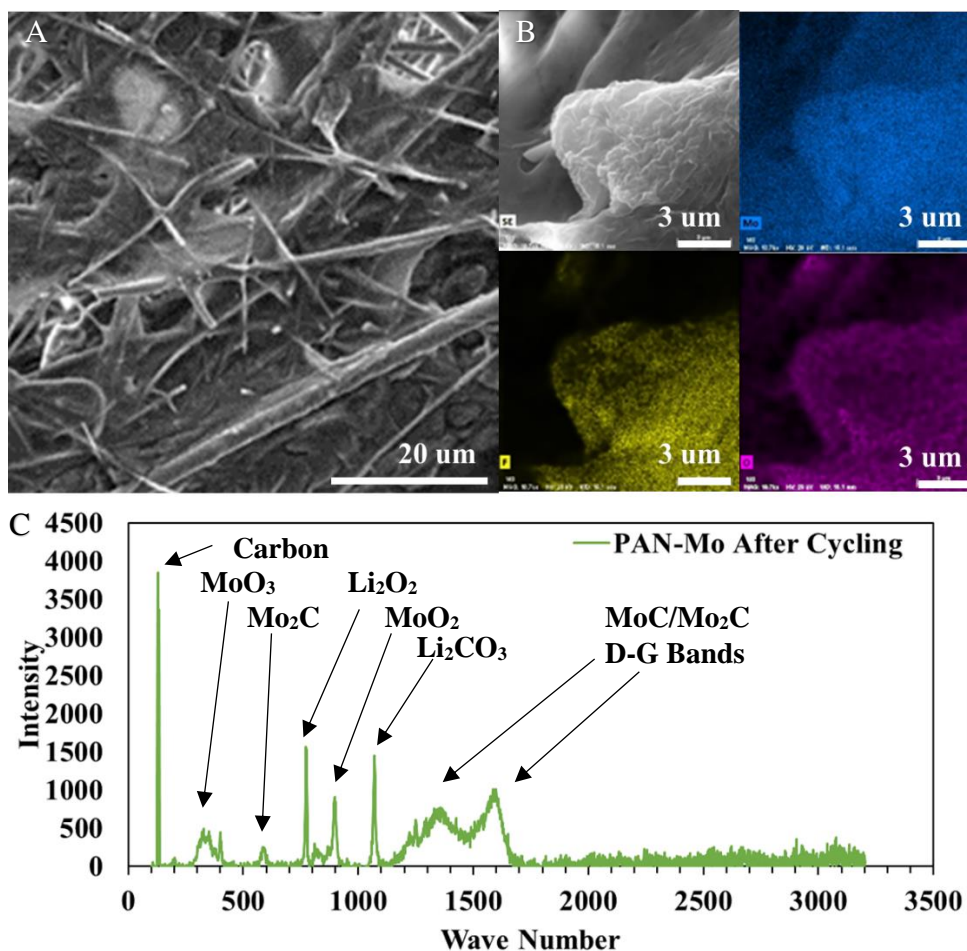


Figure 5.17: Viscous Film on Separator After Discharge of Activated PAN-Mo Cathode via SEM, EDX, and Raman: A: Separator after cycling SEM. B: EDX of film on separator. C: Raman of deposit on separator

After activation under a CO₂ atmosphere was a completely different situation for the PAN-Mo cathodes. SEM imaging of the activated fiber surface, shown in Figure 5.16, revealed fiber size reduction and significant growth of the Molybdenum Carbide/Oxide crystals, of which XRD in Figure 5.15 confirmed a large conversion of the Mo₂C into MoO₂. This crystal growth was even more noticeable after cycling, where large deposits of sharply angled MoO₂ crystals could be seen on the Li₂O₂ coated fiber surface via SEM and confirmed to be molybdenum via

EDX, as shown in Figure 5.16. PAN-Mo cathodes that were cycled without going through the activation step also showed the Li_2O_2 coating, but without the large MoO_2 crystals. Just like with the pure PAN fibers, a viscous substance was seen on the silica fiber separator after cycling; however, EDX confirmed these deposits to contain high amounts of Mo, F, and O, suggesting that the suggested MoO_3^- complex is indeed forming from the MoO_2 and is complexing with the electrolyte salt, lithium triflate being the source of the F, creating a viscous barrier in the separator during cycling. Additional identification via Raman in Figure 5.17 showed that the $\text{Mo}_2\text{C}/\text{MoO}_2$ electrocatalyst was also overperforming within this system, catalyzing the creation of the parasitic Li_2CO_3 side product, and also transferring some MoO_2 onto the separator, as well, hinting at poor inclusion into the CNF fiber matrix.

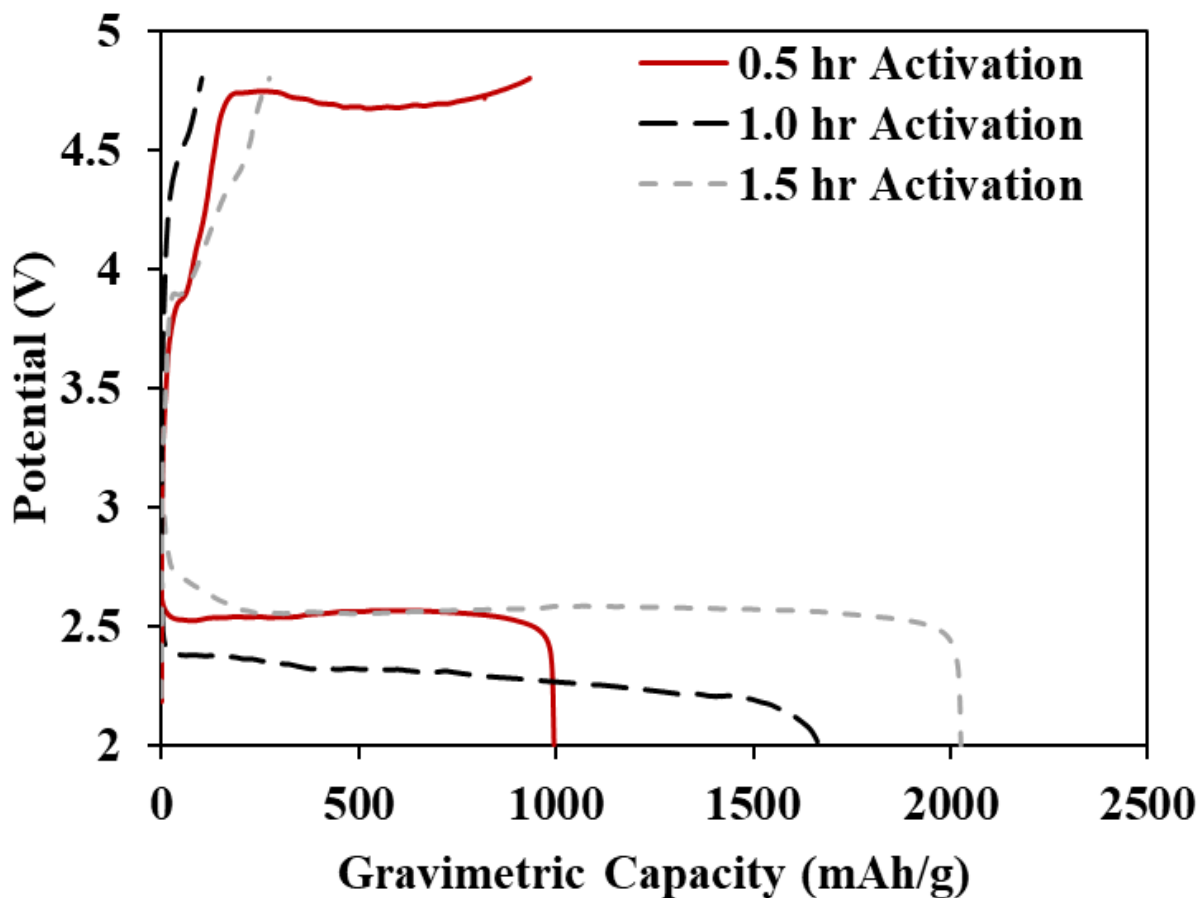


Figure 5.18: Activated PAN-Mo Cycling

The battery results for the PAN-Mo system show some expected trends and some differences from the pure PAN system. As the capacity data shows in Figure 5.18, the activation step is necessary for reaching higher capacities, and increasing the activation step time length does increase the battery capacity. However, the PAN-Mo system had significant overpotential issues during the charging cycle, very rarely reaching even 50% coulombic efficiency, meaning that the system is performing like a primary battery. This could be due to some of the same issues that were seen in the original PAN fiber system, which also had issues during the charge cycle, but the baseline system still had high coulombic efficiency. These results suggest that $\text{Mo}_2\text{C}/\text{MoO}_2$ electrocatalyst does not have a beneficial affect when added to the CNF cathode system, meaning that the additional reaction pathway for Li_2O_2 removal is outdone by the harm from the increased Li_2CO_3 production and viscous MoO_3^- clogging the separator.

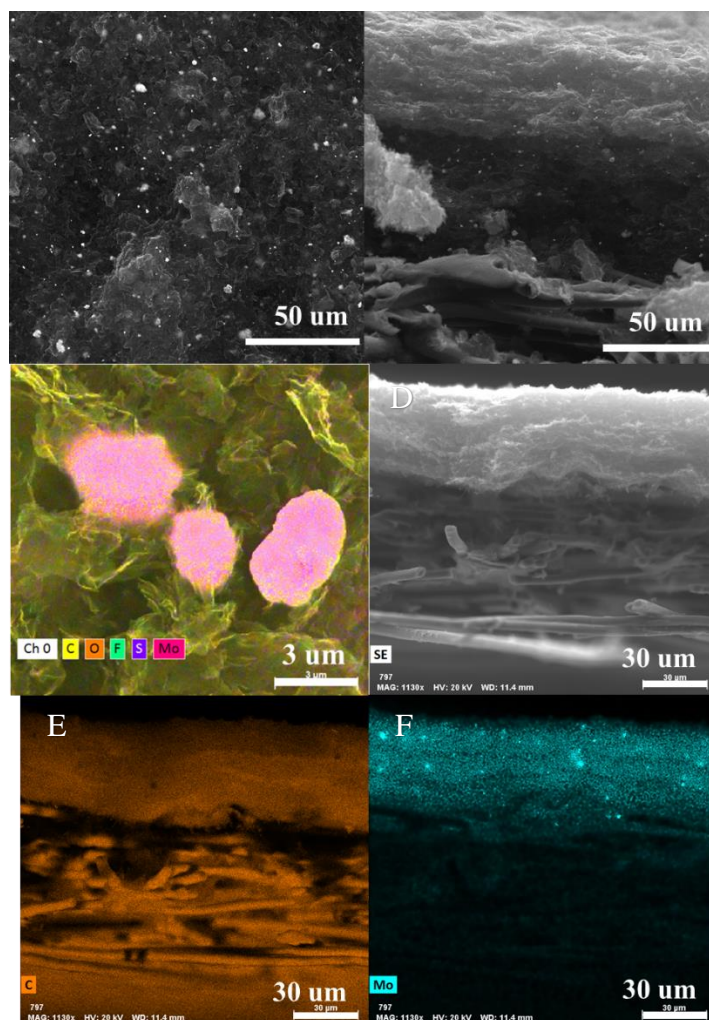


Figure 5.19: SEM and EDX of Mo_2C in rGO ACES and Dropcast Cathodes: A: ACES top view. B: ACES cross-section. C: ACES Elemental analysis close-up. D-F: Dropcast EDX

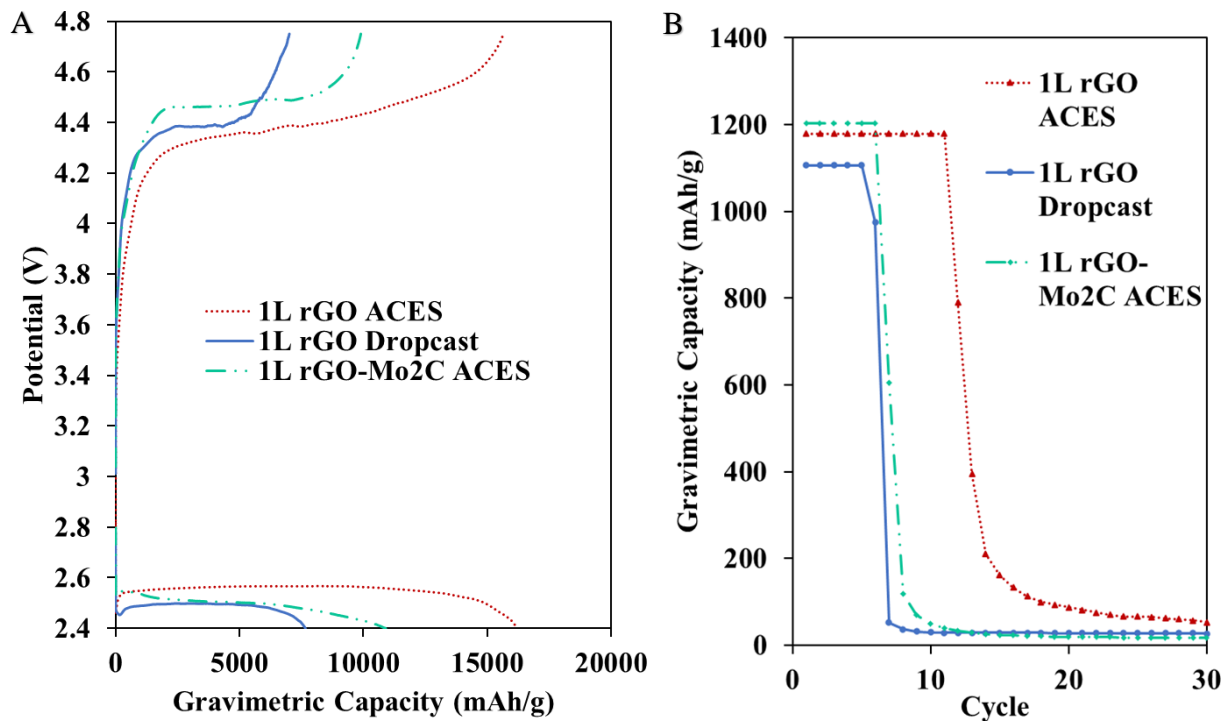


Figure 5.20: rGO-Mo₂C Battery Cycling: A: Deep Discharge Cycling. B: 1mAh, 0.50 mA/cm² limited capacity cycling

However, the Mo₂C electrocatalyst showed improved results within other battery systems. By adding Mo₂C nanoparticles to the cathode solution, Mo₂C can be added to the dropcasting and electrospinning cathode matrix, as seen in SEM and confirmed by EDX in Figure 5.19. Structurally, the addition of these nanoparticles does not seem to change the surface topography of the cathode and are found throughout the cathode cross-section, but should lower the conductivity of the system due to their lower electrical conductivity than rGO sheets. Figure 5.20 shows how the addition of Mo₂C nanoparticles to the 1L rGO spray system affects the battery cycling. Within the electrospinning system, the effect is much more muted, showing both a 40% reduction in capacity with a large 0.2 V increase of the charge overpotential. Although this case did not show the same charge issues as the CNF system, the limited capacity cycling

showed poor capacity over multiple cycles, showing that the Mo₂C electrocatalyst on a carbon support is not as useful for improving the charge cycle as originally thought.

5.3.5 Future Catalysis Work – Taylor Couette Reactor (TCR) Graphene with Imbedded Metal Catalysts

As has been discussed in multiple chapters, carbon-based electrodes are staples in many of the various battery technologies. Whereas much work has been done to look at different types of carbon and carbon-based structures, many of the formation methods of these carbons can be time intensive, cost intensive, or both. Using a TCR system, graphene can be made 2 orders of magnitude faster and without any of the harsh chemicals required of the traditional Hummers Method, which gives the added benefit of preventing the formation of oxygen defects.

Additionally, TCR's, due to their incredible shearing rates, are able to create few and single layer graphene from even very highly stacked graphite precursors. However, depending on the source quality, natural graphite is prone to having defects and additional elements, making the resultant graphene less pure, and the TCR process does introduce stabilizers, like Xanthan Gum, and surfactants, like poly acrylic acid, which are both possible sources of side reactions within the Li-Air system.

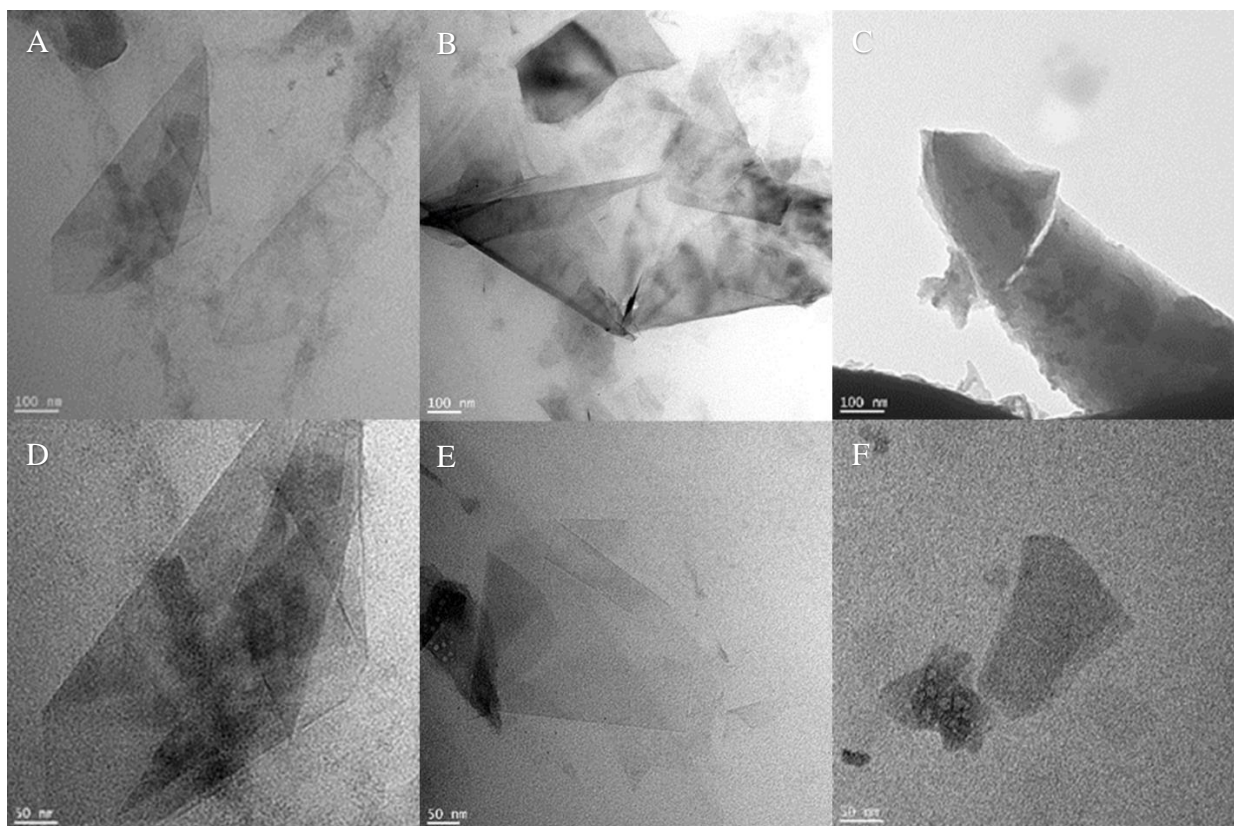


Figure 5.21: TCR Few-Layer Graphenes TEM: A/D: Natural Graphite Powder. B/E: Expanded Graphite Powder. C/F: Natural Graphite Solution

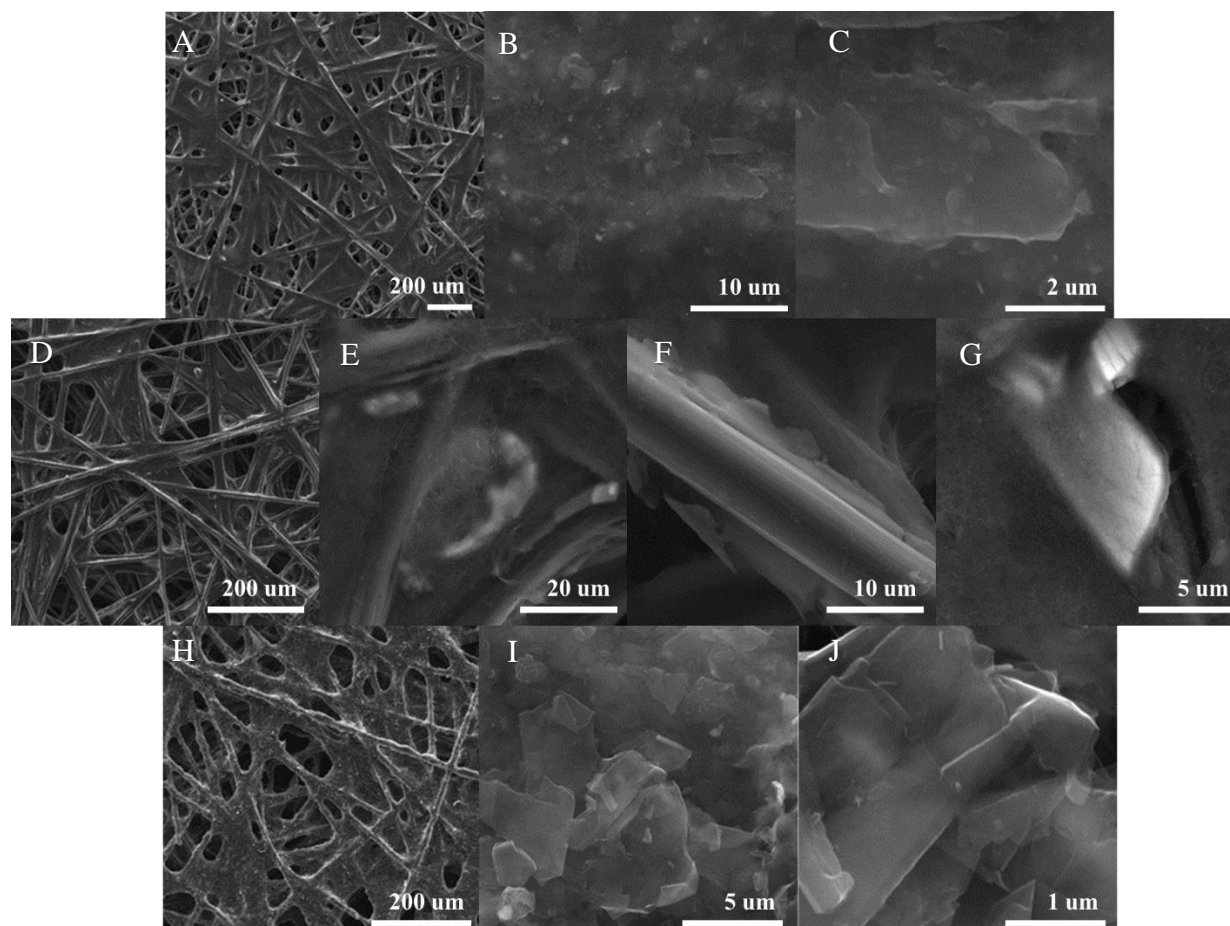


Figure 5.22: TCR Few-Layer Graphene Top-View SEM: A-C: Natural graphite powder. D-G: Expanded graphite powder. H-J: Natural graphite solution. A, D, H: Wide view. B, E, I: Layer topography. C, G, J: Flake edges. E, G: Transparency allows seeing behind layer

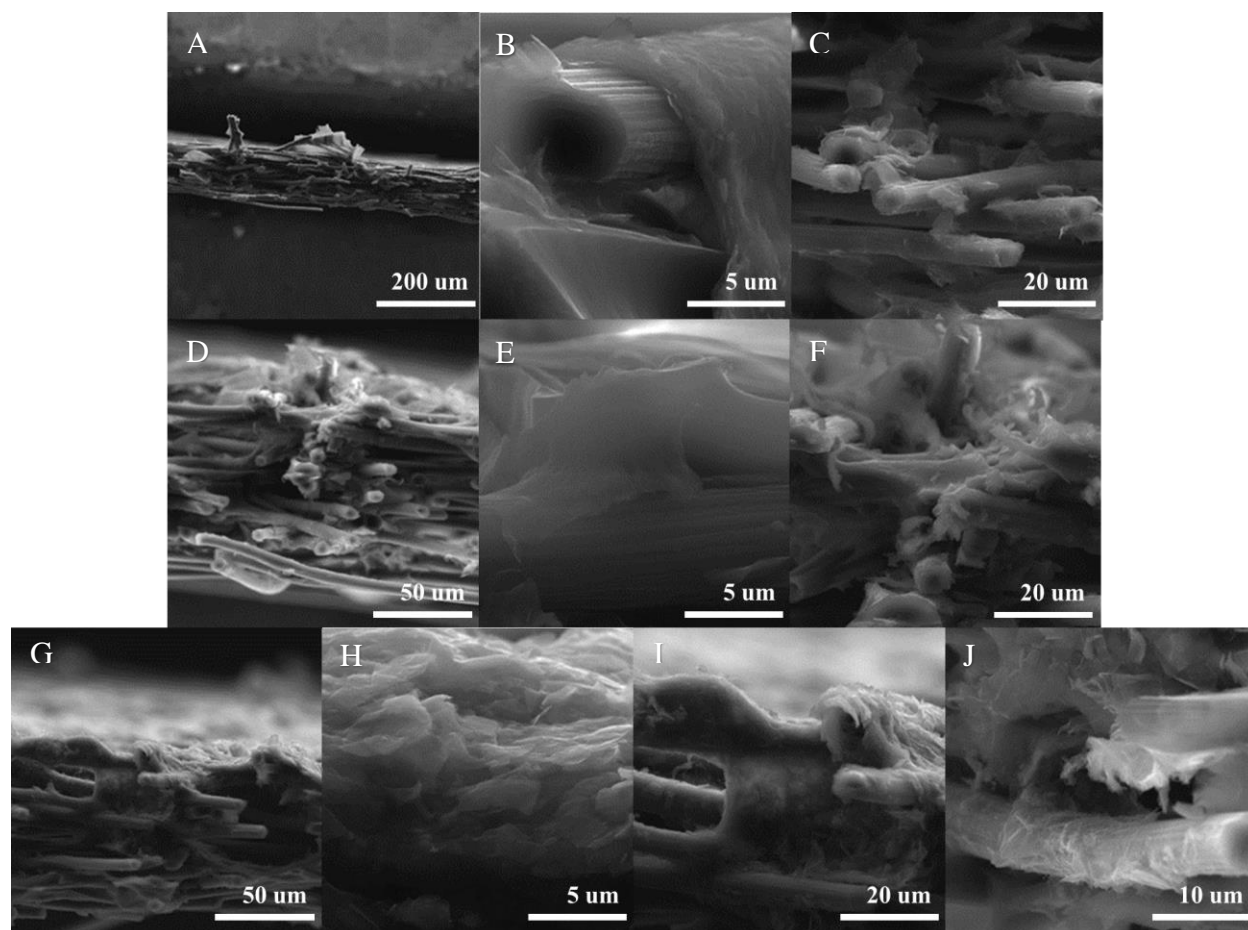


Figure 5.23: TCR Few-Layer Graphene Cross-Section SEM: A-C: Natural graphite powder. D-F: Expanded graphite powder. G-J: Natural graphite solution. A, D, G: Wide view. B, E, H: Layer thickness. C, F, J: rGO deep in C. Paper. I: Solution natural graphite-based graphene had film connectivity deeper into the carbon paper holes

We considered graphene from a few of these graphite precursors, an expanded graphite powder and two different versions of natural graphite, one in a powder form and the other in a solution form, for their use within the Air-Controlled Electro spray (ACES) Li-Air battery system. TEM images in Figure 5.21 show that each of the precursors formed into both few and single layer graphene upon going through the TCR, with most graphenes having lateral dimensions of a few microns. These micron sized sheets stacked significantly tightly during

ACES, as the topical and cross-sectional SEM images shown in Figure 5.22 and Figure 5.23. The topography of each graphene was very similar, with most of the graphene wrapping around the carbon paper, major patches of condensed graphenes near fiber intersections where the fiber support allowed for additional structural build-up, and open spaces in the larger spaces between fibers, though each allowed some amount of individual sheet structure to be seen at higher resolutions. Of differences of note, the expanded graphite created layers that allowed for some optical penetration, allowing for fibers and open spaces covered by a layer of graphene to be seen from above both in SEM, while the solution-form natural graphite created large sheets that created a rougher coat, leading to increased topography. The cross-sectional images show a more interesting story. Each of the systems show that there was penetration of the graphene deep into the carbon paper matrix, which was not very heavily seen in earlier rGO sprays. Like the GNR sprays, the graphene systems all created super thin layers upon the carbon paper surface, with some breakage and flaking near the breakage sites made for the cross-section. Of note, the rougher solution-based system had the greatest thickness, probably due to its more haphazard alignment of the graphene sheets, but it also had the greatest connectivity deeper down into the void spaces seen from the top view, creating a more continuous layer of graphene in these spaces through graphene films that formed perpendicular to the top layer. This additional perpendicular to the substrate plane part of the film leads to an interesting problem considering the bulk density, as the bulk density is usually approximated by the volume of a cylinder whose cross-sectional area is the spray area being considered; however, the graphene cathodes show some vertical continuity into deeper cathode areas, meaning that the cylindrical disk being considered (if laid out completely flat) would probably have a larger cross-sectional area than the spray area. As the amount of continuity of the spray film into the lower substrate volume is unknown for the

entirety of the cathode, the additional increase in cross-sectional area for the bulk density was considered to be a 25% increase. The bulk density of each of the different graphene systems can be seen in Table 5.2, with the natural graphite powder system showing the densest, thinnest layering of its graphene sheets. However, all three systems showed the similar issues as the earlier GNR system in consideration to their macroporous structure. Unlike the GNR system, the graphenes all did create some low diameter macropores, but like the GNR system, they created some higher diameter micropores, but the counts of all of these are extremely low (less than the natural carbon papers counts) as the Porometry data shows in Figure 5.24. Within Li-Air batteries, the preliminary tests of each of the systems showed fairly low performance. The capacity data in Figure 5.25 shows that the thicker layered systems showed the highest capacity and lowest overpotential, but each of the three systems retained the high total overpotentials of around 2.0 V. This data is different from previous battery potential curves, as it considers the ideal case of retaining 98% carbon solids in the solution and the unideal case of 80% carbon solids in the solution (assuming that more graphite crashed out than polymer additives, leading to a lower end added mass of carbon). A number of factors should be considered when comparing these results to earlier ACES systems. Comparing to the GNR system, which also had poor capacity and high overpotential, the structural topography of the systems is very similar, with extremely low layer thickness and incomplete coverage of the gaps between carbon paper fibers. The rGO has significantly higher amount of oxygen defects, which lowers the electrical conductivity, but may provide some amount of catalytic activity at these oxygen sites. Lastly, the polymers present in both systems are quite different, as Nafion D2020 binder was present in the rGO and GNR ACES system, but the graphene systems had a combination of Pluronic and Xanthan Gum stabilizer, due to the requirements of the TCR process. The Pluronic could be

removed from the graphene system by heating, but the Xanthan Gum requires temperatures above 900 C to remove it from the system, making it difficult to process and remove.

Table 5.2: 1L Graphene ACES Bulk Density

Graphite Precursor	Approx. Spray Area Bulk Density (mg/cm ³)	Approx. Expanded Area Bulk Density (mg/cm ³)
Natural Graphite Powder	3647	2918
Expanded Graphite Powder	1484	1187
Natural Graphite Solution	851	681

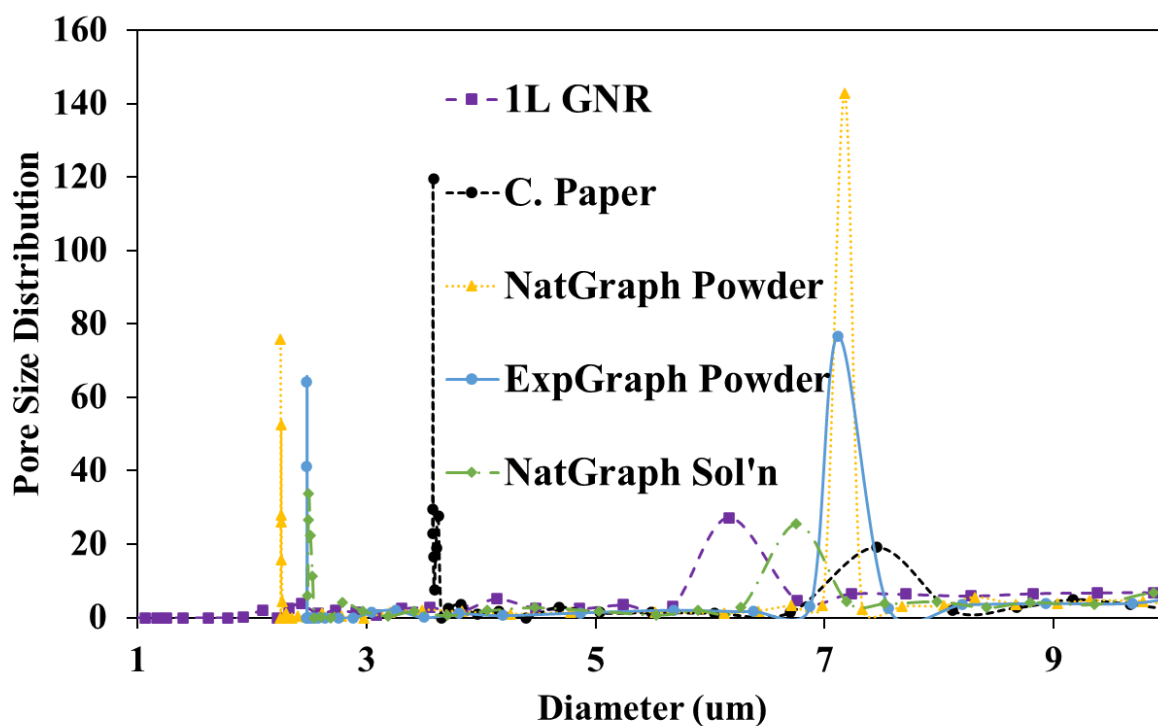


Figure 5.24: ACES Graphene Porometry Compared to ACES GNR

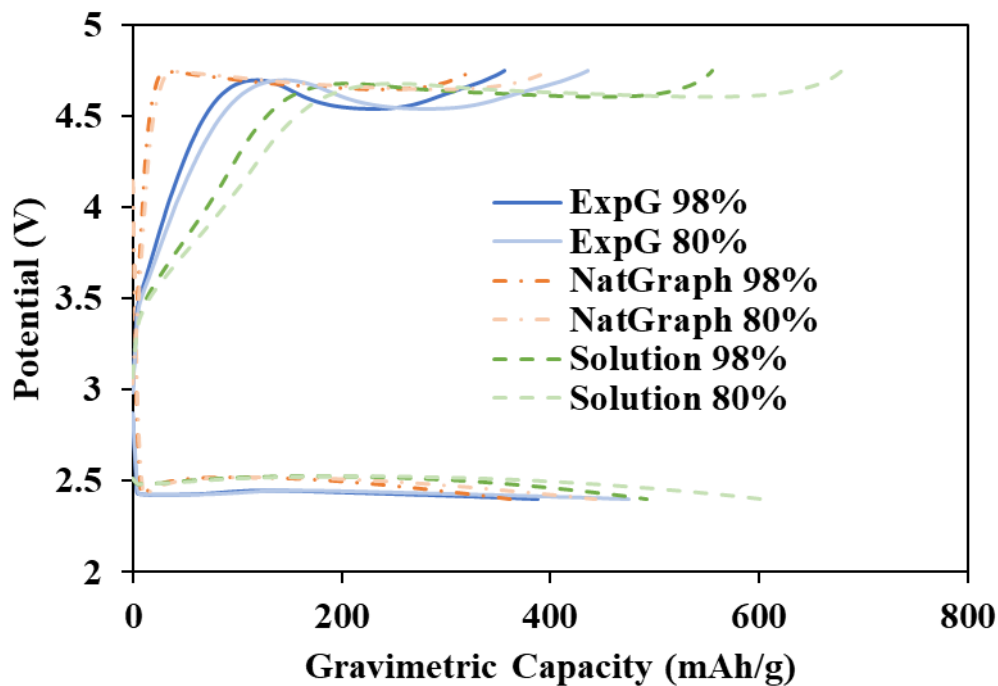


Figure 5.25: ACES Graphene Deep Discharge Cycling Curves. The darker lines represent the ideal 98% graphene solid content, while the lighter lines represent a possible lower carbon percentage, due to possible increase in the end mass fraction of polymer additives due to excessive graphite crash-out during centrifugation.

These initial graphene results show extremely poor performance within the Li-Air battery system, both with high overpotentials and an inability to maintain these overpotentials for battery capacity. There are a few different factors that could be hampering the TCR graphene cathode system: 1. The graphene sheets are too small and are not able to create a singular, interconnected reaction surface. 2. The inherent impurities within the graphite precursors are hampering battery performance. 3. The added stabilizer and surfactant are hampering battery performance. 4. The lack of a polymer binder does not allow for stability of the graphene cathode. The polymer surfactant can be easily be removed in post-processing, as poly acrylic acid can be destabilized by heating at 300°C for 2 hours in inert atmosphere. However, Xanthan Gum

degrades above 900°C, making post-processing heat treatment difficult. It is possible to complete the TCR without the Xanthan Gum, and the images of such graphenes from graphite from Sigma Aldrich can be seen in Figure 5.26. The TEM images show that the removal of the Xanthan Gum does increase the average number of layers within the graphene system. Folded single layer sheets can still be found, but there tended to also be multi-layer complexes as well. The SEM images confirm this, as the newer graphene still does not create a full coating on the carbon paper surface, just like the previous systems, but the actual graphene surface is significantly rougher, as the graphene sheets do not lie as flat upon each other. The cross-sectional images show that the newer graphene still creates a similar layer thickness to previous systems, being around 0.5 to 4 μm thick, and creating a similar bulk density of 32.63 mg/cm^3 to the earlier natural graphite system's 3657 mg/cm^3 .

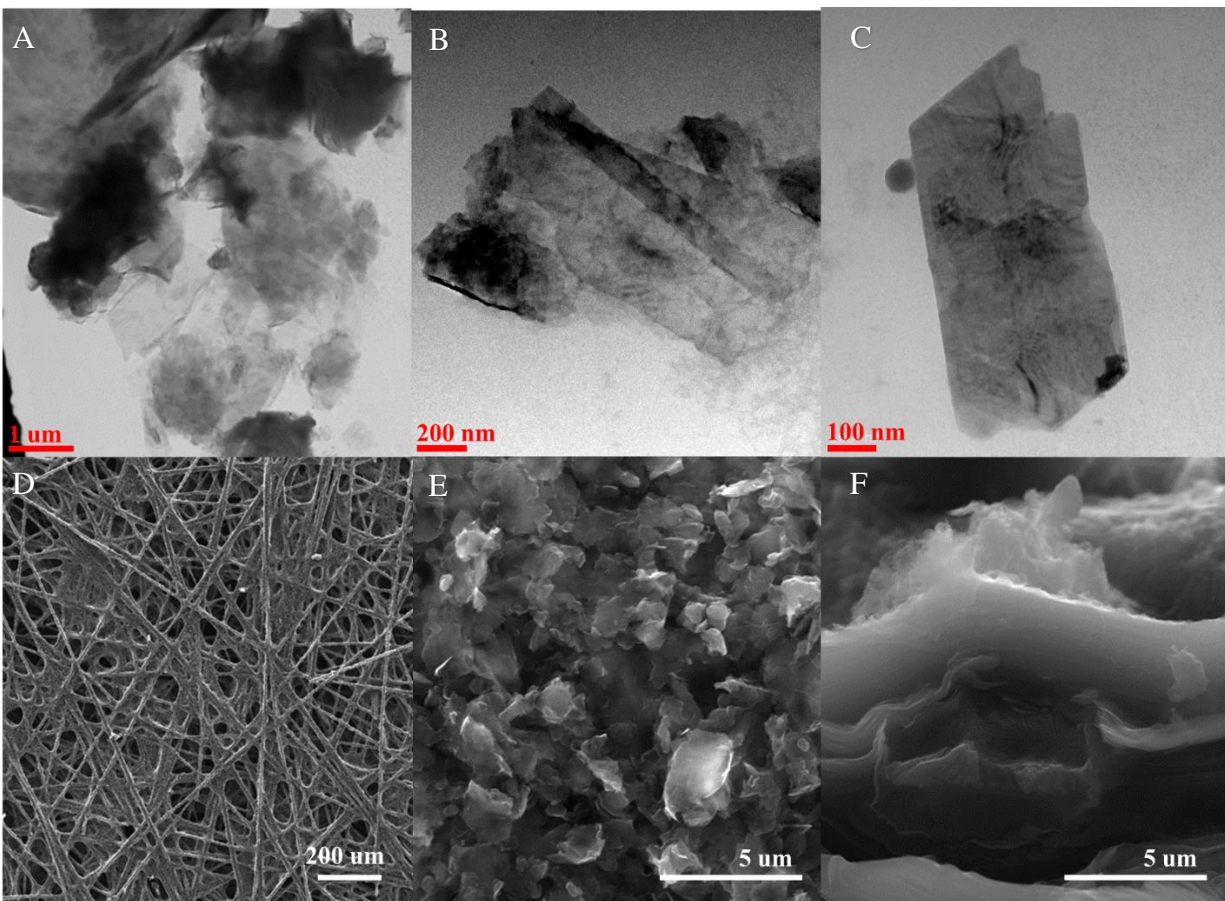


Figure 5.26: Graphene Cathode Imaging for Removed Xanthan Gum System: A-C: TEM imaging. D-F: SEM imaging. Image F is a cross-sectional image.

The battery cycling data shows significant improvement upon the removal of these additives, as can be seen in Figure 5.27. The removal of the Xanthan Gum alone caused around 0.4 V drop in the charge overpotential. Upon the removal of the surfactant and the Xanthan Gum together, the capacity nearly doubled to 880 mAh/g. Additionally, both of these systems showed much flatter charge curves than the previous natural graphite system, suggesting that fewer side reactions were present in the system to lower the overpotential after the initial overpotential was reached. Although the total capacity is still meager, this shows that the graphene system does host potential merit, once the graphite impurities and additives have been dealt with.

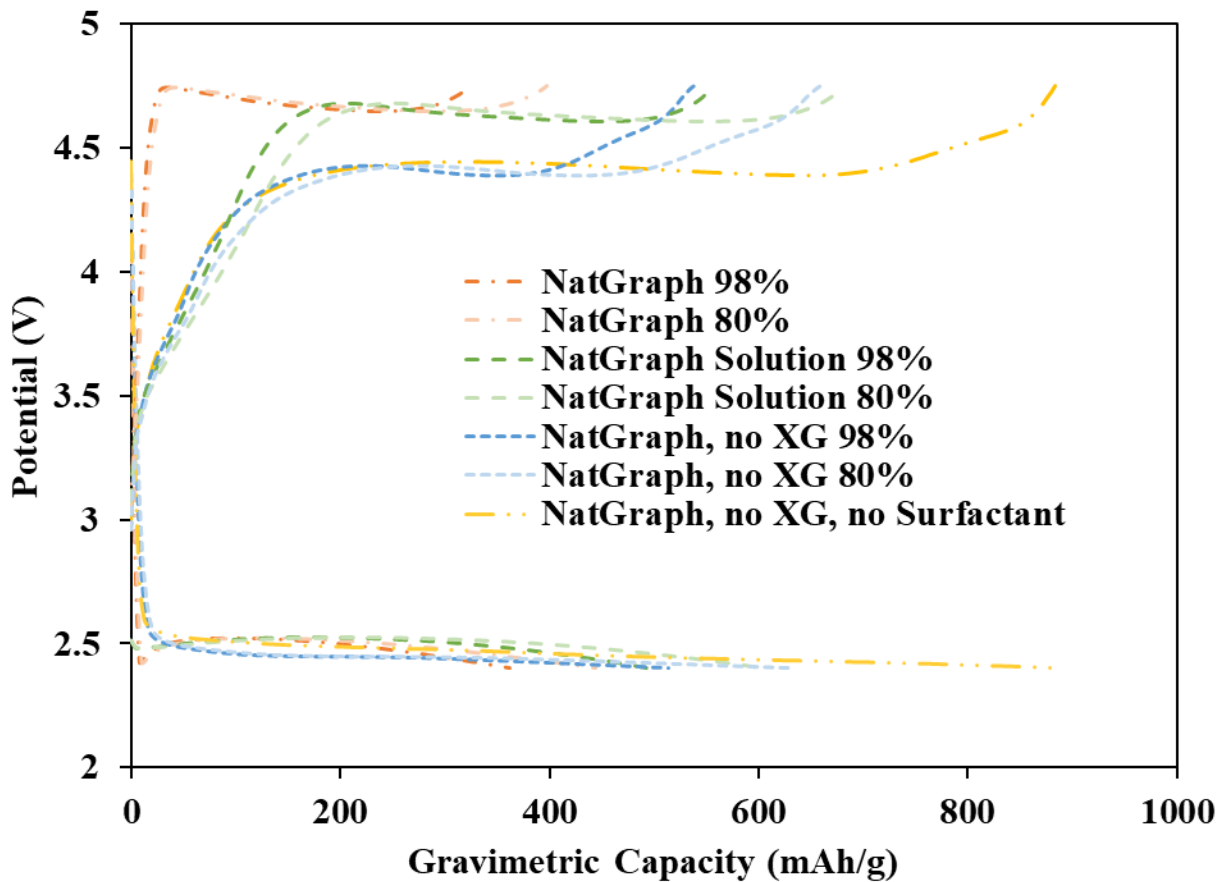


Figure 5.27: Natural Graphite Battery Comparisons with Removed Surfactant and Stabilizers.

The final system is not split into 98% and 80% because the mass loading was taken after heat treatment to remove the stabilizer, so no approximation of remaining polymer was necessary in that system.

5.4 Conclusions

Throughout this chapter, we've discussed many different ways that the Li-Air battery can be approached. Considering the success of ACES for rGO cathodes, we considered both substrateless and binderless cathodes, where the former showed that glass fiber separators are a poor spray substrate and leads to short circuits, while the later shows overpotential improvements but lacks the stability of systems with binder. Additionally, carbon nanofiber cathodes were

considered, due to their inclusion of the active material as the reaction substrate. These showed to have much greater reaction surface area than previous ACES cathodes, though had much lower capacity due to increased cathode mass, higher overpotential, and lower uniformity. Although compression of the fiber systems has shown in literature to increase fiber interconnectivity, the use of a hot press for considering high pressure ranges proved to increase fabrication complications and lead to increased mass loss. However, these fibers were a good support system for the addition of metal electrocatalysts, such as Mo_2C and Fe_2C , as shown by XRD. Upon undergoing activation for increased surface area, the Mo_2C was converted to a metal oxide catalyst MoO_2 , which while showing that increased activation increased capacity, the creation of MoO_3^- complexes and the creation of Li_2CO_3 side-products greatly hampered cyclability, counteracting the proposed benefit that the electrocatalyst would decrease the system overpotential. This was also true when Mo_2C nanoparticle were added to the rGO ACES system, showing a drop in capacity, but a large increase in the charge overpotential. Lastly, we considered a new, cheaper carbon alternative, graphene via TCR. Initial results have shown that this system produces low capacity currently, but has also shown that removal of the additives prevents side reactions and improves performance. This area could be particularly promising after the removal of the impurities from original graphite state and increasing the graphene dimensions to a few microns to create a fully interconnected active material layer for the reactions to take place.

5.5 Appendices

1. Manthiram, A., Fu, Y., Chung, S-H., Zu, C., Su, Y-S., “Rechargeable Lithium-Sulfur Batteries”, *Chem. Rev.*, **114**, 11751-11787, (2014)
2. Jiang, J., Li, Y., Liu, J., Huang, X., Yuan, C., Lou, X.W., “Recent Advances in Metal Oxide-based Electrode Architecture Design for Electrochemical Energy Storage”, *Adv. Mater.*, **24**, 5166-5180, (2012)
3. Hwang, J-Y., Myung, S-T., Sun, Y-K., “Sodium-ion batteries: present and future”, *Chem. Soc. Rev.*, **46**, 3529-3614, (2017)
4. Ji, X., Nazar, L.F., “Advances in Li-S batteries”, *J. Mater. Chem.*, **20**, 9821-9826, (2010)
5. Campbell, B., Ionescu, R., Favors, Z, Ozkan, C.S., Ozkan, M., “Bio-Derived, Binderless, Hierarchically Porous Carbon Anodes for Li-ion Batteries”, *Sci. Rep.*, **5**, 14575, (2015)
6. Zhang, G.Q., Zheng, J.P., Liang, R., Zhang, C., Wang, B., Hendrickson, M., Plichta, E.J., “Lithium-Air Batteries Using SWNT/CNF Buckypapers as Air Electrodes”, *J. Electrochem. Soc.*, **157**, 8, A953-956, (2010)
7. Yin, H., Qu, H-Q., Liu, Z., Jiang, R-Z., Li, C., Zhu, M-Q., “Long cycle life and high rate capability of three dimensional CoSe₂ grain-attached carbon nanofibers for flexible sodium-ion batteries”, *Nano Energy*, **58**, 715-723, (2019)
8. Williams, B.P., Joo, Y.L., “Tunable Large Mesopores in Carbon Nanofiber Interlayers for High-Rate Lithium Sulfur Batteries”, *J. Electrochem. Soc.*, **163**, 13, A2745-2756, (2016)
9. Chen, C., Xu, H., Zhou, T., Guo, Z., Chen, L., Yan, M., Mai, L., Hu, P., Cheng, S., Huang, Y., Xie, J., “Integrated Intercalation-Based and Interfacial Sodium Storage in

- Graphene-Wrapped Porous $\text{Li}_4\text{Ti}_5\text{O}_{12}$ Nanofibers Composite Aerogel”, *Adv. Energy Mater.*, **6**, 1600322, (2016)
10. Cho, D., Kim, M., Hwang, J., Park, J.H., Joo, Y.L., Jeong, Y., *Nanoscale Res. Lett.*, **10**, 424, (2015)
 11. Panels, J.E., Joo, Y.L., “Incorporation of Vanadium Oxide in Silica Nanofiber Mats via Electrospinning and Sol-Gel Synthesis”, *J. Nanomater.*, **2006**, 1-10, (2006)
 12. Yan, K., Kong, L-B., Dai, Y-H., Shi, M., Shen, K-W., Hu, B., Luo, Y-C., Kang, L., “Design and preparation of highly structure-controllable mesoporous carbons at the molecular level and their application as electrode materials for supercapacitors”, *J. Mater. Chem. A.*, **3**, 22781-22793, (2015)
 13. Huang, Z-H., Zhang, Y-Z., Kotaki, M., Ramakrishna, S., “A review on polymer nanofibers by electrospinning and their application in nanocomposites”, *Compos. Sci. Technol.*, **63**, 2223-2253, (2003)
 14. Hansen, N.S., Cho, D., Joo, Y.L., “Metal Nanofibers with Highly Tunable Electrical and Magnetic Properties via Highly Loaded Water-Based Electrospinning”, *Small*, **8**, 10, 1510-1514, (2012)
 15. Joh, H-I., Song, H.K., Lee, C-H., Yun, J-M., Jo, S.M., Lee, S., Na, S-I., Chien, A-T., Kumar, S., “Preparation of porous carbon nanofibers derived from graphene oxide/polyacrylonitrile composites as electrochemical electrode materials”, *Carbon*, **70**, 308-312, (2014)
 16. Mao, X., Hatton, T.A., Rutledge, G.C., “A Review of Electrospun Carbon Fibers as Electrode Materials for Energy Storage”, *Curr. Org. Chem.*, **17**, 13, 1390-1401, (2013)

17. Zhang, L., Aboagye, A., Kelkar, A., Lai, C., Fong, H., “A review: carbon nanofibers from electrospun polyacrylonitrile and their applications”, *J. Mater. Sci.*, **49**, 463-480, (2014)
18. Jung, J-W., Lee, C-L., Yu, S., Kim, I-D., “Electrospun nanofibers as a platform for advanced secondary batteries: a comprehensive review”, *J. Mater. Chem. A*, **4**, 703-750, (2016)
19. Nataraj, S.K., Yang, K.S., Aminabhavi, T.M., “Polyacrylonitrile-based nanofibers – A state-of-the-art review”, *Prog. Polym. Sci.*, **37**, 487-513, (2012)
20. Lu, Y-C., Gallant, B.M., Kwabi, D.G., Harding, J.R., Mitchell, R.R., Whittingham, M.S., Shao-Horn, Y., “Lithium-oxygen batteries: bridging mechanistic understanding and battery performance”, *Energy Environ. Sci.*, **6**, 750-768, (2013)
21. Cheng, F., Chen, J., “Metal-Air Batteries: From Oxygen Reduction Electrochemistry to Cathode Catalysts”, *Chem. Soc. Rev.*, **41**, 2172-2192, (2012)
22. Lu, Y-C., Gasteiger, H.A., Shao-Horn, Y., “Catalytic Activity Trends of Oxygen Reduction Reaction for Nonaqueous Li-Air Batteries”, *J. Am. Chem. Soc.*, **133**, 19048-19051, (2011)
23. Harding, J.R., Lu, Y.C., Tsukada, Y., Shao-Horn, Y., “Evidence of Catalyzed Oxidation of Li₂O₂ for Rechargeable Li-Air Battery Applications”, *Phys. Chem. Chem. Phys.*, **14**, 10540-10546, (2012)
24. Wang, L-Z., Xu, D., Xu, J-J., Zhang, Z-B., “Oxygen electrocatalysts in metal-air batteries: from aqueous to nonaqueous electrolytes”, *Chem. Soc. Rev.*, **43**, 7746-7786, (2014)

25. McCrory, C.C.L., Jung, S., Peters, J.C., Jaramillo, T.F., “Benchmarking Heterogeneous Electrocatalysts for the Oxygen Evolution Reaction”, *J. Am. Chem. Soc.*, **135**, 16977-16987, (2013)
26. Cao, R., Lee, J-S., Liu, M., Cho, J., “Recent Progress in Non-Precious Catalysts for Metal-Air Batteries”, *Adv. Energy Mater.*, **2**, 816-829, (2012)
27. Zhang, K., Han, X., Hu, Z., Zhang, X., Tao, Z., Chen, J., “Nanostructured Mn-Based Oxides for Electrochemical Energy Storage and Conversion”, *Chem. Soc. Rev.*, **44**, 699-728, (2015)
28. Débart, A., Paterson, A.J., Bao, J., Bruce, P.G., “ α -MnO₂ Nanowires: A Catalyst for the O₂ Electrode in Rechargeable Lithium Batteries”, *Angew. Chem. Int. Ed.*, **47**, 4521-4524, (2008)
29. Jian, Z., Liu, P., Li, F., He, P., Guo, X., Chen, M., Zhou, H., “Core-Shell-Structured CNT@RuO₂ Composite as a High-Performance Cathode Catalyst for Rechargeable Li-O₂ Batteries”, *Angew. Chem. Int. Ed.*, **53**, 442-446, (2014)
30. Yin, J., Carlin, J.M., Kim, J., Li, Z., Park, J.H., Patel, B., Chakrapani, S., Lee, S., Joo, Y.L., “Synergy Between Metal Oxide Nanofibers and Graphene Nanoribbons for Rechargeable Lithium-Oxygen Battery Cathodes”, *Adv. Energy Mater.*, **5**, 1401412 1-8, (2015)
31. Thotiyl, M.M.O., Freunberger, S.A., Peng, Z., Chen, Y., Liu, Z., Bruce, P.G., “A stable cathode for the aprotic Li-O₂ battery”, *Nat. Mater.*, **12**, 1050-1056, (2013)
32. Cho, D., Park, J.H., Jeong, Y., Joo, Y.L., “Synthesis of Titanium Carbide-Carbon Nanofibers via Carbothermal Reduction of Titania with Carbon”, *Ceram. Int.*, **41**, 10974-10979, (2015)

33. Kundu, D., Black, R., Adams, B., Harrison, K., Zavadil, K., Nazar, L.F., “Nanostructured Metal Carbides for Aprotic Li-O₂ Batteries: New Insights into Interfacial Reactions and Cathode Stability”, *J. Phys. Chem. Lett.*, **6**, 2252-2258, (2015)
34. Aurbach, D., McCloskey, B.D., Nazar, L.F., Bruce, P.G., “Advances in Understanding Mechanisms Underpinning Lithium-Air Batteries”, *Nat. Energy*, **1**, 1-11, (2016)
35. Xu, J-J., Xu, D., Wang, Z-L., Wang, H-G., Zhang, L-L., Zhang, X-B., “Synthesis of Perovskite-Based Porous La_{0.75}Sr_{0.25}MnO₃ Nanotubes as a Highly Efficient Electrocatalyst for Rechargeable Lithium-Oxygen Batteries”, *Angew. Chem. Int. Ed.*, **52**, 3887-3890, (2013)
36. Jin, C., Yang, Z., Cao, X., Lu, F., Yang, R., “A novel bifunctional catalyst of Ba_{0.9}Co_{0.5}Fe_{0.4}Nb_{0.1}O_{3-δ} perovskite for lithium-air battery”, *Int. J. Hydrog. Energy*, **39**, 2526-2530, (2014)
37. Shao, Y., Park, S., Xiao, J., Zhang, J-G., Wang, Y., Liu, J., “Electrocatalysts for Nonaqueous Lithium-Air Batteries: Status, Challenges, and Perspective”, *ACS Catal.*, **2**, 844-857, (2012)
38. McCloskey, B.D., Scheffler, R., Speidel, A., Bethune, D.S., Shelby, R.M., Luntz, A.C., “On the Efficacy of Electrocatalysis in Nonaqueous Li-O₂ Batteries”, *J. Am. Chem. Soc.*, **133**, 18038-18041, (2011)